# INVESTIGATION OF PHONONIC CRYSTALS FOR DISPERSIVE SURFACE ACOUSTIC WAVE OZONE SENSORS

A Thesis
Presented to
The Academic Faculty

by

Ryan S. Westafer

In Partial Fulfillment
of the Requirements for the Degree
Doctor of Philosophy in the
School of Electrical and Computer Engineering

Georgia Institute of Technology
August 2011

**INVESTIGATION OF PHONONIC CRYSTALS FOR DISPERSIVE SURFACE ACOUSTIC WAVE OZONE SENSORS**

Approved by:

Professor J. Stevenson Kenney,
Committee Chair
School of Electrical and Computer Engineering
*Georgia Institute of Technology*

Professor Thomas E. Michaels
School of Electrical and Computer Engineering
*Georgia Institute of Technology*

Professor William D. Hunt, Advisor
School of Electrical and Computer Engineering
*Georgia Institute of Technology*

Professor Michael H. Bergin
School of Civil and Environmental Engineering
*Georgia Institute of Technology*

Professor Gregory D. Durgin
School of Electrical and Computer Engineering
*Georgia Institute of Technology*

Date Approved: June 27, 2011

# ACKNOWLEDGEMENTS

I would first like to thank God for so blessing me in family and in friends and mentors, my champions; those who have in countless ways enabled me to pursue a lifetime of learning. For some, I can only remember faces and smiles; for others, names spring to mind and are included below. It should be clear that doctoral study need not be a lonely pursuit!

Kristin, the true complement to me and to this effort, made time for the late nights and inevitable delays, while serving as both a gifted and compassionate veterinarian and a loving mother. From jogs in Piedmont Park to tolerance of a 3-year obsession with volleyball, Kristin was my companion every step of the way. Most recently, I am grateful for little Vivian who lit up the last year of this effort with shy smiles, big grins, giggles, kicking feet, and little fingers that love to "type" on my keyboard.

I cannot in finite words describe the love and support of my mother and father, Dr. Anita S. Westafer and Dr. John M. Westafer, who cultivated and supported all of my technical interests – from Radio Shack kits and the accumulation of a complete set of "Mini-Notebooks" by Forrest M. Mims III, to an EEPROM programmer, my first copy of slackware linux, a drill press, and proper installation of an extra 240 VAC breakered circuit for a home-built arc welder – exemplifying the principle that education starts in the home and need not be left only to the schools and the "normal" or "expected" modes of learning. Special appreciation is also reserved for my siblings Lauren and Michael, for tolerating my exacting nerdiness, rounding my edges, and being a whole lot of fun. I delight in their successes, especially in carrying forward the medical profession in our family.

Outstanding teachers and educational programs have enriched my life, too. I especially remember Ms. Green, Ms. Cole, Ms. Larson, Ms. Leininger, Ms. Dickerson, Joy Grace, Judy Rowland, Ann Mazenko, Neal McLeod, Mary Easley, and Linda Knowles. Coaching the Science Olympiad teams to numerous State victories: Caroline Parker, Deborah Cathey, Melanie Waite, Merrill Bordelon, and JoAnn Parsons - along with parent and community

support. In collegiate studies at Georgia Tech, certain stand-outs were Profs. Ali Adibi, Phillip E. Allen, Bonnie Ferri, and Bill Hunt. During the college breaks, Dr. Anil Raj of IHMC in Pensacola, FL provided very stimulating, rewarding, and joyfully creative projects in support of fascinating research in human-centered systems.

Among friends, I especially appreciate Shawn M. Lankton, for life-long friendship and pace-keeping, including his exemplary execution of his doctoral work. Often conspiring together, Jon Epstein and Ian Harrison provided great camaraderie and engineering fun, including *sous-vide* steaks and unique units of measure. Other GT friends who have recently impacted my life include: Milap Dalal, Jimi Malcolm, Dave D. Muir, and Miguel A.T. Walter.

On campus, I enjoyed lunches at Tin Drum with Kevin Brenner, Jenna Fu, "Rama"samy Ravindran, and Ian Yang, conversing on topics from graphene to acoustic sensors to hockey. In extracurricular activities, I am particularly grateful for interactions with Prof. Whit Smith (IEEE Hardware Team) and Profs. Ray Vito, Craig Forest, and Merrick Furst (InVenture Prize). Exceptional student leaders also influenced me as we worked together: Abhinav Saxena and Matt Wiggins (Eta Kappa Nu); Jake Heinrichs (GT Men's Volleyball Club); Huan Du, Jason Cordero, Ann Trippe, and Alice Cheung (Tau Beta Pi); and Melissa McCoy (Enterprise 2 Empower).

In the course of the doctoral research, I first thank my advisor, Prof. Bill Hunt. As an undergraduate, I was captivated by his genuine interest in between-class discussions ranging from electromagnetics to electrophysiology and biosensing. This resonated with my desire to learn more about cross-disciplinary applications of electrical engineering. Prof. Hunt has always supported my diverse interests, especially in the culmination of nearly 6 years of work covering a wide swath of surface acoustic wave research including simulation, design, fabrication, and measurement. Along the way, Dr. Peter J. Edmonson provided conceptual and technical starting points for the early SAW tag biosensor work and also technical review and wisdom. Dr. Saeed Mohammadi (graduate of Prof. Ali Adibi's group) was also a great collaborator, offering very helpful suggestions and also thoughtful questions and critique.

I especially thank fellow graduate students of the Microelectronic Acoustics Group: Dr.

Desmond D. Stubbs, Dr. Sang-Hun Lee, Dr. Christopher D. Corso, Dr. Tony J. Dickherber, Eric W. Massey, John K. Perng, Farasat Munir, Adam Wathen, and former student affiliates Dr. Brent Buchine and Dr. George Yu. I also enjoyed working with several particularly outstanding undergraduate researchers: Matt Jordan, Sean A. McGee, Jessica K. Peters, G. "Steve" Ruff, Alice Wang, and Stephen Welch.

In the Petit Microelectronics Research Center (MiRC), key supporters were Mary Render, Sharon Lawrence, Paul Turgeon, Bob Rose, Scott Fowler, and Matt Blake. James Steinberg and Edgar Jones in the Van Leer building were ever-helpful with all the right parts and measurement equipment. In the academic office, Siri Melkote, Marilou Mycko, and Tasha Torrence made navigation of deadlines and paperwork a breeze.

Finally I would like to acknowledge funding and collaboration. The phononic crystals work was supported by the National Science Foundation under contract number ECS-0524255 (L. Lunardi) and the Office of Naval Research under contract no. 21066WK (M. Specter). The Principal Investigators were Professors Ali Adibi and William D. Hunt, both of the School of Electrical and Computer Engineering. The collaborative sensing effort was made possible by the support of Professor Mike Bergin of the School of Environmental Engineering and Professor Dennis Hess and Dr. Galit Levitin of the School of Chemical and Biomolecular Engineering. I also extend my gratitude to David Reid, Greg Kiesel, and Jim Acree of GTRI for their direct roles in connecting me to the Signature Technology Laboratory and hosting me half-time during my last year of doctoral study.

# TABLE OF CONTENTS

# LIST OF TABLES

## LIST OF FIGURES

# GLOSSARY

**CCW** Coupled Cavity Waveguide, p. 14.

**dBi** deciBels relative to isotropic radiator, p. 9.

**DBR** Distributed Bragg Reflector, p. 15.

**DoE** Depth of Energy, p. xi.

**DoS** Density of States, p. 41.

**EPA** Environmental Protection Agency, p. 1.

**FEM** Finite Element Method, p. 45.

**HERO** Hazards of Electromagnetic Radiation to Ordnance, p. 8.

**LOD** Limit of Detection, p. 161.

**OSHA** Occupational Safety and Health Administration, p. 1.

**PB** Polybutadiene, p. 5.

**PnC** Phononic Crystal, p. 12.

**QCM** Quartz Crystal Microbalance, p. 4.

**RAC** Reflective Array Compressor, p. 9.

**RSAW** Rayleigh Surface Acoustic Wave, p. 118.

**SAW** Surface Acoustic Wave, p. 1.

**SHSAW** Shear Horizontal Surface Acoustic Wave, p. 117.

**SSBW** Surface-Skimming Bulk Wave, p. 29.

**STW** Surface Transverse Wave, p. xiv.

**TB** Time(duration)-Bandwidth product, p. 11.

**TCD** Temperature Coefficient of Delay, p. 9.

**UHF** Ultra High Frequency, p. 200.

# SUMMARY

The object of this research was to investigate dispersion in surface phononic crystals (PnCs) for application to a newly developed passive surface acoustic wave (SAW) ozone sensor. Frequency band gaps and slow sound already have been reported for PnC lattice structures. Such engineered structures are often advertised to reduce loss, increase sensitivity, and reduce device size. However, these advances have not yet been realized in the context of surface acoustic wave sensors. In early work, we computed SAW dispersion in patterned surface structures and we confirmed that our finite element computations of SAW dispersion in thin films and in one dimensional surface PnC structures agree with experimental results obtained by laser probe techniques. We analyzed the computations to guide device design in terms of sensitivity and joint spectral operating point. Next we conducted simulations and experiments to determine sensitivity and limit of detection for more conventional dispersive SAW devices and PnC sensors. Finally, we conducted extensive ozone detection trials on passive reflection mode SAW devices, using distinct components of the time dispersed response to compensate for the effect of temperature. The experimental work revealed that the devices may be used for dosimetry applications over periods of several days.

# CHAPTER I

# INTRODUCTION

This introductory chapter provides a review of the motivation, application, background literature, and opportunities pertaining to the study of surface phononic crystals for passive surface acoustic wave (SAW) ozone sensors. Though much of this dissertation is devoted to the design and characterization of passive dispersive acoustic sensors, we believe that an application to personal exposure monitoring is particularly compelling and will first discuss the opportunity in some detail.

## *1.1 Motivation*

Ozone ($O_3$) is a major component of urban smog and is of particular concern due to its impact upon public health. Regulations set forth by the Occupational Safety & Health Administration (OSHA) specify a maximum allowed concentration of 100 parts per billion (ppb) averaged over an 8 hour period[1]. Further illustrating the concern for ozone levels, in 2008 the Environmental Protection Agency (EPA) revised the National Air Quality Standards (NAAQS). The "8-hour primary ozone standard" was reduced to 75 ppb. Figure 1.1 shows use of the eight hour average for outdoor data, and it reveals metropolitan ozone concentration approaching unhealthy levels for an arbitrary day of the year [1]. Indeed the EPA threshold is frequently exceeded, particularly in regions of the southeast United States, where ozone levels naturally are elevated. In Figure 1.1 the use of an 8-hour averaging window and the peak concentration near hour 20 (8 PM) imply the period of greatest ozone concentration was during the 8 hours prior; i.e. after 12 PM. In 2010, exceedances of the federal air quality standard for ozone began on May 5 and continued at a rate of approximately 4 days per month through September 2010 [1].

In 2006 the National Institutes of Health (NIH) issued a request for applications titled,

[1] 29 CFR 1910.1000 Z-1 Table

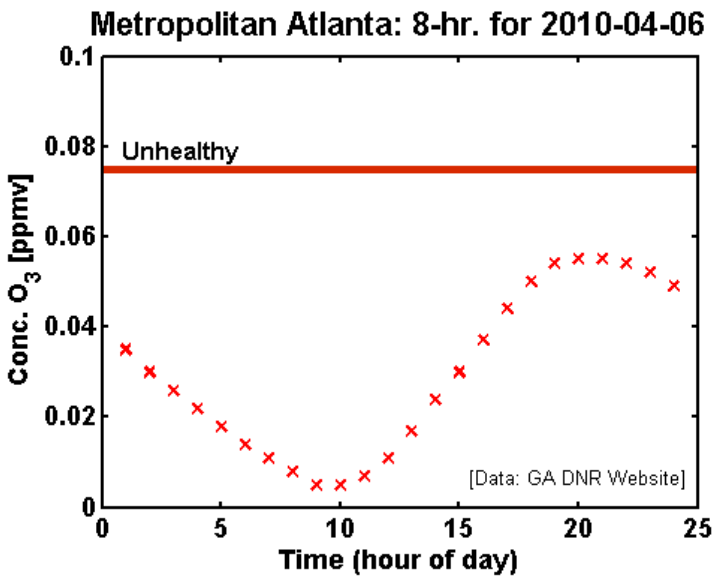


**Figure 1.1:** Outdoor ozone concentration recorded by a monitoring station in metropolitan Atlanta. The data correspond to a standard 8-hour moving average.

"Environmental Sensors for Personal Exposure Assessment" (RFA-ES-06-011). Although the influence of ozone on human health has been widely documented, a key problem has remained in the assessment of actual impact to the public: measurements are seldom performed on both personal and real time bases. Such measurements are needed for two primary reasons:

- **Location:** There are just 65 Air Monitoring Sites in the state of Georgia [1], and furthermore, ozone is a very volatile gas and substantial spatial concentration gradients have been shown to exist within just half a *meter* of test subjects [59].
- **Latency:** Studies of *personal* ozone exposure have relied on passive sampling methods requiring long exposure intervals of 12 to 24 hours [53, 13].

Thus the development of inexpensive, portable, and queryable ozone sensors is expected to be of great utility to the occupational and environmental health communities.

## *1.2 Concept*

Starting with a general system-level concept, we will proceed to discuss the sensor requirements. Figure 1.2 gives a relatively abstract view of the role of a passive sensor tag (SAW

tag) in a monitoring system. The query unit, or "reader" is responsible for processing the returned signal and extracting salient features for logging.

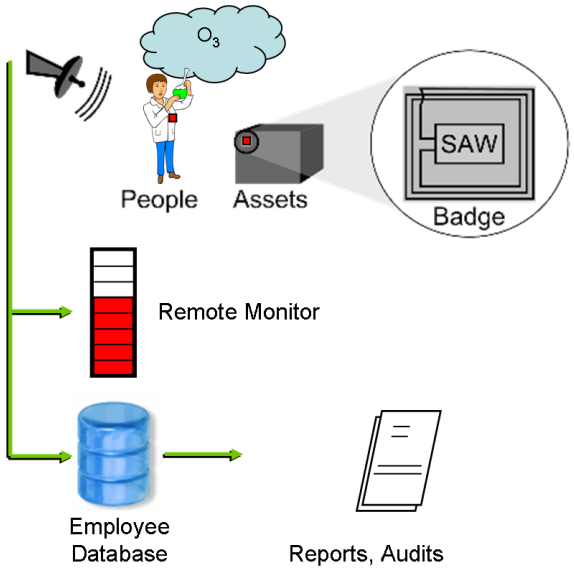


**Figure 1.2:** Conceptual diagram of the capabilities afforded by low cost passive ozone sensor tags.

Considering this system concept and the motivating factors, we next summarize the desired sensor characteristics:

- Passive wireless sensor tag
- No battery; power derived from RF signal
- Small size; 433+ MHz operation
- Sensitivity to ozone at less than 100 parts-per-billion
- Lifetime greater than 600 ppb-hours
- Inexpensive (single-use tags)

  Tags ($)

  Readers ($$$)

To our knowledge, such devices have not been used for personal dosimetry; this is likely due to the bulky measurement equipment, useful life, cost, etc.

## *1.3 Existing Technologies*

Existing technologies for the detection of ozone center around the well-known photometric and gas-sensitive semiconductor methods. Photometric analyzers employ the ultraviolet absorption of ozone to determine the concentration using Beer's law. This conventional approach requires ultraviolet lamps that dissipate significant heat. Although lower power ultraviolet LEDs are available, they operate in the near-UV, e.g. zinc oxide at 395 nm, and not near the strongest optical absorption peak at 253 nm in the Hartley band [36]. When passive wireless sensing is considered, the power consumption of these optical techniques is still prohibitive. Even alternative gas-sensitive semiconductor sensors require significant power. This is due to the necessity of heating tin oxide ($SnO_2$) above 100 °C to remove moisture. One handheld ozone sensor[2] requires 5 Watts on average; its 9.6 V and 2100 mAh battery pack only powers the device for 4 hours. Such bulky equipment is undesirable for routine and scalable personal monitoring. In this work we instead consider (and use) a so-called "gravimetric" approach.

Gravimetric methods are alternatives to the aforementioned techniques. Some materials experience a mass increase in response to ozone exposure and may be weighed in the laboratory. A more portable version of this technique is the *dynamic* gravimetric approach which similarly weighs sensitive material, except by vibration. A large class of mechanically resonant gravimetric sensors includes microelectromechanical (MEMS) devices, e.g. cantilevers, etc. These typically involve the vibration of relatively large masses with large displacements, but acoustic wave sensors operate at much smaller wavelengths and displacements with respect to a structure's volume. Notable devices include the quartz crystal microbalance (QCM), SAW resonator, and SAW delay line. Displacements at the device surface are typically a few Angstroms or less, and operating frequencies are usually above 1 MHz.

In 1985 Fog and Reitz demonstrated a dynamic gravimetric approach for ozone detection [27]. They used a quartz crystal microbalance (QCM) to conduct real time detection of

[2] Aeroqual S-200UL

ozone around welders at the Danish Welding Institute. Their bulk acoustic wave sensors were coated with an alkene polymer, polybutadiene (PB), which demonstrated mass increase during irreversible reaction with ozone. The reaction occurred under ambient temperature and relative humidity, and the sensors were not heated. This low power acoustic method of detection is extensible to passive acoustic wave devices, and so we proceed to review important principles of acoustic wave sensors.

### 1.3.1 Acoustic Wave Sensors

Acoustic wave sensors may be constructed of many materials and may be designed to support many different acoustic modes. The two used in this work are shown in Figure 1.3. The QCM (Figure 1.3a) is an acoustic sensor utilizing a piezoelectrically active shear bulk mode of crystalline quartz. The wave reverberates in the thickness direction of a thin polished plate of the material, and the resonator is made electrically excitable when electrodes are attached to the top and bottom surfaces. The surface acoustic wave (Figure 1.3b) is a solution obtained from the higher frequency modes of such a plate as it is made infinitely thick. Both illustrated solutions were computed using the finite element method (as described in Chapter 3).

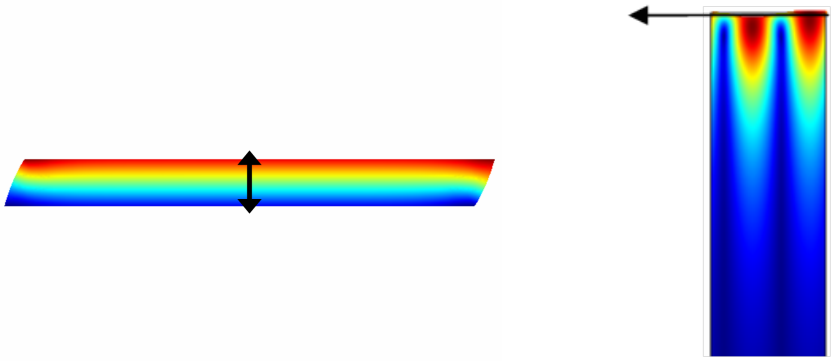

**(a)** Shear Bulk Acoustic Wave (BAW)

**(b)** Surface Acoustic Wave (SAW)

**Figure 1.3:** Comparison of bulk and surface modes. Displacements are colored and Poynting vectors are given by arrows.

To serve as a sensor, the QCM utilizes the frequency-pulling effect of mass loading at

the boundary of the resonator. For such resonant (narrow band) devices, the frequency-pulling sensitivity with respect to mass, $S_m^f = \frac{\partial f}{\partial m}$ is proportional to the resonant frequency squared, according to the Sauerbrey equation [85]:

$$\Delta f = \frac{-2{f_0}^2 \Delta m}{A\sqrt{\mu\rho}}. \tag{1.1}$$

So resonant devices with high center frequency, $f_0$, are desired to obtain large frequency shifts, $\Delta f$, for a given mass change, $\Delta m$. In (1.1), $A$ is the surface area, and $\mu$ and $\rho$ are the stiffness and density of the quartz resonator, respectively. Sauerbrey's equation was derived specifically for the thin plate quartz resonator, but in general the proportionality to ${f_0}^2$ depends upon the mode type, material constants, etc. For arbitrary devices, (1.1) may be modified according to a perturbation analysis or numerical computation. In this chapter we review the use of perturbation theory to obtain the coefficient to ${f_0}^2$. We have also used full finite element field calculations to compute the frequency shift due to mass loading.

Following development of the QCM, SAW devices were adapted for chemical sensing *circa* 1979 [99]. The next two decades brought significant advances to *wired* SAW sensors: higher operating frequencies, compatibility with fluid media, and physical, chemical, and biological approaches to detection [99, 50, 92]. Only recently have these advances been applied to *wireless* SAW sensors.

For real-time monitoring of portable acoustic wave sensors, several approaches are available. For instance, a SAW dosimeter could be remotely interrogated by radio or optical means, or it could have a power source, microcontroller, and memory for data logging. The following chapters of this work focus on devices to be used in a fully passive radio interrogation approach. Such sensors are designed to operate like RFID tags and to be worn by individuals. For typical occupational or research environments, a suitable read range is just a few meters. Furthermore, the need for small antennas and high fidelity (data rates) points to the use of higher frequency devices, typically in the UHF range. Passive SAW tags are suitable for this application, and so we will review them in more detail.

### 1.3.2 Passive SAW Tags

A fully passive SAW transponder typically features an antenna coupled to an acoustic transducer on a piezoelectric substrate. Incident electromagnetic waves then produce time varying fields at the device surface and SAWs are generated by the piezoelectric effect. A conceptual illustration is provided in Figure 1.4; it is not to scale (acoustic wavelengths would be five orders of magnitude smaller).

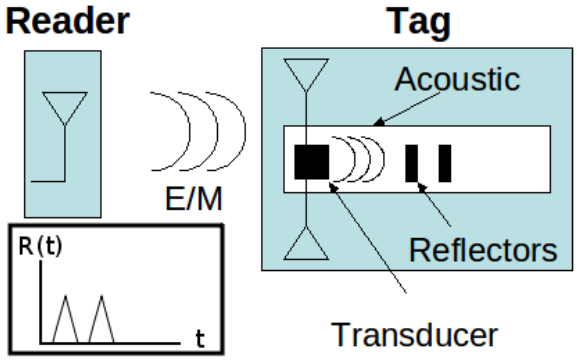


**Figure 1.4:** Conceptual diagram of reader and SAW tag. Inset at left depicts reflection response due to two primary reflectors.

In these devices, strongly piezoelectric materials are used because this transduction step contributes significant loss. A commonly used material, lithium niobate ($LiNbO_3$), has a relatively large electromechanical coupling coefficient, $K^2$, of approximately 5%. Given the transduction step must occur twice, once for input and once for output, the device's *wired* (albeit unmatched) return signal is expected to be much weaker: $10\log_{10}(K^4) \approx -26$ dB. This intrinsic loss, in conjunction with the *wireless* round-trip path loss ($r^{-4}$), presents a significant challenge for broad application of these devices.

Despite the conversion losses, key advantages of SAW tags stem from the acoustic implementation:

- *Simple metal-on-substrate fabrication.*

  Renders the devices relatively robust to ionizing radiation and extreme temperatures when compared to semiconductor tags.

- *Linear degradation of return signal with transmitted power.*

  The acoustic tags comprise linear passive elements, whereas integrated circuit devices

exhibit fundamental drop-out at or above the thermal excitation voltage, $kT/q$ [34].

- *Less transmit power.*

  Successful readout has been shown at -40 dB relative to typical semiconductor tag readers operating between 1 and 4 Watts; this is sufficiently low for certain SAW tags to meet military HERO requirements [34].

- *Insensitivity to typical electromagnetic clutter.*

  The acoustic propagation velocity is typically five orders of magnitude less than the speed of light, and so the echoes from the acoustic devices may occur at times long after the significant electromagnetic multipath returns.

Despite the advantages, only modest ranges have been reported. Loss accounting for the query and response can be performed using a typical link budget shown in Figure 1.5. We note the round-trip device return loss, although significant, amounts to only 1/16 the one-way isotropic propagation loss at three meters: 20 dB versus 32 dB, respectively [78]. A survey of devices reported in the literature revealed typical transmit power levels and

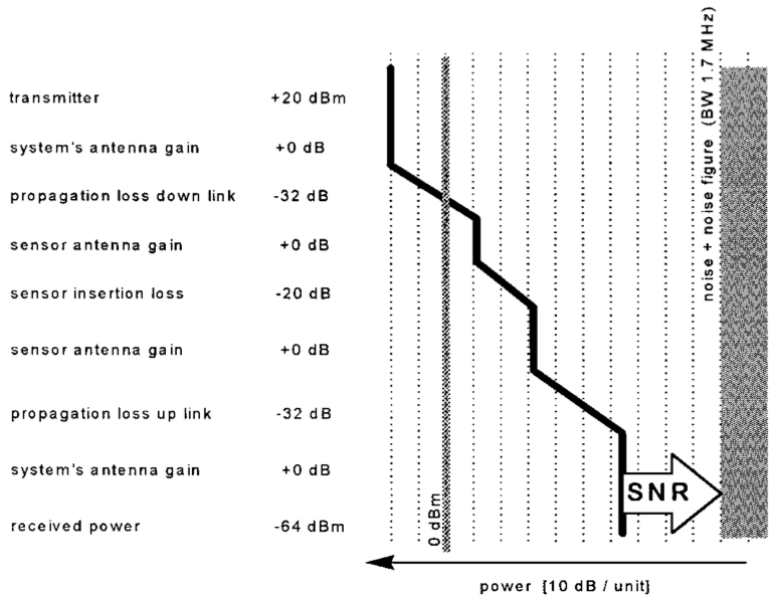


**Figure 1.5:** An example link budget calculated by A. Pohl for a passive SAW tag at a center frequency of 433 MHz and a range of 3 meters (image: A. Pohl [78]).

ranges less than ten meters. For instance, a passive carbon dioxide sensor by W. Wang et al. was demonstrated using 10 mW RF power at a distance of 0.5 meters [94]. At this distance

the 0.1 m planar loop antennas were placed just beyond the near field: $R < 0.62(D\frac{3}{\lambda})^{1/2}$, or $R < 0.4$ m. In another publication Pasternak et al. [75] reported 10 m range at 10 dBm and 433 MHz using a carefully matched printed circuit antenna. At 2.4 GHz, C. S. Hartmann reported greater than 20 m range at -3 dBm RF power and using a 15 dBi antenna [34]. The contrast in reported ranges points to the success of both system and device optimization; for instance, C. S. Hartmann [33] has also reported precision tailoring of metal strip SAW reflectors to provide diffraction compensation and allow later arrivals. Another source of variance may be different acceptable SNRs, according to the required communication data rate.

Despite these successful demonstrations, key disadvantages to the linear passive SAW tags include: (a) increased processing required in the reader device, (b) lack of writable memory, (c) one-time patterning ("programming") of unique tag identification, (d) lack of programmable encryption, etc.

Since about 1996 interest has grown for wireless SAW transponders acting as sensors, and this has occurred alongside global adoption of other radio frequency identification (RFID) technologies. The acoustic phase velocity of these sensors changes in response to perturbation of the surface boundary condition. This change has been used to measure the environmental conditions at the sensor: temperature, dielectric constant, mass loading, surface stress, etc. Recently, various wireless SAW tags have been developed to communicate time and frequency coded identification information, pressure and temperature changes, and chemical concentrations [32, 26, 28, 54, 94, 37, 58]. Table 1.1 provides typical sensitivity values.

Many SAW tags use the intrinsic temperature coefficient of delay (TCD) for temperature measurements, exploiting a historically avoided effect. Nonzero TCD causes the operating frequency and phase to scale as functions of temperature. For precision resonators used in clocks, nonzero TCD causes timekeeping error; for reflective array compressors (RACs) used in radars, nonzero TCD caused ranging error. However, the effect is useful if temperature information is desired and if this can be successfully distinguished from other changes in the signal. A reference measurement usually is necessary to distinguish the perturbation of

**Table 1.1:** Sensitivities of the SAW delay (or velocity)

| **Physical quantity** | **Linear coefficient** |
|---|---|
| Temperature | up to 100 ppm/K |
| Pressure, stress | 2 ppm/kPa |
| Force | 10 ppm/kN |
| Mass loading | 30 ppm/$\mu$g·cm$^2$ |
| Voltage | 1 ppm/V |
| Electric field | 30 ppm/V·$\mu$m$^{-1}$ |

Table after A. Pohl [78].

interest, e.g. temperature, relative to other masquerading effects, e.g. Doppler shift due to a wireless communication channel external to the sensor.

The temperature effect has been thoroughly investigated for passive SAW sensors. Neglecting response averaging, directional reader antenna, and numerous other SNR or SIR improvements, SAW sensor tags using YZ (Y-rotated, Z propagating) $LiNbO_3$ have demonstrated temperature resolution of 10 mK at about 3 meters range [78], and the TCD was 92 ppm/°C. The net SNR was better than 20 dB, yielding $10^{-5}$ $\Delta v/v$ sensitivity.

Relating this to the ozone sensor objective, we have determined a typical ozone coefficient of delay. Using a combination of measurement, mass loading calculation, and finite element computation, we obtained approximately 170 ppm/s/ppb$O_3$ at 435 MHz. Given an ozone coefficient greater than the temperature coefficient and values reported by A. Pohl), the calculations indicate it is feasible to measure ozone concentration at ppb levels and at a distance of three meters with the same relatively low transmit power. This assumes the functionalization for gas detection does not significantly increase the return loss of the sensor.

## *1.4 What Is Needed?*

In many ways the improvements needed for the passive SAW ozone sensors are ubiquitous to sensors in general. In this work, we focus on the design, evaluation, and improvement of a dispersive acoustic wave sensor, and so our consideration of the design necessities is primarily with respect to the device, not the details of the wireless interrogation system or terrestrial communications channel.

- **On-chip Reference Sensor:** Literature has shown the utility of reference sensors for removal of common mode interfering effects. More recently sensor *arrays* have been used to enhance selectivity when discriminating very similar target substances [25]. For the present work, the passive dosimeter must at least allow for compensation of temperature. Several techniques exist for differentiating the variable delay due to temperature versus that due to mass loading, etc. One such technique is also used in this work: multiple delay paths are incorporated into the devices such that differential measurements may be made. Multiplexed acoustic delay line sensors are needed.

- **Loss Reduction:** While wireless and coupling losses were already discussed, several acoustic loss mechanisms are prevalent in surface wave sensors and contribute to the parasitic dispersion. First, there is viscous dissipation typically encountered in polymer surface coatings (e.g. sensitive films). Second, diffractive losses increase with magnitude of the per-reflector SAW reflection coefficient. This causes increased scattering of waves to the bulk and in the surface plane. Ultimately the surface phononic crystal devices depend upon energy trapping methods to reduce the loss. For instance, the SAWs may be significantly slowed by use of slow materials at the surface or by use of mode coupling to extensive surface structures such as high aspect ratio ridges or pillars (Chapter 3, Chapter 5).

- **TB Increase:** The Shannon-Hartley capacity ($C$) of a communication channel with a passive sensor is proportional to the mutual bandwidth ($B$) of the transceiver and sensor: ($C = B\log_2(1 + S/N)$ [bits/sec]). We assume additive white Gaussian noise (AWGN) such that the noise power is $N = N_0B$ and the received SNR is a worst-case value limited by the transmit power and channel characteristics. Considering fixed SNR, we have $C \propto B$ because the total information received from a sensor is linear in the bandwidth and $C\Delta t \propto B\ \Delta t$, where $\Delta t$ is the signal duration. This is the time bandwidth product (TB): $\Delta t\ B = \Delta t \Delta f$. All conveyed sensing information must be managed within this constraint; whether used for *sensitivity* or *selectivity*, etc. It is important to note that additional bandwidth in the transceiver alone does not increase

the amount of information returned from the sensor; one must increase the TB of the sensor.

Radar was one of the earliest remote sensing technologies and demonstrated the effective SNR could be improved by compressing the signal energy and spreading the noise. This was accomplished by broadening both the transmitted signal and compressor device in both time and bandwidth, increasing the time bandwidth product, $\Delta t \Delta f$. RACs are dispersive SAW devices designed to achieve very large time bandwidth products for improved range precision, but this also increases sensitivity to temporal distortions [46, 86]. The threshold for degradation due to such velocity shifts was reported to be $\Delta v/v \leq (\Delta f \Delta t)^{-1}$. Therefore devices achieving time bandwidth products as high as 10,000 suffer significant degradation for velocity changes exceeding 100 ppm; i.e. they are sensitive to such perturbations.

An example of the resolution improvement enabled by large time bandwidth products is shown in Figure 1.6. Linear frequency chirps were used in the calculation, according to common practice in SAW pulse compressors. Many other dispersive structures are possible, however, and a primary objective of this work is to explore the dispersion of surface phononic crystals with relation to the passive SAW sensing paradigm.

## *1.5 Why Phononic Crystals?*

Given an allocated RF bandwidth, it has been demonstrated that significant processing gain (and therefore headroom for sensitivity, selectivity, etc.) can be achieved by increasing a signal's dispersion. Dispersive SAW sensors and design parameters are reviewed in Chapter 6. While conventional SAW pulse compressors used linear chirp gratings having quadratic phase, many other dispersive structures are possible.

Phononic crystals are lattice structures which can yield interesting dispersive features such as: forbidden frequency bands called "band gaps," anomalous dispersion, near-zero group velocity, etc. The engineered materials are inhomogeneous and have characteristic dimension(s) $O(\lambda)$. The impedance of such lattice materials varies greatly with frequency when $\lambda$ nears $2a$ (twice the lattice period); i.e. the media are dispersive.

Research in PnCs has grown in considerably since the early theoretical investigations.

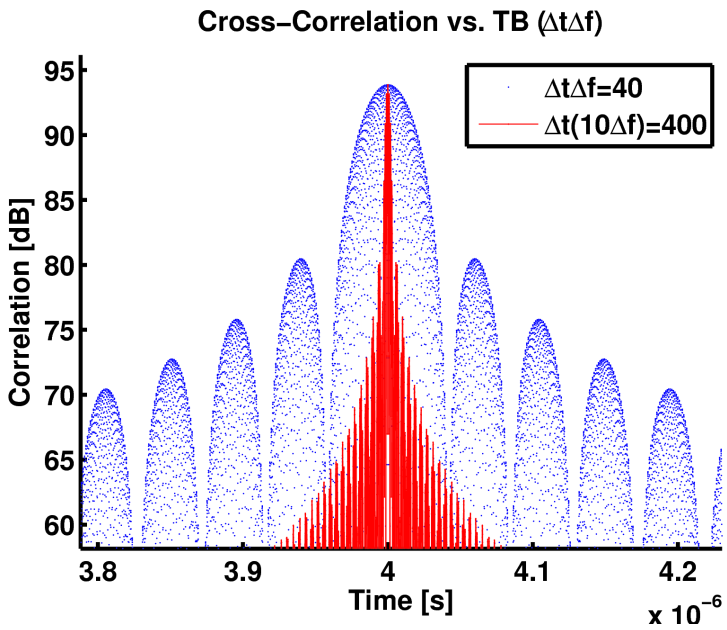


**Figure 1.6:** Example calculation of the pulse compression achieved for differing bandwidths and the same signal duration, $\Delta t$. Note the improved temporal resolution enabled by the greater time bandwidth product.

Although recent interest surfaced *circa* 1993 [48], the Floquet solutions and Bloch wave vectors characteristic of SAWs in periodic structures had been studied long before. Even Lord Rayleigh, for whom the Rayleigh SAW is named, had already addressed the propagation of waves in materials "endowed with a periodic structure" [79]. In another context, quantum mechanics, phonon dispersion had been analyzed for crystal lattices of semi- and super- conductors.

The distinctive difference for recent inquiry is the introduction of truly engineered materials. Work done in this area typically has an upper frequency limit governed by minimum patternable feature sizes. As lithographic limitations are reduced, devices are becoming feasible at higher frequencies. At least one 2-D PnC device operates at hundreds of megahertz and features PnC defect resonators etched into silicon slabs only tens of micrometers thick [72, 2, 73].

Still, dispersive designs at UHF frequencies are expensive to produce using conventional ultraviolet lithography, due to the required precision of the line widths in typical chirped grating structures (Chapter 6). Surface phononic crystals offer an engineering "toolbox"

for dispersive designs, but they too present at least two difficulties peculiar to the SAW paradigm: bulk diffraction and narrow bandwidth. These factors are addressed in computations of Chapter 5.

A structure of particular interest for increasing the temporal dispersion is the coupled cavity waveguide (CCW). This is a slow wave PnC structure created by introduction of periodic defects into a patterned lattice. The defects admit resonant modes but are partially isolated from each other by the band gap of intermediate regions. When the defect mode frequencies fall within the lattice band gap, proximal cavities are coupled only by evanescent energy distributions. For an array of such defects in a lattice, this forms a coupled resonator structure exhibiting low group velocity. Two such structures were recently reported in the literature and are shown in Figure 1.7.

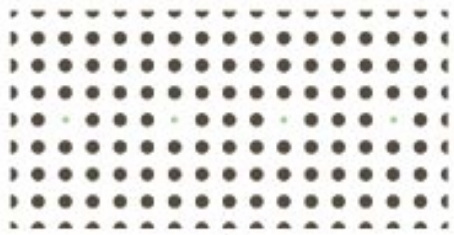

**(a)** Plan view of a 2-D coupled cavity waveguide (CCW) PtC [91].

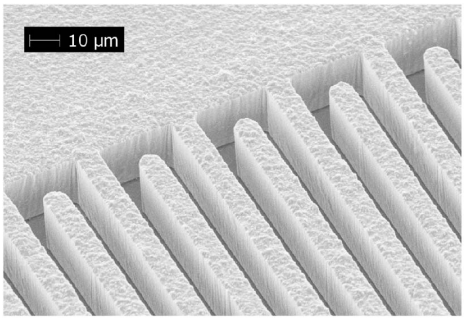


**(b)** A 1-D slow-wave PnC constructed by high aspect ratio deposition of nickel [51].

**Figure 1.7:** Two slow wave lattice structures

Slow wave structures are useful for enhancement of phase sensitivity, as described for an optical Mach-Zehnder interferometer analyzed by Soljačić et al. [91]. That device used a *photonic* crystal having a defect mode coupled cavity waveguide (CCW). Effectively a structure of distributed resonators with partial isolation, the device combined features of resonators and the operation of a delay line. An additional benefit claimed for such structures is reduced physical length required for a given delay.

One recent publication reports a SAW structure of similar effect, reducing the velocity by one order of magnitude. The reported device utilized high aspect ratio metal strips of height 30 $\mu$m instead of the typical thin films of approximately 100 nm [51]. Figure 1.7b

shows an electron micrograph of the high aspect ratio 1-D lattice structure which extends above the plane of propagation.

Noting these advances in the field of optics, it would be interesting and potentially useful to investigate such structures for SAW devices, which have historically been designed for operation in the regime of weak scattering rather than using large acoustic impedance contrasts. We have found that challenges exist in the implementation of such structures on surfaces, and Chapter 5 is dedicated to elucidation of the challenges and the possible design solutions.

### 1.5.1 Common PnCs (1-D)

At the micron scale, one dimensional PnC reflector gratings and transducers have been used in SAW devices since approximately 1970 [5]. These distributed Bragg reflectors (DBR) are common examples of 1-D PnCs having a narrow band gap corresponding to strong reflection of SAWs. An example designed by Sang-Hun Lee is portrayed in Figure 1.8 [55].

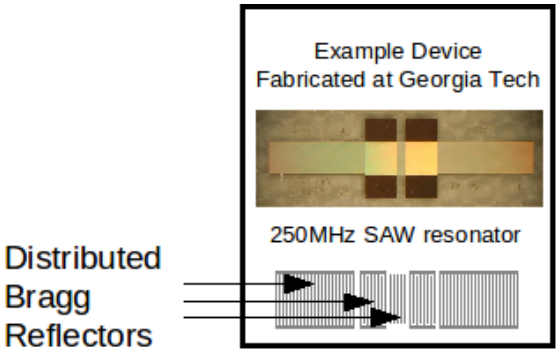


**Figure 1.8:** Conventional SAW resonator with Bragg reflectors (1-D PnCs).

The metal pattern in the photograph is very thin with respect to the wavelength ($h/\lambda \ll 1$), such that the reflection coefficient (due to the acoustic impedance contrast) is linear in the thickness of the film. Interesting dispersive structures may have greater aspect ratio and trap energy in normal modes, as is desired of PxCs having large band gaps. The array of structures examined in this work is illustrated in Figure 1.9.

By extension of concepts from electromagnetics, we could construct 1-D PnC devices by simple modification of the SAW Bragg reflector. The properties of the superlattice can

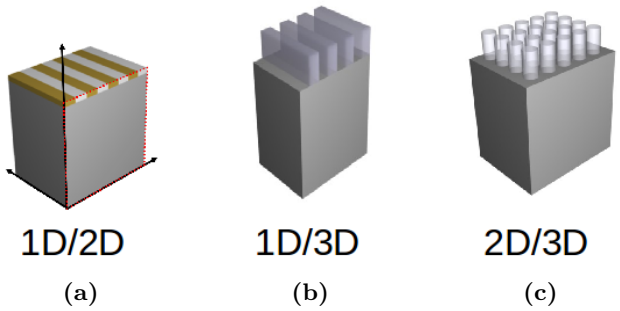


**Figure 1.9:** Computer renderings of the surface PnC structures considered in this study: conventional Bragg reflector, high aspect ratio ridge structure, and 2-D lattice of pillars.

be controlled by selective alteration or omission of the metal strips forming the lattice. More generally, spatial variation of the lattice parameters allows one to encode a dispersive signature into the reflection response. Research we conducted for such structures is reported in Chapter 5 and Chapter 6.

## *1.6 Organization of This Document*

The chapters that follow apply recent developments in microwave acoustics toward the need for personal exposure monitors. First we studied the dispersive properties of surface activated acoustic wave sensors and surface phononic crystals (PnCs). We determined that one dimensional dispersive devices were the best route forward, and so we proceeded to analyze dispersive designs for chemical sensing, examining both surface PnC designs as well as dispersive designs commonly used in radar. We then proceeded to experimentally detect ozone using UHF SAW devices in environmentally and occupationally relevant concentrations. Finally, we demonstrated the utility of temporal dispersion in SAW tag gas sensors to mitigate the impact of incidental fluctuations of the ambient conditions. This involved automated collection of microwave scattering parameter responses over time periods spanning minutes to days.

The comprehensive report of this investigation was divided into the chapters that follow, and we give an outline in terms of the primary contributions:

- *Investigation of surface PnCs for chemical sensing* (Chapters 3, 5, 6)
  * Automation of surface PnC dispersion computations by the finite element

method

* Validation of dispersion computations by laser acoustic spectrometry

* Computation of the mass sensitivity of surface PnCs on $LiNbO_3$ for ozone detection

- *Development of a new gas sensor* (Chapter 5, Chapter 7)

  * Design of on-chip chemical referencing for passive SAW gas sensors

  * Functionalization of a passive SAW sensor for ozone dosimetry in EPA and OSHA relevant range

  * Test and characterization of passive SAW ozone dosimeters

- *Analysis of dispersive sensor performance* (Chapters 6, 7)

  * Evaluation of sensitivity and detection limit for dispersive passive SAW gas sensors

  * Evaluation of selectivity with respect to ozone, given confounding factors

  * Assessment of sensitivity and selectivity trade-offs due to designed dispersion and TB

# CHAPTER II

# SAW DISPERSION

## *2.1 Overview*

Although the frequency dependent propagation of bulk and surface acoustic waves has been extensively studied in many fields including seismology and nondestructive testing, this phenomenon of *dispersion* has seen only sparse application to surface activated acoustic wave sensors. Whereas some of the most popular chemical sensing approaches measure spectra, e.g. mass spectrometry and Fourier transform infrared spectroscopy (FTIR), acoustic wave *sensors* largely have been narrowband. Three reasons for this are readily apparent:

- Operation at relatively low frequency (MHz to GHz) makes acoustic sensors relatively unable to excite higher energy characteristic intramolecular resonances associated with chemical interactions of interest.
- Narrow-band (i.e. resonant) operation allows convenient electronic interface and frequency counter read-out.
- Small change due to detection of trace analytes allows treatment by perturbation approaches.

For narrowband approaches it is reasonable to expect approximately linear loading behavior for small changes about an operating point (usually a series or parallel resonance), and so acoustic wave dispersion is often treated to first or second order, especially in mass loading studies.

This chapter reviews salient aspects of acoustic dispersion, particularly for the types of inhomogeneous structures encountered in this work. Our objectives are summarized below:

- Review dispersion in general media and its analytical representation for bulk acoustic waves.

- Calculate dispersion and demonstrate why numerical methods and computer solution are important for the surface wave structures in this work.
- Review the inherent dispersion in mass loading of acoustic sensors
- Discuss the attenuation and loss associated with dispersion.

## *2.2 Bulk Acoustic Waves*

We begin with the case of bulk acoustic waves (BAWs) because their dispersion is generalizable to that of the hybrid interfacial waves taken as the focus of this work: surface acoustic waves. Furthermore, even the simpler BAW dispersion exhibits some complicated and interesting properties in anisotropic and trirefringent media. We now lay the foundation for our eventual computation of surface mode dispersion in complicated geometries.

### 2.2.1 Dispersion and Characteristics

It can be shown that dispersion relations parameterize orthogonal characteristic solutions over the phase spaces of hyperbolic systems, e.g. $u_{tt} - c^2 u_{xx} = 0$ (wave equation). Assuming plane waves proportional to $e^{-j\mathbf{k}\cdot\mathbf{r}}$ and $e^{j\omega t}$, a dispersion relation has the general form:

$$\Omega(\omega, \mathbf{k}) = 0, \tag{2.1}$$

where $\omega$ is the angular frequency and $\mathbf{k}$ represents orthogonal components of the wave vector[1].

For plane waves in homogeneous isotropic (lossless) media, this dispersion relation yields just two characteristics representing linear relationship between $\omega$ and $k$: $\omega/k = \pm v_p$. The two phase velocities correspond to the fundamental solutions of the wave equation, representing D'Alembert's leftward and rightward waves in physical space and time. In the presence of dispersion, the relationship is no longer linear: the velocity is dependent upon frequency and wavelength. This dependence is sketched in the Fourier domain (reciprocal space and time) in Figure 2.1. One can see that, in the dispersive case, a finite bandwidth is

[1] More generally, $\mathbf{k}$ should be complex to allow evanescent wave solutions.

nonuniformly spread over a wider range of wave numbers (each with different phase velocity: $v_p(k) = \omega(k)/k$).

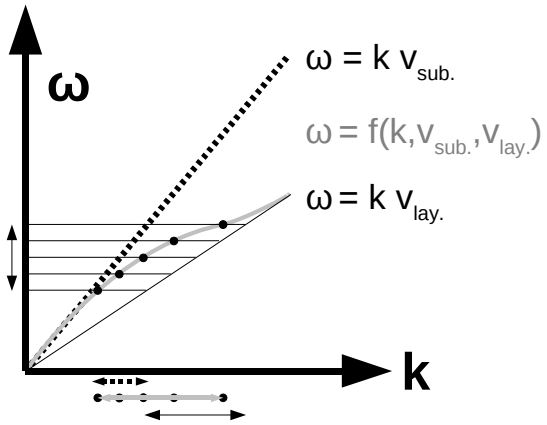


**Figure 2.1:** Qualitative ($\omega$, $k$) dispersion curves for a surface wave on a layered substrate.

In general media, i.e. having properties distributed over a Fourier basis of spatial frequencies, there may be multiple characteristic lines about which the modes fluctuate. Figure 2.1 shows an example characteristic or "band" corresponding to surface waves on a layered medium. As $k \to 0$ the substrate velocity is obtained, and as $k \gg 2\pi/h$ (small wavelengths) the layer velocity is obtained. This dispersion may be plotted other ways, e.g. in Figure 2.14 (finite element computation).

Before we continue on to composite materials, we begin with a simple case showing the utility of a computer to solve for the velocity and polarization dispersion of bulk waves in anisotropic media that are homogeneous at the scale of interest.

### 2.2.2 Computation

We begin with the case of plane bulk acoustic waves in solids. In anisotropic solids Newton's second law becomes the well-known Christoffel equation[2], written in terms of the particle velocity ($v_j$), mass density ($\rho$), and the reduced (3x3) Christoffel matrix ($\Gamma_{ij}$):

$$[k^2\Gamma_{ij} - \rho\omega^2\delta_{ij}][v_j] = 0 \ . \tag{2.2}$$

[2](Voigt notation) For brevity, a review of the tensor notation is omitted. The reader instead is referred to the comprehensive treatment in volumes *I* and *II* of B.A. Auld's *Acoustic Fields and Waves in Solids* [6, 7].

In this representation, computation of a 3x3 determinant yields the dispersion relation in $\omega/k$ for plane waves in a bulk material with arbitrary anisotropy represented in $\Gamma_{ij}$. The piezoelectric substrates used in this work are crystals; they are themselves phononic crystals having atomic-scale characteristic dimension. However, the acoustic wavelengths (in this study) are orders of magnitude larger ( $10^{-6}$ m) and correspond to patternable transducer dimensions. Therefore, transducers, reflectors, and other patterned structures may be called superlattices or phononic crystals, but they do not technically qualify as "metamaterials" because the operating wavelengths are not sufficiently large for measurements to sample only an average or "effective" medium.

The material's bulk properties thus correspond to evaluation of the *background lattice* in the small-$k$ limit; a conventional material. In this work the bulk material lattice is responsible for the intrinsic material symmetries and values of the elastic constants. The angular dependence of the material constants results in angular dispersion of the wave velocity, polarization, etc. This introduces important phenomena, such as mode coupling and self-focusing.

To begin, we use a common substrate for surface waves, lithium niobate ($LiNbO_3$). The "Y-Z" cut of this trigonal crystal is oriented such that the $y$ axis is normal to the polished surface and SAWs propagate along the crystal $z$ direction, as shown in Figure 2.2. Shear waves in the surface plane may be shear vertical ("SV" or $y$ polarized), shear horizontal ("SH" or $x$ polarized), or some linear combination thereof.

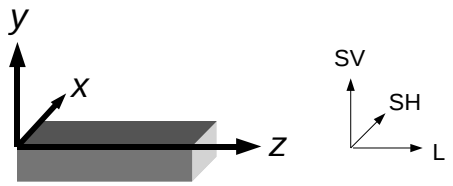


**Figure 2.2:** Coordinates for SAWs on YZ $LiNbO_3$ ($y$ cut with $z$ propagation), and polarization nomenclature.

In this case the characteristic equation ($\det\left([k^2\Gamma_{ij} - \rho\omega^2\delta_{ij}]\right)$) conveniently factors for propagation vectors ($l_i$) along the $x$, $y$, and $z$ axes, and in the $y$-$z$ plane. For example,

since the SAW propagation is along the $z$ axis, $\hat{l} = (l_x, l_y, l_z) = (0, 0, 1)$, the characteristic equation yields a root:

$$\left(\frac{k}{\omega}\right) = \left(\frac{1}{V_p}\right) = (2\rho)^{1/2} \left\{A - \sqrt{B^2 + C}\right\}^{-1/2}, \tag{2.3}$$

where $k$ is the wave number, $\omega$ is the angular frequency, $\rho$ is the mass density,

$$\begin{aligned} A &= c_{44} + c_{11}\sin^2\theta + c_{33}\cos^2\theta - c_{14}\sin 2\theta \\ B &= (c_{44} - c_{11})\sin^2\theta + (c_{33} - c_{44})\cos^2\theta + c_{14}\sin 2\theta \ , \\ C &= ((c_{13} + c_{44})\sin 2\theta - 2c_{14}\sin^2\theta)^2 \end{aligned} \tag{2.4}$$

where $c_{IJ}$ are the components of the (6x6) Christoffel matrix (reduced stiffness tensor), and $\theta$ parameterizes the solution in the $y$-$z$ plane [6].

Therefore, despite the unwieldy appearance, the angular dispersion may be obtained analytically. The piezoelectric effect can easily be added into $\Gamma_{IJ}$ but was omitted in the preceding analytical review. Fortunately, even for a strongly piezoelectric material such as lithium niobate, addition of the "stiffening" typically alters the dispersion curve by less than 10%. In scattering problems encountered in practice, e.g. a shorted array of metal strips on lithium niobate, the piezoelectric coupling may actually dominate, rather than purely mechanical factors. Results we have computed for the stiffened case are shown in Figure 2.3. The BAW curves represent the angular dependence of the eigenvalues computed from the Christoffel equation. These real numbers are true zeros of the characteristic determinant, whereas numerical solution of a *generalized* eigenvalue problem is often required for more complicated cases such as layered structures in which modes couple to one another due to matching at interfaces.

These piezoelectrically coupled plane waves exhibit polarization dispersion as the angle of propagation varies in the XZ plane. In some crystal orientations, SAWs may couple to these bulk modes and are called "leaky" SAWs. It is helpful to note the polarization orthogonality of the "quasi-shear" modes: a SAW containing a Y polarization component would couple to a BAW which is both slower and also (at least partly) Y polarized. Figure 2.3 shows both of these parameters vary significantly with direction. Avoidance of lossy SAW modes is important for efficient passive wireless sensors, and so the coupling to BAW

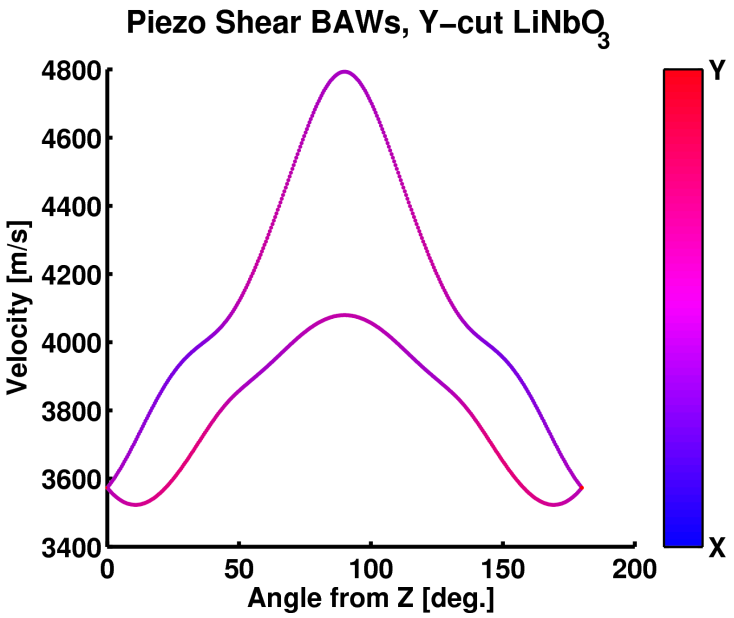


**Figure 2.3:** Quasi-shear BAW velocity and polarization dispersion in the XZ plane of lithium niobate, calculated using the Christoffel equation. (color)

modes will be reconsidered in a subsequent section.

The angular dispersion influences material choice, manufacturing tolerance, and the design of surface PnCs. For initial device design in 1-D, only the local curvature of the slowness surface is important, because this reveals self-focusing. Small deviations in $k$ due to scatterers, etc. are collimated back to $k$ due to the concavity of the power flow angle about $k$. This desirable condition is evident for propagation along the $z$ axis of $y$-cut $LiNbO_3$, as is shown in Figure 3.6 (Chapter 3).

The auto-collimating or self-focusing cut is advantageous for passive SAW delay lines due to the compensation of wave diffraction from finite transducer aperture, material imperfections, etc. The reduced diffraction improves energy recovery from distant reflectors, thereby increasing code length, bit delay, etc. Rayleigh SAWs propagating in the Z direction on Y-cut lithium niobate experience sufficient self focusing to allow a photolithography mask alignment tolerance of $\pm 6$ degrees [15]. These are reasons we use this particular crystal cut in much of this work.

The frequency domain problem solved here for bulk waves may be extended to periodic media and to special cases such as surface waves. P. M. Smith extended the method to

a generalized eigenvalue problem for the dyadic Green's function for general (multimode) SAWs on anisotropic layered substrates [90]. S. Benchabane and others have also computed BAW dispersion in periodic piezoelectric media, and they illustrated how BAW dispersion constrains the SAW band structure in surface phononic crystals [9].

### 2.2.3 Periodic (Composite) Media

Starting with Newton's second law in tensor form, we reduce the problem to propagation of $x$-directed longitudinal waves (i.e. $\mathbf{u} = u(x,t)$) in a medium with variation of the stiffness ($c$) in the $x$ direction.

$$\begin{aligned} \nabla \cdot \mathbf{T} &= \frac{\partial \mathbf{p}}{\partial t} \\ \nabla \cdot (\mathbf{c} \nabla_s \mathbf{u}) &= \frac{\partial}{\partial t}\left(\rho \frac{\partial \mathbf{u}}{\partial t}\right) \\ \frac{\partial}{\partial x}\left(c_{11}(x)\frac{\partial}{\partial x}u(x,t)\right) &= \frac{\partial}{\partial t}\left(\rho \frac{\partial}{\partial t}u(x,t)\right) \end{aligned} \tag{2.5}$$

This formulation of the field equation (2.5) with spatially varying material parameters has been well studied by other researchers. Y. Wang and B.A. Auld reported the general tensor form in 1983 [8], and they further augmented the analytical work with experimental data for 1-D and 2-D periodic composites. The key result of (2.5) is the appearance of the spatial derivative of the stiffness, due to the divergence: $\nabla \cdot \mathbf{c}(x)$. In electromagnetics problems this appears as the spatial derivative of the permittivity, due to the curl: $\nabla \times \epsilon(x)^{-1}$ [40]. This causes spatially varying PDE coefficients that may be expanded in Fourier series to capture the effect of the many space harmonics of general structures.

Next, the material is assumed to be of infinite extent, such that the Floquet principle may be applied as it is in semiconductor theory. Simply stated, solutions for fields in the lattice must exhibit modulation matching the space harmonics of the lattice, as stated by Bloch's theorem:

$$u(x,\ldots) = u(x+na,\ldots) \Rightarrow u(x,\ldots) \propto e^{-j\frac{2\pi n}{a}x}. \tag{2.6}$$

Finally, the partial derivatives reduce to an algebraic expression in $\omega$ and $k$, and an eigenvalue problem may be solved for the $n$ characteristic plane wave solutions for $\omega(k)$; the

bands of the dispersion diagram:

$$A(k,n)\,u(x,t) = -\omega^2\,u(x,t), \quad u(x,t) \propto e^{j\omega t}e^{-j(k+\frac{2\pi n}{a})x}. \tag{2.7}$$

For the usual case of composite materials, such as one with 50% "filling fraction" illustrated in Figure 2.4a, the structure is not purely periodic; the discontinuities imply infinite space harmonics are present. This gives rise to an infinite number of equations; truncation of the problem depends upon the number of Fourier series terms required to adequately approximate the spatial variation of material parameters. A comparison by Y. Wang and B.A. Auld in 1985 shows the discrepancy between solutions truncated at 2 terms versus 12 terms for different "volume fraction" of the material inclusions [95]. For a given accuracy, the number of required equations generally increases with the filling fraction and contrast of material properties across the discontinuities. Due to Bloch's theorem, the structure is

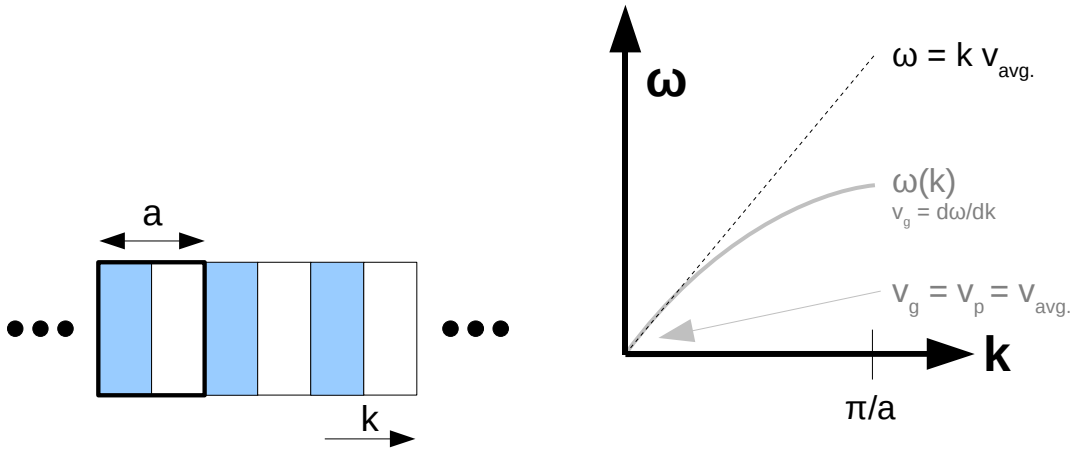


**(a)** Periodic composite: 1-D PnC **(b)** Brillouin dispersion diagram; lowest band

**Figure 2.4:** 1-D phononic crystal and qualitative ($\omega$,$k$) dispersion curve

sampled up to $a$, meaning spatial frequencies are aliased into the interval $k \in (0, \pi/a)$ of the band structure; greater values of $k$ are *redundant*. In a qualitative plot (Figure 2.4b), $v_{\text{avg.}}$ is the average phase velocity in the composite, $v_g = \partial\omega/\partial k$ is the group velocity, and $\pi/a$ is the fundamental spatial frequency. The slope of the band decreases until the acoustic wave vector is about half the material's fundamental spatial frequency. This is the Bragg scattering regime: the constructive interference of reflected waves with $k = 2\pi/2a$, where $a$ is the structure period (lattice constant).

## *2.3 Surface Acoustic Waves*

The pure Rayleigh wave mode, discovered in 1885, was the first analytically understood SAW propagating at the free boundary of a semi-infinite elastic medium. This scenario may be viewed as a limiting case of plate waves for which the structure becomes infinitely thick. Accordingly, a special case of transverse resonance analysis can be conducted, taking the partial waves from the infinite depth to be zero. A detailed review by Auld reveals that, for an *isotropic* material, a third order equation in $V_R^2 = (\omega/k_R)^2$ still must be solved to compute the exact Rayleigh velocity ($V_R$) from the longitudinal ($V_l$) and shear ($V_s$) velocities:

$$\left(\frac{V_R}{V_s}\right)^6 - 8\left(\frac{V_R}{V_s}\right)^4 + 8\left\{3 - 2\left(\frac{V_s}{V_l}\right)^2\right\}\left(\frac{V_R}{V_s}\right)^2 - 16\left\{1 - \left(\frac{V_s}{V_l}\right)^2\right\} = 0 \tag{2.8}$$

This is the dispersion relation for Rayleigh waves on an *isotropic* substrate, and despite its order, it evaluates to a constant velocity; the dispersionless case. In general, the Rayleigh velocity does exhibit angular dependence due to the material anisotropy, because the $V_l$ and $V_s$ both vary with direction in the material.

For the crystal materials of interest in SAW devices, the Christoffel equation of (2.2) may be modified to account for the mechanically and electrically free surface boundary condition. Solutions then take the form: ($u_i$,$\phi$), where $u_i$ are the displacements, $\phi$ is the electrical potential, and $e^{-jk_y y}e^{j(\omega t - k_z z)}$ dependence is assumed. An 8th order generalized eigenproblem is solved for orthogonal partial waves which must simultaneously produce the surface boundary condition(s). The four partial waves directed toward the surface must be zero (2 shear, one longitudinal, and one electrostatic). In general, four solutions remain, and they correspond to waves with complex $k$ in both the depth direction and surface directions [35, 90]. These coupled partial waves (as in Figure 2.5) constitute a basis for general SAW solutions on semi-infinite media.

#### *2.3.0.1 Leaky SAWs*

The dispersion computations for bulk acoustic waves allow one to graphically ascertain whether the Rayleigh SAW couples to BAWs. The existence of BAW coupling distinguishes

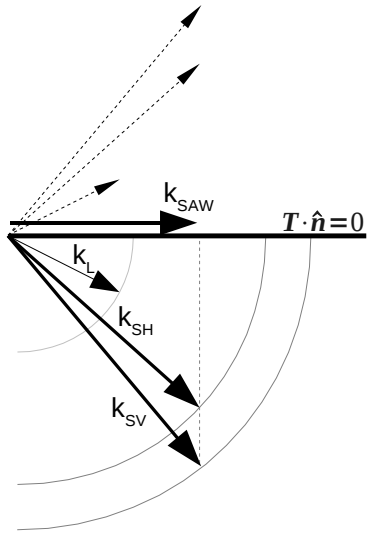


**Figure 2.5:** Diagram of partial waves which must be combined to match the surface boundary condition, mutually couple, and form the SAW. ($k_\phi$ and its B.C. are not shown.)

SAWs having a "leaky" character relative to pure surface modes such as Rayleigh waves. Figure 2.6 illustrates the coupling of surface waves to bulk waves at a critical angle $\phi_c$, for which the SAW and BAW wave vectors (of similar polarization) are phase matched.

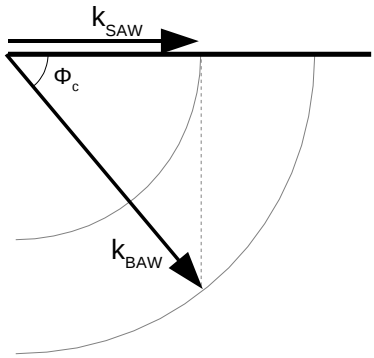


**Figure 2.6:** Phase matching at the surface boundary permits SAW-to-BAW coupling when $k_{\mathrm{BAW}} > k_{\mathrm{SAW}}$ and the SAW polarization matches that of $k_{\mathrm{BAW}}$.

Note that this can only occur when the BAW is slower than the SAW: $k_{\mathrm{BAW}} > k_{\mathrm{SAW}}$, but this is a situation that will not occur intrinsically in most materials wherein $V_l > V_s$ in the Rayleigh dispersion relation of (2.8).

The angle of BAW radiation (with respect to equiphase wave fronts), $\phi_c$, may be computed:

$$\phi_c = \cos^{-1}\left(\frac{V_{BAW}}{V_{SAW}}\right). \tag{2.9}$$

We discuss this effect with relation to design of surface PnCs in Chapter 5, showing power loss can be reduced by ensuring the SAW has lower propagation velocity for $k$ in the desired direction along the crystal surface.

It is also important to note that the BAW slowness surfaces are not generally circular (isotropic) in the sagittal section, as shown in the figures, and that the polarization may also change with angle in the depth direction. This is another reason why the $k$-matching diagrams and basic approximations are not always sufficient; computations employing the full material tensors are needed.

### 2.3.1 Layers

The case of a thin layer on a substrate may be considered as an acoustic waveguide "loaded" on one side by a semi-infinite medium. When the layer is sufficiently thick, i.e. $h \approx \lambda$, transverse modes are admitted, and the solutions have the form of plate modes coupled to modes of the substrate. This is the case of generalized Lamb waves; the coupling of plate waves, surface waves, and bulk waves, as depicted in Figure 2.7.

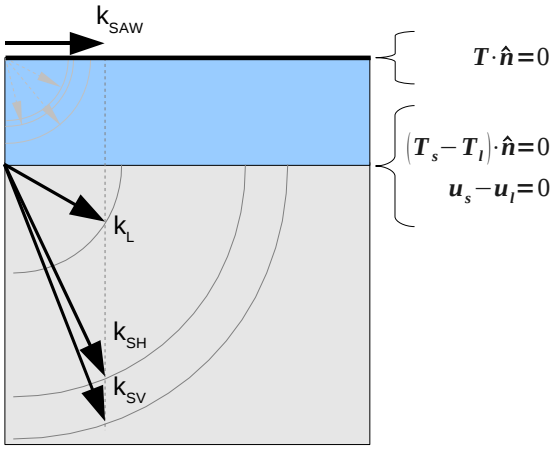


**Figure 2.7:** A fast layer on a slow substrate radiates BAWs.

The fields must be continuous at the layer/substrate interface ("l" and "s"' in the figure), and the top boundary receives the stress-free condition: $\mathbf{T} \cdot \hat{\mathbf{n}} = 0$. The associated system of equations produces up to 8 partial wave solutions, some of which must be eliminated according to radiation conditions designed to select modes that are guided at the surface, e.g. evanescent in the depth direction. In his book, K. Hashimoto provides a description of the radiation conditions used to eliminate partial waves and arrive at 4 possible solutions [35].

Because computer solution is the most appropriate means of solving these dispersion problems, it is convenient and informative to apply a full finite element approach to solve for the fields in arbitrary structures. We next show the result of angular dispersion changing the "leakiness" of a SAW propagating relative to the $z$ direction (0°) on $y$-cut lithium niobate.

As the bulk waves become faster (at in-plane rotation angles approaching 0°), BAWs along the interface become more nearly phase matched to the SAW. This reduces loss of energy from the interface; surface-skimming bulk waves (SSBW) are obtained, as illustrated in Figure 2.8b.

One may note the tilt of the field distribution in the substrate (the normalized total displacement) reveals a Poynting vector directed partly toward the bulk (leaky SAW) and parallel to the surface (Rayleigh SAW), for the -45° and 0° directions, respectively.

### 2.3.2 Gratings and PnCs

Grating structures, essentially 1-D SAW phononic crystals, have long been analyzed for their utility in SAW filters. Most popular approaches in SAW theory treat the propagation of the interfacial wave using a linear scalar wave equation; second order effects are often neglected. These simplifications have been extremely effective. Within the last fifty years linear treatments have yielded great advances, including the design of SAW filters having arbitrary impulse (and corresponding frequency) responses. Still, in select applications, the second order effects have been applied with much success, e.g. modeling of parasitic effects and design of SAW convolvers.

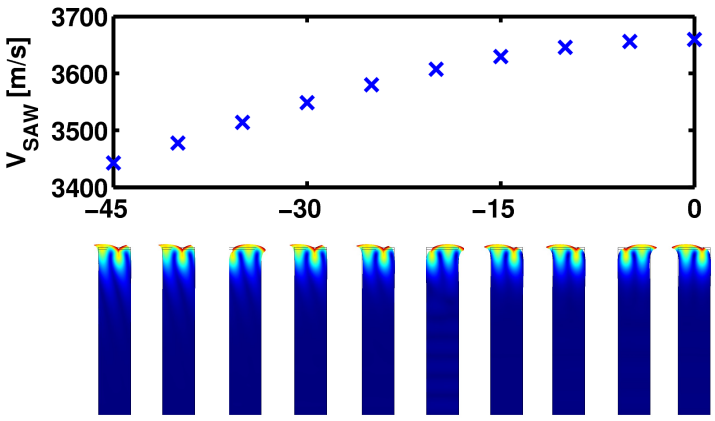


**(a)** Relatively slow layer on $LiNbO_3$

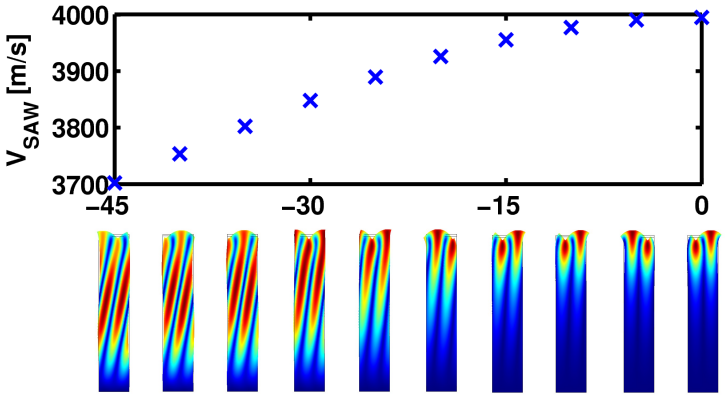


**(b)** Relatively fast layer on $LiNbO_3$

**Figure 2.8:** Mode profiles for isotropic layers ($h/\lambda = 0.0625$) on $y$-cut $LiNbO_3$. The abscissa corresponds to angle from the $z$ axis (degrees). The field plot is the normalized mechanical displacement (color).

Many analyses of complicated surface wave devices are conducted under the approximation of zero dispersion using the ideal surface wave velocities (evaluated numerically for piezoelectric materials), and the problems are reduced to scalar wave equations for which transmission line models are appropriate. We next discuss these common approaches.

#### *2.3.2.1 Delta Function Method*

PnCs have received increasing interest for design of SAW filters and other devices, but for SAWs, PnCs are not new. Conventional SAW devices employ 1-D phononic crystals which are distributed Bragg reflectors (DBR) and are commonly called "grating reflectors." An

example PnC of this type is shown in figure 2.9.

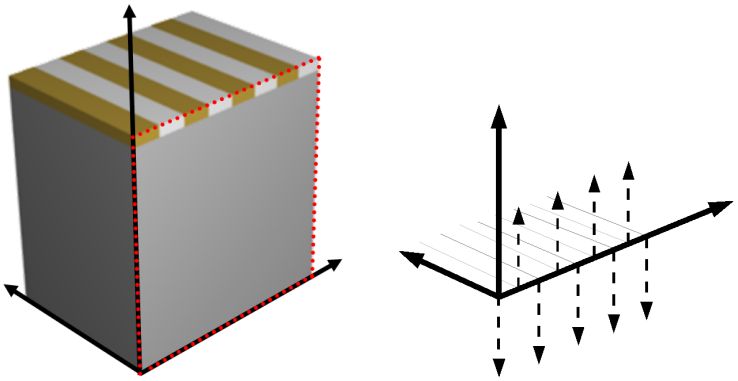

**Figure 2.9:** One dimensional surface phononic crystal (SAW reflector) and delta function model of the SAW reflection coefficient.

A popular means to model this structure is called the "delta function" method. This is a way to obtain the frequency dependent reflection coefficient, $R(\omega)$ for a surface grating. The problem is assumed to obey a scalar wave equation such that reflection coefficients may be obtained at the material discontinuities. The whole reflector grating is composed of an array of discrete reflectors, and when the reflection coefficient is known at each boundary between media, a Dirac delta function may be placed at each such point and weighted by the corresponding reflection coefficient. Each reflective strip or groove contributes two delta functions, but a structure of $\lambda/4$ spacing may be reduced to $N$ delta functions (one per strip), where $r(\omega)$ is the net reflection coefficient of a single strip or groove. The $r(\omega)$ term can also include the frequency dependence (dispersion) of each reflector, i.e. due to strip thickness or groove depth. In (2.10) $k = \omega/v_p$ is the wave vector determined by the SAW velocity, and $N$ is the total number of strips or grooves (of width $d$) in the grating.

$$R(\omega) = r(\omega) \sum_{n=0}^{N-1} e^{i2knd} \tag{2.10}$$

A plot of a response we calculated using this approach is given in figure 2.10. Note the mirror has one frequency of maximum reflection in this range (corresponding to the Fabry-Perot resonance at the fundamental period), but there are many side lobes and minima. The *sinc* function behavior is due to the finite extent of the grating, which may effectively be

represented as a square window weight function applied to the spatial impulse train. The net (summed) reflection coefficient is highly frequency dependent in these periodic structures, even in cases for which the frequency dependence of a single reflection ($\partial r(\omega)/\partial\omega$) is small or zero.

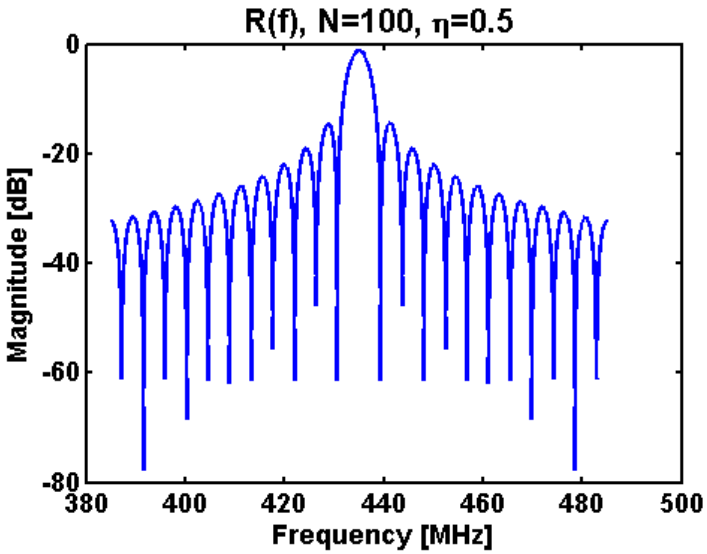


**Figure 2.10:** Magnitude of reflection coefficient ($R(f)$) for a reflective grating of $\lambda/4$ grooves on YZ-$LiNbO_3$. Computed using the delta function model.

One second order effect which may be included in this approach is dispersion due to strip height (or groove depth) relative to the wavelength: $r(\omega) = r(h/\lambda)$. The method still fails at larger reflection coefficient magnitudes because second reflections (and higher) become significant; however, we use this model for actual devices in Chapter 6 and Chapter 5, where appropriate.

#### *2.3.2.2 Transfer Matrix Method*

For PnC devices utilizing coherent multiple scattering, simulations incorporating multiple reflections are required. This can be accomplished using the common transfer or "transmission" matrix method. The technique is frequently used to model normal incidence on a layered structure such as a quarter-wave stack: a Bragg reflector. Such structures consist of discrete regions having different material constants, as previously shown in Figure 2.9. Thus the spatial width and the material wave number ($\beta_i$) of each region may be determined,

and one may then construct transfer matrices which can be cascade multiplied like the $ABCD$ two-port matrices encountered in electric circuit analysis. This is a convenient and well-known frequency domain approach to effectively convolve multiple cascaded impulse responses.

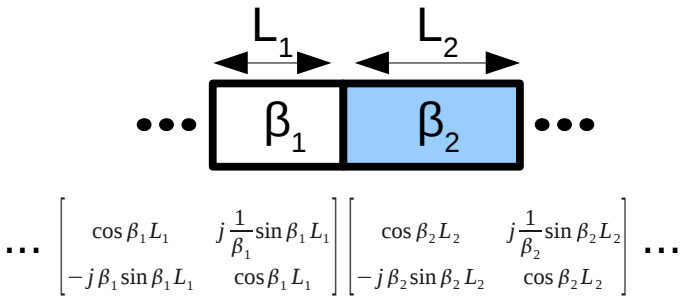


**Figure 2.11:** Application of the transfer matrix method for discrete composite media.

In Figure 2.12 we highlight the utility of the full transfer matrix method, considering all reflections and the change of groove depth (or strip height) on YZ $LiNbO_3$. This demonstrates the behavior as the effective impedance contrast is increased and multiply-reflected waves become increasingly significant. The reader may note the shift of the stop band to lower frequencies; the average (effective) wave velocity clearly decreased, implying that the reflection coefficient was achieved by incorporation of a slower material (air in the grooves). This appears in the mapping of $h/\lambda$ into the change of velocity, and therefore, into $\beta$:

$$r = Chf/v_0 \tag{2.11}$$

$$v_1 = v_0 \frac{r+1}{1-r} \tag{2.12}$$

$$\beta_1 = 2\pi f/v_1, \tag{2.13}$$

where $r$ is the reflection coefficient at a single boundary, $C = 0.33$ for YZ $LiNbO_3$, $h$ is the strip height, and $v_0$ is the velocity in the host material (corresponding to $\beta_0$) [62]. The subscript "1" denotes properties of the grooves. The form of (2.11) captures the first order dispersion as the reflection coefficient of a single groove increases approximately linearly with frequency. In the $ABCD$ matrix computation of the finite structure corresponding to the plots of Figure 2.12, the terminating medium to the left and right of the grating was assumed to be unbounded host material (i.e. $\beta_{x-,x+} = \beta_0$).

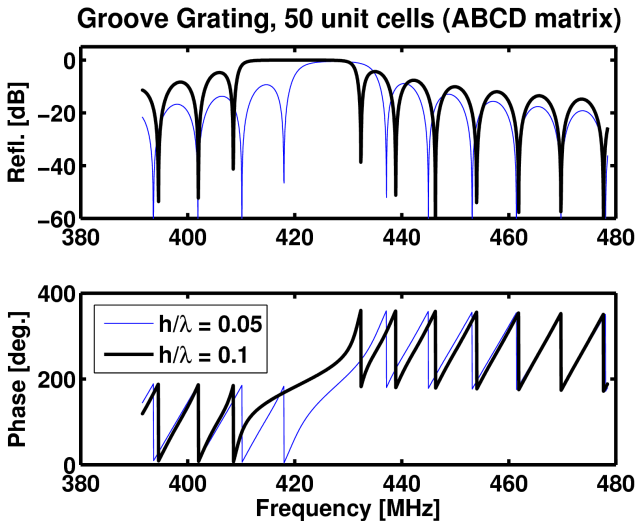


**Figure 2.12:** Use of transfer matrix method to show SAW stop band as material contrast effectively increases $(h/\lambda)$.

Unfortunately, the preceding result is not always valid for SAWs. As $(h/\lambda)$ increases, it is known that the SAWs tend to diffract to the bulk, constituting loss. We further discuss this in Chapter 5. Indeed, for SAW problems, one discovers that secondary reflections are often neglected, even in methods which ostensibly use the transfer matrix approach. This is because the general "best practice" is to use weakly scattering reflectors and to use many of them, achieving a large temporal dispersion. Therefore it is common practice to neglect multiple reflection.

For example, in the method of P.S. Cross and R.V. Schmidt [17], a device such as a SAW resonator is represented by the matrix cascade of complex acoustic grating matrices $[G]$ with delay matrices $[D]$, as in Figure 2.13b. One can see that the grating matrices should be formed by the cascade of multiple $[D]$ matrices representing the alternating regions with different $\beta$. However, for convenience, Cross and Schmidt allowed only first-order reflections when applying coupling-of-modes (COM) theory to construct the grating matrix, $[G]$. We note that this has been sufficient for many practical problems in the decades since.

This approximation of single reflections is found in both the widely applied delta function and transfer matrix approaches of SAW device design (although the latter method can be used with sufficient generality to account for the reflections, as we discussed above).

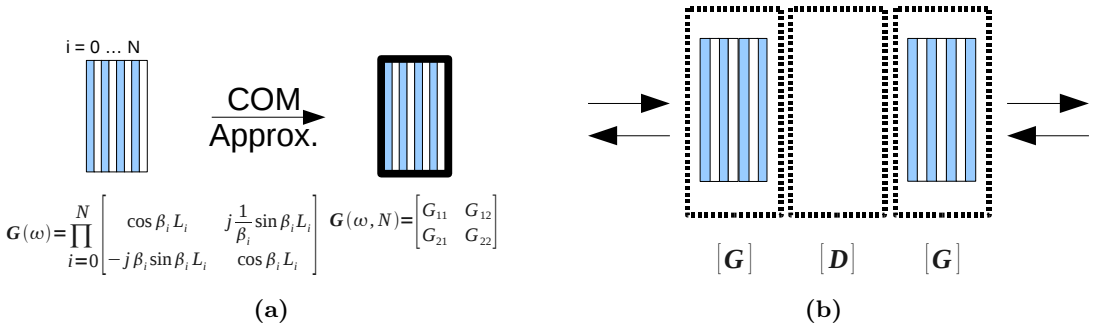


**Figure 2.13:** A coupling-of-modes approximation produces a convenient representation of the grating transfer matrix, $G$.

Improved approximations of course exist, and these typically alter the first order coupling coefficients to add frequency dependence, etc. In the case of "leaky" SAWs, the COM theory can be extended to coupling among greater numbers of modes. Hashimoto [35] shows that BAW coupling can be treated by four coupled PDEs representing the forward and backward propagating solutions for both SAW and BAW modes (compared to two PDEs in the usual COM analysis). This allows addition of a frequency dependent attenuation factor to account for the energy lost to BAW modes (the waves incident from the bulk are zero, so the coupling factor corresponds to radiated modes: loss).

COM approaches are often augmented by field analysis or empirical curve fitting to improve the approximations for arbitrary structures. A very popular (and freely available) software package called "FEMSDA" utilizes finite element field computation to find more exact coupling coefficients and other parameters of the SAW COM equations [35]. The application of the finite element approach to SAW device design is well-known and increasingly used for more exact analysis, and so our extensive use of FEM computations in Chapter 3 aligns naturally with that progression.

## *2.4 Dispersion in Sensors*

In this section we review the relationship between dispersion and the ubiquitous mass loading effect of acoustic wave sensors. The mass loading effect is commonly cited for acoustic chemical sensors, and it is the most pertinent effect for our ozone sensing application (as discussed in Chapter 5). As chemical species adsorb to or react with the sensor surface, the

surface mass density changes; hence the acoustic eigenvalues (frequencies) and eigenmodes (energy distributions) change. For a resonator, this is typically detected as a shift of the resonant frequency.

### 2.4.1 Mass Loading

The mass loading principle is widely applied for acoustic sensors, but it is only strictly valid for the case of very thin layers such that transverse modes within the layer are "cut off." For higher frequency sensors, this criterion becomes more challenging because layers must be made very thin for the usual formulas to apply. For thin layers on SAW sensors, linear perturbation theory can be applied when the solution for the unlayered surface wave is known. Both Tiersten and Wolkerstorfer have derived dispersion relations for SAWs propagating on anisotropic substrates supporting isotropic and anisotropic films, respectively. However, as we shall see, numerical methods are necessary to compute the general dispersive trends for thick or viscous films obtained in practice.

#### *2.4.1.1 Perturbation Approaches*

Considering first the case of a very thin isotropic film on an isotropic substrate, the Tiersten boundary conditions are obtained by power series expansion of the acoustic fields in the thickness direction and truncation at the zeroth order. The particle velocity is assumed uniform in the thin film and $\beta_R \approx \beta$. The guide essentially operates in the "cut-off" regime, wherein the field is evanescent, and, for a sufficiently thin guide, nearly constant across it. Elsewhere it has been shown that these assumptions may be applied to the complex reciprocity relation to yield Tiersten's formula (found in [7]):

$$\frac{\Delta\beta_R}{\beta_R} = -\frac{\Delta V_R}{V_R} = \frac{V_R h}{4P_R}\left(\rho'|v_{Ry}|^2 + \left(\rho' - \frac{4\mu'}{{V_R}^2}\frac{\lambda'+\mu'}{\lambda'+2\mu'}\right)|v_{Rz}|^2\right)_{y=0}, \tag{2.14}$$

where $\beta_R$ and $V_R$ are the Rayleigh propagation constant and phase velocity, respectively; $\rho'$, $\lambda' = c_{12}$, and $\mu' = c_{44}$ are the density and Lamé constants of an isotropic layer material, respectively; and the $v_{Ri}$ represent the orthogonal particle velocities forming the elliptical polarization. Evaluation is assumed at the substrate surface, $y = 0$, with $y$ increasing into the substrate.

It is important to note that surface interactions in sensors may cause the frequency (or phase velocity) to either increase or decrease. The net result depends upon whether the material stiffness (positive change) or mass density (negative change) dominates. This is well known from the perturbation theory result of (2.15), and it was also obtained by Hunt et al. in the application of time dependent perturbation theory to acoustic wave sensors [39, 55].

The linear mass loading dispersion of a thin layer on a SAW device (H.F. Tiersten, (2.14)) can be reduced to a form in which the frequency shift is proportional to the film height and the square of the operating frequency:

$$\Delta f \approx -\left[\mathrm{MF}_y + \mathrm{MF}_z\right]\ {f_0}^2\,\rho' h, \tag{2.15}$$

where operation at constant wavelength $\lambda$ is assumed, ${f_0}^2$ is the frequency operating point or "center frequency", and the mode factors, $\mathrm{MF}_i$, depend upon the Lamé constants and the normalized particle velocity components at the surface, as in (2.14). The latter requirement is is due to the elliptical particle polarization. The form of (2.15) is a scaled version of Sauerbrey's equation (1.1); a very thin rigid film is also assumed in this case, but the acoustic field is different, requiring components $\mathrm{MF}_i$ to compute the scale factor.

Viewed another way, the perturbation result can be rearranged as a function of the ratio of film height ($h_f$) to the wavelength ($\lambda$): $(h_f/\lambda)$. This is a parameter common in SAW scattering, and it helps illustrate the role of finite layer thickness in departure from simple mass loading. In the literature one finds that Tiersten's formula has indeed been recast in terms of $h/\lambda$, giving:

$$\frac{\Delta V_R}{V_R} = P_V \frac{K^2}{2} + F_V \left(\frac{h}{\lambda}\right) + S_V \left(\frac{h}{\lambda}\right)^{1.6}, \tag{2.16}$$

wherein the first order mechanical scattering coefficient ($F_V$) neatly includes Tiersten's $\frac{4\mu'}{{V_R}^2}\frac{\lambda'+\mu'}{\lambda'+2\mu'}$, and a second order term proportional to $S_V$ is also present. The other symbols, $P_V$ and $K^2$, are the piezoelectric scattering coefficient and electromechanical coupling, respectively.

This extension of Tiersten's formula and the associated coefficients for various materials composing surface wave gratings were reported by B.J. Hunsinger in 1981 [38]. The first

and second order velocity dispersion captured in this equation are evident in the expansion of the SAW velocity shift in terms of $h/\lambda$, which is equal to the more common normalized wavenumber ($\frac{\beta h}{2\pi}$) used in dispersion plots.

The plot of Figure 2.14 compares Tiersten's first order result (using only Hunsinger's $F_V$) with our finite element calculations for varying layer thickness, $h$. The structure is polymethylmethacrylate (PMMA) on lithium niobate (Y cut, X propagating).

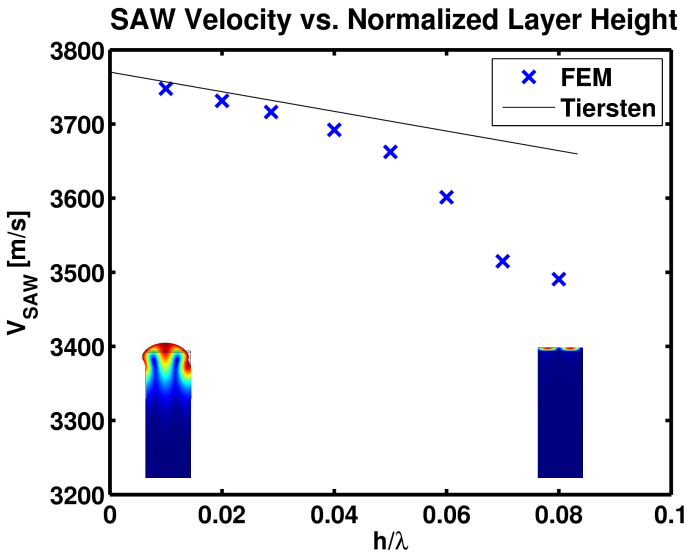


**Figure 2.14:** Calculations at the transition into non-Sauerbrey loading as a function of normalized layer height. Comparison is made to Tiersten's perturbation theory result.

A useful point to note from this result is well-known to the non-destructive testing/evaluation (NDT/NDE) community: the examination of a range of frequencies and wavelengths allows one to effectively sample the material properties as a function of the depth. This has been achieved in practice by use of either pulse mode or swept frequency continuous wave measurements.

### 2.4.2 Phase and Group Velocities

Acoustic wave gas and chemical sensors are typically evaluated using narrowband measurements. For instance, conventional instruments monitor change of the continuous wave phase of a delay line or resonator, often by monitoring the oscillation frequency when operated in a suitable feedback loop. In such cases it is appropriate to make certain approximations such

as consideration of device parameters only at resonance ($f_0$), i.e. at a particular operating point ($f = f_0$). We may omit the subscript 0 when a dominant frequency exists within a bandwidth. This treatment is convenient, but it limits each measurement to two values, e.g. the magnitude ($|S_{21}|$) and phase ($\angle S_{21}$), or center frequency ($f_0$) and damping ($\alpha$).

Signatures of acoustic wave sensors may be strongly temporally and spatially dependent, allowing significant information to be extracted. However, this is impossible to do at a single frequency or wavelength; at least some finite bandwidth is required. Just as more information may be transmitted over a channel with a wider bandwidth, more information about a general structure may be obtained by measurement over a larger acoustic bandwidth (when the measurement time interval is fixed). Pulse mode measurements and swept frequency measurements cover a greater frequency range, and more informative signatures of changes to a device may be discerned. In Chapter 6, we show how additional sensing information may be intentionally encoded in dispersive sensor devices. First, however, we will discuss the use of two key parameters determined by the *dispersive* relationship of $\omega$ and $k$: phase velocity ($v_p$) and group velocity ($v_g$).

Both the phase velocity and the group velocity of surface waves generally change with increased layer thickness or mass density increase within the layer (the latter decreases the layer velocity, making it effectively thicker). A system's dispersion is sensitive to the layer density, thickness, inhomogeneity, etc. Thus the curves could be plotted parametrically: $\omega(k, \rho_l, d, \ldots)$. In Figure 2.15 we show an example "slice" of such a higher-dimensional function when variation of the extra parameters is not considered. The shaded regions show how $v_g = \partial\omega/\partial k$ may be determined by the local slope within a range of frequencies and wavenumbers. Pulse mode measurements or other relatively wideband techniques help sample ranges of the dispersion curve for determination of the phase and group velocities. This is an advantage of pulse interrogation of the passive reflective delay line sensors described in our work.

To now discuss the phase and group velocity sensitivity to mass loading, we start with the result for $\Delta f/f$ from (2.15). This was for the case of Rayleigh SAWs with an extremely thin overlayer, i.e. one which never becomes thick (even effectively) as mass is added. The

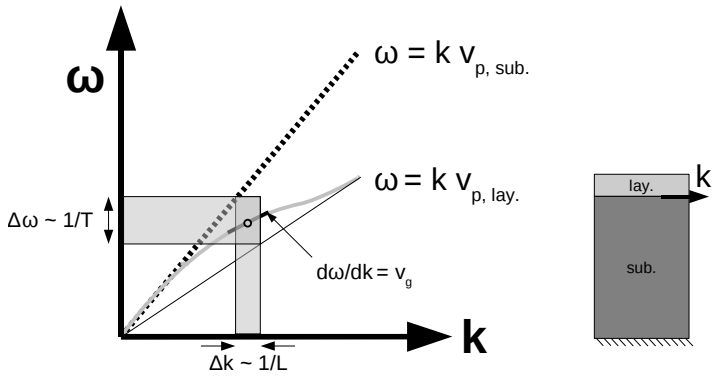


**Figure 2.15:** For a wave packet with approximate temporal and spatial widths $T$ and $L$, the region of operation is shown along with the local slope which gives the velocity of the packet envelope (group velocity).

sensitivity of the relative frequency to the areal mass change, $S_m^f$, is a negative normalized quantity:

$$S_m^f = -\frac{\Delta f/f}{\rho h} \approx -\mathrm{MF} f \ , \tag{2.17}$$

where MF represents the appropriate factor(s) for the acoustic mode.

The fractional phase velocity sensitivity can be found by some algebra upon $\omega$, $k$, and their differentials, to finally obtain the conversion factor $S_f^v$ and then $S_m^v$:

$$S_m^v = S_f^v S_m^f = \left(1 - \frac{v_p}{v_g}\right)(\mathrm{MF} f) \ . \tag{2.18}$$

In the transition from $\Delta v/v$ of (2.14) to $\Delta f/f$ of (2.15), we implicitly assumed that $\Delta\lambda$ or $\Delta k$ was zero. That was appropriate for a dispersionless device: the linear dependence of two variables allows one quantity to completely determine the other. When dispersion is present, as in the cases of acoustic plate modes, Love modes, or waves in patterned structures such as phononic crystals, the parameters will be interdependent.

The result of (2.18) raises an interesting point. For infinitesimal mass change (dispersionless loading) on a dispersionless structure, the phase velocity is unaltered by the change. A nonzero fractional phase velocity sensitivity requires a dispersive device: $v_p \neq v_g$. For instance, a cavity resonator gives a very large $S_m^v$ as $v_g \to 0$. We also note that a system having normal dispersion, i.e. $v_g < v_p$, always has $|S_m^f| < |S_m^v|$.

The ratio in (2.18) becomes $\frac{v_p}{v_g} = 1$ in the limit of large wavelengths and large time

periods. This is evident from all ($\omega$, $k$) dispersion diagrams, but the result can be mathematically verified. Although the phase velocity is indeterminate ($\omega = 0/k = 0$), one may apply L'Hospital's rule to evaluate $v_p = \omega/k$ as both $\omega \to 0$ and $k \to 0$, obtaining $v_p = \partial\omega/\partial k = v_g$. In this limit of spatial and temporal averages, the group and phase velocity are formally identical. The utility (and feasibility) of independently measuring the phase and group velocities then depends upon the availability of equipment to conduct measurements with sufficient spatial and temporal resolution.

The work of McHale et al. [66] separately treated three Love wave modes propagating in a single slow layer, but experimental results were limited to the frequency range for which only the first mode can be observed. We reason that the theoretical treatment of isolated modes should not directly correspond to experimental data at frequencies that excite multiple modes.

The use of a single band of the dispersion curve to predict the mass sensitivity should be most useful when the operating point ($\omega_0$, $k_0$) corresponds to a single mode confining energy in the region of interest within the structure. In addition to computation of dispersion curves, an analysis of mode profiles should be conducted to accurately reveal the mass sensitivity of velocity, frequency, etc. for loading of a given region or boundary of a structure. We demonstrate this approach using FEM results in Chapter 5.

As shown in the McHale data displayed in Figure 2.16, multiple modes exist over most of the frequency spectrum. In general, one does not necessarily excite only a single mode, so an aggregate measure is needed, as shown in the right panel, in which the frequencies of strong dispersion are shaded.

We computed the density of states (DoS) for the dispersion data in Figure 2.16 because this measure includes all modes within the bandwidth and correlates with the dispersive operating points McHale et al. reported to have high velocity sensitivity [66]. In the figure each mode is weighted equally, but a general measurement will not always "receive" all modes with equal amplitudes. Although the technique is not described until Chapter 5, we note here that the DOS usually correlates with the transmission loss (due to the wavenumber spread and corresponding spatial localization). An example of such high DOS occurs at

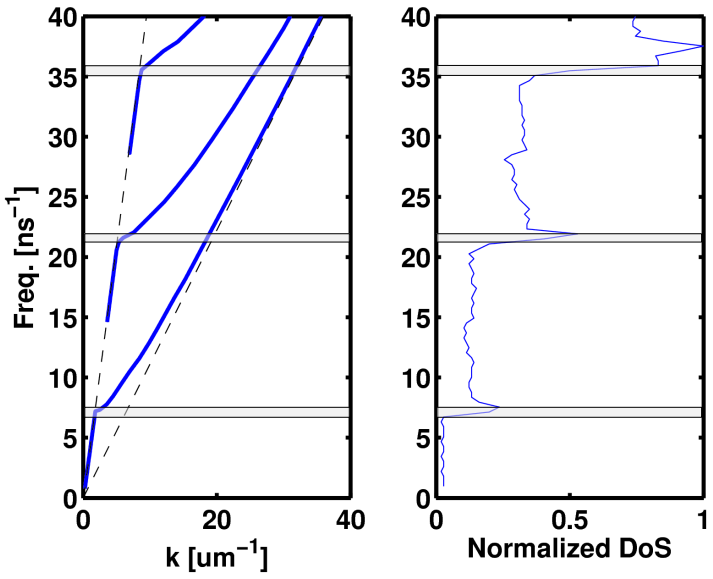


**Figure 2.16:** Love wave dispersion curves (left) and regions of high velocity sensitivity in agreement with our computed density of states (right). The highlighted regions were placed at the sharpest increases in the DOS.

the Bragg band edge in a 1-D PnC, an example of which was shown at $k = \pi/a$ in Figure 2.4b. We next discuss the trade-off due to a rigorous connection between dispersion and attenuation.

## *2.5 Dispersion, Attenuation, and Loss*

For surface activated acoustic wave sensors, the presence of a sensitive film is known to "load" devices. Furthermore, large mass perturbation shifts resonant frequencies, broadens resonances, and increases the measured loss. We next consider the relation of general mass loading and the resulting non-trivial dispersion to the signal loss.

Not shown in Sauerbrey's equation (1.1) is the concomitant spectral broadening of the resonance in response to the loading[3]. This corresponds to attenuation: at very large loadings, the resonance may become indistinguishable. In this context one would refer to the resonator quality factor, $Q \approx \frac{f_0}{\Delta f} \approx \frac{\beta}{2\alpha}$, which relates the half power bandwidth or

[3]Sauerbrey's formula assumes the loading material is identical to the resonator material; dissimilar films introduce broadening due to film resonances. It is also important to note that, at large loadings ($\Delta f/f >$ 2%), the original Sauerbrey equation typically becomes inaccurate.

broadening, $\Delta f$, to the attenuation coefficient, $\alpha$. For an unpowered resonator, the spectral broadening is necessarily accompanied by decreased oscillation amplitude at the frequency of oscillation. The effective width of the resonance in part determines the precision to which one can measure its center frequency, and so an unloaded resonator may have high $Q$ and excellent sensitivity, but these parameters suffer when sufficiently loaded.

When a *resonator* is connected to an oscillator circuit (amplifier and filters), the phase velocity change due to mass loading causes a resonance frequency shift, $\Delta f$. In many applications $\alpha$ may also be measured via the amplifier gain required to sustain the oscillation criterion (or some set-point providing a safe margin for oscillation). Both the effective phase velocity and damping constant can be measured in each sample interval, and thus both the amount of mass and the mass sensitivity (inversely related to loading) may be tracked.

For wave propagation in general inhomogeneous media, such as periodic structures, the acoustic wave number becomes complex, e.g. $k(\omega) = \omega/v_p(\omega) + j\alpha(\omega)$, and the amplitude of a particular mode can be represented by a factor $\exp(-\alpha x)$. This term also appears in viscous media, and it is not surprising that the viscosity, $\eta$, is a function of the material's "internal" (molecular) structure.

We must look carefully at the modal origins of the attenuation to determine whether such dispersion is helpful or detrimental to a given measurement. More generally, a measurement integral should be computed over the modal basis - if the energy is spread outside the bounds of measurement (e.g. a finite frequency bandwidth or spatial aperture), then the excess spread probably corresponds to *loss*.

### 2.5.1 Apparent Loss

In the dispersive devices of this work, it is important to distinguish between attenuation and loss. For causal systems having square integrable responses (two requirements of the Titchmarsh theorem), the Kramers-Krönig dispersion relations imply that a frequency dependent velocity necessarily implies frequency dependent attenuation (Hilbert transform).

We find it important to note that this phenomenon can be distinct from the bulk material attenuation. For instance, we showed in Figure 2.8b the leaky SAW dispersion occurs as a

function of the constructed geometry, i.e. when the wavelength is comparable to the scale of layer thickness; it is not a significant function of the atomic or molecular resonances which yield the material absorption. Thus the LSAW velocity dispersion and corresponding loss are present even when the material $\alpha$ is zero. We reiterate that losses due to material quality are not relevant to the majority of this work.

If a perfectly isolated structure is assumed, true acoustic energy loss is not possible without considering multiphysical effects such as radiative cooling. In this work, we do not consider the scalar or tensor bulk viscous damping; it is assumed negligible for the materials of interest. Understanding this, we consider loss to be a matter of perspective, i.e. due to the conserved (unitary) transformation of energy over a modal basis which may only partially excite a given detector. This results in perceived loss due to the spread of energy over the basis, a concept that is particularly useful in Chapter 3 for the analysis of observable structural eigenmodes. The concept also appears in the context of matched filter designs we put forth in Chapter 6.

## *2.6 Summary*

In this chapter we discussed the inherent dispersion of BAWs and SAWs in general media, the importance of dispersion in acoustic wave sensors, and some implications for sensors. We noted that inhomogeneous mass loading is inherently dispersive and that the mass sensitivity of nominally dispersive devices depends upon the region of operation on ($\omega$, $k$) dispersion diagrams. We computed several different forms of dispersion including: polarization and azimuthal velocity dispersion due to material anisotropy, and guided mode velocity dispersion for thin layers. In Chapter 3 we describe our finite element computations and a mode sorting post-processing technique to constrain the very general solutions to those that can be observed at the surface.

# CHAPTER III

# COMPUTATION OF SAW DISPERSION

## *3.1 Introduction*

Simulation of surface waves using the finite element method (FEM) is advantageous in the present study for several reasons: to predict surface wave dispersion due to various surface coatings, to simulate mass loading frequency shifts for SAW sensors, and especially to reveal general surface wave dispersion and band gaps for surface PnCs.

Both analytical and numerical evaluation of SAW dispersion in piezoelectric media have been conducted for various modes, mechanical and electrical boundary conditions, and surface corrugation and roughness. Several notable investigators in this area include: Abbott, Auld, Biryukov, Plessky, Solie, and Tiersten [7, 77, 35]. Typical approaches apply perturbation theory, coupling of modes (COM) theory with fitted parameters, or exact numerical calculations. As expected, for small loadings, the linear perturbation theory is sufficient, but the method gives increasing error at greater loadings (as in Figure 2.14). In practice the original and perturbed fields are not truly identical, and this implies higher order dispersion. In the case of phononic crystals, it is the spread of energy into space harmonics: geometric dispersion due to the inhomogeneous spatial distribution of material properties.

Compared to perturbation theory approaches, numerical methods that discretize the domain can more faithfully represent the actual distribution of energy within the structure, and the calculation can be performed to arbitrary precision. V. Laude, et al. have already extended the plane wave expansion method from the case of bulk waves, specifically to bound the existence of surface waves propagating through 2-D lattices on YZ $LiNbO_3$ [52]. For inhomogeneous and discontinuous media the finite element method (FEM) increasingly has been used to compute accurate solutions [44].

The rest of this chapter is dedicated to describing and validating the FEM computations used throughout the rest of this work, especially in Chapter 2 and Chapter 5.

## *3.2 Method*

In this work, we use FEM and eigenfrequency analysis. We compute the general SAW mode spectra for many test cases which may pertain to the design of surface PnCs for wireless passive sensors. Our computations employ recently developed MATLAB code extending the COMSOL MULTIPHYSICS software suite [97]. The approach adopts a relatively simple mathematical formulation of the problem such that intricacies are incorporated into the computational domain: complicated structures, disparate material parameters and boundaries, etc.

The numerical problem follows closely from first-principles physics, namely Newton's Second Law of motion. Equation (3.1) shows the structural mechanics formulation, where $\mathbf{u}$ is the solution vector containing displacements $\mathbf{u}_x$ and $\mathbf{u}_y$. For our analysis, the equation is homogeneous, i.e. there is no independent forcing term, $\mathbf{F}$.

$$\rho\frac{\partial^2\mathbf{u}}{\partial t^2} - \nabla\cdot\mathbf{c}\nabla\mathbf{u} = \mathbf{F} = 0 \tag{3.1}$$

Assuming a time-harmonic (resonant, steady-state) solution is one way of finding persistent solutions having measurable lifetimes. This becomes a typical time-independent eigenproblem, as we describe next. Equation (3.1) is Fourier transformed and the resulting harmonic time dependence, $e^{i\omega t}$, is factored out, leaving $-\omega^2$ to replace the time derivatives. This factor represents the eigenvalues we seek: the mode frequencies.

What remains is similar to (3.2) and may be solved as a linear eigenvalue problem in which both the canonical matrix, $\mathbf{A}$, and solution, $\mathbf{u}$, vary over the subdomain(s) and boundaries.

$$Au = \phi u \qquad A = \frac{\nabla\cdot c\nabla}{\rho} \qquad \phi = \omega^2 \tag{3.2}$$

The eigenvalues, $\phi$, yield the mode frequencies. In our study, we use COMSOL Script to iteratively vary the structure and/or boundary conditions. In an effort to see the important modes, we collect many mode frequencies, typically 30 per wavelength. We then sort the solutions in a post-processing step.

Many solutions to the eigenproblem exist due to the very general formulation of the problem and many degrees of freedom. For instance, compare Lamb waves and Rayleigh waves in Figure 3.1. Whereas the Lamb waves are plate modes and have free upper and lower boundaries, the Rayleigh modes are single-surface modes having displacement profiles decaying with depth into the substrate. The antisymmetric and symmetric Lamb modes are often called "flexural" and "dilational," respectively.

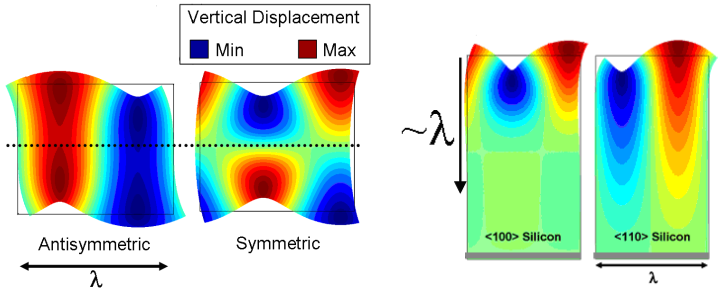


**Figure 3.1:** Lamb wave (plate mode), and Rayleigh wave (surface mode). The structure scale corresponds to the acoustic wavelength, $\lambda$, but the scale of the deformations is uniformly magnified.

This work involves thick substrates and small wavelengths (500 $\mu$m vs. 8 $\mu$m), so we expect surface wave solutions. This indicates operation similar to the limit in which $h/\lambda \gg 1$, as discussed in Chapter 2. We seek general Rayleigh-type solutions, so we enforce a typical rule of thumb for the penetration depth: two wavelengths [7]. Therefore, in most of our SAW simulations, the structure is resized to be at least 1.8 wavelengths tall and the bottom boundary is fixed to zero displacement: $\mathbf{u} = 0$. This is, of course, only an approximation to the ideal semi-infinite case; however, we will show it to be a very good approximation for certain cases later in this chapter. The approximation is especially needed because the available perfectly matched layers (PMLs), infinite elements, etc. are not broadly applicable to general acoustic propagation (3 orthogonal wave polarizations) in anisotropic/piezoelectric media[1].

We desire surface waves propagating parallel to the top surface, implying periodicity

[1]PML codes in the literature and known to the author were almost exclusively designed for electromagnetic problems, and they appeared to be very difficult or impossible to implement in COMSOL Multiphysics as an end-user.

leftward and rightward. Thus the leftmost and rightmost boundaries and vertices share the state variables $u$, $v$ ($x$ and $y$ displacements), and also $V$ (electrical potential) when appropriate. The assignment is shown in (3.3).

$$\begin{aligned} u_{x=0} &= u_{x=\lambda} \\ v_{x=0} &= v_{x=\lambda} \end{aligned} \tag{3.3}$$

Thus, periodic boundary conditions apply to the left and right boundaries along the $x$ axis, i.e. at $x = 0$ and at $x = \lambda$ when the domain width is $\lambda$. In the case of a domain uniform in the $x$ direction, this is sufficient; the structure period equals the solution period. For the periodically patterned structures, where in general the structure period does not equal the solution period, we will show an adjustment to the equation.

Throughout this work, we apply the MEMS Module operating under the 2-D "Piezo Plane Strain (smppn)" Application Mode. The two-dimensional mode is suitable because we assume infinite extent of the structure in the $z$ direction. This has the added advantage of reducing the spatial domain to two dimensions. Figure 3.2 shows a patterned layer structure (one-dimensional surface PnC) and the 2-D computational domain in $x$ and $y$ directions only.

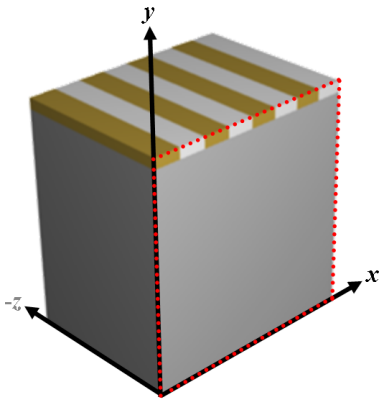


**Figure 3.2:** Example cross-sectional view of a patterned thin film on a substrate. A slice representative of the 2-D computational domain is enclosed by red dots.

The two-dimensional surface wave FEM simulations were conducted using the plane strain assumption. This reduces a 3-D volume to a 2-D slice for which only three strains are nonzero. Thus, the strain tensor has only three independent components, $u_x$, $u_y$, and

$u_{xy}$. The 2-D computational domain represents the in-plane propagation direction of the SAW ($x$ axis), and the depth of the substrate ($y$ axis). Because displacements are only longitudinal and shear vertical with respect to the in-plane propagation direction, only modes with polarizations along these bases will be revealed. Such modes include: Rayleigh SAW, "leaky" Rayleigh waves, and the film-guided Sezawa mode (generalized Lamb mode $M_{21}$). Solutions are assumed uniform in the third dimension, the direction normal to the 2-D slice. Thus the solutions are the in-plane "line waves" analogous to the 3-D "plane wave."

The key guidelines for specification of the computational domain are:

- Width of the domain (in $x$) is one acoustic wavelength
- Periodic boundary condition on $x = 0$ and $x = a$ boundaries
- Fixed bottom boundary (for surface wave case; not for Lamb waves)

The geometry aspect ratio is approximately 1.8 : 1 (for surface wave case; the ratio is height:width, and this condition requires the acoustic field decay to zero in less than 2 wavelengths from the surface). A conceptual aside: due to the $\mathbf{u} = 0$ boundary condition, one can treat the problem by the method of images, as is common for perfectly conducting boundaries in electromagnetics; the solution we obtain is identical to the case of the symmetric Lamb wave for a plate thickness equal to twice the domain height.

We used unaltered material constants and tensors from the MEMS Module material library. The anisotropic or piezoelectric option was chosen where appropriate, e.g. single crystal silicon substrate or zinc oxide film, respectively.

The number of degrees of freedom (DOF) allowed in the 2-D cross-section models was at least 500 and at most several thousand (piezoelectric film on silicon). The DOF was allowed to change in each iteration as the structure and mesh were automatically scaled to accommodate nearly $2\lambda$ penetration depth as $\lambda$ changed. This is important in order to reduce the occurrence of *systematic dispersion*. The simulation was run on various desktop personal computers running COMSOL 3.5a on Microsoft Windows XP Professional with

**Table 3.1:** FEM solver settings.

| Parameter | Value |
|---|---|
| Solver Mode: | Eigenfrequency Analysis |
| Matrix Symmetry: | Hermitian |
| Eigenvalues: | 30 |

1+ GHz 32-bit processor and 1+ GB RAM. Each iteration required about one second, completing a typical dispersion plot or band diagram in thirty seconds to one minute for less than 50 iterations (wave numbers).

The following are the settings typically used in this work:

We require the Hermitian condition because we introduce complex valued boundary conditions for the case of the periodically patterned layered structure. This structure requires additional modulation of the periodic boundary to enforce the solution period distinct from the structure period. We allow a large number of modes, e.g. 30, over a wide frequency range because we are able to sort them and cull those irrelevant to experimental observation.

This work was accomplished exclusively with default mesh settings. The adjoining rectangular subdomains used the "Triangular (Advancing Front)" mesh with Schlag quadratic elements. The number and size were determined automatically by COMSOL Multiphysics for re-meshing in each iteration. We found that COMSOL's numerical implementation of FEM automatically handled meshing of arbitrary geometries and treatment of complex valued fields; many of the details of the FEM implementation were conveniently abstracted away. However, as conveyed in this document, we verified test cases and solution convergence in order to gain confidence in the results.

It can be cumbersome to completely define a model geometry and mesh, configure the solver, and post-process solutions using COMSOL Script. We recommend the creation and solution of a model in COMSOL before saving as a MATLAB-compatible ".m" file. The file can then be edited to include an iteration loop, plotting commands, etc. We found it helpful to recreate a model and solve it with the minimum number of steps and no mistakes, because COMSOL (version 3.5) records a complete history of commands in the ".m" file,

regardless whether they affect the final output.

Given the eigenproblem of (3.2), we use the following equation to obtain the real and positive frequency eigenvalue for the $j$th iteration:

$$f_j = \frac{|\Im(\text{fem.sol.lambda(j)}|}{2\pi} \ , \tag{3.4}$$

where fem.sol.lambda(j) is the $j$th eigenvalue of the raw FEM solution, $\Im$ indicates the imaginary part, and the absolute value is taken because of the sign convention of the phasor. As an iterative procedure, our script accepts an array of wave vectors and other parameters specifying layer thickness and/or phononic crystal parameters. The general procedural flow is provided in Figure 3.3.

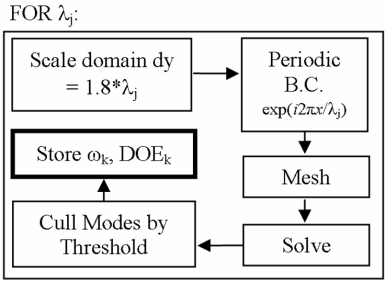


**Figure 3.3:** Script procedural diagram showing the iteration loop over wavelength. An array of modes, $\omega_k$, is stored for each wavelength, $\lambda_j$.

### *3.3 Mode sorting*

As previously discussed, multiple modes satisfy the eigenvalue problem. The modes have different frequencies and/or spatial energy distributions, and some modes may not be surface modes at all; though all modes satisfy the surface boundary condition(s), the problem is under-constrained with respect to surface waves. This is similar to the case of the generalized eigenvalue problem discussed in Chapter 2, which requires careful selection of partial waves having complex wave number, $k_i = \beta_i + j\alpha_i$, to satisfy the surface boundary condition. This imposition of radiation condition(s) is tedious and programmatically nonlinear; several conditional statements are conventionally used[2]. In a more abstract sense the problem becomes a task of separating "signal" from "noise," or relevant modes from irrelevant modes,

[2]As in K. Hashimoto's Appendix A [35], and P.M. Smith's part A [90]

respectively. For example, if a measurement is only sensitive to the upper boundary of a structure, e.g. a laser beam reflected by the top surface of an opaque solid, then we only expect to measure modes for which the energy is sustained at the top surface.

We devised and implemented a single metric for this. The surface-most modes carry the majority of the acoustic energy near the surface, so we define a depth-of-energy (DoE) using a depth-weighted centroid formulation over the independent field quantities contributing to the total energy: independent strains and electric potential (for piezoelectric materials). This allows selection of the surface modes; an important operation for simulation of surface phononic crystals that scatter waves to the bulk. In a conference paper [97], we took the energy as proportional to the norm square of two components of the strain field, $S_{xx}$, and $S_{yy}$:

$$\mathrm{DoE} = y_{\max} - \frac{\iint \left(S_{xx}S_{xx}^{*} + S_{yy}S_{yy}^{*}\right) y \, dxdy}{\iint \left(S_{xx}S_{xx}^{*} + S_{yy}S_{yy}^{*}\right) \, dxdy} \,, \tag{3.5}$$

This is sufficient when electric fields are not present, or when the electromechanical coupling is small: the maximum kinetic energy equals the maximum potential energy (differing only by 90 degree phase shift). Figure 3.4 serves to conceptually validate the method. The depth of energy increases as modes transition from surface to bulk. Phrased another way, as energy is dispersed into $y$-propagating modes, $k_y$, the depth of energy increases.

A limitation of the formulation in (3.5) was lack of generality. For instance, the shear stress was not included. For more general applications, all the stress components should be included, and since we expect the field solution to obey the boundary conditions, some components may be zero at certain locations. For example, although each $\mathbf{S}_{iy}$ strain is zero at the free boundary (top surface, $\mathbf{T} \cdot \hat{\mathbf{n}} = 0$ or $\mathbf{T}_{iy} = \mathbf{c} : \mathbf{S}_{iy} = 0$), in general this surface normal strain component can be included. This leads to generalization for problems of higher dimension, those considering multiple layers, etc.

Extension to three dimensions and inclusion of the electric field are required for assessment of 2-D surface phononic crystals on strongly piezoelectric substrates. Though the surface acoustic superlattice is in the surface plane, it forms a surface grating and may diffract bulk modes, yielding very lossy surface modes. We examine this more in Chapter

| DoE [um] | Frequency [GHz] | Type | |
|---|---|---|---|
| 0.5323 | 1.216 | SAW | 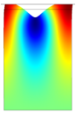 |
| 0.5323 | 1.216 | SAW | 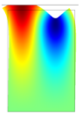 |
| 2.4478 | 1.485 | PSAW | 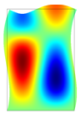 |
| 3.1441 | 1.109 | Bulk | 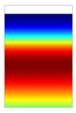 |

**Figure 3.4:** Solutions generated by a custom MATLAB script automating the COMSOL MULTIPHYSICS solver. Depth of Energy (DoE) is given for each mode.

5.

When the time harmonic dependence is considered, (3.5) is similar to B.A. Auld's formulation of the total energy, and follows a form used in the complex reciprocity relation [7]. By Hooke's Law and time harmonic reciprocity, the mechanical energy may be determined from the strain field ($\mathbf{S}$). The total energy in a volume, including that due to the electric field ($\mathbf{E}$), may be defined:

$$\iiint (\mathbf{S}^* \ \mathbf{c} \ \mathbf{S}) + (\mathbf{E}^* \ \mathbf{e} \ \mathbf{E}) \ dxdydz \ , \tag{3.6}$$

where $\mathbf{S} = \nabla \mathbf{u}$, $\mathbf{E} = -\nabla V$, and $\mathbf{e}$ is the piezoelectric coupling matrix.

This is a convenient form for post-processing in COMSOL Multiphysics because both $\mathbf{u}$ and $V$ are the independent solution variables. Though stored energy is proportional to the square of the strain or electric fields (as used in the 2-D case), for generality we must include the material stiffness tensor ($\mathbf{c}$), piezoelectric coupling ($\mathbf{e}$), and material permittivity ($\epsilon$), to ensure each term has comparable units. For the inhomogeneous structures of interest, both the stiffness and permittivity are allowed to vary through the volume. The numerical integration must then evaluate $\mathbf{c}(x, y, z)$ etc. at each point.

To construct a broader generalization, we note the general depth-of-energy is analogous

to quantum mechanical observation: the integral for expectation value. One could view the eigenmodes as solutions of a "particle in a box" canonical problem, and we wish to obtain the expected position of energy (i.e. a wave function or "particle") within the domain. The average position of the energy along the $z$ direction for an eigenmode, $\psi$, may be defined:

$$\begin{aligned} < z >_{\psi} &= \frac{\iiint \psi^* \, \mathbf{M} \, z \, \psi \, dxdydz}{\iiint \psi^* \, \mathbf{M} \, \psi \, dxdydz} \\ \psi &= \begin{bmatrix} u_{xx} & u_{yy} & u_{zz} & u_{xy} & u_{yz} & u_{xz} & -\nabla V \end{bmatrix}^T \\ \mathbf{M} &= \mathrm{diag}(\mathbf{c}, \mathbf{c}, \mathbf{c}, \mathbf{c}, \mathbf{c}, \mathbf{c}, \mathbf{e}), \end{aligned} \tag{3.7}$$

wherein $\mathbf{M}$ contains the material constants (matrices in Voigt notation) from which $\psi$ selects components. $\mathbf{M}$ may vary with position when integration is performed over multiple domains representing different adjacent materials. The subscripts within $\psi$ correspond to Voigt notation of partial derivative and direction, i.e. $u_{xx} \equiv \mathbf{S}_{xx} \equiv \mathbf{S}_1$, and $u$ is the generalized displacement, rather than the coordinate $u$ found in COMSOL's internal variables.

For an ideal measurement depending upon total energy at the surface, solutions $\psi$ minimizing the integral of (3.7) produce the least expectation value for $z$, and therefore, have least DoE and are most measurable at the surface. The DoE and the total energy formalism are applied in subsequent sections of this work because the study focuses upon surface waves, regardless the dimensionality of the PnC considered.

We also note that an analytical approach using Laguerre polynomial expansion [45] provides an inherent DoE constraint because the solutions form an orthogonal basis according to an inner product of the form:

$$\langle f, g \rangle = \int_0^{\infty} f(y) g(y) e^{-y} \, dy \; . \tag{3.8}$$

In (3.8), $e^{-y}$ is a weight function tapering off with the depth, $y$, and its argument may be scaled by a factor of $\lambda$ to specify a certain penetration depth of the surface wave solutions. The reader may compare this to the integral for the energy expectation value in (3.7). As others have already determined, the Laguerre polynomial expansion is not the best choice for all substrate configurations [57]; when the material parameters are discontinuous in the

depth, sharp features are found in the field profile that are not well represented by the eigenfunctions (giving rise to Gibb's phenomenon, requirement of an infinite number of polynomial terms, and convergence only in the mean). The COMSOL software package encounters the same challenge representing sharp variations of the field, but its adaptive domain meshing procedure automatically improves resolution in thin layers without increasing the computational burden of the rest of the structure. We will compare our FEM computations to the Laguerre polynomial approach in a subsequent section.

## *3.4 Computed SAW Dispersion*

### 3.4.1 Numerical Dispersion

Before discussing the structures of interest, we give an example case of *numerical* dispersion, a systematic error that occurs due to the way a problem is discretized and computed. For the simple Rayleigh wave computations, we identified two sources of numerical dispersion and we determined that the error was less than 1.5% with the default mesh settings. However, this was further improved by limiting the mesh element size, as shown in Figure 3.5.

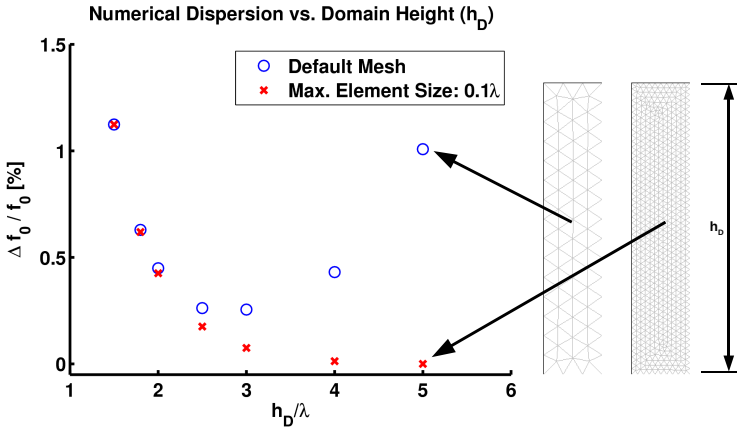


**Figure 3.5:** Numerical dispersion for a pure Rayleigh mode on YZ $LiNbO_3$. Beyond $h_D/\lambda = 3$ increasing the domain height only improved the error when the maximum element size was constrained.

The example we give relates to the approximation of the infinite substrate depth. This is represented by the domain height, $h_D$. Setting $h_D/\lambda \approx 2$ is sufficient for some cases we have reported [97]. The depth that is sufficiently deep depends upon the substrate crystal cut and the allowable error, as in Figure 3.5. A second complication is that increasing

the relative domain height, $h_D/\lambda$, does not lead to improvement if the mesh element size increases. We therefore enforce the "maximum element size" to be $\lambda/10$ where necessary.

We were also concerned that the accuracy of computations of SAWs in piezoelectric materials would suffer under the approximation of finite substrate depth. The reason for this is that the electromagnetic wavelengths are orders of magnitude larger and, operating in the range of the quasistatic approximation, the electric field will not necessarily be zero at the bottom boundary. However, by lack of a forcing term and by reciprocity of the piezoelectric effect, if the acoustic field experiences a certain penetration depth, then so must the linearly coupled electromagnetic field. To quantitatively confirm the numerical results, we computed the electromechanical coupling coefficient, $K^2$, for YZ $LiNbO_3$. We chose the widely accepted calculation [35]:

$$K^2 = 2\frac{v_{\text{free}}^2 - v_{\text{metalized}}^2}{v_{\text{free}}^2} \approx 2\frac{v_{\text{free}} - v_{\text{metalized}}}{v_{\text{free}}} \equiv 2\frac{\Delta v}{v} \ . \tag{3.9}$$

We applied a "short" boundary condition ($\vec{E} \times \hat{n} = 0$, or $V_x = 0$ in this problem) to the top boundary without adding a layer, and we used the shift in eigenfrequency instead of the velocity. The result was $K^2 = 0.049$, which is within 2% of literature value of 4.82 [100]. The FEM computation was performed using a 2-D domain with aspect ratio 4.75 (height/width) and maximum element size $\lambda/10$.

### 3.4.2 Angular Dispersion

When choosing crystal cuts for design of SAW sensors or phononic crystals, it is helpful to know the background angular dispersion ($k$ space parameterized by Euler angles) prior to device design. For example, C.S. Hartmann has compensated for the angular dispersion in the design of efficient acoustic reflectors in SAW tags operating at 2.4 GHz [33]. Likewise, for the design of surface phononic crystal devices, one should obtain the properties of the anisotropic substrate before introduction of the anisotropic superlattice structure; both affect the net angular dispersion.

The SAW substrate most frequently used in this work (and in our passive SAW sensors) is Y-Z $LiNbO_3$ (y-cut, z-propagating), and so we computed the angular dispersion (velocity curve) for this material using the finite element approach already introduced. Figure 3.6

gives a comparison of our computation with both numerical data and measurement. This reveals the degree of velocity dispersion attributable to the host material (relevant to the design of 2-D surface PnCs, not the 1-D case, for which we utilize self-focusing propagation near 0°). The figure shows the angular dispersion of the Rayleigh SAW velocity is less than 12% for this cut.

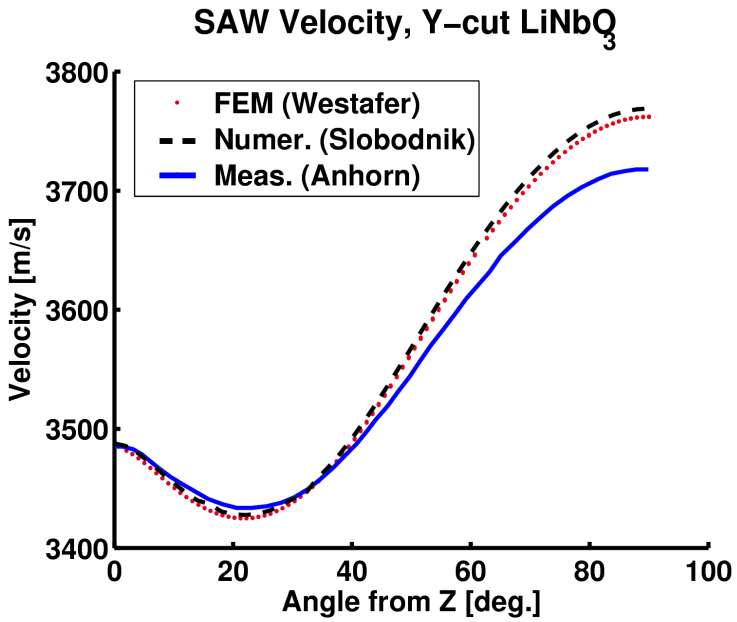


**Figure 3.6:** Comparison of our FEM result to calculations by A.J. Slobodnik, et al. [89] and measurements by M. Anhorn [4]. The useful self-focusing effect occurs near 0°.

### 3.4.3 Layers

#### *3.4.3.1 Piezoelectric Thin Film*

We next present calculated dispersion for a layered structure commonly used to generate SAWs on silicon: a piezoelectric zinc oxide thin film over a crystalline silicon substrate. Saeed Mohammadi of Professor Ali Adibi's group at Georgia Tech recently used such a structure to create transducers for some practical PnC devices [73, 2].

We compare our results [97] to those obtained by a Laguerre polynomial method, as shown in Figure 3.7 and reported by Kim and Hunt in 1990 [45]. For this unpatterned layered structure, one intuitively expects a transition of behavior: as the acoustic wavelength decreases the wave energy is confined closer to the surface of the film, rather than the

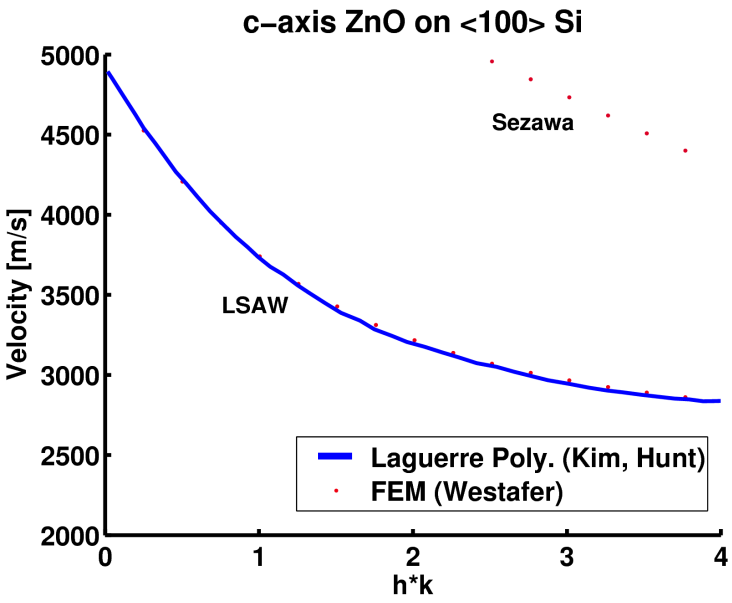


**Figure 3.7:** Velocity dispersion diagram for a ZnO layer over a silicon substrate. The wave vector is normalized by layer thickness. Comparison is made to data computed by Laguerre polynomial expansion [45].

interface, and so the wave interacts only with the film. Thus the Rayleigh velocity decreases from that of silicon to that of the ZnO film as the wavelength decreases ($k$ increases).

Note the mode with greater velocity in Figure 3.7. This mode is the first generalized Lamb mode which becomes guided in the thin film on the semi-infinite substrate. This mode for the thin film / substrate waveguide structure, specifically denoted $M_{21}$, is commonly called the Sezawa mode [7]. While the excellent agreement between the two traces demonstrates the utility of the sorting technique, the presence of the Sezawa mode demonstrates its generality.

We also conducted laser probe measurements that corroborated our computations for SAWs in homogeneous thin films. In Chapter 4 we compare our experimental results and computed values.

### 3.4.4 Patterned Layer (1-D PnC)

For periodically patterned structures, we adjusted the simulation to have a specified domain period corresponding to the lattice constant, and we allowed a varying solution period corresponding to the acoustic wavelength. We reported this method and result in a paper

at the 2009 COMSOL Conference in Boston, MA [97]. The primary structure of interest, a SAW grating composed of copper and silicon dioxide on a silicon substrate, was chosen because it had already been measured using the laser technique [63]. Figure 3.8 shows the default (and relatively coarse) meshing of the imhomogeneous structure we simulated.

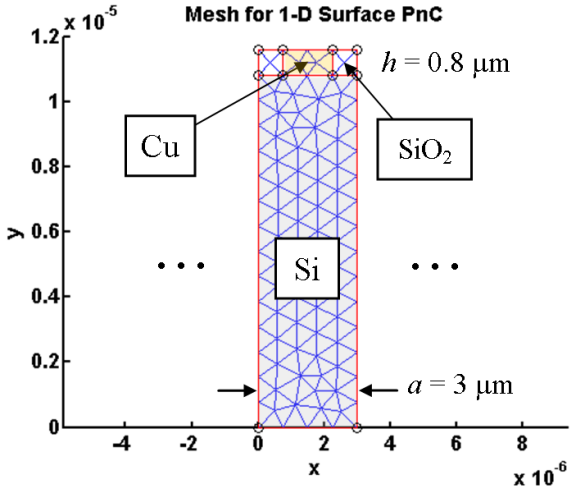


**Figure 3.8:** Computational domain and FEM mesh used to compute the SAW band diagram reported by A. Maznev in [63].

The eigenmode spectrum (Figure 3.9) corresponding to the dispersion diagram for this structure was computed by iteration of $k$, as previously described. Interpreting the figure, we note the clear velocity spectrum illustrated by the purple dots corresponds to BAWs having some component ($k_x$) along the surface ($\mathbf{k}_{\mathrm{BAW}} = k_x\hat{x} + k_y\hat{y}$). The various characteristic lines correspond to different mode polarizations and angles of radiation.

The leaky Rayleigh wave is found as the lowest band of red dots, and at sufficiently large wave numbers ($k_x a/(2\pi) > 0.3$), the $x$-directed SV BAW becomes trapped near the surface (the band transitions to red dots (lower DoE) at smaller wavelengths. As expected, the trapped BAW has a greater phase velocity than the Rayleigh-like LSAW band, even at the Brillouin zone boundary where $ka/(2\pi) = 0.5$ and the group velocities are zero. The optical analog of this structure has already been reported and is summarized on page 146 of the book by J.D. Joannopoulos [40].

The effect of the BAW radiation thus causes what would be called an "indirect" band gap between LSAW and Sezawa modes, due to the lower band maximum near $ka/(2\pi) = 0.35$,

and also due to the many "avoided crossings" appearing in the upper surface wave (Sezawa) band. A. Maznev has reported significant characterization of this structure, showing the opposing elliptical particle polarizations for the Rayleigh and Sezawa modes (retrograde and prograde, respectively) and their incomplete cancellation at the band edge [64]. In this work, it serves as a good illustration of SAW-to-BAW mode conversion in a 1-D surface PnC structure which has been analytically and experimentally characterized.

The many linear purple bands appearing where one would desire a complete band gap are not surface modes at all; they propagate and radiate energy away from the surface and so are purple in color. Surface modes are the focus of the study, so we place a threshold on the surface energy measure, selecting only modes with a normalized depth-of-energy (DoE) $< 0.2$. This implies the strain energy centroid is within the top 20% of the total structure height.

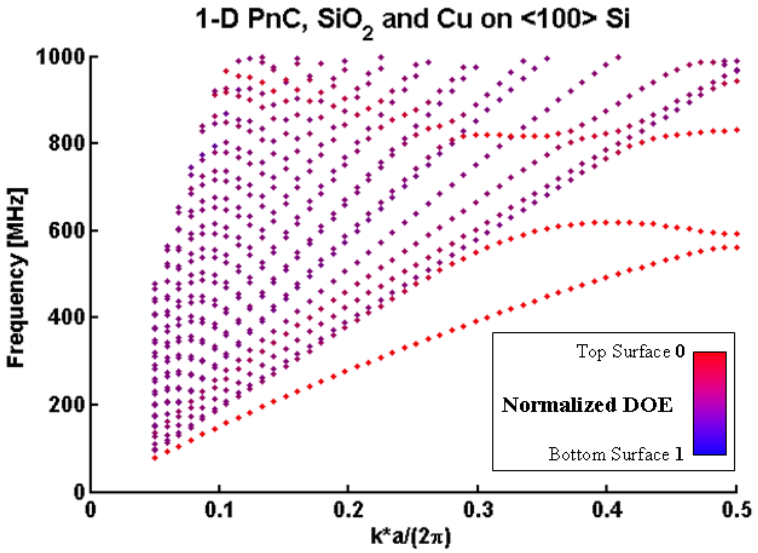


**Figure 3.9:** Our computed eigenmode spectrum for the 1-D surface PnC reported by A. Maznev [63]. Modes are colored according to a depth of energy measure over the eigenfunction.

Figure 3.10 shows the automatically selected surface modes agree well with measurements from an impulsive laser acoustic spectrometer [63]. No fitting of parameters was performed, and default material constants (tensors) were used. Surface wave band gaps appear when energy can no longer propagate with certain wave numbers, $k$. In the figure

there exists a range of frequencies and wave numbers for which *surface* modes do not exist; this implies a complete *surface* phononic band gap in one dimension. This agrees with measurements at the surface, but excitation at frequencies within the surface band gap can produce the BAWs, resulting in true loss *with respect to measurements of the surface.*

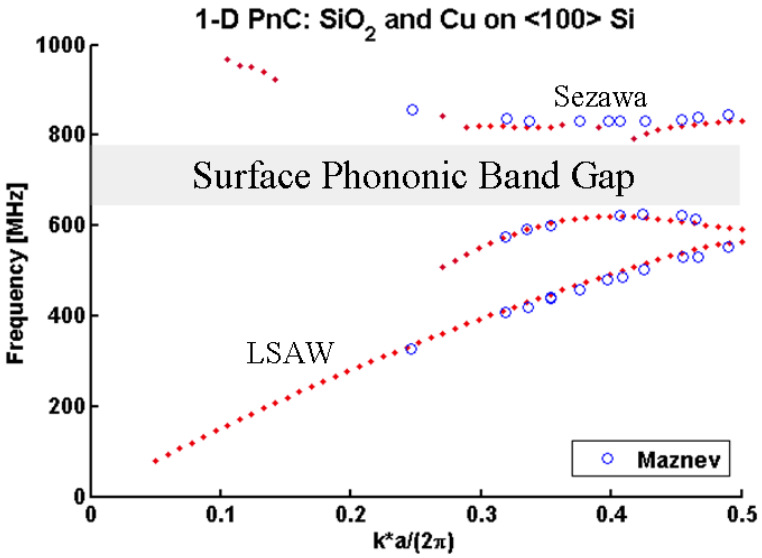


**Figure 3.10:** SAW dispersion showing a surface wave band gap along one dimension. FEM simulation (solid dots) and laser probe measurements by A. Maznev (open circles) show both leaky SAW and Sezawa modes.

We note that the plot shows an incomplete LSAW band gap where $ka/(2\pi) \in (0.3, 0.5)$ and that the group velocity of the upper LSAW band changes sign near $ka/(2\pi) = 0.4$, indicating the occurrence of slow guided waves having nearly stationary energy distribution between 500 and 600 MHz.

We also notice that the Sezawa band is periodically broken by the bulk wave modes, and we attribute this to the periodic diffraction of the surface mode to the bulk at certain angles as the frequency changes. Indeed, the 1-D PnC is a surface grating and should exhibit diffracted orders dependent upon the incident frequency. We have not yet confirmed whether the characteristic BAW diffraction angles concur with experiment. They may not agree exactly because the artificial fixed boundary approximation to an infinite substrate is appropriate for surface waves but not for bulk waves; however, the data at least indicates the existence and nature of the phenomenon.

## *3.5 Summary*

In this chapter we demonstrated extension of a commercial FEM software package to study the behavior of SAWs and layer-guided acoustic modes in anisotropic, piezoelectric, and thin film *surface* phononic crystal structures. We investigated the extent of numerical dispersion, we confirmed the piezoelectrically stiffened anisotropic SAW velocity curve, and we determined the piezoelectric coupling coefficient for Rayleigh SAWs – all on YZ $LiNbO_3$ – to further demonstrate the accuracy and general utility of our approach.

In the analysis, we leveraged a feature of the FEM eigenvalue computations: the solutions are not constrained *a priori* to certain mode types, as sometimes occurs with series expansions used in perturbation theory. That is, one need not presume a certain complete orthonormal basis to express the solutions. We used a desktop personal computer to solve the FEM systems and to produce the general mode spectra, and the author wrote a post-processing algorithm to display the modes "matching" or "overlapping" a certain measurement (e.g. a certain energy distribution and/or polarization).

Finally, we computed mode spectra for a 1-D thin film surface PnC for which experimental data were reported in the literature. The results agreed with experiment to better than 10% without any fitting of material constants. In this way we have demonstrated the utility of our FEM computations to produce data corresponding to measurements.

Continuing forward, we desired to confirm the computations through more experiments and to learn which structures could be readily fabricated. In Chapter 4 we describe both fabrication and measurement of dispersive structures using a laser acoustic spectrometer and also an RF wafer probe station.

# CHAPTER IV

# MEASUREMENT OF SAW DISPERSION

## *4.1 Introduction*

After we computed the SAW dispersion for the layered and patterned structures, we collected measurements to validate the computations and to experiment with the characterization and fabrication techniques. Two experimental approaches were used to obtain SAW dispersion data. The first technique used lasers to excite and measure SAWs on material surfaces. The second technique required fabrication of transducers on either side of PnC test structures to measure the two-port transmission and reflection of SAWs. This chapter describes fabrication and experimental characterization work performed by the author within the Microelectronic Acoustics Group at Georgia Tech.

## *4.2 Laser Acoustic Spectrometer Measurements*

We explored use of a laser acoustic spectrometer capable of optical excitation and detection of SAWs. The laser acoustic spectrometer, which we also refer to as the "laser probe," employs impulsive stimulated thermal scattering (ISTS) by the transient grating (TG) method. This allows generation and measurement of surface acoustic waves on a flat substrate, typically a wafer.

Capabilities of the tool include:

- Non-contact generation of surface acoustic waves
- Excitation of 6$\mu$m to 18$\mu$m wavelengths
- Measurement of frequency dispersion curves
- Measurement of angular dispersion curves

The advantage of using such an all-optical tool is that one may design a dispersive structure using FEM or other computations and subsequently fabricate and measure that structure to ascertain whether the expected dispersion was obtained. We used the tool to

validate some of our FEM calculations and also in attempts to characterize surface phononic crystal structures. Our first experiments used planar structures for simplicity, while 3-D "woodpile" structures were eventually tested.

### 4.2.1 Overview

The laser spectrometer used in this work was an Impulse 300 system donated by Alex A. Maznev of Philips Advanced Metrology Systems (now AMS, LLC). Details about this tool may be obtained from a review paper by J.A. Rogers, et al. [82]. The author and Eric W. Massey [61] received, installed, aligned, calibrated, and wrote automation software for the system. The author also designed, installed, and calibrated a networked (CANopen bus) motion control system that allowed control of all stage and optics positioning through a single RS-232 serial interface. An illustration of the system is given in Figure 4.1, and a photo of the optics head assembly is shown in Figure 4.2.

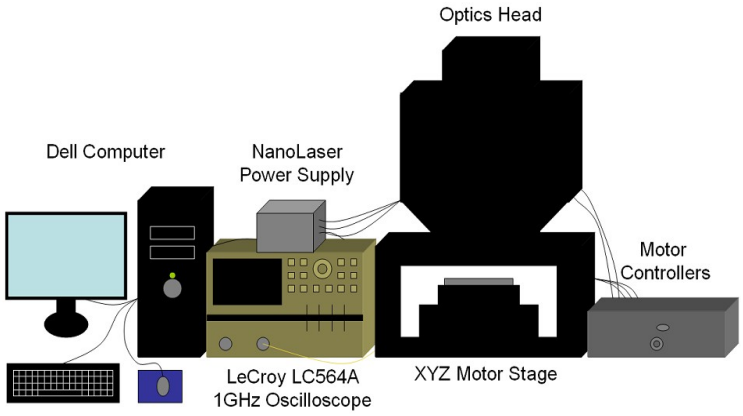


**Figure 4.1:** Drawing of components of the laser probe system [61].

This non-contact optical excitation and measurement tool uses a $Q$-switched picosecond laser to generate optical pulses that interfere to form a pattern of high intensity light bands on the surface of a test structure. The wafer regions illuminated by the bright fringes absorb the optical energy and undergo rapid thermal expansion. Figure 4.3 shows the configuration of the optics. Of particular importance in the configuration is the phase mask, which diffracts the beam into two primary orders such that they can be recombined on the substrate surface to generate the diffraction pattern. Because the wavelength of

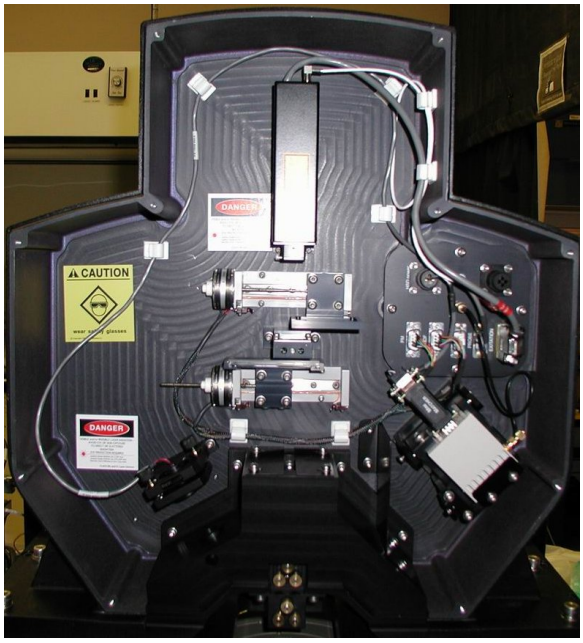


**Figure 4.2:** Photograph of the optics head assembly of the Impulse 300 laser acoustic spectrometer.

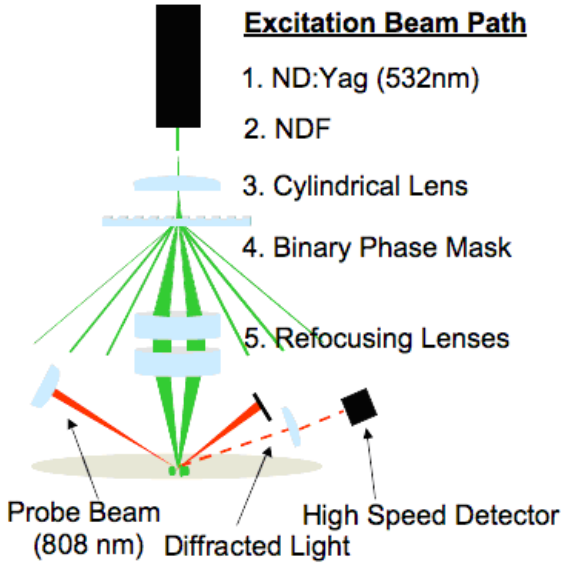


**Figure 4.3:** The excitation beam path is illustrated from laser housing to substrate [61]. The probe beam path is also included in red.

the light from the frequency doubled Nd:YAG laser is 532 nm, the test structure must absorb this wavelength strongly for sufficient optical/thermal/mechanical transduction. We recommend a thin copper film of about 100 nm for absorption of the laser pulses within the film's optical skin depth while still allowing sufficient thermal diffusion. The film must

also be thin enough to reduce its perturbation of the acoustic waves. At higher optical intensities the absorption can be sufficient to melt the film. By intentionally melting the copper surface, we are able to confirm the surface wave excitation pattern by SEM. An example, shown in Figure 4.4, reveals an acoustic wavelength of 17.5 $\mu$m.

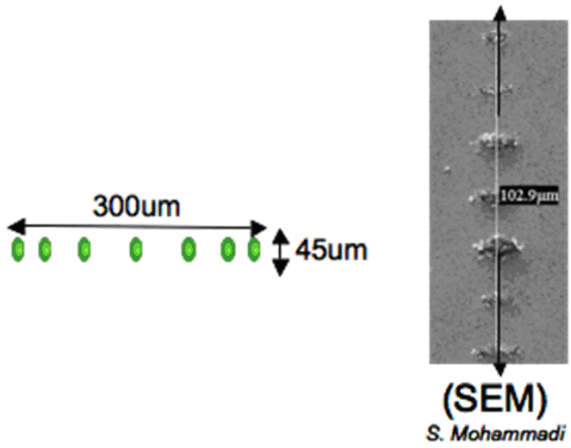


**Figure 4.4:** Diagram of diffracted orders (left), and SEM of a melted test sample.

### 4.2.2 Measurement technique

The continuous wave probe laser beam is incident on the test surface oblique to the excitation beam. The beam diagram at the wafer surface is shown in Figure 4.5. Counter-propagating acoustic waves on the sample surface appear as a standing wave pattern with periodic amplitude. Ideally this is a surface relief grating with constant spatial period and time-varying amplitude. Thus, the incident probe beam is intermittently diffracted from the surface according to the frequency at which the standing wave antinodes appear and disappear [61].

The transient grating exhibits both thermal and acoustic components. The thermal contribution is large and exponentially decays, whereas the acoustic component is oscillatory and relatively small. This is due to the intensity of the diffracted light. The diffraction efficiency for a particular diffraction order is proportional to the square of the grating amplitude, i.e. the thermal grating or standing wave's out-of-plane displacement. The acoustic wave's surface normal component is typically less than 1 Angstrom, whereas the expansion at the excitation spots is significantly greater. The total amplitude is the sum of

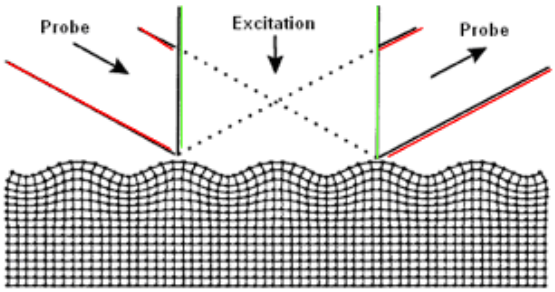


**Figure 4.5:** Coincidence of the excitation and probe beams. The stimulus occurs only within the excitation region. The surface displacement is exaggerated.

the two components, and since the intensity is proportional to the amplitude squared, we have:

$$I \propto (A_{\mathrm{T}} + A_{\mathrm{Ac}})^2 = \left({A_{\mathrm{T}}}^2 + \underline{2A_{\mathrm{T}}A_{\mathrm{Ac}}} + {A_{\mathrm{Ac}}}^2\right) \tag{4.1}$$

where $I$, $A_{\mathrm{T}}$, and $A_{\mathrm{Ac}}$ are the intensity of the diffracted light and the amplitudes of the surface displacement gratings caused by thermal and acoustical components, respectively. Though the thermal grating ($A_{\mathrm{T}}$) does not move, the impulsively induced acoustic waves ($A_{\mathrm{Ac}}$) travel and give rise to the standing wave pattern. The strictly thermal term then only contributes an exponentially decaying diffraction intensity. The pure acoustic term is very small and is often undetectable compared to the other two. The underlined cross-term, however, is sufficiently large due to the thermal contribution, and it is also modulated by the time-varying acoustic intensity. This term then is measurable and still contains the acoustic signal. Furthermore, the standing wave frequency equals the acoustic wave frequency because there is much stronger diffraction when the wave passes the stationary thermal grating compared to when it passes an opposing wave (yielding twice the frequency for the $A_{\mathrm{Ac}}$ term). Given these considerations, the experimental signal agrees with expectations, as shown below. With this time-varying diffracted intensity signal, we run an FFT to observe the frequency content and then compute the velocity. The phase velocity is calculated by the formula $v = f\lambda$, given the known excitation wavelength, $\lambda$, and the measured frequency peak in the FFT, $f$. In Figure 4.6, a filtered version of the above waveform and an FFT power spectrum are displayed, clearly illustrating the Rayleigh wave peak.

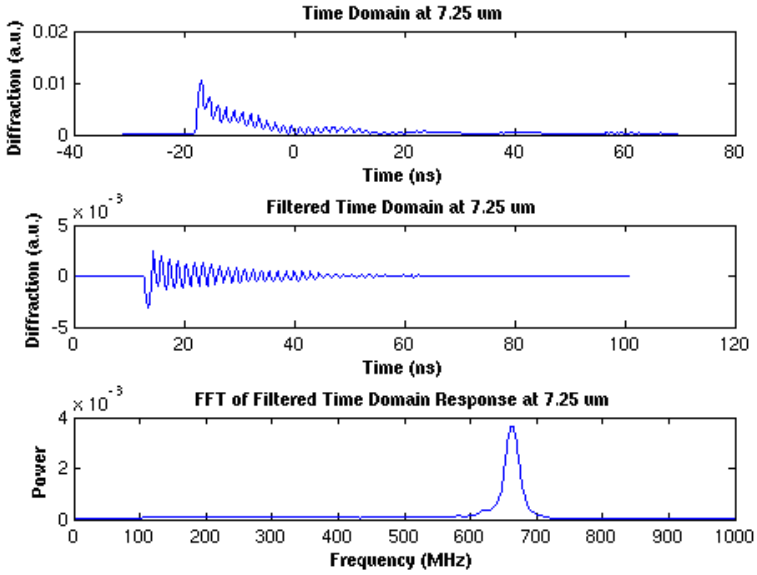


**Figure 4.6:** An example of the time-varying diffraction intensity and its spectrum.

### 4.2.3 Sample preparation

Copper efficiently absorbs the 532 nm excitation energy. We have obtained best results using a copper absorption layer, e.g. 100 nm Cu over Si. However, the diffusion of Cu into the substrate material could alter the results. A thin underlying barrier, e.g. Ta is recommended. The intent is that the total metal film thickness be about 1% of the acoustic wavelength or otherwise such that the perturbing contribution of the film is small. For a 10 $\mu$m acoustic wavelength, the 0.1 $\mu$m film is acceptable.

For structures incompatible with copper metallization, we have considered an alternative method. A polymer could be used as the absorptive layer. The material must not significantly perturb the electric field (piezoelectric substrate) or acoustic field, yet it must absorb the optical energy and convert to heat without melting. We thought that an epoxy or similar layer could possibly be doped with Rhodamine 6G dye to absorb the optical energy, but a response was not observed. This could be attributed to a bleaching or other action, rather than impulsive generation of phonons, as in a metal.

### 4.2.4 Azimuthal Velocity Dispersion

Using our acoustic characterization tool, we successfully measured slowness surfaces for Rayleigh waves on [100] silicon wafers with a 100 nm copper coating. Figure 4.7 shows and compares the results. Though the film is quite thin compared to the acoustic wavelength

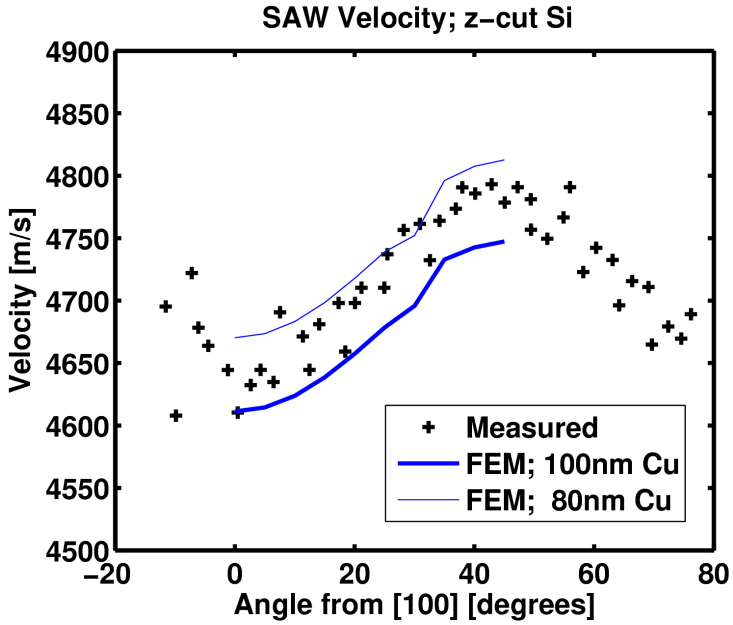


**Figure 4.7:** Measured SAW velocity versus propagation direction in the plane of [100] silicon; compared to computed values. The excitation wavelength was approximately 8 $\mu$m.

(0.1 $\mu$m vs. 8 $\mu$m), copper is known to have a lower Rayleigh wave velocity than silicon, approximately 3.5 and 4.9 km/s, respectively. The actual velocity for the coated wafer is therefore expected to be slightly less than nominal for silicon. The spread in the experimental values is within the bounds for thickness variation of 20% as the wafer was rotated beneath the optics head.

Since we have demonstrated the capability to measure the directional dependence of the velocity (angular dispersion), it is also possible to measure velocities for a range of wavelengths at each angle, thereby creating a dispersion curve for each angular increment. This is how we could extend this technique to discern the angular dependence of the band gap in a surface phononic crystal.

### 4.2.5 Wavelength Dispersion

We confirmed the calculations of leaky SAW (LSAW) dispersion due to a surface layer. The experimentally determined SAW dispersion was plotted by selecting the dominant SAW frequency corresponding to each excitation wavelength of the laser probe. The computed values were similarly produced by iteration of wavelength and solving for the corresponding eigenfrequency at each wavelength. The comparison is shown in Figure 4.8. Given the wavelength range of 5 $\mu$m $< \lambda <$ 15 $\mu$m, the 100 nm film results in a very minor perturbation. Default material parameters were used, and this may have led to the small error of less than ten percent.

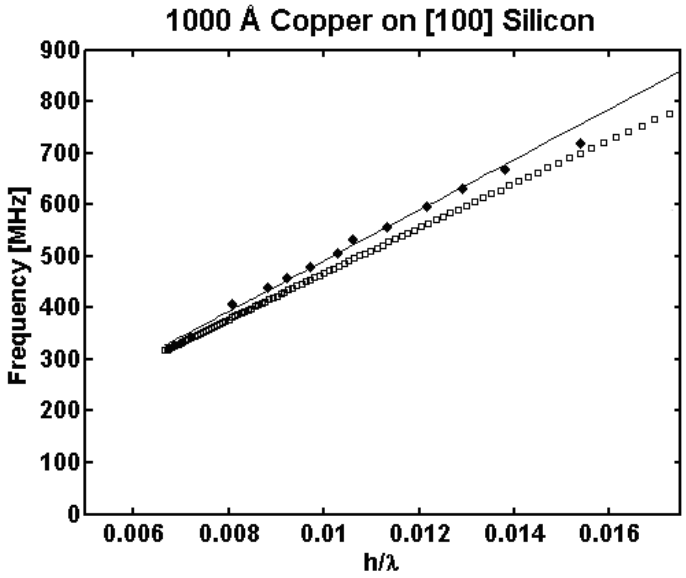


**Figure 4.8:** Comparison of measured and computed SAW dispersion for a thin copper film on a [100] single crystal silicon substrate. Open symbols were computed by FEM, and closed symbols were measured by laser probe.

### 4.2.6 PnC Measurements

#### *4.2.6.1 Tool Modifications*

After collecting data from several phononic crystal geometries, a problem was discovered. Oscillatory diffraction from the surface acoustic waves is accompanied by static diffraction due to the phononic crystal lattice. In the typical silicon/void structure of holes produced by deep reactive-ion etching (DRIE), the periodic structure contributes diffracted orders to

the probe beam in addition to the time varying components from the very small amplitude surface wave grating.

The laser probe system was originally designed to accommodate a range of diffraction angles corresponding to the range of testable acoustic wavelengths. However, the phononic crystal lattice period is typically within this range and its diffraction orders therefore are also present at the photodetector. This static diffraction due to the static grating formed by the superlattice appears to saturate the photodetector and thereby overwhelm the time-varying diffraction caused by the traveling acoustic waves.

To mitigate the problem, we considered two courses of action: (a) reduce the static diffraction from the phononic crystal using a damascene technique and chemical mechanical polishing to create phononic crystals with flat surfaces[1], or (b) allow the two simultaneous diffraction patterns and optically select an acoustic diffraction order. Due to challenges with chemical mechanical polishing of various material types, we chose the latter approach (b).

In a "stop band," at the Brillouin zone boundary, the spatial period of the lattice is approximately half that of the acoustic wave. We show in (4.2) that the first diffraction orders corresponding to the two "grating" wavelengths (static and acoustic) are separable by angle.

$$\begin{aligned} \sin(\theta_{\mathrm{i}}) + \sin(\theta_{\mathrm{r}}) &= m\frac{\lambda_{\mathrm{optical}}}{n\Lambda_{\mathrm{surface}}} \\ \theta_{\mathrm{r}} &= \sin^{-1}\left(\frac{\lambda_{\mathrm{optical}}}{\Lambda_{\mathrm{surface}}} - \sin(\theta_{\mathrm{i}})\right) \end{aligned} \tag{4.2}$$

Given the 2° difference between the static and acoustic diffraction orders ($m = n = 1$), we can select one by translating a thin slit aperture normal to the target surface. For the following experimental results corresponding to surface relief structures, we used a 500 $\mu$m by 3 mm rectangular slit to select the diffraction component of interest. We also used a 3-D

[1]It is known that the differing optical reflection coefficients of the two composite materials will still cause some diffraction

**Table 4.1:** Parameters defining competing diffraction angles.

| | $\lambda$ | $\theta_i$ | $n$ | $m$ | $\Lambda$ | $\theta_r$ |
|---|---|---|---|---|---|---|
| Lattice | 532 nm | 45° | 1 | 1 | 10 $\mu$m | 40.8368° |
| Acoustic | 532 nm | 45° | 1 | 1 | 20 $\mu$m | 42.8833° |

translation mount to properly reposition the slit for each change in acoustic wavelength, i.e. the operator must change the selected diffraction angle to accommodate a change in acoustic wavelength. In practice, this adjustment required trial and error due to variability of the mount. Another difficulty and inherent trade-off is the reduced intensity at the detector due to the elimination of most of the scattered light. The diagram of Figure 4.9 illustrates diffraction angle selection. Further development would use a servoed mount for computer control of the slit position.

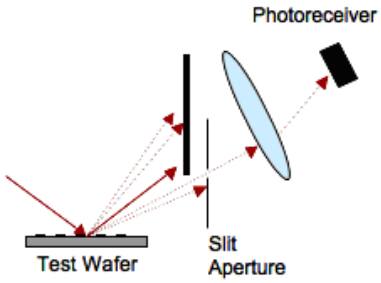


**Figure 4.9:** Geometry of probe beam reflection, diffracted orders, and slit aperture

In literature, the ISTS technique has been applied to the characterization of 1-D phononic crystals such as surface acoustic wave reflectors, i.e. arrays of surface grooves [63, 65, 64]. This existing work demonstrates the suitability of the method for characterization of polished 1-D surface PnCs, but surface relief structures remain a challenge with only a few reported solutions.

Though we reduced the received parasitic diffraction contributed by the superlattice, the surface relief structure imposes another difficulty: the inhomogeneous absorption of the optical energy. In void regions, the light penetrates into the depth of the holes and is not absorbed at the sample surface. Similarly, we expect reduced surface absorption for transparent filler materials. This geometry constraint causes relatively low wave amplitude

because less surface area is excitable. In effect, the optical excitability is inversely proportional to the phononic crystal filling fraction[2]. An alternative is to generate and measure the waves outside the phononic crystal when possible. For instance, wave reflection or transmission measurements do not require imaging the excitation pattern on the superlattice surface. Another possibility, as we have already mentioned, is the use of filler material and chemical mechanical polishing to produce a smooth phononic crystal surface and metal excitation film.

### 4.2.7 Velocity and Attenuation Spectra

We have explored use of the Kramers-Kronig (K-K) relations to allow our laser dispersion measurements to be represented in an additional way. Pairing the frequency of the FFT peak with its corresponding excitation wavelength allows us to produce $\omega$ vs. $k$ curves. The K-K relations allow conversion of such curves to another useful representation: attenuation versus frequency ($\alpha$ versus $k$). In application of the Kramers-Kronig (K-K) relations, we first confirmed their validity for SAWs. We maintain (and mathematical generalities show) that dispersive propagation of surface waves, even in heterogeneous systems, necessarily implies attenuation. An example is a layered structure composed of intrinsically lossless materials and having surface waves propagating on the top surface. Such structures yield so-called leaky surface waves and admit corresponding Green's functions [68, 90]. Thus the dispersion relations are appropriate because the causality and square integrability requirements of the Titchmarsh theorem are satisfied by the linear system. The general necessary conditions for application of the K-K relations are satisfied.

Despite the applicability of the approach, there is a challenge. Our laser probe tool allows stimulus/measurement of acoustic wavelengths in a relatively narrow range (approximately one decade). In this bandwidth the dispersion must be very strong, e.g. having a sharp resonant feature, if one is to successfully apply the K-K relations. This is due to the issue of finite bandwidth and residues in evaluation of the Hilbert transform [71, 70, 69]. One must know where the poles lie to model-fit or otherwise evaluate the principal value integral.

[2]We still use the term "filling fraction" when referring to the fraction of void space.

#### *4.2.7.1 Strongly dispersive structures*

Our measurements of surface waves on semiconductor and piezoelectric surfaces demonstrated only modest dispersion. We expect significant dispersive measurements from two- and three-dimensional phononic crystals. Moving to these periodic structures has proved challenging due to the undesired static diffraction, so-called for its production by the structure itself (not by the traveling surface waves). We require a smooth surface with a composite or heterostructure beneath. Because damascene processes were unavailable, we attempted other approaches.

In our effort to measure dispersion in acoustic superlattices, we have fabricated and tested various structures. For each structure, we examined the dispersion, looking for band gaps and attempting to apply the K-K relations.

As a first attempt, we covered Bragg reflection grating structures with polymer. We coated 500 nm thick Shipley 1805 resist over SAW reflector gratings that were 1500 Å Cr/Al metal on ST-X quartz. Unfortunately, the solvent bake-out prior to copper deposition caused the resist to shrink. Thus, for reasonably thin films, the surface still exhibits the grating pattern beneath.

In another attempt, we coated dispersions of microparticle laden photoresist, e.g. 5 to 10 $\mu$m aluminum nitride particles suspended in 2025 SU-8 resist. Baking was again required, and this brought out the out the texture of the solid particles at the surface as the solvent evaporated and the polymer contracted. Laser probe trials indicated excessive diffraction.

In final coating attempt, various photoresists were deposited on a DRIE-etched phononic crystal structure of holes (fabricated by Saeed Mohammadi). Despite careful deposition over the air holes, the films did not span the holes after spinning and evaporation of the solvent.

These difficulties highlighted a conflict between the sensitivity of the tool to periodic surface displacements and the fabrication of dispersive structures. The periodicity must be optically hidden but acoustically excitable.

#### *4.2.7.2 Measured Spectra*

To better interpret the laser probe data and evaluate dispersion in heterogeneous structures (especially in the presence of strong background diffraction), we wrote new visualization software for MATLAB. This software plots both single-location and wafer-averaged spectra from the various laser probe stimulus wavelengths. Plots were produced for various layered and unlayered structures. It is clear that the layered structures and woodpiles exhibit additional modes which are expected in such cases of "generalized" surface waves rather than strictly Rayleigh waves. When we test smooth surface PnCs, we will expect folding of the acoustic bands in these diagrams.

For a homogeneous silicon substrate, there is very little dispersion. Figure 4.10 illustrates this through a plot of frequency spectra collected at multiple excitation wavelengths. It

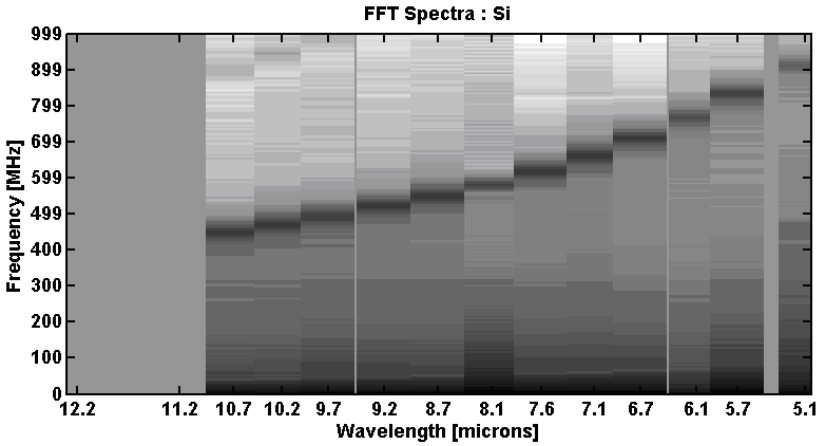


**Figure 4.10:** Measured spectrum shows the Rayleigh mode (dark band) for a silicon substrate covered with 100 nm of copper.

is clear that additional modes are not present. The copper is thin enough relative to the wavelength scale that it does not contribute an additional mode (dark band). The next figure, Figure 4.11, demonstrates the case of a thick isotropic polymer layer over a crystalline silicon substrate. Secondary dark bands are noticeable, and they indicate additional resonances due to the dimension of the top layer. The modes for such systems of multiple layers can be solved using matrix techniques (discussed in Chapter 2, or using finite element analysis software, e.g. COMSOL MultiPhysics). We used the finite element method to compute the modes for a PMMA film 35 $\mu$m thick on a silicon substrate. Only the

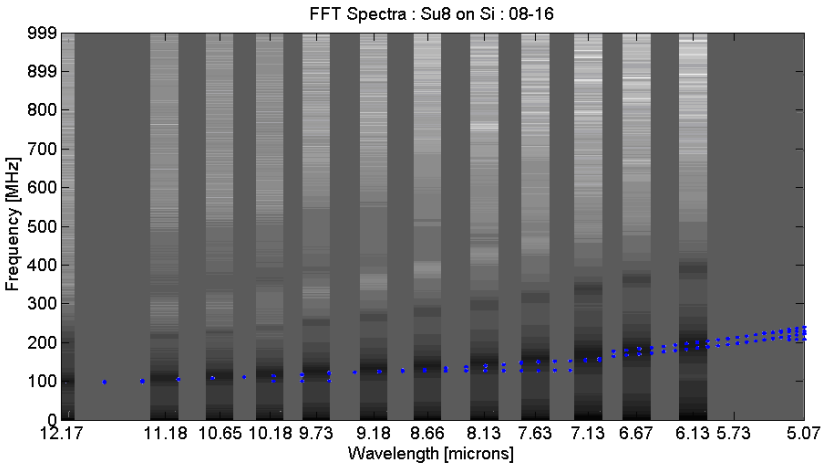


**Figure 4.11:** Measured spectrum for surface modes confined to an SU-8 surface layer on silicon. Multiple dark bands are visible. Modes computed by FEM are overlaid (dots).

surface modes were selected (according to the procedure described in Chapter 3). Though the film was actually SU-8 photoresist, the computations using the known PMMA properties still agree well with our measured data. We also note the spread in frequencies at smaller wavelengths approximately corresponds to the measured bandwidth. The upper dark band corresponds to twice the computed Rayleigh wave frequency, an effect which can be observed in transient grating experiments when the displacements are large[3].

#### *4.2.7.3 Woodpile structures*

We collaborated with Professor Joseph Perry's group (School of Chemistry, Georgia Tech) to evaluate custom three dimensional phononic crystals using the laser acoustic spectrometer. The objectives were:

- To produce a subsurface heterostructure with a smooth top layer, thus reducing static diffraction
- To produce novel 2-D and 3-D PnCs: both in dimensionality and in structure
- To bring the so-called "woodpile" structure to acoustical study

[3]The counterpropagating SAWs have twice the closing velocity, and so the standing wave formed by the purely acoustic term of (4.1) occurs at twice the frequency of the cross term.

One immediate challenge of the woodpile structure was diffraction, but we rotated the structure such that the ridges on the top surface were parallel to the probe laser's plane of incidence, as in Figure 4.12a. This greatly reduced the static (i.e. structural) diffraction and still allowed for arbitrary structure beneath. Because the woodpiles were stereolitho-

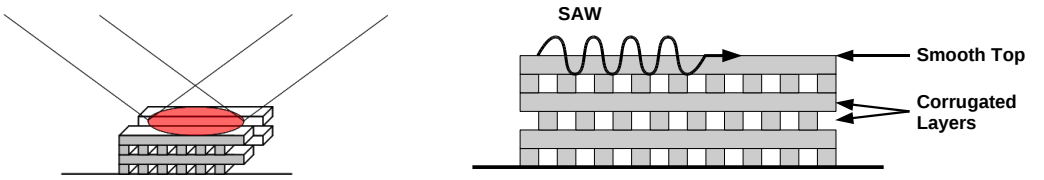


**(a)** Schematic illustration of properly rotated woodpile structure

**(b)** Sagittal section of a modified structure having an isotropic top layer suitable for sweeping propagation direction in the surface plane

**Figure 4.12:** Illustrations of "woodpile" structures

graphically formed in polymer, there was some concern about the thermal power handling of material. However, trials with several photoresists proved the opto-acoustic energy conversion and power handling characteristics of the metal-coated polymers are satisfactory at sufficiently low excitation intensities. As part of the PnC characterization work as part of the APEX program at Georgia Tech, we analyzed custom-designed polymer lattices. We first examined a nanoimprint PtC structure from R. A. Norwood's group (University of Arizona), but the sample was damaged in the course of laser testing. Vincent Chen of Professor Joe Perry's group (Georgia Tech) fabricated acoustic woodpiles using two photon absorption (TPA) lithography. The polymer structures were designed with features much larger than used in optical devices. Instead of producing the usual sub-micron lattice constant, the group pushed the fabrication tool to larger dimensions using an objective lens with less magnification. This enabled the production of structures with dimensions appropriate for our laser SAW evaluation tool (several microns).

We obtained two different types of acoustic wood pile from the Perry group. The first was the typical variety having layers stacked with alternating 90-degree orientation. The top layer thus had a corrugated appearance which significantly diffracted the probe laser beam when the sample was rotated. A second version provided a fused top layer, as in Figure 4.12b, and this worked much better. We used specular reflection apparent in a camera

image to visually distinguish these as the structures having smooth tops. The two structures are shown in Figure 4.13. Standard preparation required deposition of a thin layer

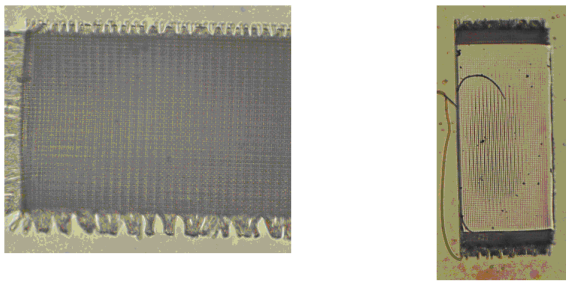

**Figure 4.13:** Optical micrographs of the woodpile structures (20X magnification; lines and spaces $\approx 2.5$ $\mu$m). A typical woodpile with striated top layer (left) is compared to a copper-covered woodpile designed/intended to have a smooth top (right). Corrugations are still visible for the structure having the altered top layer.

(50 nm) of copper on the small polymer woodpile structures by electron beam evaporation. Subsequent measurements revealed the effective surface wave velocity of the air/polymer matrix. Professor Joe Perry's group performed optical (FTIR) assessment of these structures. Figure 4.14 shows the optical reflectance for the relevant optical wavelengths (infrared spectrum). Because the structure's lines and spaces are $\approx 2$ $\mu$m, the lattice constant is $\approx 4$ $\mu$m, the in-plane band gap should be near 8 $\mu$m. However, the FTIR measurement was performed at normal incidence, and the woodpiles made by V. Chen are known to have a larger lattice constant in the thickness direction, typically about 1:3 aspect ratio (width:height). Stop bands are near 5.5 $\mu$m and 11 $\mu$m. In the laser probe data that follows, although we did not observe significant dispersion, we were able to use the weak surface wave spectral peaks to compute a SAW velocity of 970 m/s. This places the structure's effective material properties somewhere between those of polystyrene and low density polyethylene, and this confirms our setup is capable of measuring such custom fabricated structures. Because the acoustic tool does not have wavelength resolution (excitation patterns) comparable to the FTIR machine, an acoustic notch was not detected. Figure 4.15 gives an example. Each spectrum is an average of power spectra measured at multiple ($N \geq 4$) wafer locations at the same wavelength.

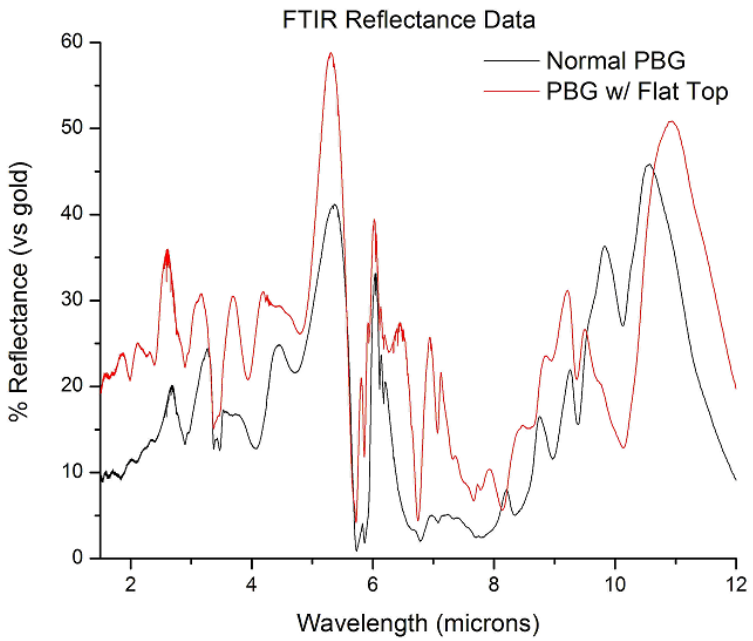


**Figure 4.14:** FTIR reflectance data for normal incidence upon both both corrugated and smooth ("flat top") polymer 3-D PnCs.

#### *4.2.7.4 Woodpile Velocity Spectra*

We have investigated the dispersion of surface waves on various substrates: silicon, silicon/polymer stacks, and polymer/air "wood pile" structures. In some cases the energy spectrum flattened considerably. This represents loss. So, in this part of the work, we aim to discern the loss mechanism(s). The measured losses could result from acoustic scattering in the structure itself or due to optical scattering.

To illustrate loss in the surface wave spectra of Figure 4.15, one may compare to Figure 4.10. The first demonstrates good coupling to (and detection of) surface waves, because the bands are prominent. If this is visualized as a topographic "bump" map, where energy is elevated normal to the plane of the image, it is clear there is a nonuniform distribution of energy along the frequency axis at each wavelength. Each energy maximum (black band) corresponds to an acoustic wave mode.

Having previously collected many conclusive measurements as in Figure 4.10, we decided to analyze lossy measurements to determine causes. A first step was to determine whether the loss is direction-dependent, so we measured velocity curves indicating the change of

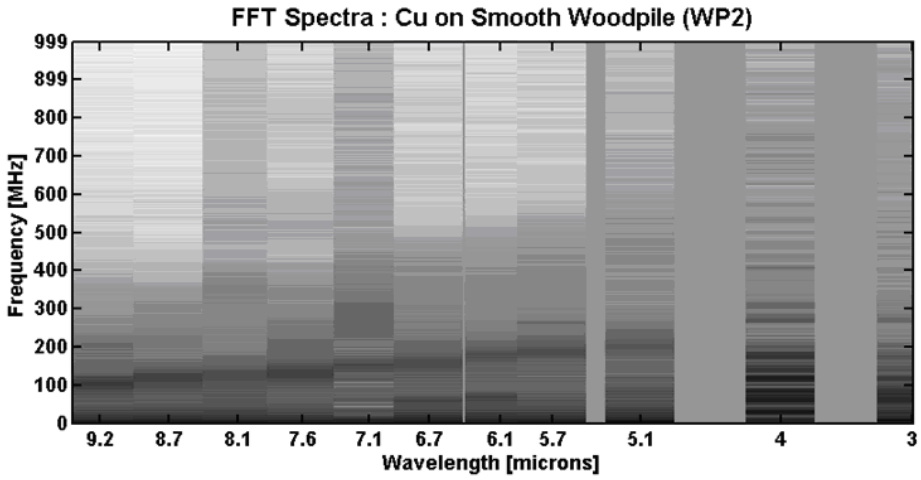


**Figure 4.15:** Lossy but predominately single-mode spectrum obtained from a polymer woodpile.

surface wave velocity versus azimuth (in-plane rotation).

#### *4.2.7.5 Woodpile Scans (Azimuth)*

To produce velocity curve scans, we rotated the sample stage in five degree increments over 180 degrees. We deemed this procedure sufficient in resolution and span to discern any expected anisotropy. While the quartile 90-degree symmetry of silicon or other square lattice materials was expected for the woodpile structure, we desired a wide enough scan to reveal bilateral symmetry as well.

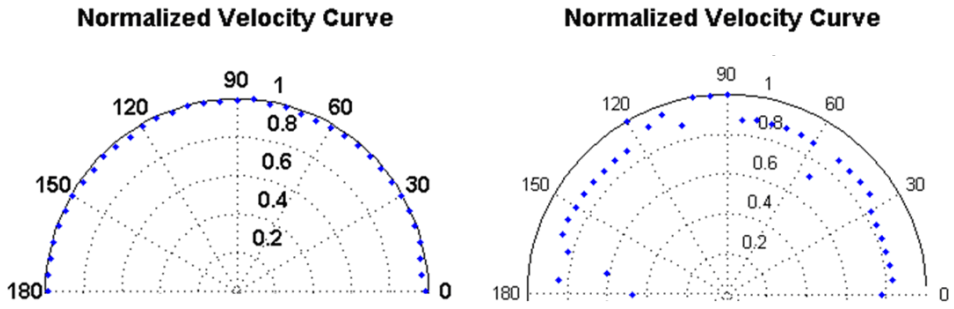


**Figure 4.16:** Angular spectra for Rayleigh velocity for two cases: blank glass slide (left) and woodpile PnC on glass slide (right). The structure and slide were coated with 100 nm copper.

Figure 4.16 illustrates the precision of velocity scans as well as the utility in revealing anisotropy. It is clear from the figure that the glass substrate is isotropic. However, the 3-D

pile structure gives a very anisotropic scan, but the result is not as expected for a structure with ninety degree symmetry. Of particular interest is the extreme decrease in velocity along the 0 and 180 degree directions. This is either due to optical or acoustical scattering when measuring in that direction.

In the case of optical scattering, we know rough surfaces diffract the probe laser light which can saturate the detector for corresponding wavelengths on the surface. In the case of acoustical scattering in materials with little damping, the most likely loss mechanisms are lateral in-plane scattering or radiation of bulk waves into the material under test. We examined the directional dependence of the diffraction intensity in Figure 4.17.

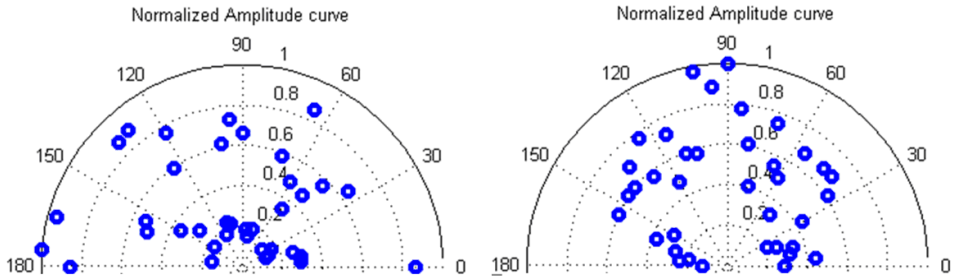


**Figure 4.17:** The amplitude plots show difference in anisotropy. The scan at left was acquired over the copper coated glass slide and the one at right was obtained over the polymer structure.

The amplitude plots show several features. One is that there is a wide range of amplitudes present for both samples. For a homogeneous material type, this is typically due to surface defects or dust particles which scatter light into the probe laser detector. So, whereas this scattering effect is roughly isotropic in the left panel of Figure 4.17, there is a clear bias for greater amplitudes at the 90 degree direction (right panel). This indicates a significant geometrical (static) diffraction in the 0 and 180 degree directions which masks the transient grating amplitude by increasing the baseline diffraction. Furthermore, while both plots exhibit a wide range of amplitudes, the woodpile plot in the right panel has a clear maximum velocity at 90 degrees, and clear minima at both 180 and 0 degrees. Thus there appears to be a surface relief grating on this structure with ridges normal to the zero and 180 degree directions (despite the intentionally designed smooth top for the woodpile).

#### *4.2.7.6 Surface Analysis*

Optical microscope images of the structures allowed us to see the surfaces are not smooth. To quantify the magnitude and period of the surface roughness, we used a Veeco atomic force microscope (AFM) in the Petit Microelectronics Research Center at Georgia Tech. The AFM analysis software computed maximum spatial power spectral density of 4.07 $\mu$m for the surface relief plot shown in the right panel of Figure 4.13. We show the region investigated and the surface profile in Figure 4.18.

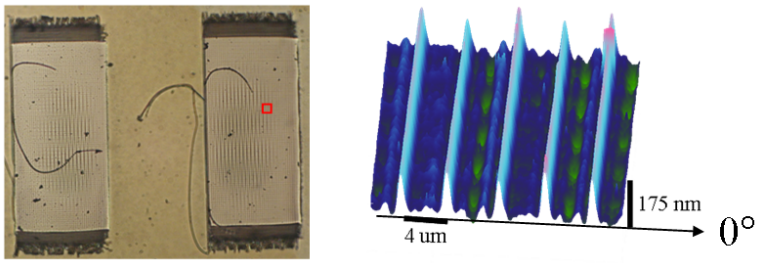


**Figure 4.18:** An optical image (left) of the investigated region, and a topographic measurement conducted via AFM (right).

Though the surface in this region has ridges predominantly in one direction, the transverse layer is visible between the ridges. Thus the ostensibly smooth structure actually has periodic ridges. One would expect this to form a diffraction grating, and indeed this was confirmed by the laser measurement results showing strong anisotropic optical diffraction (e.g. Figure 4.17). We can compute an estimate of the signal-to-interference ratio (SIR) for the woodpile structure, by using the ratio of the diffracted intensities:

$$\mathrm{SIR} \approx 10 \log_{10} \left( \frac{(1 \text{ nm})^2}{(175 \text{ nm})^2} \right) \approx -45 \text{ dB}. \tag{4.3}$$

Although we found that the detector becomes saturated by the larger parasitic diffraction component (the interference), even if it was not, at least 7 bits of *additional* analog to digital conversion headroom would be required to bring the tiny acoustic signal into quantitative range. This means that obtaining a quantitative measurement of the signal with 16-bit resolution would require an instrument with at least 23-bit/full-scale acquisition hardware to resolve the signal beneath the interference.

To move forward with optical measurements of the phononic crystal lattices, it is clear

the surface diffraction must be reduced. This will likely require much further refinement of the fabrication or a finishing technique such as chemical mechanical polishing (CMP). A drawback of these results is that only smooth composite layer structures (damascene fabrication processes) and/or micromachining methods that produce sub-surface voids will create structures conducive to measurement of the acoustic diffraction.

## *4.3 Fabrication of Surface PnCs*

In Chapter 2 we noted the weak reflection from metal dots of conventional thickness (ca. 1500 Angstroms) and materials (e.g. chromium, aluminum, and gold) on lithium niobate substrates. We desired to increase the reflection coefficient of each unit cell to allow us to observe greater dispersion with the same photo masks (having fewer than 10 lattice periods within the wave path).

One must take care with increasing the reflection coefficient magnitude for surface waves, because they can be scattered into bulk waves. While this phenomenon can be useful for the rejection of signals in filters, the energy lost by a surface wave to the bulk typically cannot be recovered (due to scattering from the unpolished bottom interface). Given this challenge, we have explored several varieties of surface perturbations for each unit cell. For the passive wireless sensors this is particularly a challenge due to severe losses.

Initial measurements of these structures did not reveal band gap characteristics, and they further indicated that shallow etched holes provide low reflection magnitude that is comparable to thin metal dots deposited on the substrate ($|\Gamma_{\text{hole}}| \approx |\Gamma_{\text{dot}}|$). This result is supported in the literature [15]. The high aspect ratio structures were investigated next. Without electroplating equipment or deep reactive ion etching (DRIE / "Bosch") process capabilities for high aspect ratio pillars and holes, respectively, we turned to patternable polymers (photoresists) to achieve greater impedance contrast, taller structures, and ease of fabrication.

We have fabricated and tested several varieties of surface features for modulation of the acoustic impedance. The first is a 2-D extension of the common reflective metal strip used in 1-D SAW reflectors. The 2-D element is a round metal dot or etched hole. Sagittal sections

of the features are shown in Figure 4.19. The pillar is a dot with much greater aspect ratio ($h/\lambda$ or $h/a$), which greatly increases the mechanical component of the reflection coefficient, as in (2.16). We show it separately because it is a special case of interest. Preliminary measurements showed the greatest perturbations were realized by milled holes

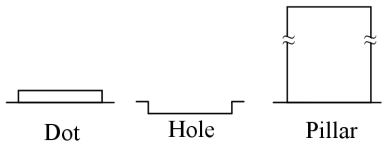


**Figure 4.19:** Schematic sagittal cross-sections of deposited metal dots, ion-etched holes, and deposited polymer pillars.

and high aspect ratio cured polymer structures.

### 4.3.1 PnCs of holes

Figure 4.20 shows optical and atomic force microscope (AFM) micrographs of the milled holes. A faithful reproduction of the pattern, steep side walls, and the desired depth (100 nm) were achieved. We milled the honeycomb lattice structure into the lithium niobate substrate using the anisotropic ion mill port of a UniFilm PVD 300 sputtering system. The two images show patterns on the same wafer which differ in $r/a$ ratio, where $r$ is the hole radius and $a$ is the lattice constant) (Mask design by Saeed Mohammadi).

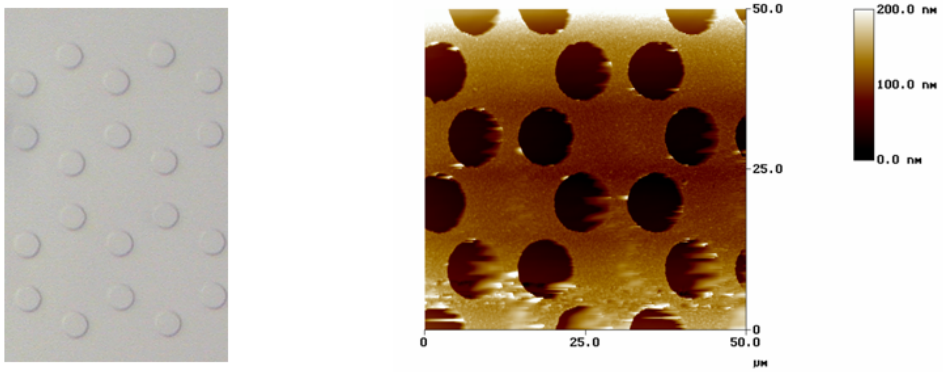


**Figure 4.20:** Optical micrograph (left, 612X) and AFM image (right) of a honeycomb surface PnC milled 100 nm into lithium niobate.

Figure 4.21 gives an overview of the ion milling process we developed to preferentially etch lithium niobate in the surface normal direction, regardless the orientation of the crystal

lattice. This is particularly advantageous because either YZ cut or 128° YX cut crystals might be desired for Rayleigh waves, and lithium niobate is also resistant to many chemical etches. A trade-off associated with this milling process is time versus hole depth; creating

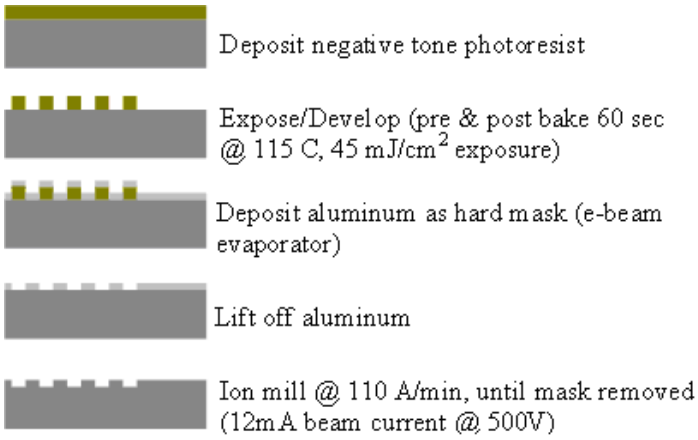


**Figure 4.21:** Fabrication process using highly anisotropic ion milling to produce holes in lithium niobate.

high aspect ratio holes would require milling several microns ($h \approx \lambda \approx 10$ $\mu$m), requiring roughly 15 hours to complete using the recipe in Figure 4.21.

### 4.3.2 Deposited Surface PnCs

An example of a surface relief phononic crystal fabricated by deposition and patterning of a surface film is shown in Figure 4.22. This is the case of relatively high aspect ratio dots, termed "pillars."

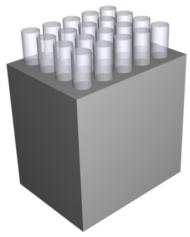

**Figure 4.22:** Square lattice 2-D PnC of polymer pillars (computer rendering).

These PnC pillars were devised to present relatively large acoustic perturbation per unit cell. We expected the mass loading effect and relatively low acoustic velocity in the polymer

would help achieve energy trapping in which the surface acoustic wave would be preferentially guided along the surface despite the presence of scattering locations. This trapping effect could allow use of pillars having sufficient aspect ratio to support micromechanical resonances of their own. An example of relatively low aspect ratio pillars ($h/d = 0.2$) is shown in Figure 4.23.

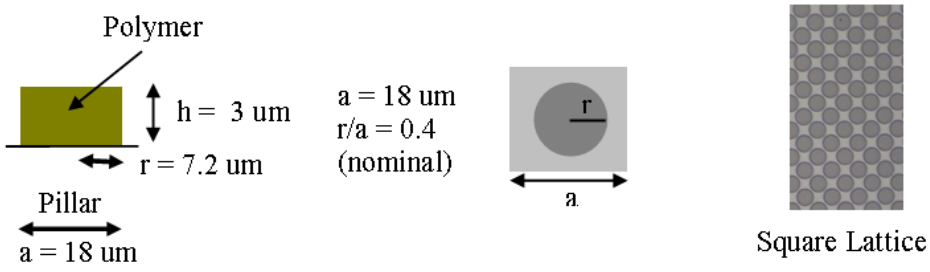


**Figure 4.23:** Parameters defining a square lattice of relatively short polymer pillars (left) and optical micrograph approximately 190X the actual size (right)

A PnC constructed of sufficiently tall ($h \approx \lambda/2$) pillars would be an array of distributed resonators. As mentioned in the introduction, recent work to create SAW PnCs shows high aspect ratio structures provide an alternative approach to the conventional thin materials [44].

## *4.4 Electrical 2-Port Measurements*

To assess the effect of different types of perturbations, we performed several experiments using deposited metals, deposited polymers, and etched holes as SAW scatterers. The scatterers were positioned within a SAW path between two fabricated interdigital transducers. A sagittal section drawing of such a fabricated structure is shown in Figure 4.24.

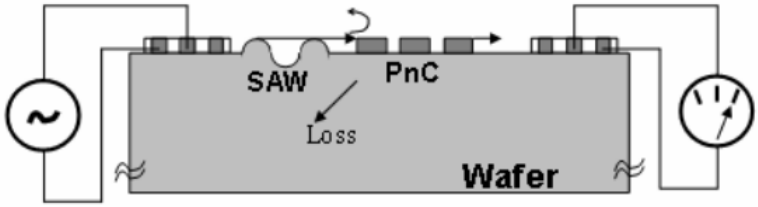


**Figure 4.24:** Sagittal section of the 2-port scattering measurement configuration.

### 4.4.1 PnCs on piezoelectric substrates

For the remote sensing application, strong piezoelectric coupling is desired to reduce losses. We use lithium niobate substrates to achieve coupling efficiency, $K^2$, of approximately 0.05. Figure 4.25a is a photograph showing input and output transducers on either side of a center surface phononic crystal on lithium niobate. The acoustic aperture is 1000 $\mu$m and the number of finger pairs in each transducer is $N = 10$. The lattice of thin metal dots did not provide enough impedance contrast for the very narrow phononic crystal (about 10 lattice periods wide; represented by "2" in Figure 4.25). In those first experiments, both the transducer structures and the center lattice region were produced by deposition and patterning of a thin metal layer. Both square and honeycomb lattice phononic crystals were fabricated on 128 degree rotated $LiNbO_3$ with y-axis propagation. We used the same photomasks originally designed (by Saeed Mohammadi) for silicon/hole band gaps. In this work, however, we evaporated 300 Å Cr and 1200 Å Al onto the $LiNbO_3$ to create electrodes and PnCs composed of metal dots Figure 4.25.

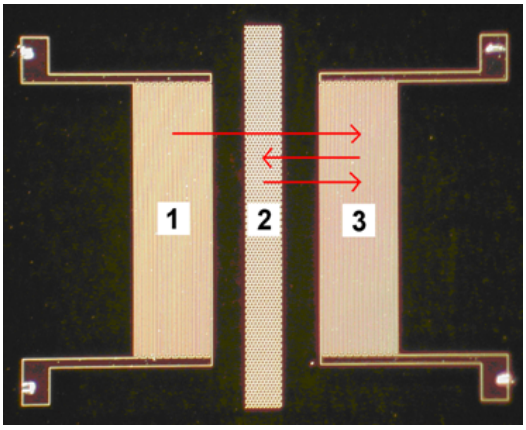


**(a)** Photograph of a test structure for excitation at one $\lambda$, showing multiple reflection. The 2-D PnC ("2") consists of metal dots.

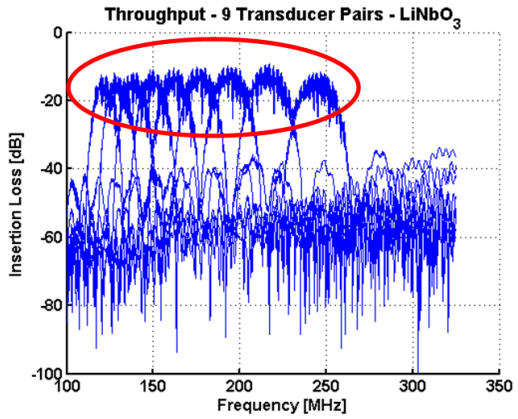


**(b)** Frequency response ($S_{21}(f)$) overlay for the case of no PnC at position "2." The red oval denotes passband ripple due to triple-transit reflections.

**Figure 4.25:** Two port measurement configuration and baseline data.

In Figure 4.26 we show the transmission responses for SAWs through PnCs of 1500 Å thick Au dots (300 Å Cr beneath) versus wave paths without dots.

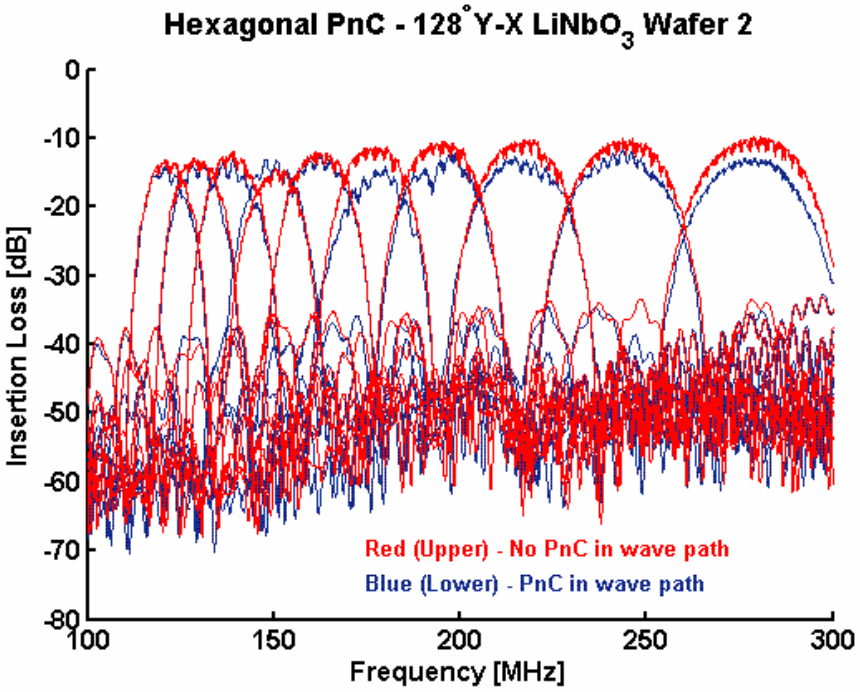


**Figure 4.26:** Slight frequency-dependent attenuation of Rayleigh waves due to gold dot hexagonal lattice

#### *4.4.1.1 Polymer PnC*

In another series of measurements, we tested one of the simplest configurations of all: patterned polymer PnC lattices. Rather than etching holes or depositing metal, we constructed polymer surface PnCs. This approach utilizes the mass loading effect, does not greatly affect the electrical boundary condition, and does not introduce such sharp acoustic impedance discontinuities as with etched holes. In Figure 4.23 we give the dimensions of the lattice and an optical image of a fabricated polymer pillar lattice. Note the actual PnC filling fraction may be greater than intended; the optical micrograph shows very little separation between polymer pillars. This could be attributed to either overexposure or to "blooming" of the pattern due to the thick photoresist film. Fabricating this lattice structure did not require any special equipment or procedures; we performed standard photolithography with a negative tone resist. Because polymers are typically acoustically slow materials, the effective height of the structures is much greater than those fabricated using aluminum or gold.

Figure 4.27 shows a measurement of the square lattice pillar PnC with a lattice constant, $a$, of 18 $\mu$m. The pillar PnC appears to have strongly attenuated a narrow band of frequencies near 175 MHz. The two responses, open wave path and PnC wave path, are quite similar throughout the measured bandwidth except in the passband region, the main peak of the graph corresponding to the majority of acoustic transmission from input IDT to output IDT.

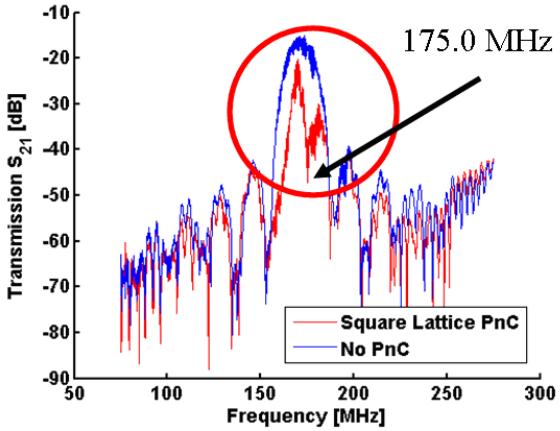


**Figure 4.27:** Passband notches formed by presence of a 2-D square lattice PnC. The other excitation bands did not exhibit deviations of this scale, and so they are omitted for clarity.

Analysis of experimental data collected from transmission measurements through this structure indicated strong dispersion and possible band gap behavior. A significant perturbation was obtained though the lattice width was only ten unit cells ($10a$).

The lower trace corresponds to the transmission through the crystal, whereas the upper trace corresponds to the situation without a fabricated crystal between input and output transducers. We will discuss the common and differential losses for the two measurements.

The $S_{21}$ plot represents approximately continuous wave measurements, as recorded by a vector network analyzer. The peak transmission suffers 16 dB loss, even for the measurement without a PnC interposed in the wave path, and this overall (common) insertion loss is partly due to mismatch of the transducer radiation resistance with the 50 Ohm measurement system. The equation for IDT radiation conductance, $G_a$, is given by Campbell [15]:

$$G_a(f_0) = 8K^2 f_0 C_s N^2, \tag{4.4}$$

where $K^2$ is the piezoelectric coupling coefficient, $f_0$ is the IDT center frequency, $C_s$ is the

static capacitance of one finger pair (one period; aperture dependent), and $N$ is the number of IDT finger pairs (periods). Clearly the piezoelectric coupling and number of finger pairs dominate the radiation conductance, $G_a$. Considering these input losses and the reciprocal phenomena at the output transducer (2 port transmission measurement), approximately -14 dB transmission, $-10\log_{10}(|S_{21}|^2)$, is expected. This calculated transmission is common to both traces in the previous figure, and is slightly greater than measured (-16 dB).

We also desired to know the contribution of bulk attenuation (intrinsic scattering to thermal phonons, sub-wavelength defects, etc.). The intrinsic scattering gives rise to the general SAW attenuation coefficient for the substrate. YZ lithium niobate has frequency-dependent acoustic attenuation [15]:

$$\alpha = 0.88F^{1.9} + 0.19F, \tag{4.5}$$

where $F$ is the frequency in GHz and the attenuation is in dB/$\mu$s. Near 200 MHz this corresponds to approximately 0.079 dB/$\mu$s. For the structures under test, the delay is approximately 600 $\mu$m / (3487 $\mu$m/$\mu$s) = 0.172 $\mu$s, which corresponds to significantly less than 1 dB. This accounts for just a very small part of the already small discrepancy between the estimated transmission and the measured transmission. We expect the remainder can be attributed to misalignment and bulk wave generation. The transducers in this work have relatively few finger pairs, yielding approximately 10% bandwidth. It is known that as the fractional bandwidth for an IDT nears 20%, the fraction of energy radiated into bulk waves becomes significant, and the fractional SAW power decreases. Rather than considering these transducer non-idealities in detail, we move forward to discuss the main feature of Figure 4.27: the differential transmission (PnC vs. No PnC). A subtracted version of the two datasets reveals the response due to the PnC alone (Figure 4.28). Clearly the two measurements were not identical because the subtracted transmission shows values above 0 dB – a nonphysical result for a passive structure – indicating that the PnC actually increased transmission beyond what was possible without it. Therefore we expect the positive excursions are due to experimental differences between the two measurement configurations; although both measurements used the same design transducer design, they were performed

**Table 4.2:** Comparison of assumed $\lambda/4$ film thickness resonance (extensional mode) for different materials. The bold values were calculated using the other values.

| Material | Velocity (m/s) | Thickness ($\mu$m) | $f_0$ (MHz) |
|---|---|---|---|
| Polyethylene (LDPE) | 513 | 3 | **42.8** |
| Polystyrene | 1075 | 3 | **89.6** |
| Polypropylene | 2740 | 3 | **228.3** |
| AZ N6020 photoresist | (unknown) | 3 | (unknown) |

at two different test structures on the same wafer.

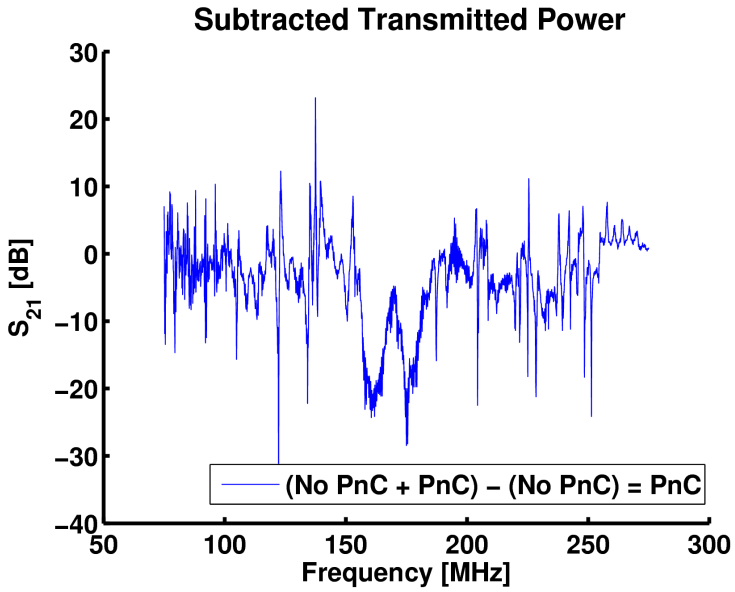


**Figure 4.28:** Subtracted data showing transmitted power due to PnC only.

We first thought the notches in the pass band of the PnC measurement (circled in Figure 4.27 and clearly shown in Figure 4.28) could be caused by Fabry-Perot reflections associated with the PnC. However, the associated periodic modulation in the frequency domain (with $\Delta f \approx v_{\mathrm{SAW}}/(10(2a)) \approx 10$ MHz) is not evident.

Next we estimated the first quarter wavelength film resonance for relatively fast and slow polymers 3 $\mu$m thick. In Table 4.2, the bold numbers represent calculated values. All others were known or measured. Unfortunately, the actual mechanical parameters of the AZ N6020 photosensitive resin remain unknown. For a polymer film of a given thickness, the fundamental longitudinally polarized thickness resonance could be found in a very wide

frequency range including our region of interest: 150 MHz to 200 MHz. Even the slower materials could give overtones in this range, so the contribution of thickness resonance absorption is plausible.

We also examined prior FEM computations which revealed film modes in this frequency range for polyethylene and polystyrene films. The calculations reveal that thin polymer films provide a way to achieve large reflection coefficients and simultaneously maintain the energy at the surface. One can operate arbitrarily near a thickness resonance by adjusting the thickness or polymer type. Unfortunately, slower polymers tend to be more viscous, so there is an expected trade-off between slowness of the polymer and loss.

To further examine the effects of the scatterers on the $S_{21}$ response, we consider the location of the scattering structure in the wave path. The acoustic system in this regime is coherent, so interference of direct and scattered waves results in enhancement or suppression of the transmission; thus we can clarify the contributions from multiple spatially distributed scatterers. Next we show computation of the time response and truncation of the time data according to the spatial region of interest.

### 4.4.2 Use of time gating

The application of time gating allows us to decompose the frequency response into components from early, middle, and late arrivals. Elimination of the earliest echoes corresponds to the common removal of the electromagnetic "feed through" in 2-port measurements of acoustic devices. Likewise, we can remove electromagnetic "reflection" in 1-port measurements of the reflective delay line sensors (discussed in Chapter 7). A typical threshold used in this work was a few hundred nanoseconds. Ungated responses are shown in Figure 4.27 comparing transmission for a square lattice PnC versus the same configuration without any PnC interposed between the transducers. Gated responses are shown in Figure 4.29. The data at late times (multi-transit; beyond 0.5 $\mu$s) and at very early times (electromagnetic feed-through; before 75 ns) are removed. This produces a response more clearly matching the expected *sinc* function behavior for SAW delay line with unapodized transducers. The times were selected using the known structure spacing and the Rayleigh velocity for YZ

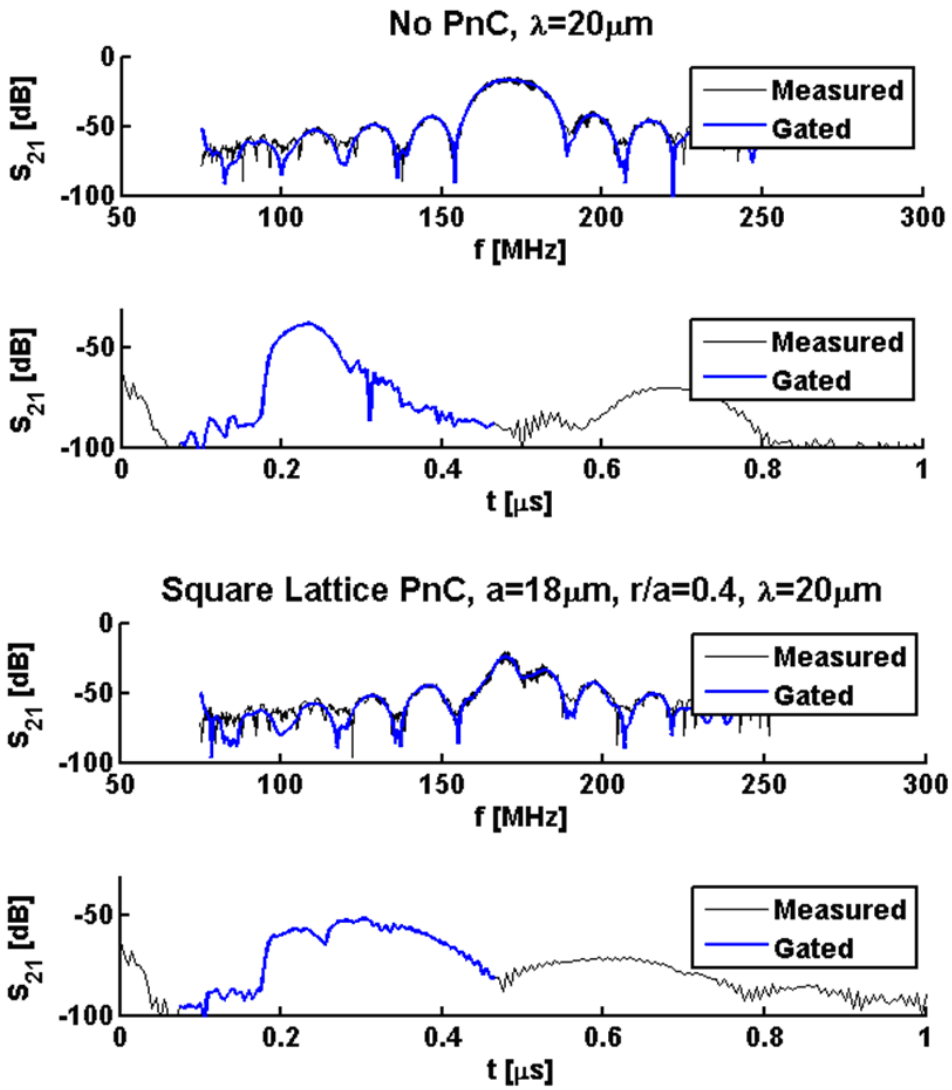


**Figure 4.29:** Comparison of measured and gated responses for paths without and with the square lattice polymer PnC.

lithium niobate ($v_R$ = 3487 m/s). The broad second peak near 0.7 $\mu$s corresponds to the triple-transit of the wave path, commonly called triple-transit interference (TTI).

Given the time window, the bold (blue) traces correspond to a single transit of energy from the input transducer to the output transducer. Interference of multiple waves is therefore due to single-transit scattering as the wave passes through the PnC. Multiple scattering at the scale of the wavelength is of interest and is permitted by the appropriately chosen time window. In Figure 4.30 we compare an open path with a PnC wave path, and we allow the trailing energy due to multiple reflections, diffraction, etc.

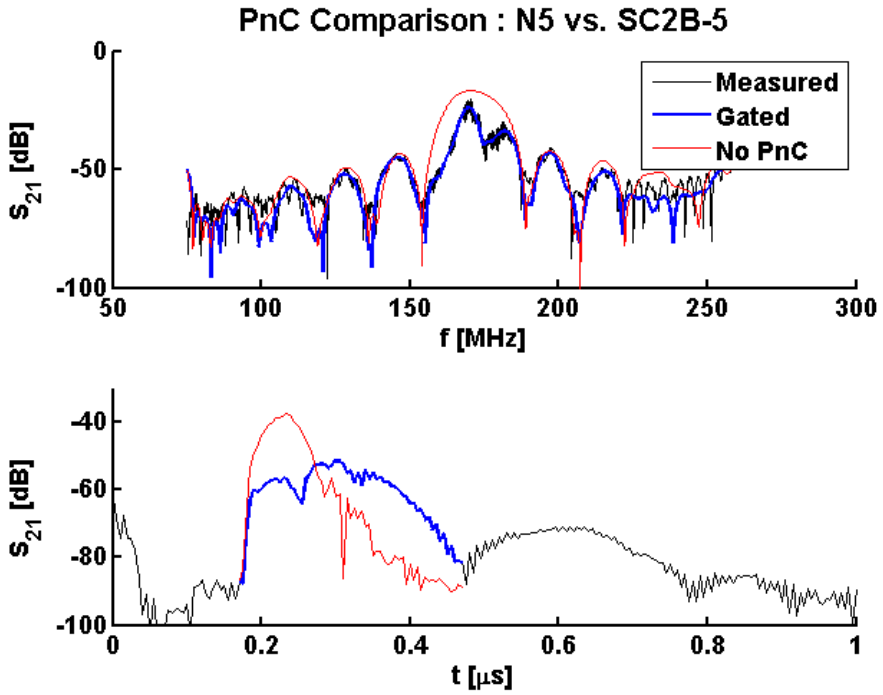


**Figure 4.30:** Overlay of gated transmission responses for single-transit through the polymer pillar PnC. The red trace indicates measurement without any PnC.

In view of this analysis, both the overall attenuation of the PnC signal ("measured," "gated") and the local frequency suppressions are attributed to the scattering properties of the square lattice PnC. Both bulk wave scattering and in-plane diffraction are likely. The transmission through the surface PnC may be written according to the dominant loss mechanisms:

$$|T_{\mathrm{PnC}}|^2 = 1 - |\Gamma_{\mathrm{SAW}}|^2 - |\alpha_{\mathrm{SAW}}|^2 - |D_{\mathrm{SAW}}|^2 - |D_{\mathrm{BAW}}|^2, \tag{4.6}$$

where $\Gamma$ represents the reflected SAW, $\alpha$ represents the dissipation or energy storage (which can be included in a complex $\Gamma$), and $D$ represents the diffracted surface and bulk acoustic waves. In our measurement setup, $\Gamma_{\mathrm{SAW}} = S_{11}$ when the transducer response is removed. A diagram of the various reflection, transmission, and loss components is provided in Figure 4.31.

We examined the time-gated $S_{11}$ scattering parameter to help distinguish the components of the transmission loss (Figure 4.32). When $\Gamma_{\mathrm{SAW}} = S_{11}$ is known for the polymer structures, we recognize $D_{\mathrm{BAW}}$ is small, and so $\alpha$ and $D_{\mathrm{SAW}}$ dominate the energy balance.

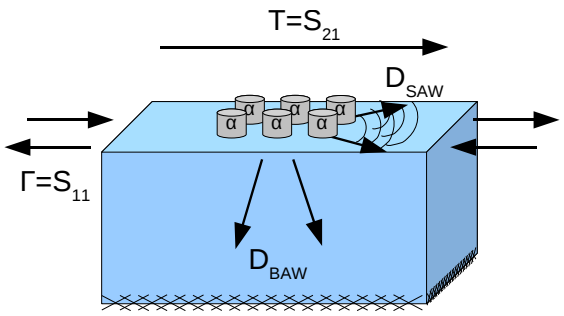


**Figure 4.31:** Diagram indicating the incident, transmitted, diffracted, and absorbed waves.

Because part (a) of Figure 4.32 has no PnC, there is very little energy returned at times corresponding to scatterers in the open wave path. Part (b) shows energy returned from the output IDT, which acts as a reflector. The final plot in part (c) of Figure 4.32 is gated exactly as in (a), but reflections are present due to the polymer PnC within the wave path.

We calculated the gating interval using known properties of the substrate and photomask. The transducers are spaced approximately 850 $\mu$m apart (center-to-center), corresponding to approximately 0.47 $\mu$s round-trip transit when $v_{\mathrm{SAW}} = 3488$ m/s on YZ lithium niobate. When the square lattice polymer pillar PnC is present, as in (c) of Figure 4.32, small echoes are observed beginning around 0.15 $\mu$s. This delay corresponds to a reflector approximately 260 $\mu$m away. According to the corresponding optical micrograph, the IDT center to PnC edge distance is approximately 270 $\mu$m.

The reflections from the PnC are about 15 dB greater than the "floor" established in (a) of Figure 4.32. From this we have determined that a greater $\Gamma_{\mathrm{SAW}}$ is achieved using this particular polymer PnC on lithium niobate, when compared to the other structures we tested in this frequency range. If we assume the reflection is distributed equally among the 10 rows of scatterers, then $|\Gamma_{i,\mathrm{SAW}}|^2 \approx 1.5$ dB per row of polymer dot scatterers. $D_{\mathrm{SAW}}$ and $D_{\mathrm{BAW}}$ remain to be evaluated. For instance, $D_{\mathrm{SAW}}$ could be discerned by temporal spreading at the output transducer, whereas the diffracted BAW energy is not recovered at all. Laser methods are recommended for their ability to spatially map the acoustic energy and frequency distribution; however, a known disadvantage of the optical measurements is the typical requirement of an optically smooth and reflective surface.

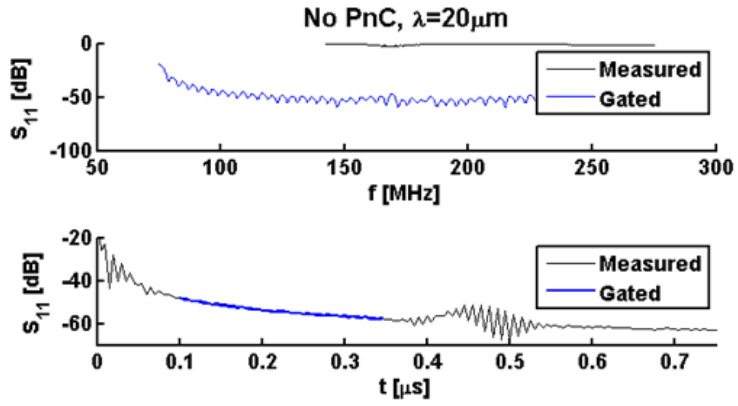


(a)

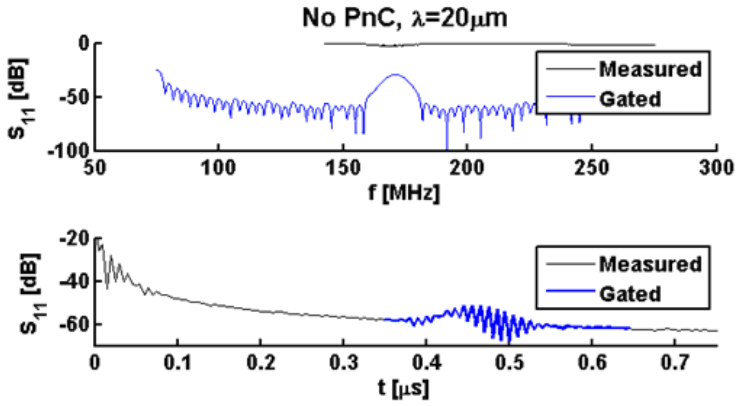


(b)

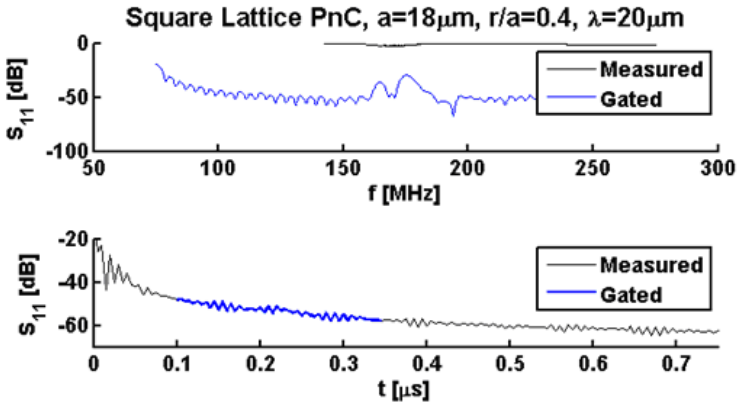


(c)

**Figure 4.32:** Comparison of gated $S_{11}$ responses to show the frequency dependent *reflection* attributable to the polymer PnC.
(a) gives the reflection before double-transit reflection due to the output transducer,
(b) gives the reflection corresponding to the output transducer, and
(c) gives the reflection due to the PnC (prior to double-transit; compare to (a)).

It was supposed that the scattering response could be attributed to some fabrication defect not visible upon inspection, but localized to the test structure "SC2B-5." To reduce this concern, we also extracted the reflection responses due to excitation of the structure from the left transducer and the right transducer. When overlaid in Figure 4.33, the agreement is excellent. We conclude the left and right transducer responses were substantially identical, including the PnC reflections.

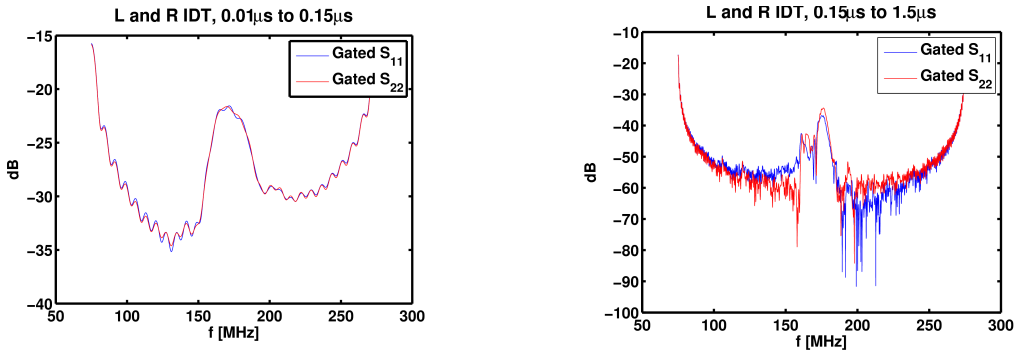


**(a)** Left and right transducer self-reflection

**(b)** Left and right reflection from interposed PnC

**Figure 4.33:** Comparison of PnC excitation from both sides. The first figure selects and compares the self-reflection of the transducers, while the second figure compares the PnC reflection measured by the transducers. Time gating windows were [0.01, 0.15] $\mu$s and [0.15, 1.5] $\mu$s, respectively.

### 4.4.3 Discussion

We consider for a moment the contrast between the present study of surface phononic crystals and slab PnCs studied by Mohammadi et al. Slab or acoustic plate mode (APM) PnCs more naturally follow from the similar structures reported in the photonics literature, though in the acoustic case, the partial waves comprising each mode may include longitudinal polarization. Still, a marked difference for the SAW PnCs is lack confinement in the $z$ direction; the interfacial waves guided at the interface are periodically interrupted by geometries that do not support the incident mode.

Although we knew scatterers formed of slow materials could reduce energy loss to the substrate, $|D_{\mathrm{BAW}}|^2$, their relatively low cutoff frequencies for thickness modes cause them to appear reactive, having an appreciable imaginary part of $\Gamma$, at lesser thicknesses than

with faster materials. A thin polymer usually gives much greater effective $h/\lambda$ than a metal of the same thickness. Additionally, spin cast polymer films are also usually thicker than vacuum evaporated metals and dielectrics, because experience shows that surface effects tend to disintegrate thinner films during the subsequent curing process. Vacuum polymer deposition processes, such as that used for parylene, typically do not suffer this limitation and can produce nanometer thin films with precision.

We note several positive outcomes from the time gating study:

- The total energy of the response was largely conserved between $\Gamma$ and $T$, indicating $|D_{\mathrm{BAW}}|^2$ and $\alpha$ are small, as desired – despite using polymer as a mechanical material at MHz frequencies.

- $|D_{\mathrm{SAW}}|^2$, due to diffraction in the plane, appears in the increased temporal spread of $T$ (Figure 4.30).

- We did not observe the usual BAW cutoff frequency in the frequency domain; $|D_{\mathrm{BAW}}|^2$ was not evident.

- The polymer dot scatterers gave an average reflected power at least 10 dB greater than any other of the other scatterers attempted using the same mask design. We estimated reflection of 1.5 dB per transverse row of the lattice structure for dots with $h/\lambda = 0.1$.

Considering low BAW generation and ease of deposition (milling holes to an equal depth would require many hours of machine time), the polymer structures remain the preferred approach to realization of high impedance contrast surface PnCs.

## *4.5 Summary*

In this chapter we reviewed our use of optical and electrical measurements to study the dispersion of surface acoustic waves in anisotropic and inhomogeneous substrates. We used the laser acoustic spectrometer tool to confirm several of our FEM computations, finding that the model results agreed well with the measured dispersion even in the weakly dispersive case of thin copper layers on silicon. We also fabricated surface PnCs in the

lab of the Microelectronic Acoustics Group at Georgia Tech, producing both deposited and etched superlattice structures. Finally, we detailed the electrical two-port characterization of surface PnCs using a probe station and network analyzer. We applied time gating to extract the response due to the surface scatterers. After reviewing the results, we determined that the polymer pillar structures remain the preferred candidates (of tested structures) for surface PnCs providing strong dispersion, reduced BAW generation, and insignificant material loss.

A significant challenge encountered in the laser evaluation approach was the optical surface diffraction accompanying the use of patterned structures. The additional processing required to produce smooth damascene patterned surfaces is undesirable due to increased cost of production. Surface structures that can be left as-deposited are preferred to those that require time consuming polishing or etching steps. Therefore, we proceeded to compute strong scattering effects for relatively high aspect ratio surface structures.

We desired to know whether some choices of lattice parameters yield a wide SAW band gap with low loss. Another question of interest was whether the mass loading dispersion would change due to the inhomogeneous spatial distribution of energy in a PnC operating near a frequency band gap. Finally, we noted the success of easily fabricated polymer structures to effect strong SAW scattering. We expect this is due physical thickness of the structures and furthermore due to their greater *effective* thickness due to a low acoustic velocity. In Chapter 5 we report the computation-based design of high aspect ratio deposited surface PnC structures.

# CHAPTER V

# COMPUTATIONAL EVALUATION OF SURFACE PNC STRUCTURES

## *5.1 Introduction*

In Chapter 3 and Chapter 4 we demonstrated and experimentally validated finite element computations of surface acoustic wave dispersion in both layered and patterned piezoelectric media. We particularly desired to know more about the effects of extensive surface scatterers, a departure from operation in the usual regime of weak scattering and first or second approximations.

In this chapter, we report our investigation to:

- Highlight an important loss mechanism in surface PnCs
- Assess design parameters and strategy for large SAW band gaps
- Make use of partial band gaps for surface guided waves
- Assess the efficacy of energy dispersion of the various eigenmodes for sensing applications

To our knowledge, this investigation provides the first computational evaluation of the dispersive mass loading phenomenon within dispersive surface phononic crystals (PnCs). Others have studied the analogous dielectric loading in *photonic* structures, including devices such as coupled cavity waveguides (CCWs) that achieve enhanced nonlinear phase sensitivity [91].

## *5.2 Overview*

At first look, the criteria and objectives of PnCs are very different from existing SAW modulation technologies. Designers of PnC devices strive to create wide frequency stop bands using periodic sequences of highly contrasting materials (for large reflection coefficients).

SAW filter designers historically used Bragg reflection in the narrowband limit, creating extremely narrowband reflector arrays (low impedance contrast per reflector) or high order filters with large delays (small individual reflection coefficients). This approach has allowed production of electronic devices with transfer functions meeting challenging filter specifications.

As we consider design of dispersive surface acoustic wave sensors, we look to the progress in phononic crystals to see what is possible. A focus within that field is to achieve large frequency band gaps using periodic materials with large impedance contrast. This is known to allow creation of structures for tuned energy confinement, e.g. waveguides, resonators, and filters. These may be created by adjustment of the local structural parameters to create "defects" that admit modes within the frequency gap. The requisite feature is a sufficiently wide band gap.

### 5.2.1 Challenge of Surface PnCs

The review of SAW dispersion in (Chapter 2) leaves a particular point of guidance for the construction of phononic crystals having large band gaps: create sharp discontinuities in the material properties in order to increase the influence of higher space harmonics. However, this poses a challenge for interfacial waves such as SAWs, because the periodic discontinuities collectively form a diffractive element that diverts energy away from the interface. In photonics parlance, surface bound states may be momentum matched to bulk "extended" states. This is analogous to the role of phonons assisting emission and absorption in indirect band gap semiconductors. Completing the analogy, the bound state is the SAW, the phonon is the surface grating, and the radiation state is the BAW.

For phase matching of the SAW and BAW in a grating, we show the synchronism condition in Figure 5.1 and provide the equations:

$$\begin{aligned} k_{\mathrm{R}} - k_{\mathrm{G}} &= \pm k_{\mathrm{B}} \sin\theta \\ f &= \frac{v_{\mathrm{R}}}{\lambda} \frac{1}{1 \pm (v_{\mathrm{R}}/v_{\mathrm{B}}) \sin\theta} \ , \end{aligned} \tag{5.1}$$

where $k_{\mathrm{R}}$ and $k_{\mathrm{G}}$ are the Rayleigh wave and grating wave numbers, respectively, $v_{\mathrm{B}}$ is the BAW velocity (assumed isotropic in this example), and $\theta$ is the angle of the scattered BAW.

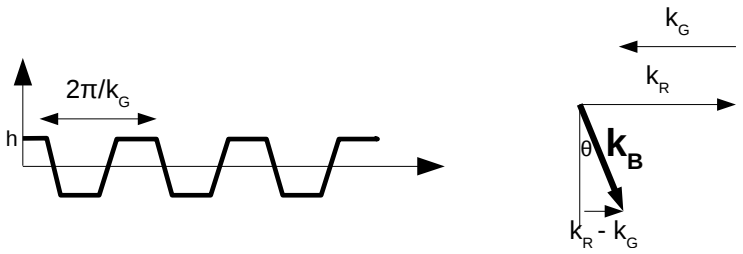


**Figure 5.1:** Diagram of $k$-matching in Brekhovskikh damping. The grating facilitates interconversion of SAWs and BAWs.

The same effect has been recently demonstrated in microwave electromagnetics, by creation of a steerable leaky-wave antenna [88]. In that case the damping is desired; it corresponds to the radiation of the antenna into the adjoining space. In acoustics, this principle was described by Brekhovskikh prior to 1960 [14], and has long been applied in the design of corrugated surfaces for structural transducers. SAWs are coupled to BAWs at angles determined by the difference in SAW and grating wavenumber. This phenomenon is useful, i.e. dominant, for a structural transducer primarily under two conditions: (a) absence of the Bragg harmonic (second space harmonic) due to purely sinusoidal surface variations or those with only odd space harmonics, and (b) weak scattering.

When the Rayleigh wave period is less than or equal to the structural period of sinusoidal variation ($\lambda \leq a$, respectively), the Rayleigh waves scatter to BAWs. The general problem in anisotropic media having general surface irregularities requires numerical methods. However, Brekhovskikh applied the Born approximation to arrive at a rule of thumb for the damping, $\alpha$:

$$\alpha_{\mathrm{BAW}} = C(\nu)(h/\lambda_{\mathrm{SAW}})^2 \ , \tag{5.2}$$

where $h$ is the amplitude of the surface variation and $C(\nu)$ is a parameter dependent upon Poisson's ratio, $\nu$, and upon the space harmonics (i.e. the shape of scatterers).

We note that the usual rule excluding the production of even space harmonics (e.g. Bragg harmonic, $n = 2$) by interdigital transducers of alternating polarity is not generally appropriate for reflectors formed from deposited metal, etc. Indeed, one must consider that it is the total phase shift experienced by the wave that is important. Designers of solidly

**Table 5.1:** Comparison of damping mechanisms in a surface grating, where $\lambda$ is the Rayleigh wavelength, $a$ is the structural period, and $h$ is the height of the surface corrugation.

| Mechanism | Dependence | Scale |
|---|---|---|
| Bragg | $(h/\lambda)$ | $a = \lambda/2$ |
| Brekhovskikh | $(h/\lambda)^2$ | $a = \lambda$ |

mounted BAW resonators know this well; the thickness of each layer is chosen to be $\lambda/4$ *with respect to the phase velocity of the mode in that layer*. So, as in the case of electrical lengths in transmission lines, arbitrary impedances may be used (and layers sized accordingly) if one does not care about the trade-off between number of layers and reflection magnitude.

We summarize some characteristics of the relevant SAW damping mechanisms in Table 5.1. Although the effects are contrasted by their order in $(h/\lambda)$, the height, $h$, is not necessarily the best measure. This is because many of the historical treatments in the literature have assumed a surface relief pattern formed by etching of the substrate, i.e. only a single material is present and so the absolute height is relevant. For general surface scatterers such as metal strips or other deposited material, one must also know the material parameters. The mass loading at a given thickness is greater for denser materials. Furthermore, beyond the linear mass loading regime, a stub transmission line approach or full field computation may be necessary to account for the acoustic modes of the scatterer.

Clearly the desired effect (Bragg reflection) is dominant for a given thickness (or impedance contrast). Although one might expect a very large impedance contrast for a corrugated surface due to the extreme difference between solids and air or vacuum, traditional SAW designs have kept $(h/\lambda)$ sufficiently small to limit the *effective* impedance contrast at the wavelength of operation, $\lambda$. We have discussed that longer SAW wavelengths also have deeper evanescent tails and probe more of the depth.

So generally, we expect the lossy radiation of BAWs when a typical PnC (having high impedance contrast) is introduced at the surface of a solid. The loss of energy to BAWs occurs for modes above the BAW "sound line," as evident in the computed data of Figure 3.9 and as illustrated in Figure 5.2. This occurrence has been reported in the literature,

e.g. for a square lattice of air holes in lithium niobate [9] and in reports by A.A. Maznev [63, 64].

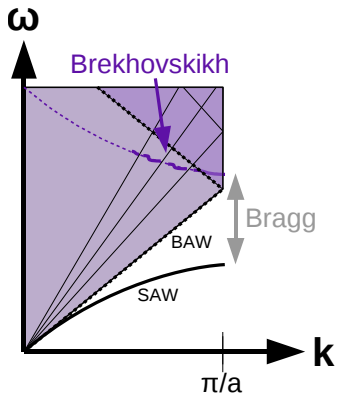


**Figure 5.2:** Brillouin diagram illustrating Bragg reflection and Brekhovskikh damping of the entire reflected branch. BAW radiation can damp SAWs at frequencies in and above the band gap.

### 5.2.2 Toward Devices

In order to maintain SAW energy near the surface, slow layers are often employed, e.g. as with Love waves. We recall the results for layers in Chapter 2. In other cases, e.g. STW modes, a metal grating guides a BAW along a piezoelectric surface. Use of contrasting materials that give an average velocity below that of the substrate BAW velocity helps, but the approach becomes useless when solid/void structures are desired, because the impedance contrast is extreme.

In this work we must circumvent the loss mechanisms present for surface relief scatterers in YZ $LiNbO_3$. We desire to suppress BAW generation by slowing the surface modes to keep both the lower and upper Bragg band edges below the BAW "sound line" (called the "sound cone" when at least two propagation directions are considered).

Our approach is to use surface scatterers supporting BAW resonances help to create SAW band gaps below the sound line through mutual coupling of SAWs and BAWs. By using relatively slower material for the scatterers, e.g. Al ($v_s = 3103$ m/s) or Ni ($v_s = 2920$ m/s), we expected to confine energy within them. We note that such structures have been very recently reported (2010) [44]. Our investigation began in 2005 and is timely

considering the recent report of 2-D pillar devices (V. Laude, A. Khelif, et al.). We originally selected polymer materials (Chapter 4) for very low velocities, allowing a thin layer to appear acoustically thick. This worked well in computations, but we have previously encountered practical complications using polymers as mechanical materials, especially the issues of dimensional consistency and residual viscosity.

To couple energy among the surface structures, we rely upon the surface wave in the faster substrate material. The slowest substrate mode, the Rayleigh SAW, is still faster than the shear velocity of the scatterer, but it can synchronously exchange energy with the cavities. There is a discrete phase matching condition along the interface between BAW cavities and the SAW (Figure 5.3). The rule of interfacial continuity of the acoustic field

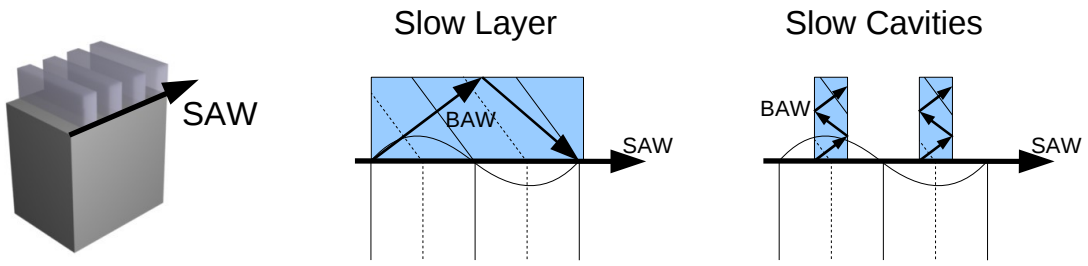


**Figure 5.3:** Rendering of surface ridge waveguide and illustration of phase matching.

applies in discrete regions under the cavities, at a length scale less than the wavelength along the interface. For fast waves in the layer, we may treat this as point-wise phase matching, assuming nearly constant phase across the interface of each scatterer. In this case we obtain extensional solutions similar to that illustrated in Figure 5.4. For slower waves in the narrow cavities, transverse resonance leads to Lamb modes (flexural and dilational). The Lamb modes propagate away from the surface and back, reverberating along the height.

We have investigated such high aspect ratio structures on lithium niobate, aiming to enable manufacturable surface PnCs with loss characteristics appropriate for passive sensors. First, the etching of deep holes requires many hours of processing time. This was not a desirable solution. We instead turned to deposited structures, preferring metal that can be deposited using an electroless technique (e.g. nickel) or by electroplating (the thicknesses

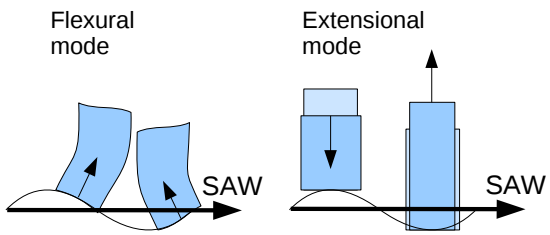


**Figure 5.4:** Illustration of flexural and extensional ridge modes. Displacements are exaggerated.

we consider are approximately half to 1.5 times the SAW wavelength).

### 5.2.3 Recent Literature

The design of surface phononic crystals in solids at microwave frequencies has been an area of active research in the 21st century, as high frequency PnC devices transitioned from slabs to solidly-mounted configurations [52, 9, 72, 2, 43, 44, 47].

Very relevant to our work is a 2005 study that reported a full band gap for SAWs in the plane of Y-cut lithium niobate [52]. Laude et al. used the plane wave expansion method to compute the BAW band structure for a square lattice of cylindrical voids in the substrate. We presume the holes extended through the depth of the substrate. Such a structure has historically been difficult to fabricate, requiring many hours of deep reactive ion etching (DRIE) or other processes necessary to achieve the extremely high aspect ratio in thick SAW substrates. Experimental results were provided for holes 9 $\mu$m wide and 10 $\mu$m deep in Y cut $LiNbO_3$. Finite element computations were also applied, but the study treated only bulk wave propagation since the aforementioned 2005 study revealed that this was sufficient to establish a SAW gap [9]. Experimentally, the researchers found the lower edge of the frequency gap, but the upper edge was indistinguishable due to BAW losses.

A 2010 report by Khelif et al. gave computations for a square lattice of cylindrical pillars on an anisotropic silicon substrate [44]. The intent was to achieve strong dispersion for surface-guided waves, exploiting Bragg stop bands below the onset of BAW radiation. The investigation was not reported for piezoelectric media, likely because of challenges implementing a piezoelectric perfectly matched layer (PML) for the transmission calculations.

The modes above the slowest bulk shear wave on the reported Brillouin diagrams were covered up with gray overlays, so the detailed behavior of surface mode diffraction above the sound line was not evident.

We show in Figure 5.5 the modes above the slowest BAW sound line of the structure reported by A.A. Maznev. The coloring of the modes has greatly aided our intuition into the behavior of modes in the oft-ignored region; indeed, some are actually SAWs (BAW nonradiation condition). The diffraction behavior of alternating "light" and "dark" fringes (optics terminology) is evident as alternating SAW (red) and BAW (purple) regions.

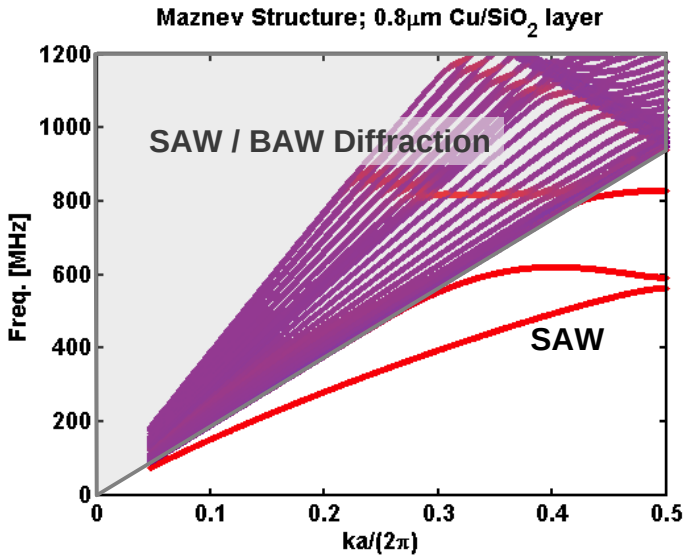


**Figure 5.5:** A finely sampled mode diagram colored by DoE reveals the diffraction of bulk modes and the limited existence of SAWs in the shaded region above the shear vertical BAW sound line.

## *5.3 Surface PnC Parameters*

We investigated the influences of design parameters on the band structures of 1-D and 2-D surface PnCs. The work that follows considers several different structures because some models have been experimentally validated (e.g. Cu and $SiO_2$ composite layer on Si), and because some are of particular interest to enable passive sensors leveraging phononic crystal technology (e.g. YZ $LiNbO_3$). We show the absolute frequency, rather than normalized frequency ($fa$), since our YZ $LiNbO_3$ devices reported in Chapter 7 operate at 435 MHz.

### 5.3.1 1-D Surface PnCs

#### *5.3.1.1 Density*

Variation of the density of one of the materials of a composite layer (as in Figure 3.2) alters the gap width and its center frequency. Both the LSAW and the SV mode in the layer then have reduced effective (average) velocities, reducing the slope of the asymptotes as $k \to 0$, if plotted on a $\omega$-$k$ diagram. As shown in the computations of Figure 5.6, increasing the density of the nominally denser material increases the impedance contrast, widens the band gap, and causes a net slowing, meaning both the upper and lower band edges shift downward in frequency. The difference in frequency slope with density ($df/d\rho$) was 12.5% for the two different modes at the zone boundary.

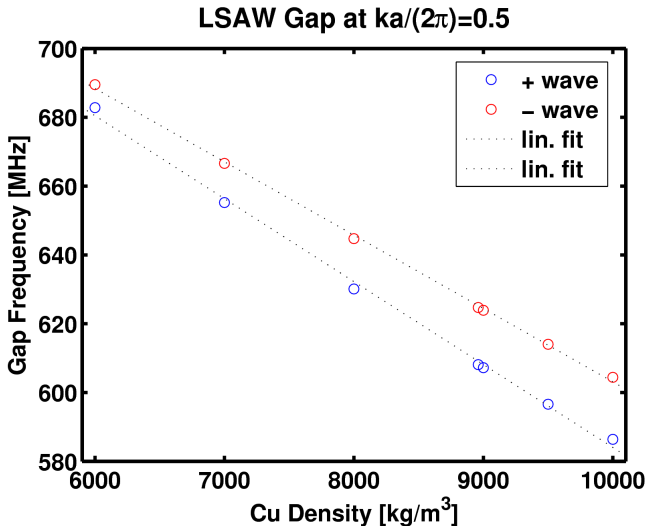


**Figure 5.6:** Effect of varying copper density on the gap width in the thin film 1-D PnC of A.A. Maznev. The gap at each density corresponds to the LSAWs at $ka/(2\pi) = 0.5$.

To learn more, we examined the energy distribution within the composite materials. We used the calculations for the 1-D PnC structure of Chapter 3, for which the change of elliptical particle displacements due to coupling of SAW modes was recently investigated by A.A. Maznev [64]. That work also investigated the mass loading effect, showing the gap opening and closing with change of material parameters. We confirmed this with our FEM calculations, and we proceeded to suggest a sensing application.

To illustrate the modal transitions in the band diagram, we calculated the normalized

strain energy within the composite surface layer. We then plotted the Brillouin diagram (Figure 5.7) with points shaded according to location of the energy. The formula for shading was $E_{\mathrm{S,SiO_2}}/E_{\mathrm{S,layer}}$, such that the greater the fractional energy in the silica, the lighter the shade on the plot. We found that this result agrees with the reference work, except we have displayed the strain energy rather than displacements. In the upper band the normalized

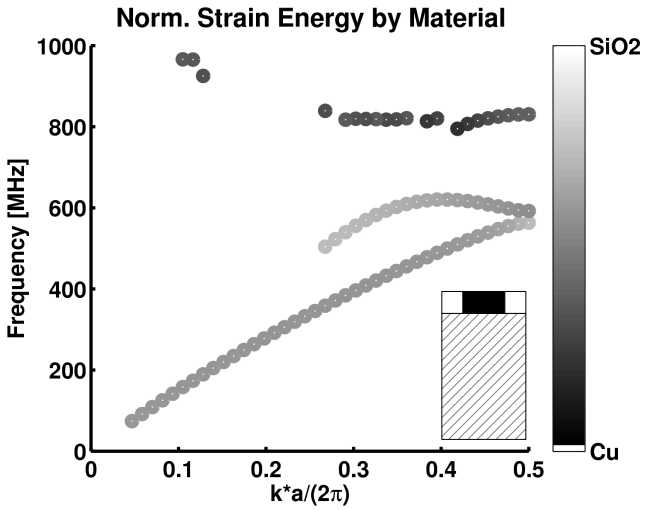


**Figure 5.7:** Spatial distribution of energy in a 1-D surface PnC. Across the LSAW/Sezawa frequency gap the energy shifts from the silica to the copper regions.

strain energy is greatest in the copper, whereas in the other band (lower), it is greatest in the silica. One could consider these two energy distributions to be somewhat like the carrier states in semiconductors: they may travel with different group and phase velocities and occupy different "sites" in the lattice. Because the wave energy is concentrated in different regions at different operating points, it appears possible to discriminate mass loading applied to one material from the other. In photonics literature, the upper band may be the "air" band and the lower the "dielectric" band, depending upon the material constituents.

For sensing applications, we use the *kinetic* energy density. That is because, in the limit of infinitesimal mass loading, the energy of the mode shifts by an amount $\Delta E = \Delta m|\mathbf{v}|^2/2$ when a small mass is rigidly coupled to the system, vibrating with a time harmonic particle velocity $\mathbf{v}$. This implies that the perturbation to the system energy will be greatest if a certain mass is applied to a region of greatest particle velocity.

Therefore we compared the fractional *kinetic* energy of the silica and copper, seeing that they approach equality ($E_{K,SiO_2}/E_{K,Cu}$=0.96) in the effective medium limit (as $k \rightarrow 0$). The contrast becomes apparent at the frequency gaps. For the Rayleigh gap, we found $E_{K,SiO_2}/E_{K,Cu}$=0.262, implying a greater effective material contrast in that regime (as expected for the creation of a frequency gap). Indeed, as we have already discussed, as the wavelength decreases the surface wave "sees" more exclusively the material(s) closer to the surface. In a later section we discuss the physical connection between the energy distribution and mass sensitivity.

Because the surface materials have very different chemical properties in addition to acoustic impedance, we note that it might be possible to perform differential adsorption of sensitive layers to copper and silica regions of a surface using two different surface chemistries. That would allow sensing of two different loading conditions at two very different frequencies (i.e. 600 MHz vs. 800 MHz). One could use one of many silane chemistries to immobilize on the silica [16], and an alkanethiol chemistry on the copper [101]. This should be possible with two-step bulk immobilization process wherein the PnC lattice pattern dictates the immobilization regions. Such a structure would provide good

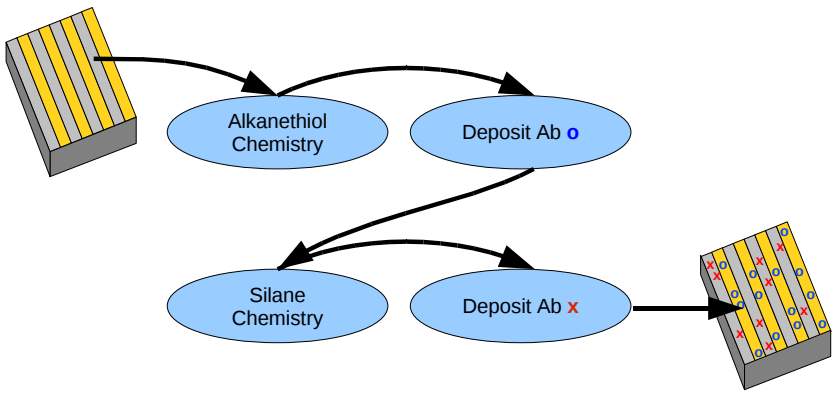


**Figure 5.8:** Suggested method of differential immobilization by bulk incubation steps, each targeting a distinct material.

spatial averaging by interleaving chemical selectivity on a smaller scale (and larger area) than could be conveniently obtained by robotic spotting methods. Despite the feasibility

of the approach, there may be significant challenges. We note that our deposited copper begins oxidizing when removed from vacuum, so this is an immediate complication of thiol chemistry on copper rather than gold. A recent investigation found that thiol surface chemistries on copper often produce multiple layers [42]. Furthermore, oxidized copper may also be silanized in the step targeting silicon oxide, especially in the presence of moisture and elevated temperature [18]. These challenges indicate the value of experimental study of such a structure and preparation method.

#### *5.3.1.2 Thickness*

In a second study we computed the Brillouin diagrams for surface modes propagating in the presence of nickel ridges (1-D "line" PnCs) on a YZ $LiNbO_3$ substrate.

In Figure 5.9 we show the BAW and SAW modes on the Brillouin diagram to emphasize the need to consider all modes within the Brillouin zone rather than just at the zone boundary. The onset of Brekhovskikh attenuation is visible for the higher frequency surface mode near the sound line of the shear (SV) BAW. In this figure and particularly in Figure 3.9, one can see "broken" surface modes above the BAW sound line. Just as the BAW radiation condition is met at discrete angles, so is a *nonradiation* condition: the BAW diffraction minima alternate with the diffraction maxima. We have noticed that this occurrence is seldom discussed in recent work on SAW PnCs. In other reports, the states above the BAW sound lines are typically assumed to be lossy BAW radiation states, and they are excluded from consideration. We show them and allow them to factor into calculations, e.g. the acoustic density of states.

Below the slowest BAW sound line, the situation is simpler. Within this guided wave region is a 25% frequency gap for guided SAW modes. As discussed in another section, the designer can choose to operate a device within this region to utilize the gap.

Figure 5.10 gives a sample of the coupled ridge and surface modes. The $x$ and $y$ displacements are shown for the three surface modes at the Brillouin zone boundary, i.e. at the Bragg scattering point. Knowledge of the energy distribution and type of mode supported by the surface structure are important to the designer. In sensor design for example, one

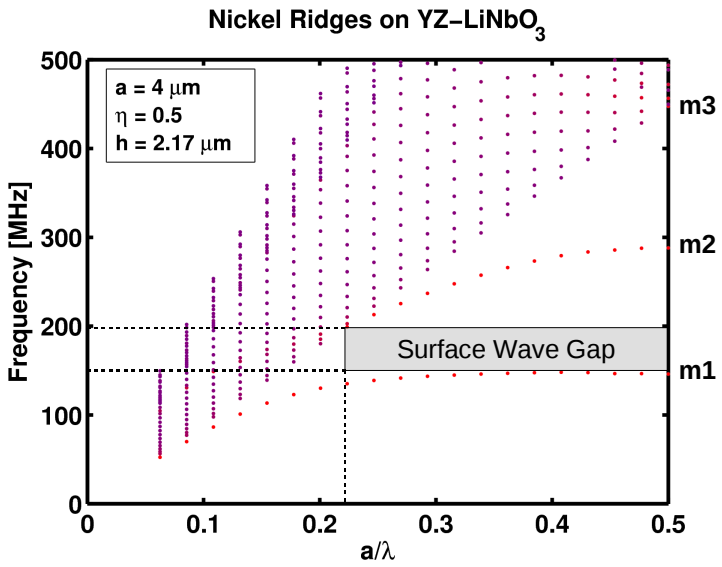


**Figure 5.9:** Brillouin diagram for nickel ridges on $LiNbO_3$; all modes are shown. A guided wave gap is indicated by the gray box, and the corresponding $f$ and $a/\lambda$ ranges are indicated. The box reveals the intersection of spectral gaps in both $\omega$ and $k$.

could compare sensitivity of different modes (polarizations and energy distributions) to gain more information or "perspective" about a certain perturbation.

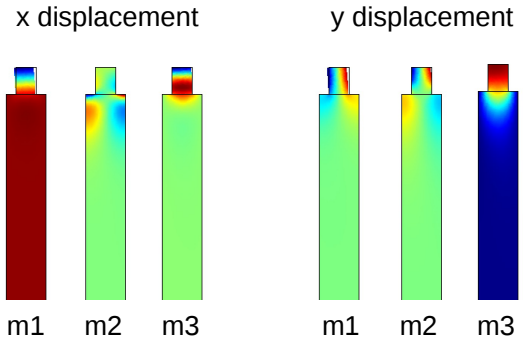


**Figure 5.10:** Displacement fields for nickel ridges on YZ $LiNbO_3$. The three modes (m1, m2, and m3) correspond to $\lambda = 2a$, i.e. resonance at the zone boundary.

Figure 5.11 shows the modes over the first Brillouin zone for three values of the ridge aspect ratio, $h/a$. The SV BAW lines correspond to the velocity obtained for $z$ propagation on Y-cut $LiNbO_3$ (0° in Figure 2.3), and the gray boxes indicate *surface* wave frequency gaps drawn through the BAW radiation region to the vertical scale for clarity. The ridge width was $0.5a$.

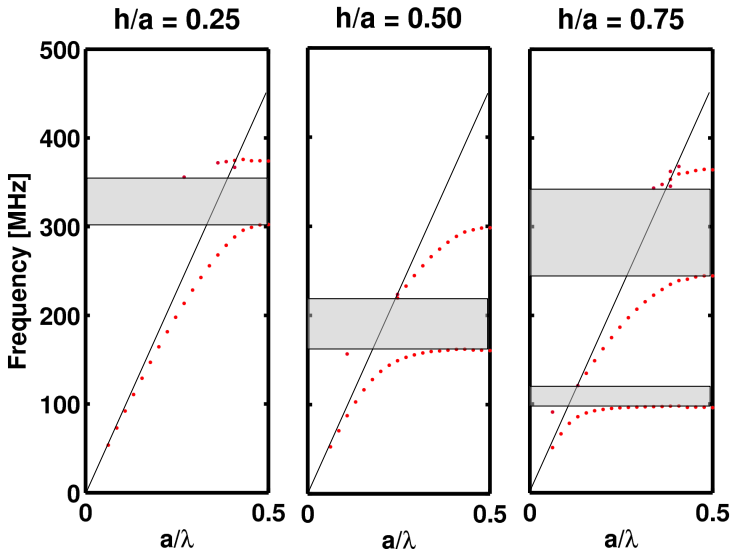


**Figure 5.11:** Three Brillouin diagrams for nickel ridges on YZ $LiNbO_3$. Computations for three values of the ridge aspect ratio, $h/a$ are shown. Black lines mark the shear (SV) BAW sound lines; gray boxes highlight frequency gaps for *surface* modes.

In Figure 5.12 we plot the parametric evaluation of the ridge aspect ratio for nickel ridges on YZ $LiNbO_3$. The wavenumber range at each value of $h/a$ was within the first Brillouin zone, $ka/(2\pi) \in (0, 0.5]$. The increase in the number of bands as $h/a$ grows is due to the greater number of cavity modes in the taller ridges. If we neglect the cavity width, the number of cavity modes supported below a given frequency is proportional to the ridge height. We expect small cavities (narrow and short) to have reduced mode density, allowing larger frequency gaps, however, they must be of sufficient extent to allow modes below the BAW radiation region in the first Brillouin zone.

In addition to the existence of the guided modes, we note that the frequency spacing of modes is inversely proportional to the thickness (for a guiding layer or narrow scatterers) and also the normalized difference in wave velocities. This is a general extension of the transverse resonance behavior of Love waves (as illustrated by B.A. Auld on page 101 of his Volume II [7]) to the case of generalized Lamb waves in a layer on a piezoelectric solid.

We note that the computations in this section consider surface modes to be those at the top of the *substrate*, i.e. beneath the ridges: we extract from the mode spectrum those modes that correspond to SAWs in the substrate, despite the coupling to standing modes

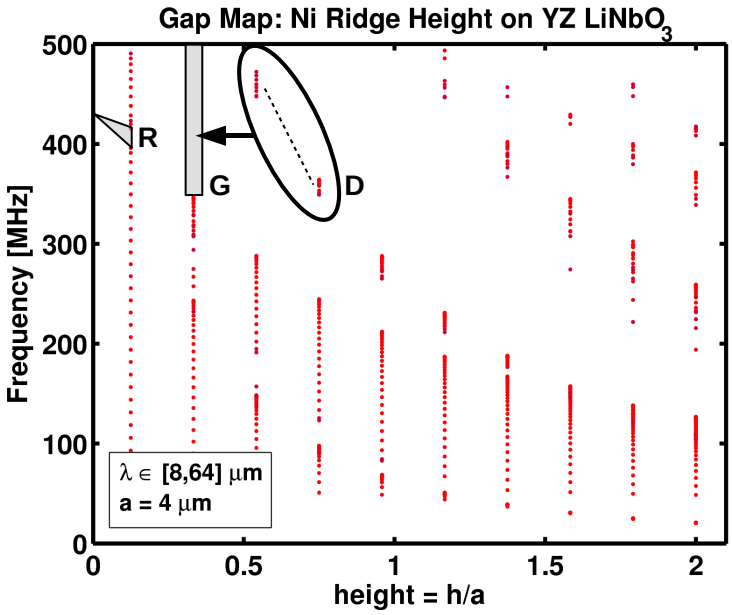


**Figure 5.12:** SAW frequency versus normalized ridge height for nickel on YZ $LiNbO_3$. "R," "G," and "D" denote the Rayleigh gap opening, a wide gap for insertion of defects, and a range of defect modes to place into the wide gap, respectively.

of the tall structures.

#### *5.3.1.3 Filling Fraction*

Next we varied ridge width, $rw$, with respect to the lattice constant, $a$. The ratio of the two is $\eta$, typically referred to as "metallization ratio" (SAW literature) or "filling fraction" (2+ dimensional PC literature). Figure 5.13 shows the dependence of the SAW band gap upon values of $\eta$. We investigated smaller values of $h/a$ for typical filling fractions, e.g. $\eta$=0.5.

The gap found at the Brillouin zone boundary for each $\eta$ in Figure 5.13 is applicable near $ka/(2\pi) \approx 0.5$. For a general surface mode frequency band gap, one must consider the frequency distributed modes summed over all $k$ at each filling fraction. This gives a more complete frequency "gap map."

In a concurrent study by A. Khelif, et al., the effect of filling fraction was explored for a 2-D pillar array on silicon [44]. Although the investigators noted the use of *low* filling fractions, i.e. $F = 0.28$ or $r/a = 0.3$, they did not discuss the rationale. It may not be obvious why a low filling fraction would be desired in this case, in contrast with prior

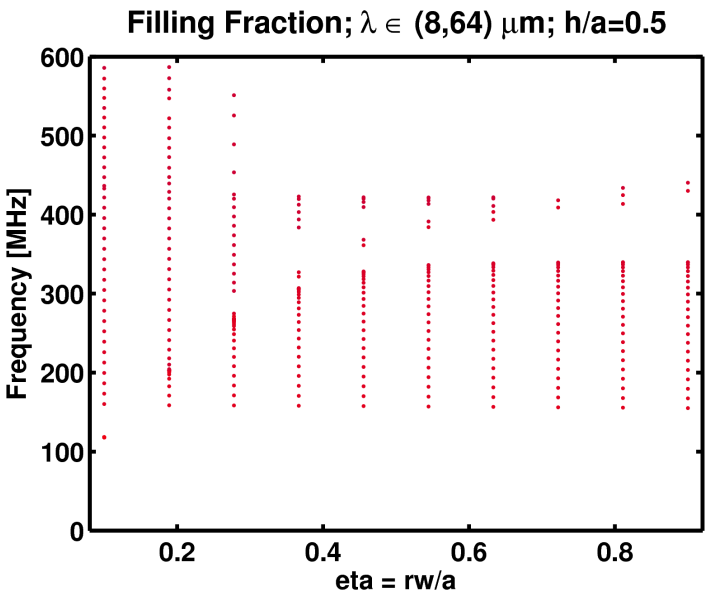


**Figure 5.13:** Gap opening for guided waves when $\eta > 0.2$ and $h/a$=0.5.

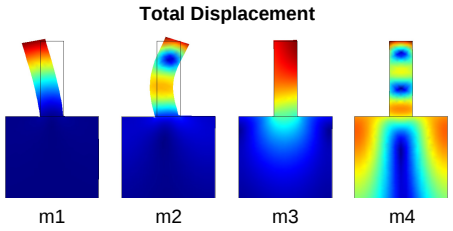


**Figure 5.14:** Total displacement field in narrow ($\eta = 0.25$) nickel ridges on YZ $LiNbO_3$. Four modes at the zone boundary are shown for $h/a = 1$ and $\eta = 0.25$. Compare to $\eta = 0.5$ in Figure 5.10.

literature for holes and slabs (e.g. gap opening for $d/a > 0.88$ in a silicon slab [72]).

We note that a design challenge with coupled BAW resonances is constraining the onset and number of resonant modes. By increasing the cutoff frequency for lateral modes (reducing the width of the cavities), the thickness becomes the dominant parameter at lower frequencies such that the thickness sets the frequency of the lowest cavity resonance.

### 5.3.2 2-D Surface PnCs

To compute dispersion in 2-D PnC lattices, we extended the domain to three dimensions. This allows many more surface modes of both surface transverse and in-plane shear varieties. So-called "surface skimming" modes may also be found. In this explorative study, we

examined both dot and line arrays, and we did not limit the results to only Rayleigh waves. Figure 5.15 illustrates surface wave solutions for two different 2-D PnC lattices. In the

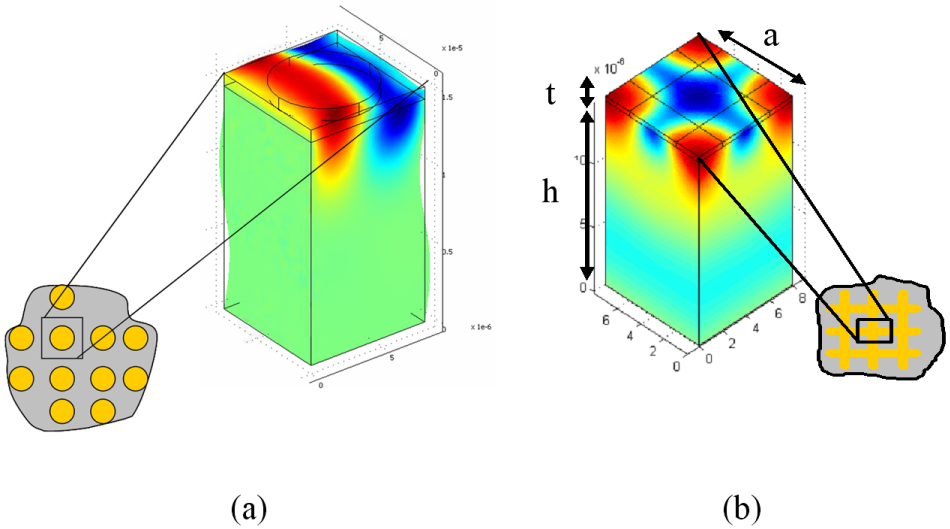


**Figure 5.15:** (a) shows one unit cell of a square lattice surface PnC of dots, whereas (b) corresponds to a square lattice of lines; a cross "hatch" pattern.

diagrams that follow, the direction of propagation is given in terms of the points of high symmetry in the reciprocal space of the 2-D PnC. As depicted in Figure 5.16, the $\Gamma X$ direction is defined along the box edge of a square lattice PnC, whereas the $\Gamma M$ direction is along the diagonal.

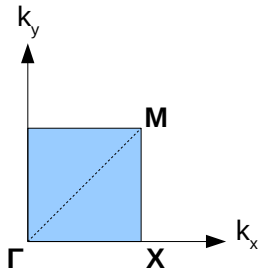


**Figure 5.16:** Points of high symmetry for the Brillouin zone of a square lattice PnC.

The next result, Figure 5.17, shows the surface mode spectra computed for the crossed-line PnC consisting of gold lines in a silica background layer on a silicon substrate. Near 0.2 on the $k$ axis, three positive group velocity modes are found below 300 MHz. Additional modes found in this simulation are due to the 3-D computational domain which allows in-plane polarized shear waves, etc. We have in some cases modified the DoE measure to

return only the SHSAW modes by changing the formulation of the energy. When searching for SAW band gaps, however, this level of detail is not required; we look at all surface modes. For these two dimensional surface phononic crystals, we do not see any full surface band

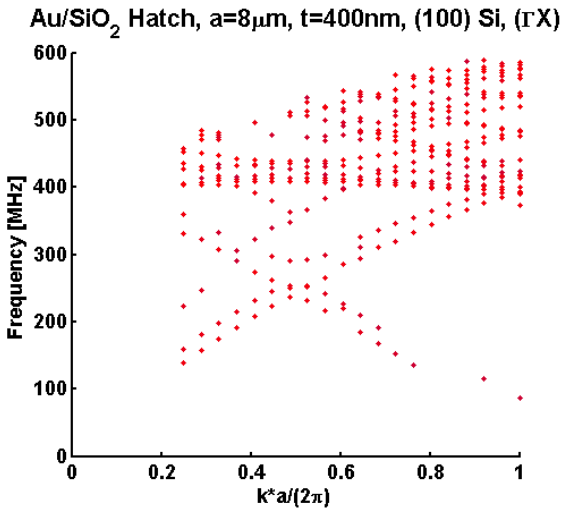


**Figure 5.17:** Thin "hatch" lattice of Au and $SiO_2$ on silicon.

gap. Some modes have gaps and others do not, i.e. there are modal avoided crossings - the expected adiabatic transitions of mode character at the Brillouin zone boundary ($ka/(2\pi) = 0.5$) - but not for every mode. In these diagrams the modes are not visually distinguished, but they are restricted to surface modes. To elucidate mechanisms for gap formation across all surface modes, we examined the unit cell parameters.

In 1-D PnCs, a "filling fraction," $\eta$, of 0.5 is commonly used for 1-D SAW band gaps. These are the very common SAW reflector gratings in which $\eta$ is called the "metallization ratio." In the 2-D structures, the corresponding filling fraction may be different. One might suspect an equivalent 2-D filling fraction would correspond to a ratio of areas equal to 50%. Calculation reveals a dimensionally equivalent $d/a = 0.797$, where $d$ is the dot diameter and $a$ is the 2-D unit cell lattice constant. However, the actual fraction will depend upon the effective size of the dot determined by the wave velocity in the material. The work by A. Khelif shows gap opening begins at $d/a = 0.81$ for air holes in lithium niobate [11]. The gap was greatest for the largest holes, i.e. when $d/a \approx 1$. While this composition of host material (substrate) and void (air) achieves maximal acoustic impedance contrast, it

is suspected to have greater bulk wave radiation coefficient per unit cell when compared to other possible structures.

The filling fraction is a key reason why SAW reflector gratings are typically produced using very thin metal strips and a large number of strips; the reflection coefficient and bulk wave radiation coefficient per unit cell are reduced, and the Bloch wave vector is more precisely defined, respectively. This gives high $Q$ reflections, both due to reduction of BAW loss and formation of a very narrow Bragg stopband.

To aid visualization of the many modes present in the very cluttered dispersion diagrams for 2-D surface PnCs, we plot two distinct eigenmodes to illustrate the very different natures of surface modes in the structure (SHSAW and RSAW, Figure 5.18).

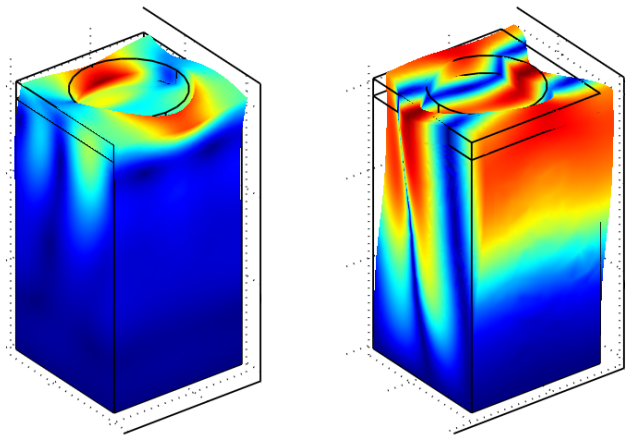

**(a)** Rayleigh SAW eigenmode **(b)** SHSAW eigenmode

**Figure 5.18:** Modal solutions for square lattice of air holes in polyethylene film on $LiNbO_3$; $\Gamma X$ direction. Due to the layer, the modes are not *pure* Rayleigh and shear horizontal (SH) SAWs, respectively.

It may help the reader to see a plot distinguishing these modes on a Brillouin diagram. Due to the anisotropic media we consider, polarization dispersion may occur. In Figure 5.19 we show only surface modes (DoE within $0.36\lambda$ of the surface), and we color them to indicate the polarization. Near the $\Gamma$ point, $k = 0$, one can clearly distinguish the SH and Rayleigh lines (velocities). In this computation, there were several deviant modes because the mesh element size was not sufficiently constrained. Still, the existence of and difference in velocity between the two modes are clear.

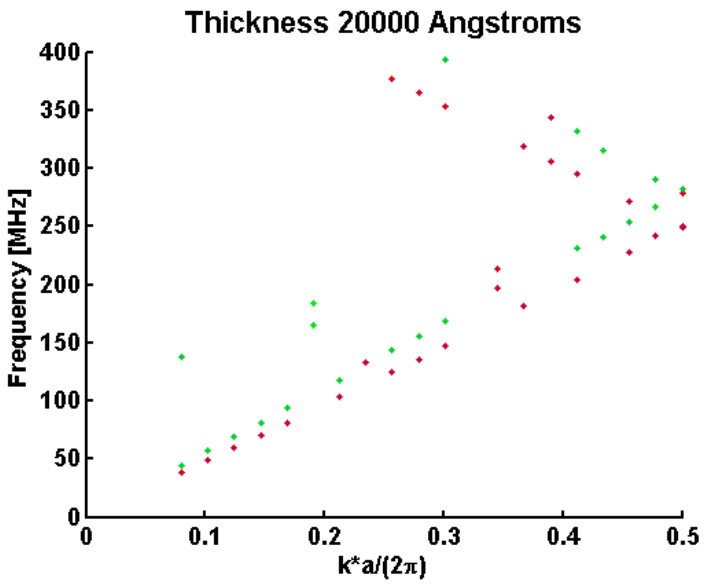


**Figure 5.19:** Distinguishing SHSAW from RSAW in the Brillouin diagram for a 2 $\mu$m thick polyethylene layer on lithium niobate. The upper data series has greater velocity and is the SHSAW mode.

#### *5.3.2.1 Host Material Anisotropy*

Another point to investigate was the anisotropy of the host material. For a given lattice and material thickness, we also simulated a change of propagation direction with respect to the superlattice (and host material). We began with the square lattice surface PnC and the silicon substrate primary axes aligned. Then the $\Gamma X$ and $\Gamma M$ points corresponded to (100) and (110) directions in the silicon substrate. Figure 5.20 compares mode spectra for these two propagation directions.

In Figure 5.20, the same square lattice structure was evaluated for two different propagation directions. We note the lower band curvature and the occurrence of multiple upper subbands due to enhanced confinement of the energy in the film with this substrate orientation. We surmise that the angular dispersion of the anisotropic host material can critically influence the degree to which the PnC layer controls the surface mode dispersion. We attribute the greater velocity to the host material anisotropy because the effect is opposite what one would expect for $\Gamma M$ propagation: higher frequency at the Brillouin zone boundary although the wavelength is a factor $\sqrt{2}$ greater than in the $\Gamma X$ direction.

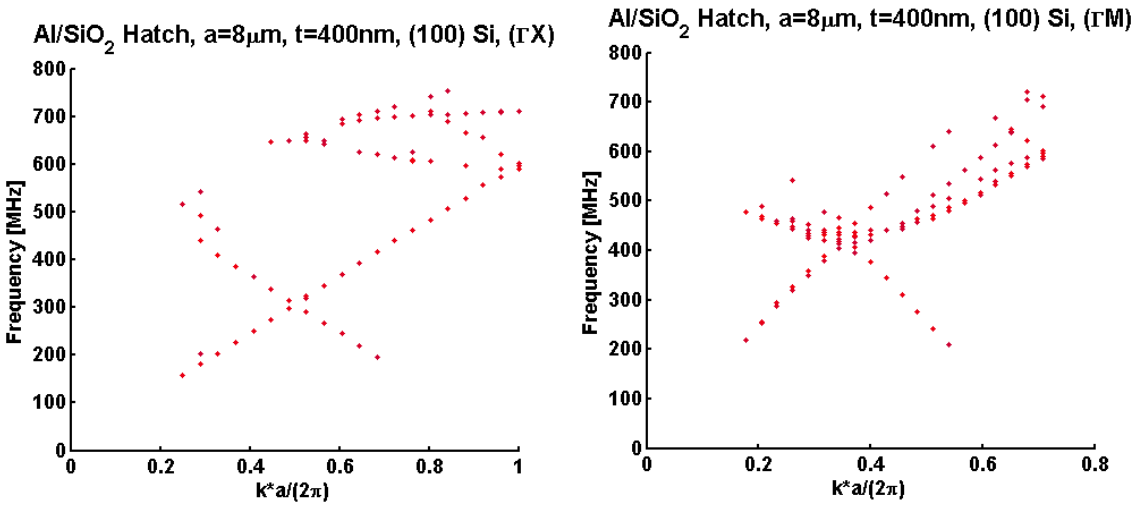


**(a)** $\Gamma X$ direction (superlattice and Si substrate) **(b)** $\Gamma M$ direction (superlattice and Si substrate)

**Figure 5.20:** Comparison of mode spectra for two points of high symmetry in the first Brillouin zone for a square lattice (2-D) surface PnC.

Figure 5.21 demonstrates the effect of increased thickness and acoustic impedance contrast (gold and $SiO_2$ instead of aluminum and $SiO_2$). In comparison to Figure 5.20, the occurrence of layer guided bands is prominent in both panels due to the thicker layer (which is also effectively thicker due to a lower average or "effective" velocity). The propagation direction does not have as pronounced an effect on the band structure because of the energy confinement in the layer.

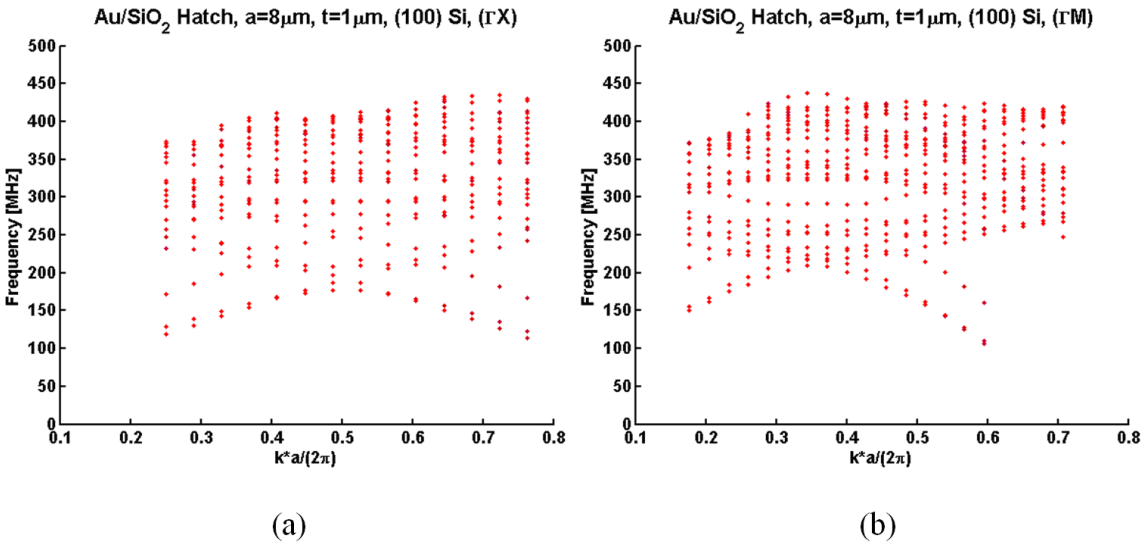


**Figure 5.21:** Comparison of modes for a similar square lattice, but in a thicker layer.

#### *5.3.2.2 Layer Thickness*

As the thickness of the slower over-layer is increased, the band structure flattens due to the inclusion of film modes. The guiding of modes in the patterned surface film helps to better confine the acoustic energy within the surface PnC. Figure 5.22 compares SAW propagation in a square lattice with different thicknesses. The superlattice orientation matched that of the silicon substrate.

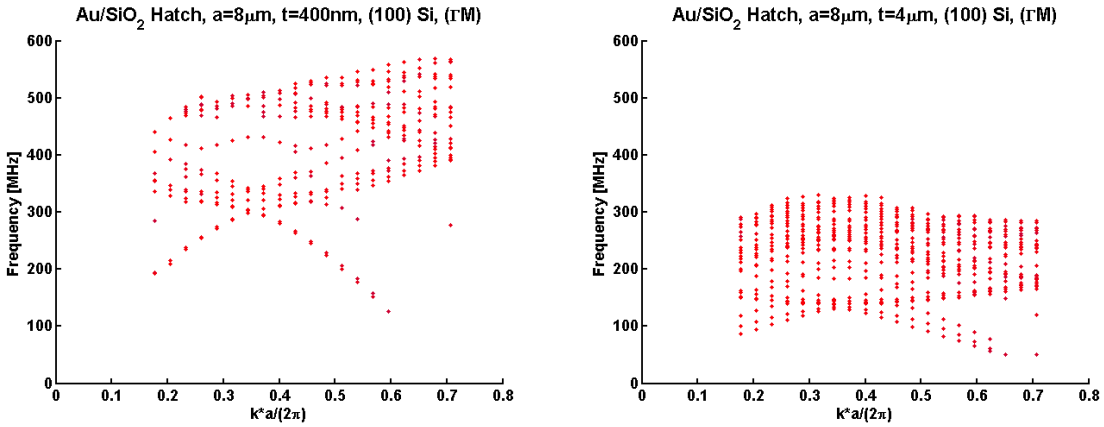


**(a)** 0.4$\mu$m thick, $\Gamma M$ direction **(b)** 4$\mu$m thick, $\Gamma M$ direction

**Figure 5.22:** Mode spectra for a 2-D crossed-line PnC. The propagation direction is $\Gamma M$ for both, but the layer thickness decreases the band curvature, center frequency, and partial gap widths.

The preceding figure gives eigenfrequency spectra for two different thicknesses in the same square lattice structure. The mode density (or density of states, DoS) is clearly nonzero throughout the simulated frequency range. Thus we have not observed complete SAW band gaps in these simulated 2-D infinite PnC structures. However, for ranges of $k$ and $f$, we have small surface mode gaps. It is also evident that the surface wave DOS changes significantly due to variation of the finite thickness surface PnC layer. Figure 5.22b of the previous figure shows a greater number of subbands at frequencies just below the lower band maximum near 150 MHz. In further contrast, the subbands below the lower band's maximum are nearly degenerate for a very thin surface PnC. The layer PnC and substrate combination acts to disperse the partial wave components rather than permit a hybrid (e.g. Rayleigh) mode.

## *5.4 Analysis*

### 5.4.1 Operating Point

Despite obtaining band gaps for guided waves at the surface, significant losses would be encountered if all frequencies or all wavenumbers were excited; the suitability of the solution remains bounded by the sound line(s) of the substrate. Therefore, it is important to note the desired operating point (or region) on the Brillouin diagram; one may design the space harmonics of the transducer and the spectrum of the electrical stimulus in order to excite modes in a region ($\Delta\omega$, $\Delta k$).

Having solved the normal mode eigenproblem for $\omega$ over a range of $k$, we have essentially obtained the spectral Green's function, $G(\omega, k)$; the normal modes of the structure are known for both $\omega$ and $k$. Therefore, for a general source, $S(\omega, k)$, we can compute the response, $\psi(\omega, k)$:

$$\psi(\omega, k) = G(\omega, k)S(\omega, k) \ , \tag{5.3}$$

where $G$ contains the eigenfunctions: the spectral representation of the usual convolution in space and time. Spectrally, we see that excitation of all modes of $G$ is the response to an impulse in space and time: $S = 1$. This agrees with the notion of the Green's function as the spatiotemporal impulse response.

The source distribution may be calculated in the same way as $G(\omega, k)$ or determined empirically. $S(\omega, k)$ can be interpreted as a mask overlay that selects which modes in the $(\omega, k)$ diagram are excited. The Fourier transform of the scalar interrogation pulse (voltage waveform) may be represented as normalized weights on the $\omega$ axis, and the spatial Fourier transform of the transducer may be represented on the $k$ axis. Typically both waveforms will have a $|\sin(x)/x|^2$ or Gaussian appearance, depending upon the temporal pulse shape and transducer extent and apodization (spatially distributed weight function). Such a plot is shown in Figure 5.23. We have illustrated approximately a joint spectral operating point corresponding to excitation of a 111 wavelength (or finger pair) transducer with a 20 ns tone burst at 500 MHz (the scale was skewed when the plots were overlaid). When the transducer is driven, the $\omega$ and $k$ distributions may be considered independent because the

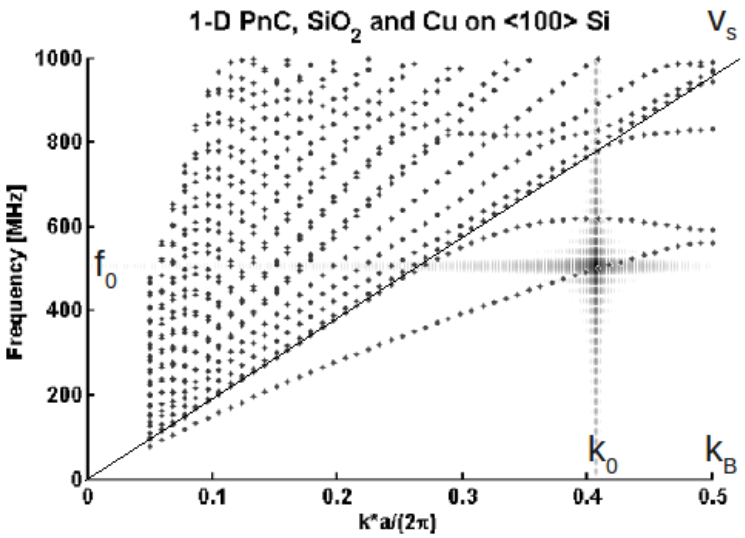


**Figure 5.23:** Overlay of material modes and source function for device design. The source function approximately represents a transducer having $N_p$=111 finger pairs and driven with a $\tau$=20 ns tone burst at $f_0$=500 MHz.

time component of the waveform is determined by the electromagnetic signal source (acting effectively instantaneously across the space of the transducer), and the space distribution is set by the fixed transducer structure.

### 5.4.2 Density of States

A measure often reported in *photonic* crystal calculations is the density of states (DOS, $D$). As shown in Chapter 2, the energy density of states, or number of frequency eigenstates per unit frequency range depends upon the $\omega(k)$ relationship. We consider this measure in the design of dispersive sensors because it incorporates all the modes at each frequency and because general energy transport in materials (e.g. transmissivity, heat capacity, and conductance) scales with the quantum mechanical DOS. Key points include:

- The rate at which a system leaves or returns to certain configurations, e.g. rate of emission or absorption, is proportional to the frequency DOS.
- Sensitivity of photonic devices is well-known to correlate with the DOS, and this has been applied to photonic sensors, e.g. one used for bioassays [84].
- The designer may choose the spatial and temporal density of states depending upon

the application.

We next discuss the application of the DOS to sensitivity of acoustic devices. For a defect mode resonator created within a PC, there is an oft-cited advantage of having a wide frequency gap: there is a greater energy threshold for transition to another frequency. This may be summarized in an increased state lifetime, smaller absorption, and greater quality factor, $Q$. Even a structurally perfect, i.e. unimodal, acoustic resonator does not have a pure or "sharp" resonance because thermal fluctuations and material defects give a best-case broadening function having a fractional bandwidth inverse to $Q_{\mathrm{m}}$, the material quality factor at the frequency and temperature of interest. This means that theoretical results will be subject to material quality limitations.

Even in the case of intrinsically lossless materials, the bandwidth of a peak in the surface density of states (SDOS) gives an estimate of inverse lifetime of the surface energy ($\tau \propto 1/\Delta f$) about a given frequency operating point ($f_0$). As discussed in Chapter 2, the loss is due to the conversion of SAWs to other modes, e.g. BAWs.

#### *5.4.2.1 Perturbations*

The concern for spontaneous transitions away from a defect state (giving a lumped attenuation factor, $\alpha$) for "defect" states within a gap is a very common reason for reporting the DOS in the PxC literature. From semiconductor theory, the definition[1] of transition probability for a perturbation goes according to Fermi's "Golden Rule." The transition rate ($W_{\mathrm{if}}$) from an initial state ($\psi_{\mathrm{i}}$) to a final state ($\psi_{\mathrm{f}}$) is:

$$W_{\mathrm{if}} \propto |M_{\mathrm{if}}|^2 D_{\mathrm{f}} \tag{5.4}$$

$$M_{\mathrm{if}} = \int \psi_{\mathrm{f}}^* H' \psi_{\mathrm{i}} \, dV \ , \tag{5.5}$$

where $D_{\mathrm{f}}$ is the final density of states, and $M_{\mathrm{if}}$ is the "matrix element" or correlation amplitude for the system perturbation, $H'$, coupling the initial and final states.

The transition rate is simply proportional to $D$, a projection of the eigenspace onto the

[1] Our application of this method in acoustic continuum mechanics is valid; J.P. Dowling, J.M. Bendickson, et al. have already discussed the applicability to electromagnetic band gap devices, in terms of the Green function [19, 10].

frequency basis. Thus $D$ indicates the degeneracy at each frequency. The details are in the matrix element: $|\langle\psi_{\mathrm{f}}^{*}|H'|\psi_{\mathrm{i}}\rangle|^2$, wherein the implied overlap integral includes the other degrees of freedom of the system: mode polarizations, spatial profiles, etc..

We will not discuss here the many transitions possible for a state in an acoustic sensor. The simple case of infinitesimal and spatially uniform mass loading is assumed not to change the field distribution, such that $\psi_{\mathrm{f}} \approx \psi_{\mathrm{i}}$ (Born approximation), and one then can see that a perturbation of the mass density corresponds to a vertical shift on the Brillouin diagram due to the new Hamiltonian, $H = H_0 + H'$, where $H' \propto 1/\delta\rho$, and we are using the system matrix, $A$ from (3.2), as the phononic Hamiltonian. Increased mass density reduces transition rates to the original frequency $\omega_0$ and increases transition rates to a lower frequency, $\omega = \omega_0 - \delta\omega$. This is in large part because $D(\omega_0) < D(\omega - \delta\omega)$; for a general transition in the perturbed structure, the rate to the lower frequency state is greater. In this way, increase of the mass density simply lowers the frequency of the operating point (Figure 5.24).

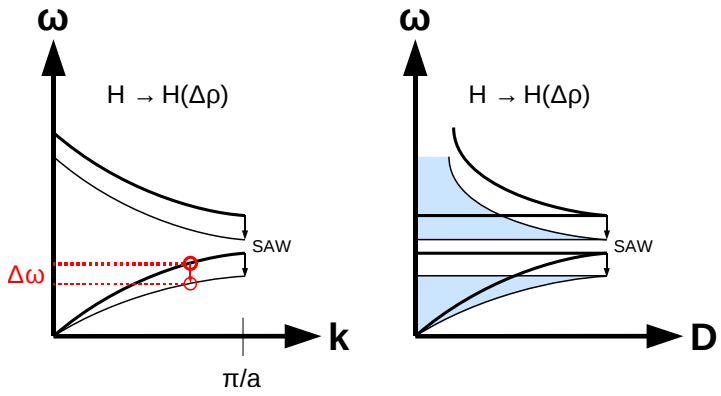


**Figure 5.24:** Illustration of band shift on Brillouin diagram and shift of the density of states, $D(\omega)$.

In dispersive sensor designs, the designer might like to leverage spatial distribution of energy to obtain more informative signatures. Indeed this case would be an augmentation of the work of Hunt et al. investigating the time dependent signatures of acoustic wave biosensors, except the field dependence would also be used. One must then account for the stronger dispersion associated with spatial multiplexing and isolation in contrast to

the small mass loading dispersion. For such devices, the transducer(s) and guides must be designed to couple to all sensitive regions, whether perturbed or unperturbed. This requires auxiliary computational design techniques (e.g. perfectly matched layers, transfer matrix method, etc.) taking into account finite terminations of structures previously assumed infinite.

#### *5.4.2.2 Device Sensitivity*

In 1995, F. Josse gave the relative frequency sensitivity to mass loading for a plate mode device in terms of the group velocity and velocity sensitivity: $S_m^f = v_g/v_p S_m^v$ [41]. This shows that the presence of normal dispersion, $v_g < v_g$, reduces the *frequency* sensitivity. One may also consider the phase velocity sensitivity. Following Tiersten's result, (2.14), McHale et al. have noted that the *velocity* sensitivity to mass loading for a guided acoustic wave depends upon the ratio of squared surface particle displacement to acoustic power flow down the waveguide:

$$S_m^v \propto \frac{1}{P}|u_i|^2 \propto \frac{1}{U_s v_g}|u_i|^2 \propto D \ , \tag{5.6}$$

where $P$ is the acoustic power flow down the waveguide (equal to the stored energy per volume, $U_s$, times the energy velocity, $v_g$), and $u_i$ are the particle displacements of the mode. The density of states is $D$. We note that (5.7) reveals a scaled version of the quality factor, $Q \equiv E_s/P_l$, of a resonant structure. The velocity sensitivity for a waveguide is greatest at transverse resonance, i.e. when the group velocity is zero. Because a waveguide may be viewed as a distribution of coupled resonators, it is reasonable to consider the $Q$ of one such resonator. In this way our study of dispersion, loss, and device sensitivity has traveled full circle, returning to the oft-quoted $Q$ figure of merit. Next we discuss how to compute the DOS, $D$, in order to assess the device sensitivity for very general structures using Brillouin diagrams.

#### *5.4.2.3 Computing the DOS*

The frequency DOS can be qualitatively observed as the density of eigenmodes along narrow $d\omega$ slices in Brillouin diagrams; or it can be more formally computed according to the

number density of modes per frequency or energy ($dN/dE$). One may compute the DOS either from the dispersion relation or from the Brillouin diagram, e.g. as we produce by FEM. The latter allows determination of the DOS for very general structures. In the case of discrete numerical calculations, we compute the DOS, $D(E) \propto D(\omega)$, by approximating the expression of (5.7) with a simple histogram over $\omega$. We collect modes for all values of $k$ into bins of width $\Delta\omega$, where $\Delta\omega$ is chosen to suit the computational sampling of the space. When the bin width goes to 0 Hz, the discrete modes are collected as follows:

$$D(\omega) = \sum_i \delta(\omega - \omega_i) \ , \tag{5.7}$$

which treats each mode as a delta function and sums them at each frequency.

It was apparent in observation of the Brillouin diagrams that $D$ was at least inversely proportional to the group velocity, $v_g = \partial\omega/\partial k$. In fact this already had been formally discussed for the electromagnetic mode density of a single mode by Bendickson et al. in 1996 [10]:

$$D(\omega) \equiv {v_g}^{-1} \ . \tag{5.8}$$

Rather than use numerical differentiation to obtain $v_g$ for distinct bands within the discrete eigenmode spectrum obtained by solution of the FEM problem, we preferred the aforementioned histogram method. In this way we avoid Debye and Einstein approximations of the mode branches, and we arrive at a measure that is valid even when the group velocity is multivalued (several distinct branches at a given frequency). This approach is valid for all frequencies in general media.

The DOS at a single band's edge depends upon device parameters affecting the concavity of the band, $\partial^2\omega/\partial k^2$, i.e. its effective mass. For SAW devices such parameters are the film thickness, material impedance contrast (in composite layers), and finite extent or end effects of a structure. The finite thickness of a layer constrains its extended states, giving a transverse resonance cut-off frequency above which acoustic energy can be transmitted along the layer. This behavior was noted for the Love waves of McHale et al. in Figure 2.16 of Chapter 2. At the onset of layer-guided propagation, the group velocity abruptly attained its lowest value, enhancing the $v_p/v_g$ ratio in (2.18). These regions of the dispersion

diagram are frequency turning points; $\partial\omega/\partial k \approx 0$, corresponding to peaks in the DOS.

Finding the DOS over real $k$ and $\omega$ corresponds to the frequency density of *propagating* modes. We have shown Brillouin diagrams containing only purely real modes according to the definition of the eigenproblem (Chapter 3). Although states above the BAW lines are partly propagating in $y$, the depth direction, they are true extended states. When we prefilter the dispersion diagram to include only surface modes, the DOS computed from that subset of modes is then actually the surface DOS, SDOS, an applicable measure for surface wave sensors. Example results for the DOS and SDOS are given in Figure 5.25 for a certain design of the YZ $LiNbO_3$ ridge structure. As we have discussed, the SAW frequency sensitivity to mass, $S_m^f$, peaks at the maxima of the SDOS. We note especially that some peaks in the DOS do not correspond to surface modes, and therefore, their elimination is essential for evaluation of surface sensitivity.

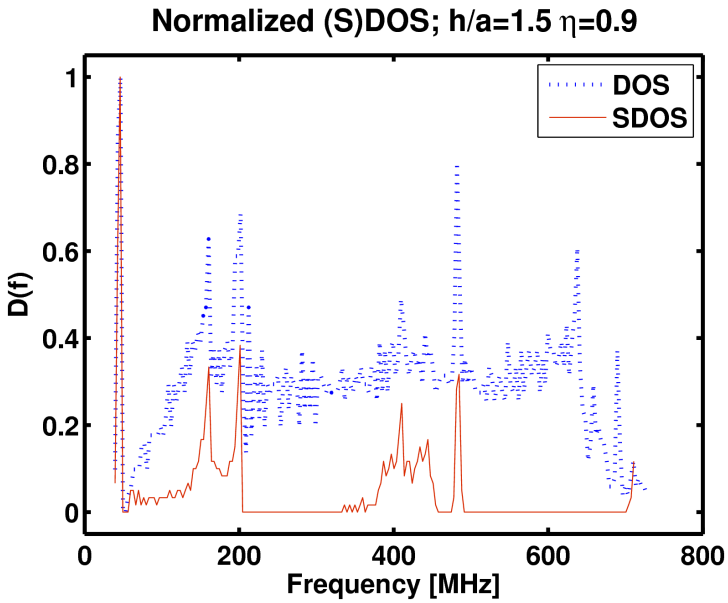


**Figure 5.25:** The density of states, $D(f)$, computed for the ridge structure using the histogram method and comparing all modes with the case of surface modes only.

## *5.5 Summary*

In contrast with conventional practices in SAW design, we investigated relatively high aspect ratio "ridge" structures (1-D surface PnCs) such that large band gaps could be obtained

for surface waves. This has been a topic of much concurrent interest in the PnC research community [52, 9, 43, 44]. Aiming to enable the design of sensors based upon surface PnCs, we parametrically explored "gap maps" and mass sensitivity in SAW PnC structures. Ratios of height to width of the unit cell ($h/a$) were in the range (0.25, 1.5), and the filling fraction ($\eta$) took values in the range (0.05, 0.9). The investigation led us to suggest a method for differential acoustic mass sensing using the prevalence of the kinetic energy in one material relative to another at different frequencies.

We also computed Brillouin diagrams for 2-D surface PnCs on anisotropic substrates. A demonstration of the extension to two-dimensional PnCs required a second set of periodic boundary conditions, increased the domain size and computational degrees of freedom, and revealed additional modes (e.g. shear horizontal) that were not revealed in the 2-D analyses of 1-D surface PnCs (ridge structures). Investigation of layer thickness and substrate orientation led to the observations that thicker layers increase the number of subbands, increase the density of states and modal effective mass, and reduce the effect of substrate anisotropy on the band structure.

In evaluation of the designs of surface PnCs we considered the very general utility of the Brillouin diagrams in terms of the spectral Green function. Overlay of the transducer spectral properties masks the diagram and overlapping modes that may be excited. Unlike the concern of a thermal Fermi function in semiconductor devices (exciting all states of lower energy), SAW devices are usually excited by transducers having certain operating points ($\omega_0$, $k_0$) and spreads ($\Delta\omega$, $\Delta k$). Thus, operation within a partial band gap is feasible.

We also applied the well-known density of states from photonics, showing the ability to determine highly sensitive operating points for acoustic wave sensors having very general dispersion relations. We used a histogram approach to plot the mode density over frequency for both the whole structure and for surface modes only.

We recognize that 1-D surface PnCs provide a suitable research platform for more exploration. Indeed, there is still not a well-known need for higher dimensional surface PnCs in the SAW research community. PnC structures do not relax the photolithographic constraints of SAW design in the GHz range; in fact for 2-D PnCs they may require greater

resolution to define circular features with $d/a$ close to 1. Very high quality factors are already attained in SAW devices; so although PnC defect mode resonators operating in wide spectral gaps could reduce space requirements, the necessary increase in material contrast and use of tiny cavities increase acoustic energy density, and we expect this to increase losses to nonlinearities and to create challenges for excitation and transduction. In sum, we expect interesting and significant practical challenges to the implementation of surface PnCs exceeding current SAW performance. However, an integrated phononics approach, developing a full set of 2-D and 3-D engineered waveguides, cavities, and reflectors, could yield unexpected advances for device integration. This remains a field for much future exploration.

In our evaluation of more conventional and easily manufactured dispersive SAW designs, we found interesting uses for the dispersion in application to passive sensors. In Chapter 6 we simulate spatial gradients and discrete phase coding of distributed reflectors for their utility in the passive sensing problem. We have found this is a well-known and interesting departure from the typical perfectly-periodic PnC approaches. Indeed, advanced devices are realized by judicious engineering of inhomogeneities in superlattice structures [40]; in the next chapter we give examples in which the spatial encoding of "defects" is useful in dispersive design.

# CHAPTER VI

# THE RADAR CONTEXT OF DISPERSIVE SAW TAG SENSORS

## *6.1 Overview*

In evaluating the utility of dispersion in passive SAW sensors, we first explore the similarities to well-known use of dispersion in radar. In the conceptual diagram of Figure 6.1, one can see how the passive antenna-coupled sensor modality can be applied to tactical scenarios in challenging environments. Once a device is deployed, the situation is essentially a conventional radar problem in which a return signature is augmented with information about the *local* chemical composition of the air, i.e. in the vicinity of the antenna-coupled device. Of course a wide variety of sensors can be constructed, depending upon how the SAW is exposed to the environment; a list of sensitivities (to temperature, pressure, etc.) was given in Chapter 1.

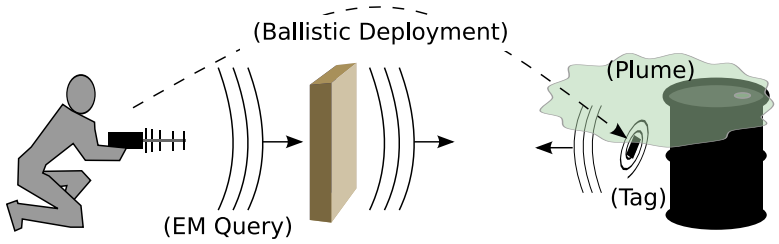


**Figure 6.1:** Conceptual illustration of the antenna-coupled SAW tag in a stand-off detection scenario.

This method contrasts with other remote chemical sensing techniques, including several lidar approaches, which integrate effects occuring over the propagation path, rather than providing point detection[1]. A significant advantage for the antenna-coupled passive sensors is relative insensitivity to atmospheric properties (RF versus optical), allowing the chemical transduction to take place *at the antenna*.

Although it is not the focus of this chapter, we briefly consider a *wireless* scenario,

[1]We note that a recent technique described by Furstenberg, et al. at the U.S. Naval Research Laboratory reveals how interfacial chemistry may be used to accomplish point detection in an all-electromagnetic (optical) approach [29].

including wave reflections both within and external to the device. Due to a range-scaling effect illustrated in Figure 6.2, the primary electromagnetic clutter from both near and far reflectors can be removed by time gating (removing the approximate interval $0 < t < 1\ \mu$s). Clutter multipath effects can be reduced by time-gating the measured pulse response. In

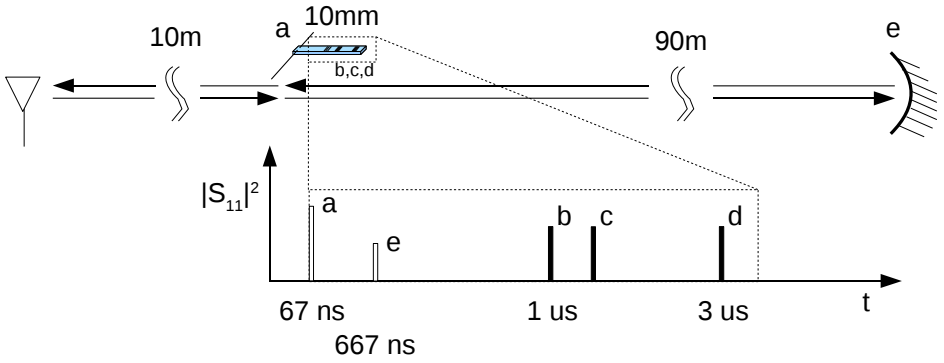


**Figure 6.2:** Diagram of time response scaling due to acoustic velocity $10^{-5}\ c$.

both wired and wireless systems, the early reflections are due to electromagnetic reflection, whereas the later arrivals are assumed to include acoustic propagation within the device. The efficacy of this technique depends upon sensor design, because sensors with great return loss may not stand out against the weak electromagnetic reflections from great distances. For instance, the $r^{-4}$ law of radar return power implies that a device having 40 dB return loss (at the terminals) allows 1/10 the readout range of a lossless device.

We recognize the conventional electromagnetic radar problem has been thoroughly investigated. Our focus is in the sub-problem occurring within the SAW device. As mentioned in Chapter 1, SAW devices have long been used in radar units to compress pulses and to filter signals. This is because high order linear system transfer functions can be constructed with impulse responses several microseconds in duration and at frequencies into the gigahertz range. As we will discuss, the information density in these devices is primarily limited by lithographic resolution and precision micro and nano fabrication processes.

In this chapter, we:

- Consider the radar problem *within* the SAW passive sensor
- Compare dispersive SAW sensors to conventional SAW sensors ($Q$, etc.)

- Review conventional dispersive SAW designs (weak scattering)
- Demonstrate acoustic/RF dispersion design for *chemical* selectivity
- Discuss Doppler-like perturbations and compute cuts of the ambiguity function
- Compute the device-constrained limit of detection

## *6.2 Propagation in SAW Tags*

The high material quality and low propagation velocity of SAW substrates allows storage of a lengthy and nearly arbitrary RF impulse response in a relatively small package. This property was very successfully applied in the 1970's to produce filters, compressors, etc., and has sustained their popularity into the 21st century - in the midst of a modern revolution of digital signal processing.

The type of SAW filter considered in this study is the reflective delay line device, essentially a one-port filter. The linear response may be completely characterized by the ratio of the complex-valued backward and forward waves at the electrical input port as a function of frequency. Although the associated electromagnetic scattering parameter ($S_{11}$) could be computed in terms of the acoustic field variables, we are interested in the action of the device to modulate and reflect electromagnetic energy. In this work, we consider the electrical response of devices at the transducer interface: the two electrodes to which an antenna can be connected. In the following computations, we assume conventional SAW design, weak reflection, and transmission line theory assuming scalar wave propagation, i.e. abstracting away the details of of the mode type, incident and scattered fields, etc. Using a full coupling-of-modes approach in conjunction with FEM or other field solutions, one may compute first-order parameters for use in the following work[2].

To obtain the device transfer function, the individual block responses must be applied twice; once as the energy passes into the device and once again after reflection. A block diagram is given in Figure 6.3. Although the delay paths may be sequential as in (a), linear superposition is helpful when waves reflected multiple times can be ignored (b).

[2] An example is the assumption of linear frequency dispersion of the SAW reflection coefficient of a single reflector, as given in (6.11).

The reflection response consists of a sinusoidal variation weighted by a frequency domain

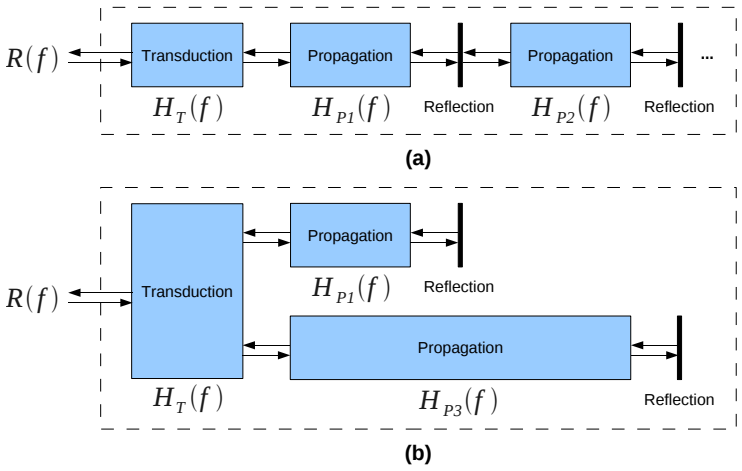


**Figure 6.3:** Diagram of component transfer functions comprising the reflection response, $R(f)$, for a SAW delay line sensor. Serial paths in (a) may be approximately superposed as in (b).

envelope given by $H^2(f)$. Calculations for a device having a perfect (although unrealizable) broadband transducer ($H(f) = 1$) and three distinct gratings of varying separation are shown in Figure 6.4.

The sharp ripple in the power spectrum is due to the shifted delta functions in the impulse response. The Fourier transform of the shifted delta functions is the complex exponential, so the reflection frequency response becomes, for an ideal transducer with response $H_{\mathrm{T,ideal}}(f)$ :

$$R(f) = [H_{\mathrm{T,ideal}}(f) = 1] \left[ e^{j \frac{2\pi f}{v_{\mathrm{SAW}}} \Delta x_1} + e^{j \frac{2\pi f}{v_{\mathrm{SAW}}} \Delta x_2} + \ldots \right] , \tag{6.1}$$

allowing addition of other distinctly delayed reflections at distances $\Delta x_i$ in place of the ellipsis (...). In actual devices the broadband modulations imparted by the distributed reflectors are band limited by the transducer response, which effectively serves as a spectral window function. The broadband *sinc* behavior observed in Figure 6.4 is due to the short length of a reflector; each consists of just a few metal strips (square window or 'top-hat' weight function applied to an impulse train (Shah function or Dirac comb) in the time domain).

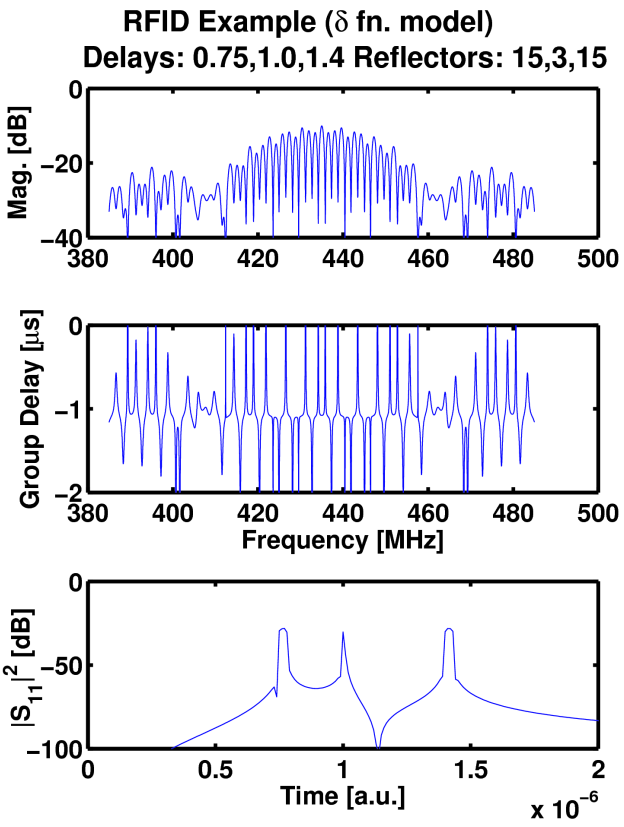


**Figure 6.4:** Frequency responses and impulse response for three grating reflectors. An ideal broadband transducer was assumed, and the reflector array lengths were (15, 3, 15 strips) as indicated. Multiply-reflected waves were assumed negligible.

In the bottom panel of Figure 6.4, there is a notable absence of electromagnetic reflections before 0.5 $\mu$s. Experimentally, significant energy is found in that region, but it is not present in purely acoustic computations.

### 6.2.1 Narrowband vs. Broadband

We have discussed the response of a broadband device, but passive reflection mode SAW tags have been reported with narrowband and broadband responses. A review paper by A. Pohl discusses the merits and trade-offs of each [78].

The major disadvantage of conventional narrowband (resonator) devices is their inherently narrow bandwidth - and the implied inability to report information - as we shall discuss. One could gang together multiple resonator devices with different center frequencies, achieving space and frequency multiplexing of the acoustic energy (dispersion). In

fact, this has been reported [23].

The common theme among such devices is the dispersion of the signal, whether it is spread in time, space, frequency, or some combination of these. One exemplary capability of a passive acoustic reflector device is the ability to precisely reverse the phase slope of a transmitted chirp several microseconds in duration. To accomplish this with a passive electromagnetic delay line device would require it to be hundreds of meters long, depending upon the relative dielectric constant. A diagram of what others have demonstrated using an acoustic device is shown in Figure 6.5 [76]. Chirp reversal represents a transformation uncommon in typical environments and so this characteristic was applied as a matched filter for some SAW tags.

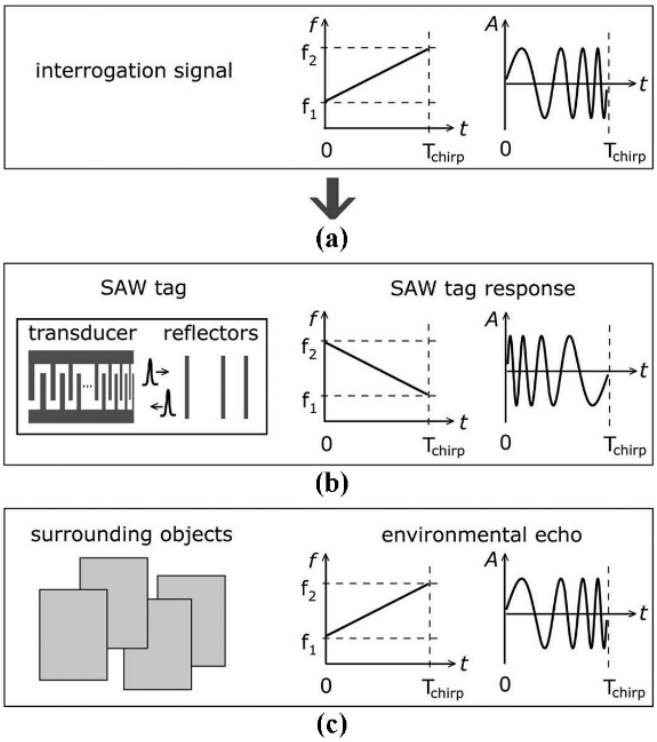


**Figure 6.5:** Ultra-wideband use of a SAW tag to reverse the phase slope, helping to differentiate its response from typical environmental echoes (image: Plessky et al. [76]).

### 6.2.2 Quality factor

Most reported acoustic wave gravimetric sensors are narrowband resonators or delay lines that are operated in the feedback loop of an oscillator. Thus the measurand (oscillation

frequency) is very sensitive to the *phase* (Barkhausen criterion; loop gain $1\angle 0°$).

A "sharper" resonance has a greater phase slope $d\phi/d\omega$, and its frequency power spectrum peak is more sharply defined, allowing greater frequency tracking precision. Statistically, the frequency variance is reduced, so there is greater probability of measuring the mean frequency; the error rate for tracking of the mean frequency is reduced.

The fractional bandwidth of a resonant (narrowband) sensor is often extracted from the frequency spectrum in a figure of merit called "quality factor," $Q$, which is inversely proportional to the damping coefficient. A very common definition of quality factor in electrical engineering is: $Q = \frac{f_0}{\Delta f}$, which is clearly proportional to the resonant frequency, $f_0$, and inversely proportional to the half-power bandwidth $\Delta f$; it is the inverse fractional bandwidth of a single resonance.

In acoustic devices, the material quality factor, $Q_{\mathrm{m}}$, serves as the upper bound on $Q$ in otherwise perfect devices. The limiting quantity is the material absorption. Impurities, surface defects, viscosity, etc. cause acoustic waves to lose energy to other modes. In spectroscopy, a common sensing scheme across disciplines, the $Q$ of a spectral line is proportional to its characteristic energy and inversely proportional to the line broadening.

In many optical and acoustic sensors, the integration of small perturbations over a very long propagation path (according to Beer's law) is utilized to detect minute quantities of a substance. However, one may notice that a given path length may be attained by either repeated reflections across a short distance or by a single transit over a very large distance (Figure 6.6).

The energy distributions of the cavity resonator and delay line are approximately spatial duals; both store acoustic energy, but the former compresses the energy in space and the latter spreads the energy in space. Both configurations of SAW resonator (Figure 6.6) have been employed in oscillator loops for frequency control and for sensing.

We can choose one energy distribution over the other depending upon the quantity we wish to sense. For our gas sensing application, an integrated measurement over a greater surface area should be more robust in at least two ways: (a) random deposition of particulate matter is less likely to critically affect device operation as when a particle lands within a

**(a)** SAW delay line **(b)** SAW cavity resonator

**Figure 6.6:** Schematic comparison of SAW cavity and delay line resonators.

microcavity, and (b) high energy density associated with a cavity resonator can excite material nonlinearities, e.g. hysteretic loss, in a plastic sensing film.

### 6.2.3 Equivalent quality factors

For a narrowband acoustic wave sensor, regardless whether it is a delay line or a cavity, the $Q$ is the most commonly cited figure of merit. Typically $Q$ will be given for delay lines and resonators independently and using different equations, but we will emphasize that at least two forms are equivalent:

$$Q_{\mathrm{C}} = \frac{f_0}{\Delta f} \text{ and } Q_{\mathrm{DL}} = 2\pi f_0 \Delta\tau \ . \tag{6.2}$$

These two definitions simply employ dual representations of the spectral width: $\Delta f$. The impulse response is the Fourier transform dual of the frequency response, such that the scaling theorem implies a reciprocal relationship of the spectral width, $\Delta f$, and the delay spread, $\Delta\tau$:

$$\frac{1}{\Delta f} \iff \Delta\tau \ . \tag{6.3}$$

Therefore, there exist appropriate equivalent definitions of the variables $\Delta f$ and $\Delta\tau$ in (6.2). The factor of $2\pi$ appearing in (6.2) is found in most definitions of $Q$ for delay lines [78, 80]. The appropriate factor depends upon the definition of spread in each domain.

For frequency dispersive sensors, a center frequency and spread may be difficult to unambiguously define according to different shapes of non-Gaussian spectra (refer to Figure 6.4). In fact, for large duration bandwidth products, spectra increasingly depart from normal distribution; it is common practice to report over-unity fractional bandwidths according to a different definition [93]: $f_h/f_l$, rather than $2(f_h - f_l)/(f_h + f_l)$ as in the (inverse) definition

of $Q_C$. The challenge becomes the problem of equivalent widths: the appropriate measure of width varies by signal and by application.

Borrowing from common practice in the characterization of wireless channels, we suggest use of RMS values wherever comparisons must be made. For example, we may work with an acoustic device response as a wireless channel although the device is intentionally designed rather than stochastic. To handle such general responses, one may use the RMS delay spread [20]:

$$\Delta\tau = \sqrt{\sigma_\tau^2} = \sqrt{\overline{\tau^2} - (\overline{\tau})^2}\ ,\ \overline{\tau^n} = \frac{\int_{-\infty}^{+\infty} \tau^n S(\tau)\, d\tau}{\int_{-\infty}^{+\infty} S(\tau)\, d\tau}\ , \tag{6.4}$$

where $S$ is the delay spectrum (e.g. the energy profile of the device impulse response, $|h(t)|^2$).

Using this measure, we compute $\Delta\tau$ and $Q$ for the response of a delay line sensor device that we used for ozone measurements (Figure 6.7). Without removal of the early reflection

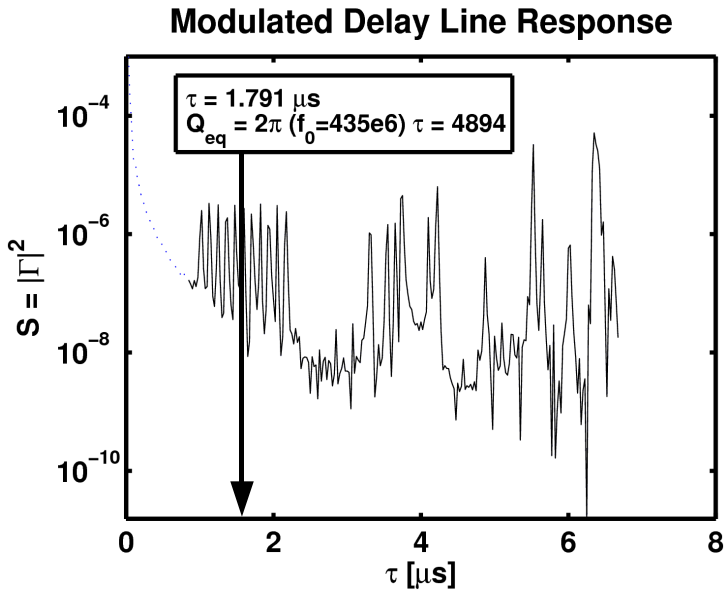


**Figure 6.7:** Response of a delay line sensor and determination of its equivalent quality factor by way of the RMS delay spread.

(presumed electromagnetic), the calculated $Q$ was 450. Thus we have bounds on the $Q$ within roughly a factor of ten, 450 to 4894. This measurement would best be conducted

with an electrically matched device, i.e. terminating the electromagnetic reflections at the 50 Ohm interconnect, such that the acoustic components dominate. It would also help to measure a "blank" response, still using the transducer but without any acoustic reflections. Rather than gating, this frequency response then can be divided out (deconvolved) from the subsequent measurements before calculation of the RMS width. Thus in this section we have shown a general calculation for an equivalent quality factor that is applicable to modulated delay line sensors, and we have shown a way for further improvement.

### 6.2.4 Information and Quality Factor in Design

The signal from a high $Q$ resonator consists of a nearly perfect sine wave that would be entirely defined by its variation over any single period, except for a very small modulation (e.g. damping). In communications terms, the period of the characteristic repeating component can be defined as the bit interval: $T_b = 1/f_b$. Then $Q$ is a measure of the *gross bit rate* ($f_b = f_0$, bits/s) divided by the *entropy rate* ($B = \Delta f$, bits/s). Accordingly, $Q$ may be interpreted:

$$Q = \frac{f_b}{B} \ , \tag{6.5}$$

and we see that, so defined, $Q$ corresponds to the temporal *redundancy* of a given signal: maximized when the gross rate is high and when the rate of introduction of information is low. Although this $Q$ is unitless, as expected, we note that it is composed as the ratio of an absolute rate to a relative rate.

The material quality factor quoted for materials is defined by an absorption coefficient of exponential decay in either time ($\alpha_t$) or space ($\alpha_x$),

$$Q = \frac{\omega}{2\alpha_t} \ = \ \frac{\omega}{2\alpha_x v_\mathrm{p}} \ , \tag{6.6}$$

where $v_\mathrm{p}$ is the acoustic phase velocity [83]. We do not distinguish phase and group velocities when the attenuation is constant. According to the relationship between information and $Q$, we see that $\alpha$ represents either a temporal bit rate ($\alpha_t$), or a spatial bit rate[3] ($\alpha_x$). By the spatial definition using $\alpha_x$, we see that a low material quality factor corresponds to a

[3]It may be instructive to think of spatial *bit density*, [$\mathrm{m}^{-1}$]

large amount of parasitic information stored in a material. For example, one may consider the spatial density of crystal defects, grain boundaries, or other unknown degrees of freedom as contributing to the lumped attenuation parameter for wave propagation in the medium. Indeed wave propagation in a general material may be modeled using transmission line theory. We reviewed the transfer matrix technique in Chapter 2, and we will employ it later in this chapter but for materials assumed to have high bulk material $Q$.

If we wish to create a certain device response within a maximum spectral spread, then we allow ($B = \Delta f = \alpha_t/\pi$) into which the material absorption and designed (encoded) absorption sum:

$$\alpha_{t,\max} \geq \alpha_{x,\text{material}} v_\text{p} + \alpha_{t,\text{design}} \ . \tag{6.7}$$

Naturally, a large material absorption limits the amount of information a designer can embed in the material per unit distance when the total bit rate or bandwidth is held at a maximum.

We would like to know the number of bits of information we can encode in a reflection response. If we assume a material of high quality (as discussed in another section) and use binary phase coding by offset of each reflector, then for bit (reflector) $N$, the transmitted wave reaching bit $N+1$ has power $1-|\Gamma|^2$ relative to the previous bit, $N$. Thus the normalized return power $R_N$ from the $N$th bit is:

$$R_N \approx \left(1-|\Gamma|^2\right)^{2(N-1)} |\Gamma|^2 \ . \tag{6.8}$$

We have assumed no triply reflected waves, an approximation best made when $|\Gamma|$ is small. The equation otherwise is expected to hold for a reflection coefficient, $|\Gamma|$, regardless the type of scatterer but while mode conversion is small. For small $|\Gamma|^2$ we have $R_N \propto |\Gamma|^2$ and the higher order terms are negligible. As noted on page 382 of [62], the reflectivity may be large on high coupling substrates, making multiple reflections significant. This limits the number of bits that may be encoded with at least a given return power ($R_N$). As Figure 6.8 demonstrates, for small $|\Gamma|$ it may not be possible to encode any bits providing at least a certain $R_N$, e.g. $R_N > -35$ dB when $|\Gamma| = 0.01$. For large $|\Gamma|$ there is very uneven distribution of energy among bits. On lithium niobate, the reflection coefficient of a single

shorted bi-finger metal strip reflector approaches 0.1, so SAW tag devices in the literature typically achieve greater $|\Gamma|$, when desired, by increasing the number of strips per bit[4].

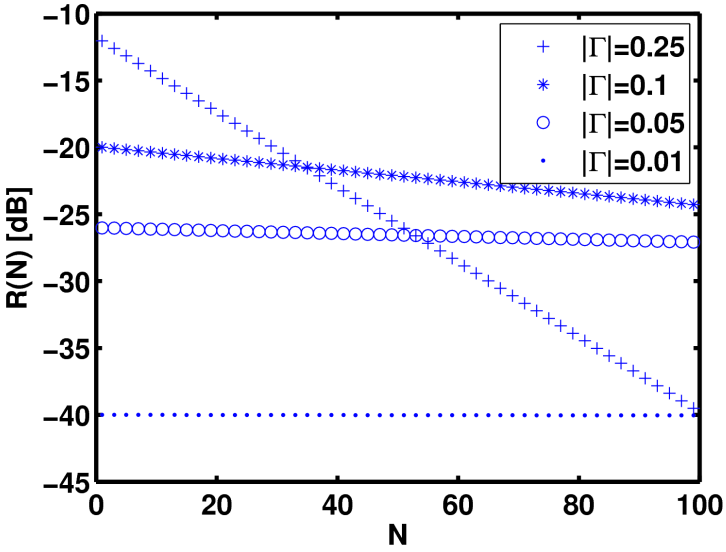


**Figure 6.8:** Dependence of power reflected from the $N$th bit of an array depends upon the magnitude of the reflection coefficient per bit, $|\Gamma|$.

We note that many of the second order effects, such as multiple reflections, are not necessarily as detrimental in design of passive tag devices as in historical filter design. SAW filter designers were required to meet many difficult specifications, but for a tag to be used in a matched filter application, the matched devices need only have suitable and identical characteristics. For instance, the temporal spread of multiply-reflected energy in one device serves as a "rake receiver" in the conjugate device.

### 6.2.5 Laboratory Measurement

Considering typical laboratory measurements in the context of radar, the VNA serves as a sort of monostatic FM-CW device. For a lengthy frequency sweep time, the measurement is nearly CW at each frequency. The figure of merit for the performance of the system could be specified in terms of the time bandwidth product, where $T$ and $B$ are the sweep time

[4]One may increase the number of consecutive strips per bit to increase the reflection coefficient while keeping the bulk scattering small. This is commonly used in the on-off keying found in SAW tag sensors.

and frequency span specified via the front panel, respectively[5].

The resolution of the frequency spectrum is inversely proportional to the duration ($T$) of the measurement, whereas the resolution of the time data is inversely proportional to the bandwidth ($B$). Therefore, as is well-known in the field, to increase the time *and* frequency precision simultaneously, one must increase the time bandwidth product. A VNA with infinite data storage capacity would be preferred, but in practice, the frequency span is sampled by a finite number of points (e.g. at most 1601 points for the HP8753X VNAs). For the TBs encountered in this work, the spectral sampling of the VNA over a single calibration range was sufficient. When required, however, it is possible to: (a) enable interpolation over a 1601 point calibration, such that multiple 1601 point sub-spans can be measured *within* the calibration bandwidth, or (b) measure and recalibrate over multiple frequency spans to construct a larger dataset. The latter, (b), would be preferred but requires much more effort. Recent programmable network analyzers (PNAs) contain much more memory and faster processors such that calibrations and measurements may be performed over many thousands of points. In this work high speed personal computers with gigabytes of memory were available, enabling us to at least *calculate* the responses with excellent precision; we give the results in subsequent sections.

### *6.3 Dispersive SAW tags*

When wireless channel characteristics external to a device preclude the use of a high-$Q$ response, engineers may turn to dispersive designs. Before passive SAW tag sensors existed, SAW pulse compressors were used to both spread and despread radar signals in both time and frequency.

One could just use a compressive radar to read out the reflective sensors, assuming sufficient mutual bandwidth of the antenna, matching network, and sensor (including a transducer, etc.). This would improve the resolution for ranging of the internal acoustic reflectors without need for dispersive device design. However, as was already mentioned,

[5]This analogy is not exactly correct, because the VNA actually divides the frequency span into a number of "bins" (often 1601) and measures an IF bandwidth at each bin. Hence the sampled bandwidth may be much less than the frequency span.

devices with TB $> 1$ can be used to provide processing gain with respect to undesirable wireless channel characteristics, e.g. chirp reversal to reduce the effect of typical multipath reflections.

Since at least 2002, many patents have been issued for frequency dispersive SAW tag sensors, by both conventional chirp and coding techniques [21, 22, 58], and even by ganging together multiple narrowband resonators at different frequencies [23, 24]. We now review some of the approaches to disperse SAW signals.

### 6.3.1 Discrete Delays

SAW tag sensors typically include several reflectors for identification and a set of three reflectors used to resolve phase ambiguity in temperature measurement [81, 49]. This simple pulse reflection scheme could be called on-off keying or pulse position coding, and it is typical of manufacturable SAW tag sensors [78, 76, 54]. While this approach does assist with the sensing problem, the compression is small. We apply the pulse position coding technique for multiplexed ozone sensing in Chapter 7.

### 6.3.2 Chirps

We briefly review the frequency response of a chirped grating reflector. In the interest of simulating a realizable filter, the spatial variation was interpolated on a discrete grid corresponding to a mask process allowing $\Delta x$ of just 0.1 $\mu$m. An upward chirped reflector array is shown in Figure 6.9. The ordinate, $v_r(t)$ in the figure, corresponds to the relative velocity as a function of time within the array. This factors into the value of the velocity used to produce each transfer matrix of the cascade:

$$v(t) = v_0 - v_r(t)\frac{\Delta v}{2} \ . \tag{6.9}$$

The logarithmic abscissa in the figure is used only to emphasize the change of scale since the chirp rate is low. The square edged time series corresponds to the binary representation of the chirp for implementation as a surface relief grating. The spatial sampling is 0.1 $\mu$m, and the minimum dimension is greater than 1 $\mu$m, allowing reproduction with a reasonably

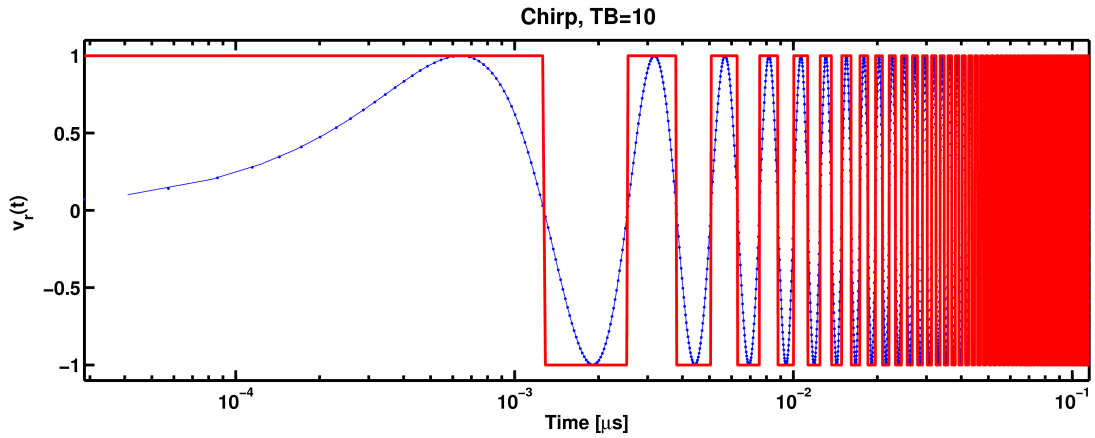


**Figure 6.9:** Upward chirped reflector array with TB=10. Regions of relatively higher and lower wave velocity alternate. A logarithmic abscissa emphasizes the change of scale.

priced photomask. Ideally this response would also be apodized, e.g. amplitude tapered, to improve the peak-to-sidelobe ratio upon correlation.

In Figure 6.10 we show ideal computed responses for a linear chirp with target values: TB = 10, T = 117 ns. We first computed the array approximating the chirp, as in Figure 6.9. Second, a series of transfer matrices were constructed to match the array. Third, the frequency response of the $S_{11}$ scattering parameter was computed (Figure 6.10a), and finally the complex $S_{11}(f)$ was inverted by a windowed Fourier transform to produce the band limited impulse response (Figure 6.10b). The procedure is outlined in Figure 6.11.

Next we evaluated the actual reflected TB, considering the fabrication tolerances, computation method, etc. Application of the RMS spread on the *amplitudes* of both series gave T = 28.5 ns, B = 93.48 MHz, and TB = 2.66. The desired bandwidth was obtained, but the time spread was not. The lithographic constraints and the need for response apodization by amplitude tapering are two reasons we investigate synchronous gratings having discrete phase codes in the next section.

### 6.3.3 Codes

We next show two the of many ways in which the reflection may be encoded (Figure 6.12).

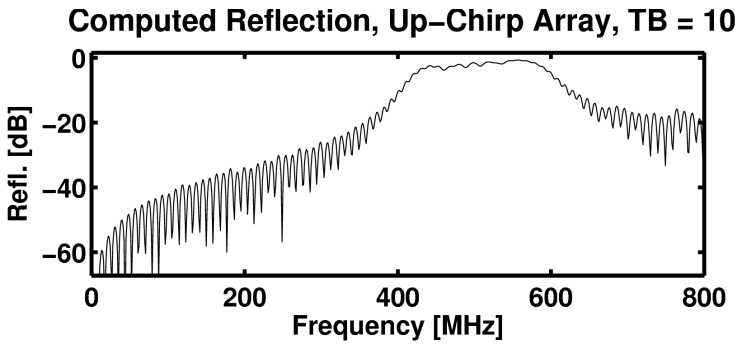


**(a)** Frequency response

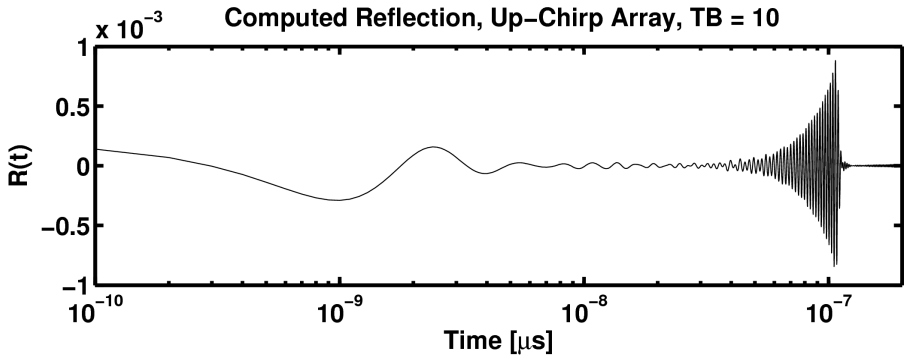


**(b)** Time response (Band limited: 10 MHz to 600 MHz)

**Figure 6.10:** Calculated frequency response and band limited temporal response for upward chirped reflector. Note the amplitude nonuniformity in both panels due to greater spatial density of reflectors at the end of the chirp.

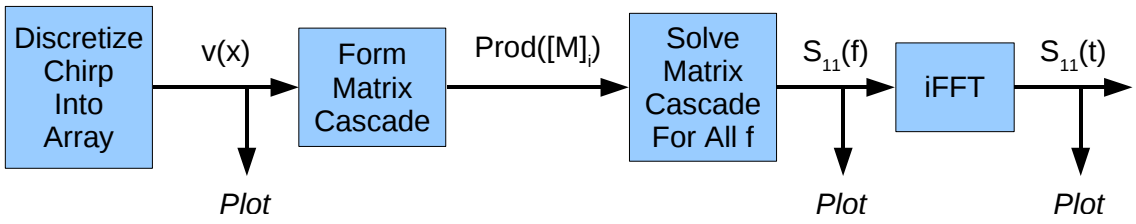


**Figure 6.11:** Outline of the operations required to produce the responses in Figure 6.10.

This scheme for amplitude modulation, by variation of the acoustic aperture, is practically limited by diffraction; small scatterers diffract energy laterally[6]. It is also possible to alter the reflection coefficient amplitude (and phase) of a strip reflector by altering its thickness, as described in Chapter 2. Despite the feasibility of these approaches, it has been

[6]Dithering the positions of the reflectors across the aperture can help improve amplitude and phase uniformity among reflectors, but this does not reduce the loss [62]

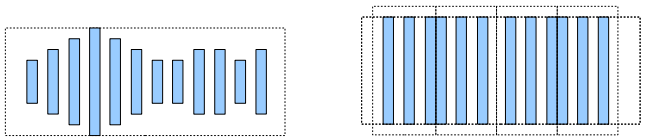

**(a)** amplitude modulation (4 levels: 2 bits/symbol)

**(b)** phase modulation (180°: 1 bit/symbol, 3 chips/symbol)

**Figure 6.12:** Structures for temporal modulation of the magnitude and phase.

reported that the discrimination of amplitudes is typically inferior to phase for systems subjected to a wireless channel [80]. We note that the SAW devices produce synchronous responses yielding reflections with precise relative phases.

The given scheme for phase modulation is practically limited by the lithography: the phase may be varied in smaller increments, e.g. 90° as in QPSK. These tradeoffs again assume a maximum device dimension, either in aperture (width), or propagation distance (length).

The BPSK phase modulation of Figure 6.12b includes redundancy: three subunits comprise each illustrated symbol block. This comes at a cost of increased device length, but it increases symbol energy and the probability a receiver will determine a symbol correctly. In direct sequence code division multiple access (DS-CDMA) systems, and in the SAW literature, the subunits of each symbol (depicted in triplicate within Figure 6.12b) are often called "chips." However, in such applications, the chips are arranged into pseudonoise codes to further spread the signal. For instance, Barker-13 codes (13 chips per symbol) may be used; these are the maximum length true Barker codes. The 22.3 dB compressed peak-to-sidelobe ratio for these codes is insufficient for practical radars (must have low clutter and target densities), and so longer codes are desired.

Next we demonstrate use of the reflection grating to achieve a broad bandwidth using a Barker-13 code for BPSK. For a given magnitude of the reflection coefficient per reflector, a greater number of reflectors can be used to encode and return otherwise wasted, i.e. unreflected, energy. For instance, one may use a much longer code. We adopt a multiscale or "nested" scheme to extend beyond the maximum known code length (Figure 6.13). In general, this nesting approach increases the compressive power gain but does not improve

the side lobe rejection. The power gain scales as $10\log_{10}(N^M)$, where $M$ is the highest nesting level. In a once-nested (two-level) scheme, $N^M = 13^2 = 169$, so a compressive gain of 11 dB may be achieved relative to the maximum length "true" Barker code ($N = 13$, $M = 1$) [15, p. 308].

The spreading factor, which indicates the relative spread of the power spectrum, is given by the chip rate divided by symbol rate, or chips per symbol:

$$\text{SF} = \frac{\text{chip rate}}{\text{symbol rate}} \left[\frac{\text{chips}}{\text{symbol}}\right] . \tag{6.10}$$

A spreading code, SF $> 1$, may *not* be singly periodic, e.g. a simple alternating sequence having the same chip rate and symbol rate. This indicates, as could be expected, that traditional Bragg reflectors or conventional PxC band gap structures do not serve to spread a signal without introduction of defects; information[7].

Figure 6.14 shows frequency responses for two different arrays of phase shifted grooves on $LiNbO_3$. The transfer matrix method was applied (as in Chapter 2), using the known approximation of the reflection coefficient on lithium niobate for a given groove depth [62]:

$$\Gamma = Chf/v , \tag{6.11}$$

where $C = 0.33$ for Y-Z lithium niobate, $h$ is the groove depth, and $f$ is the frequency, and $v$ is the SAW velocity (3488 m/s). The latter three variables form the familiar quantity $h/\lambda$ discussed in Chapter 2. We chose to explore grooves in this part of the work due to their historical use in RAC devices, requiring less phase compensation than metal strips when high coupling substrates are used.

In the transfer matrix calculations, the desired reflection coefficient was obtained by velocity mismatch between adjoining sections. We computed the necessary deviation of the velocity from the substrate velocity, $v_0$, as in the equation:

$$\Delta v/v_0 = \frac{1 + |\Gamma|}{1 - |\Gamma|} . \tag{6.12}$$

[7]We acknowledge that the edges terminating all finite PxC reflectors break symmetry; some degree of dispersion

This follows from the equation for wave impedance ($v_{\text{ac.}} = \sqrt{c/\rho}$), when the density, $\rho$ is assumed constant, and $c$ is the stiffness. The same equation is used in electromagnetic problems where, instead of $Z_{\text{ac.}} = \rho v_{\text{ac.}}$, one has $Z_{\text{EM}} = \mu v_p$, and $\mu$ is the permeability.

Figure 6.13 shows the $N = 13 \times 13 = 169$ sequence and its amplitude normalized autocorrelation. In this example the number of reflectors, $N$, is the total number of bits forming the extended sequence. Next we give a comparison of the magnitude and phase

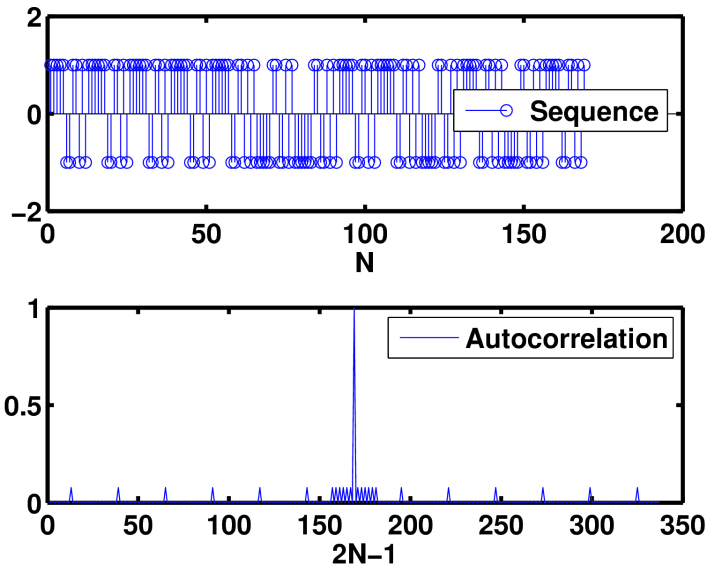


**Figure 6.13:** Recursive Barker-13 sequence and amplitude normalized autocorrelation function.

responses for the Barker-13 and recursive (N=169) reflector arrays (Figure 6.14).

We also computed the frequency and time series for the Barker grating reflection response according to the procedure of Figure 6.11. We again calculated the actual reflected TB. Application of the RMS spread on the *amplitudes* of both series gave T = 53.2 ns, B = 163.6 MHz, and TB = 8.70. The temporal spread was about twice that of the chirp, and the bandwidth was 60% greater. This design came much closer to realizing TB=10 by the RMS width calculation than the linear chirp device, yet the photolithography requirements were significantly relaxed. The minimum feature size was $\lambda/4 = 2$ $\mu$m, when $f_0 = 435$ MHz.

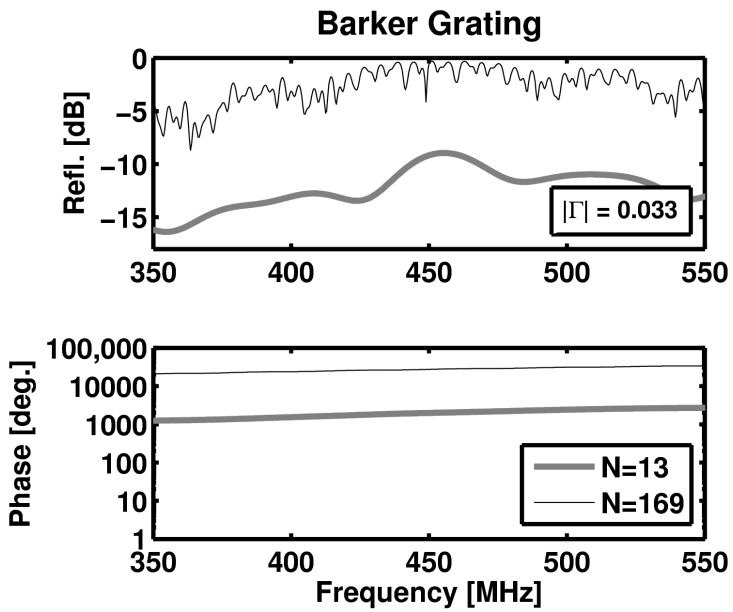


**Figure 6.14:** Frequency responses of dispersive Barker gratings. The half power bandwidth of the 169-bit nested code device is greater than 33% at 450 MHz.

It is important to mention that practical excitation and emission of the encoded reflection requires a transducer having sufficient bandwidth. For linear phase bidirectional IDTs having $\lambda/4$ spacings on YZ lithium niobate ($K^2 = 0.045$), there is a maximum intrinsic fractional bandwidth (B $< 23.6\%$) within which the insertion loss is less than 6 dB [15, p. 92]. For a bidirectional IDT on a free substrate, this is a best-case value. However, transducers need not be linear phase. One known technique is to similarly phase encode the finger positions that form the grating of an interdigital transducer; we will not revisit this approach. Instead, we now consider the utility of such dispersive responses for SAW tag sensors.

## *6.4 Compression for Sensing*

What can we do with the passively retrievable information? We recognize three main improvements to sensors through the matched filter technique of pulse compression and expansion: resolution, sensitivity, and selectivity.

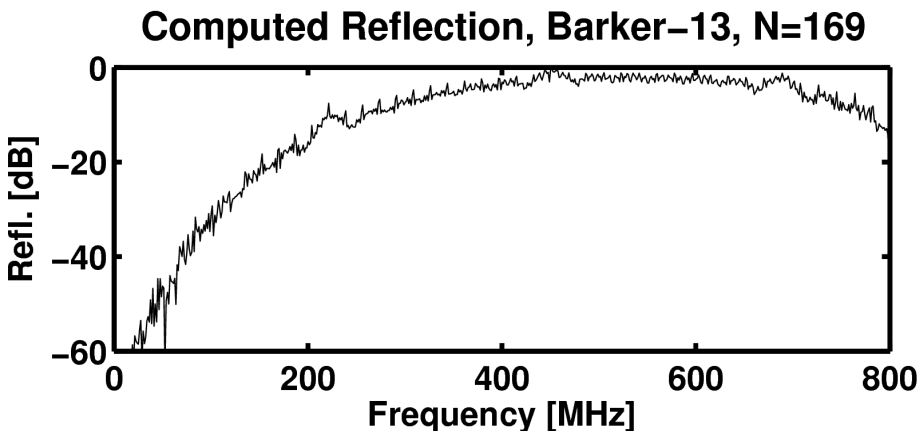


**(a)** Frequency response

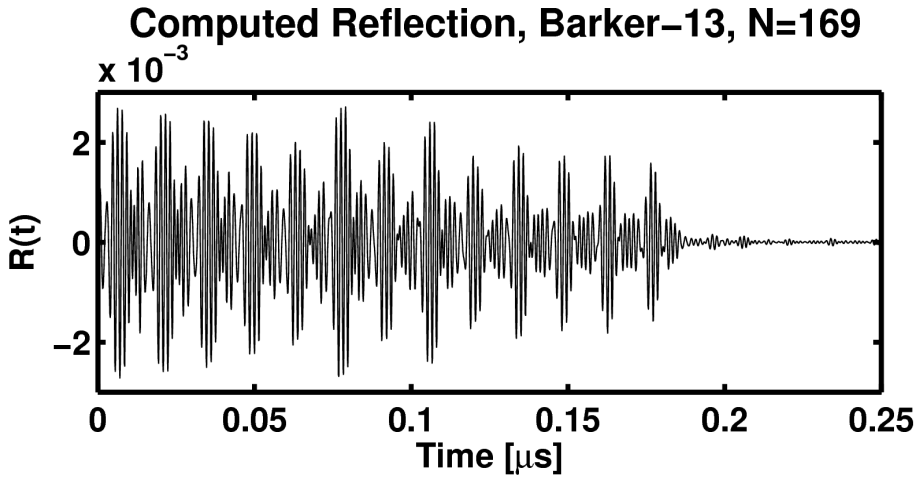


**(b)** Time response (Band limited: 10 MHz to 600 MHz)

**Figure 6.15:** Calculated frequency response and band limited temporal response for a pseudonoise grating implementing a two-scale Barker-13 code ($N = 13 \times 13 = 169$). Note the improved amplitude uniformity in both frequency and time domains when compared to the chirp results of Figure 6.10

### 6.4.1 Resolution

It is generally evident that the scaling property of the Fourier transform implies increased resolution in one domain due to decreased resolution, i.e. spread, in the other. Using the classic example, a Gaussian power spectral density with standard deviation $\Delta f$ corresponds to a Gaussian pulse in time with temporal standard deviation, $1/\Delta t$. This of course gives an uncertainty principle, which may be equivalently interpreted as the lower limit on the

time bandwidth product, TB:

$$\mathrm{TB} = \Delta t \Delta f \geq 1 \ . \tag{6.13}$$

It is therefore evident that, for a required temporal precision of measurement, there is a minimum necessary bandwidth. The benefit of TB increase can be seen in the narrowing of the autocorrelation function, as was illustrated in Figure 1.6.

### 6.4.2 Sensitivity

The improvement of sensitivity with increased TB may not be clear at first, although one is assured that more information is contained in a measurement of duration $T$. As already mentioned, both Seifert and Reindl have investigated the sensitivity enhancement obtained using compression techniques for passive SAW tag sensors. Radar techniques have in fact been employed in many other fields, including spectroscopy (V. Maslov, 1965 [60]). An important tradeoff in the field of SAW devices is found in the requirement of larger substrates in order to realize the necessary TBs of 100 or more. This assumes the lithographic minimum feature size cannot be further reduced.

To clarify the sensitivity improvement, Figure 6.16 shows the shift in chirp line due to a loading function change ($\Delta y$) [80]. At each frequency (horizontal line), a lower chirp rate (slope, $B/T$) produces a larger shift of the group delay ($\tau$) for a given $\Delta y$.

A device demonstrated by L. Reindl in 2002 employed a double-chirp reflector (Figure 6.17) that gave the temperature sensitivity data shown in Figure 6.18. The relationship for the dispersive sensitivity enhancement for double-chirp (differential compressed group delay $\Delta\tau = \tau_2 - \tau_1$) measurement is shown in (6.14):

$$S' = 2\frac{T}{B} f_0 \tag{6.14}$$

wherein $Q$ appears as the factor $f_0/B$, and $T$ is the duration, $B$ is the bandwidth, and $f_0$ is the central frequency. Thus, a narrow band of frequencies with a large delay spread is desired to enhance the delay sensitivity. This situation is the same as in (2.18) of Chapter 2.

For that reported 434 MHz device, this amounted to a 10x improvement in temperature sensitivity, i.e. 89 ppm/°C (intrinsic) vs. 889 ppm/°C (differential compressed reflections:

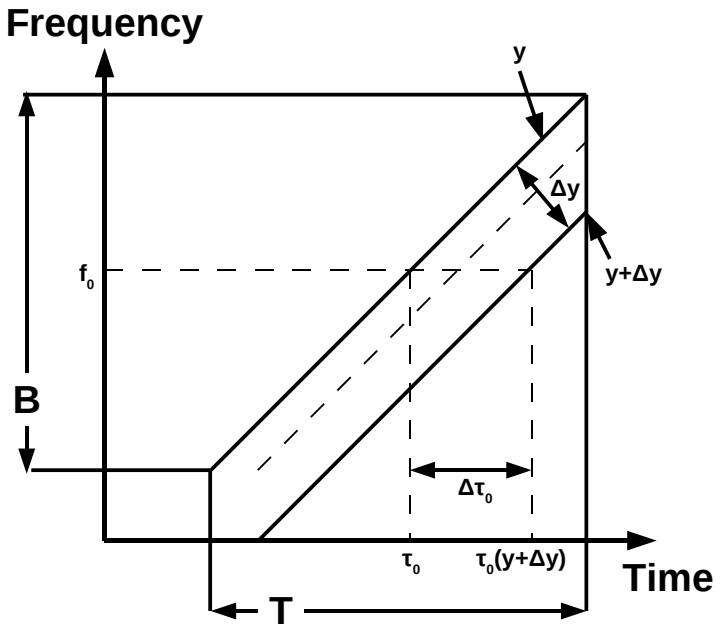


**Figure 6.16:** Time and frequency diagram for a linear up-chirp device demonstrating group delay dependence upon loading, $\Delta y$, and chirp rate, $B/T$ (diagram: Reindl et al. [80]).

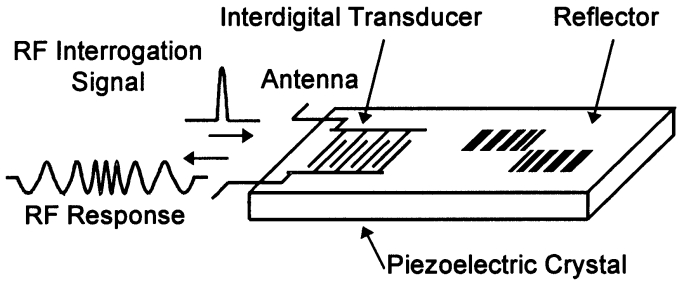


**Figure 6.17:** Double chirp SAW tag reported by Reindl et al. (image: Reindl et al. [80]).

up - down). The improvement in temperature sensitivity is an important known result because increased sensitivity to the TCD also implies increased sensitivity to other coefficients of delay, e.g. that due to ozone (Chapter 7).

### 6.4.3 Selectivity

For a passive sensor there are multiple types of selectivity and multiple ways to achieve each. In this section we will consider the chemical selectivity and its relation to design of a dispersive device. The chemical selectivity can be increased by use of multiple chemical preparations on different sensors or upon distinct regions of a single sensor. The latter

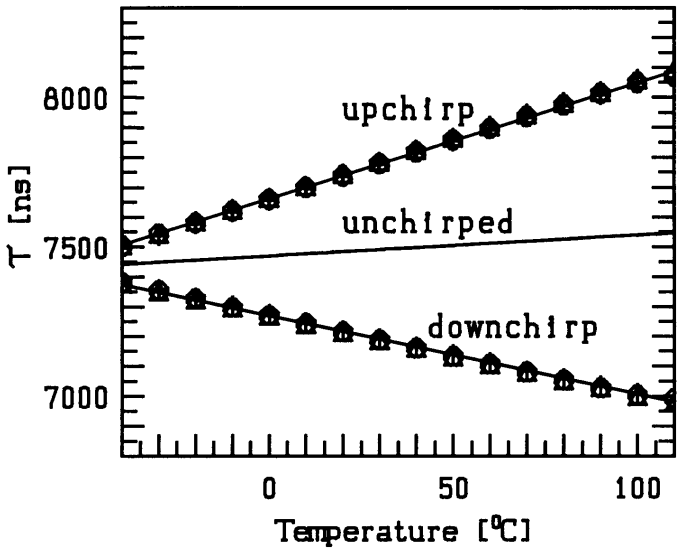


**Figure 6.18:** Group delay temperature sensitivity reported for a double-chirp compressive SAW tag sensor (image: Reindl et al. [80]).

approach is essentially a way to monitor multiple orthogonal (or semiorthogonal) chemical sensitivities by spatial multiplexing. Recently an interesting analogy has been made between the chemical detection problem using multiple semiorthogonal chemical sensors and the symbol discrimination problem in digital radio [25]. The relative responses may be compared using classification and regression techniques to pinpoint a particular chemical within a large space of possibilities.

The inherent tradeoff in passive SAW sensors is between the selectivity and sensitivity achievable for a given bandwidth and query duration, i.e. for a given TB. The communications channel may be divided into multiple subchannels of lesser resolution than might be obtained from a single distinct channel utilizing the full bandwidth for compression (Figure 6.19).

In this section we consider an upward chirped grating with nominal duration bandwidth product TB=10 (as in Figure 6.9). One way to improve *chemical* selectivity is to divide up the bandwidth according to different spatiotemporal regions. For instance, a linearly chirped grating exhibits greatest effective reflection coefficient (Bragg peak) at locations in the array linearly corresponding to the frequency. Thus, the sensitivity in a certain bandwidth corresponds to a certain region in the array. Figure 6.20 shows the change in

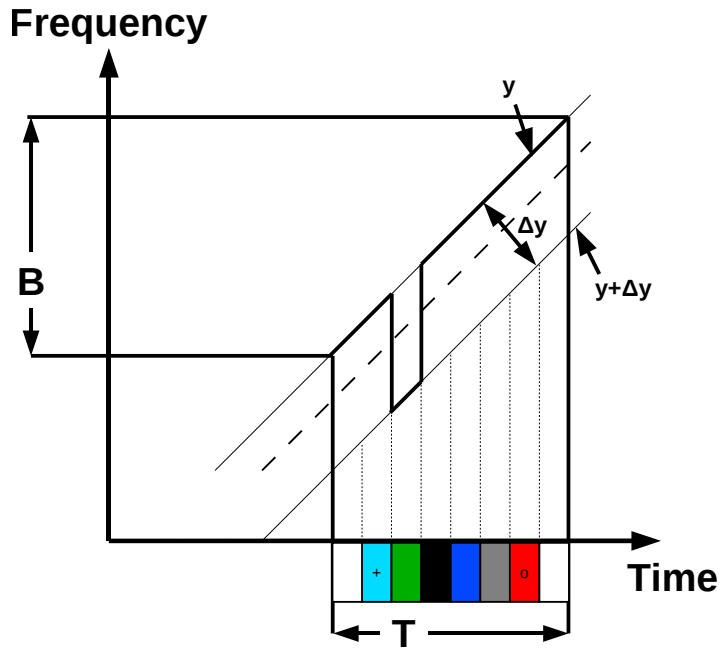


**Figure 6.19:** Time and frequency diagram for a linear up-chirp partitioned into 8 time slots, with loading $\Delta y$ applied within the third lowest frequency range.

the frequency response due velocity shift (such as that due to mass loading or temperature) within 6 of 8 regions of a linear chirp grating. The fractional slowing of the wave was large:

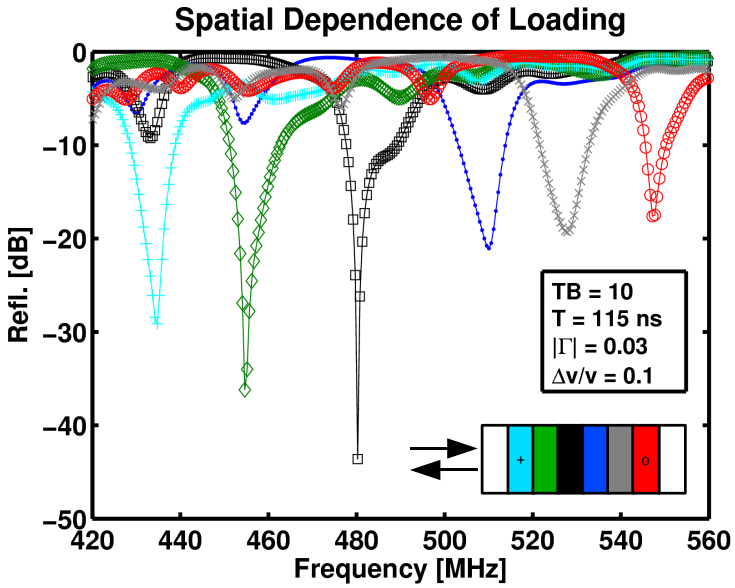


**Figure 6.20:** Computed spatial dependence of mass loading encoded in the frequency response of a linear up-chirp dispersive sensor. The reflective grating was divided into 8 sections, and a large (10%) velocity shift was applied to each independently.

0.1. The response of the perturbed section was shifted enough for its frequency region to approximately coincide with that of its neighbor (exaggerated in Figure 6.9). This much loading is generally extreme for sensing; this would correspond to approximately 1280 °C temperature shift on lithium niobate[8]. Furthermore, we considered only the linear TCD, which does not usually hold over such a large range.

We next consider several degrees of loading of a single section, as shown in Figure 6.21.

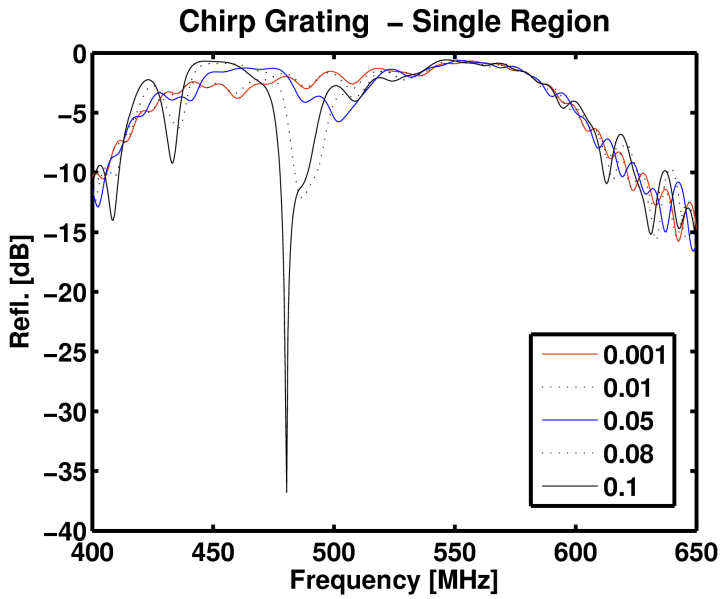


**Figure 6.21:** Trend of increased loading within a single region (legend shows $\Delta v/v$ decrease from $v_0$). The loading effect contrasts with that of a nominally resonant sensor; here increased loading forms and *narrows* a notch but still shifts it downward in frequency.

To explore a bit further, this multiplexing arrangement of the time and frequency dispersion of the signal is similar to the channelization of an allocated radio spectrum. When each channel may be perturbed independently, we would like to know the interchannel interference. After plotting a sort of eye diagram in the power spectral domain (Figure 6.22), one can see there is as much as 12 dB interference from other channels for loading in the range: $0.09 \leq \Delta v/v \leq 0.11$.

[8] Assuming the oft-quoted linear TCD would still apply to such a large change

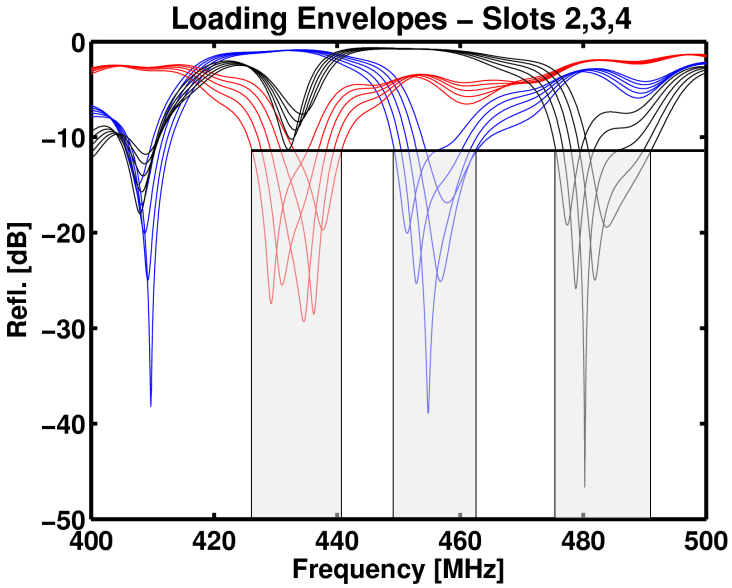


**Figure 6.22:** Spectral version of an eye diagram showing overlaid channel spreads due to loading. Channel width below the level of co-channel interference is highlighted.

The channelization approach described in this section could be used with multiple chemically selective films (one per region) to produce a more robust chemical sensor, although with a trade-off in terms of sensitivity. The grating was simulated with lithium niobate substrate material, such that the entire length was about 200 $\mu$m. This implies each of the 8 spatial regions is just 25 microns wide in the direction of propagation. Dimensions of the transverse in-plane direction (acoustic aperture) are much larger: 500 $\mu$m or greater. The 8 narrow strips could be masked by photolithography, or special pipette or dip pen techniques could be used to deposit analytical material [56].

### 6.4.4 Ambiguity

Because a matched filter is used in a compressive receiver, any modulations of the transmitted waveform due to properties of the propagation channel cause deviation from ideal conjugate match $(h(t), h^*(-t))$, and therefore, some spread in the compressed response. The ideal matched reflection response is given by the autocorrelation of the waveform from which the mainlobe and sidelobe behavior can be evaluated.

A typical occurrence of ambiguity, or spread in the autocorrelation, is due to Doppler

shift from relative movement of a "target." On a SAW device, an analogous effect occurs due to local change of the acoustic wave velocity. An ambiguity diagram then may be computed as the cross correlation of the receiver's impulse response, $h(t, \Delta v = 0)$, with its matched filter counterpart including the velocity perturbation: $h(\tau, \Delta v)$. This allows parametric evaluation of the sensor effect.

The ambiguity function, $X(t, \Delta v)$, may be plotted in two dimensions by parametric evaluation of the cross correlation:

$$X(t, \Delta v) = \int h(\tau, \Delta v) h^*(t + \tau, \Delta v = 0)\ d\tau\ . \tag{6.15}$$

In this work, we plot overlaid temporal cross sections of the two dimensional ambiguity surface for several small shifts of the SAW propagation velocity ($\Delta v$, the *effective* Doppler variable) within the sensor.

For a reflective delay line SAW sensor, an *effective* Doppler shift occurs when the temperature changes. Devices cut from the same crystal will exhibit different SAW velocities when held at different temperatures. The degree to which this occurs is specified by the TCD (usually in the low ppm range), and this coefficient is inversely proportional to the acoustic wave velocity. This effect could lead to a doubly ambiguous Doppler ambiguity if external, i.e. wireless, Doppler channel characteristics were considered.

A previous study of compression, sensitivity, and ambiguity in SAW tag sensors was conducted by Seifert in 1994 using chirped devices [87]. In 2001, Ostermayer published a study of determination of the temperature by correlation analysis of on-off key (OOK) coded sensor responses using a wavelet transform [74].

We next give some of the ambiguity cross sections for loading of chirped and Barker coded reflector gratings. The computations were performed as before, but with an additional comparison of the temporal autocorrelation and cross correlation with loading included.

Because of the linear relationship between time and frequency in the chirped reflector, the spatial mapping of loading with position occurs in both the frequency response (Figure 6.10a) and the ambiguity diagram (Figure 6.24). The single Barker-13 grating has a low TB product, and therefore will not be useful for compression in this configuration. The

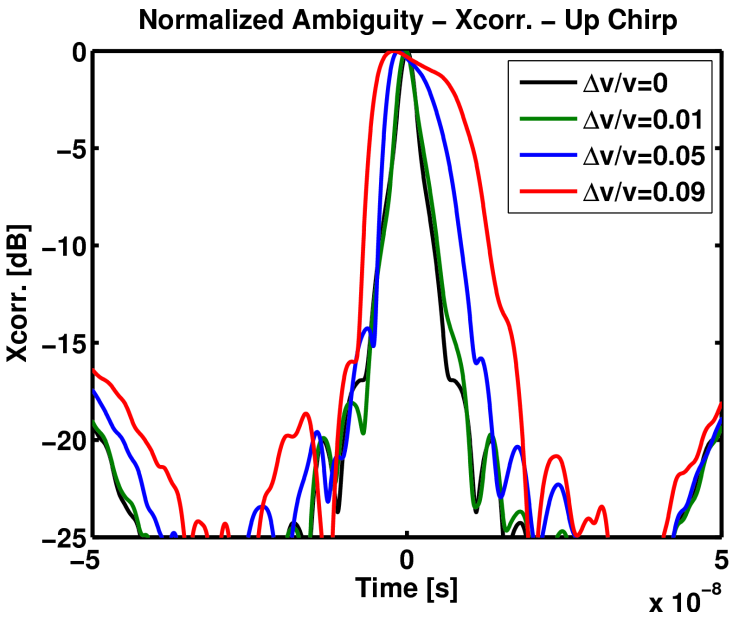


**Figure 6.23:** Cuts of the the up chirp ambiguity function for several degrees of loading applied to the entire chirped grating.

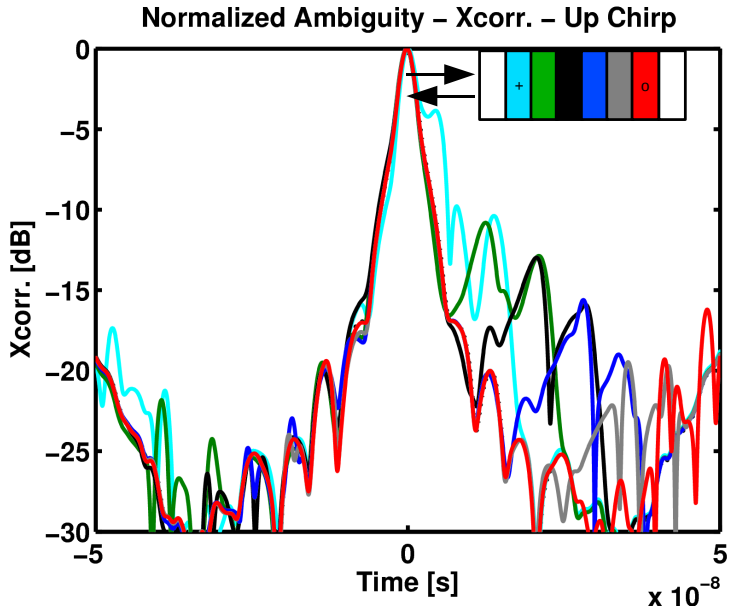


**Figure 6.24:** Ambiguity of up chirp reflection response for loading at each of several positions in the array (slots 2 through 6); $\Delta v/v = 0.02$.

ambiguity diagram is shown in Figure 6.25.

Figure 6.26 gives an example of loading across the entire recursive Barker sequence array. As with the chirped array, we also computed the effect of perturbation to a single section of

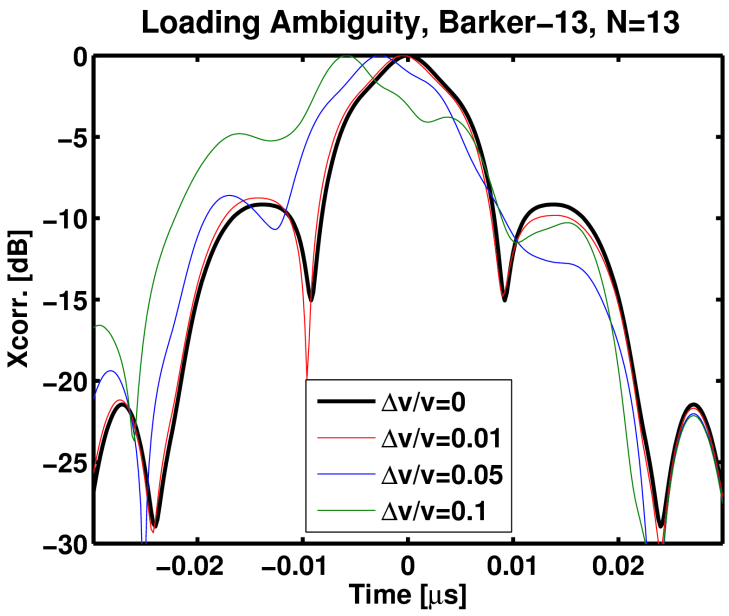


**Figure 6.25:** Ambiguity of Barker-13 reflection response with respect to loading over the entire array.

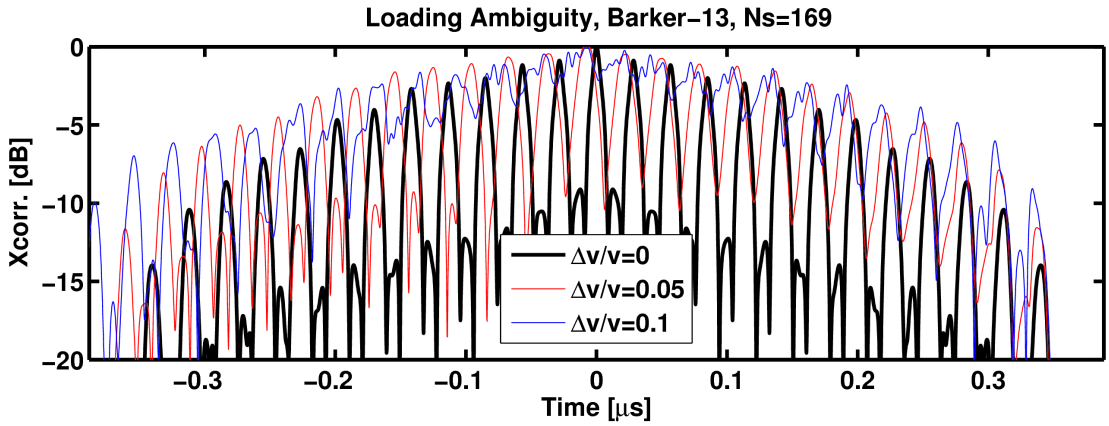


**Figure 6.26:** Ambiguity of recursive Barker-13 (Ns = 169) reflection response with respect to loading over the entire array.

the array. Due to the use of a nested code for spreading, the effect of the perturbation over a single 13 chip Barker code is spread among neighboring correlation peaks corresponding to other nested codes. We also note that the effect of multiple reflections leads to some degree of interference among codes and among chips within a code. A possible solution to improve the nested correlation properties is to fragment the acoustic aperture into 13 parallel tracks, each independently reflecting a Barker-13 code with an appropriate delay to

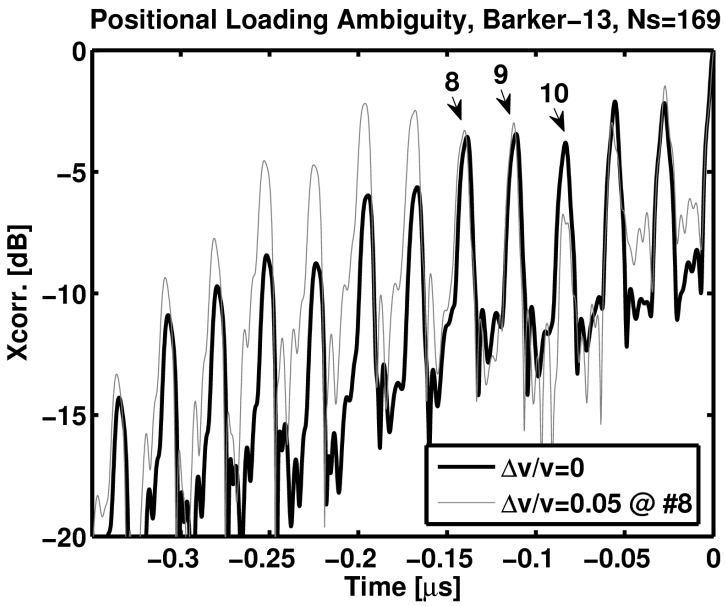


**Figure 6.27:** Ambiguity of recursive Barker-13 reflection response with respect to loading over code number 8.

construct the full 169 chip nested Barker-13 sequence by superposition at the transducer. We also note that it should be possible to form a response "library" to allow multiple software rake receivers, operating in parallel, to determine both the degree and position of loading.

As a final point regarding the ambiguity, we note that there is a classic trade-off in compression problems between mainlobe width and relative sidelobe suppression, i.e. between detectability and resolution. The design of choice for a particular application will utilize FM chirps, direct sequence spread spectrum, etc. to tailor the response for sensor requirements and environmental limitations.

### 6.4.5 Limit of Detection

We have reviewed and demonstrated the ability to enhance sensitivity or selectivity with a dispersive SAW tag sensor. We next discuss the constraining factors with respect to matched filter operation and the limit of detection of a chemical sensor.

The IUPAC (International Union of Pure and Applied Chemistry) convention for the chemical limit of detection (LOD) is the reading three standard deviations ($3\sigma_N$) from the

mean "blank" reading [67]. For background noise presumed to be Gaussian, this corresponds to the usual 1% probability that a reading beyond the LOD is attributable to the noise.

For a symmetric Lorentzian response of a simple high frequency and high $Q$ *resonant* sensor, the variance is not formally defined, so the quality factor figure of merit (6.2) is given by the full width at half maximum spread: $\Delta f_{-3\text{dB}}$. Halving this for a one-sided measure, and using the corresponding Cauchy probability distribution, we see that the $Q$ usually reported for acoustic sensors uses a more lenient measure of the frequency spread than the IUPAC detection limit: 85.2% or $\Delta f_{-3\text{dB}} \approx 1.5\sigma$. For cases in which thermal or other random Doppler broadening allows a Gaussian approximation, the half maximum frequency spread is still just $2.35\sigma$.

In sensor design, there is a best-case limit of detection due to design trade-offs and parasitic components of the device response (which may or may not be related to thermal and other noise). In other fields of research this may be called the instrument function, the response to minimum or zero input.

For dispersive sensors used with compressive filters, the best-case LOD may be determined from the autocorrelation function. For instance, if the time of arrival of the main lobe is to be tracked, then the main lobe width is the first limiting component. The autocorrelation function always attains its maximum at zero delay (peak of the main lobe) and thus the main lobe contributes to the RMS width, but the first (and subsequent) side lobes may significantly increase the effective spread depending upon their relative amplitudes.

In Table 6.1 we give several RMS delay spreads, $\Delta\tau$, calculated according to (6.2) and using (6.4). As discussed, this approach weights all data, including side lobes, so we do not report the suppression of side lobes. The corresponding LOD ($3\sigma_{\text{RMS}}$) is also provided for each row. We note that the relatively short chirp and Barker-13 sequence both give smaller RMS widths than the Barker-169 sequence.

After review of Table 6.1, the direct sequence phase coding gave the best performance in terms of TB, amplitude uniformity without apodization, and expected manufacturability. To produce the time data, significant bandwidth was required: nearly 800 MHz. In applications, this could pose challenges for the design of sufficiently broadband transducers,

**Table 6.1:** Comparison of RMS widths and limits of detection for responses in this work.

| Response Type | TB | Ref. | RMS Width | LOD |
|---|---|---|---|---|
| Linear chirp | 2.66 | Figure 6.23 | 20 ns | 60 ns |
| Barker-13 | 1.65 | Figure 6.25 | 7.8 ns | 23 ns |
| Barker-169 | 8.70 | Figure 6.26 | 170 ns | 520 ns |

or exceed space constraints, because dispersive transducer design is governed by many of the same principles as used here for reflectors. Two routes are possible when return loss is bounded: either (a) the reflector array and its accompanying transducer will grow in proportion to TB, or (b) the designer must press to smaller dimensions and higher operating frequencies requiring electron beam lithography, etc.

## *6.5 Summary*

We discussed the radar sub-problem existing within SAW tags and made comparisons to conventional SAW sensors, revisiting the equivalent quality factors for narrowband phase-tracking sensors. Next we reviewed the use of compression within SAW tag sensors, and the demonstrated sensitivity improvement. We then devised dispersive means to improve chemical selectivity by spatially multiplexing a chirped reflective delay line. Next we demonstrated the effect of the amount and position of loading upon the ambiguity function after compressive reception. Finally, we discussed the calculations for a relevant limit of detection in dispersive devices.

We remark that, although the practical challenges of passive "clutter," etc. may be mitigated by dispersive techniques, a growing challenge exists: interference from active and semi-active wideband devices. Considering increasing ubiquity of wideband devices at higher frequencies, one might expect the effective background noise to "whiten," pushing into higher frequencies. Still, as electrical energy storage density, patternable line density, and quantum efficiency increase - and new technologies such as energy harvesters become available - we may anticipate greater benefit from the efficiencies already gained through the study of truly passive devices.

In this chapter the device responses were calculated using the transfer matrix method,

assuming the validity of a transmission line model for scattering of uniform SAWs in one direction in the plane. Although narrowband SAWs exhibit very low parasitic losses in this configuration, the duration bandwidth product was primarily achieved through the temporal dispersion rather than the bandwidth. This is the usual approach in design of SAW devices, rather than use of PnCs having large frequency gaps and strong scattering. For ease of fabrication, and in preparation for more sophisticated dispersive designs, we began the experimental ozone detection work with the conventional weak scattering approach to dispersive SAW design. In the next chapter, we report the experimental evaluation of temporally dispersive SAW delay lines for ozone dosimetry.

# CHAPTER VII

# CHARACTERIZATION OF DISPERSIVE OZONE SENSORS

## *7.1 Overview*

An advantage of the radio frequency remote sensing modality is the ability to overcome environmental limitations of optical remote sensing techniques, e.g. line-of-sight obstruction, ambient weather, and solar background. We would like to bypass the chemical properties of the propagation medium and instead measure conditions local to an antenna. A small sensor "tag" may be deployed manually or ballistically and electromagnetic query signals transmitted to it. Such a tag modulates an incident RF signal with sensor and identification information and reradiates it, so for fully passive devices this reflection process requires no battery. Among radio query techniques, SAW tag[1] technology has significant range and readout advantages over fully passive semiconductor technology [34]. Although reflection mode one-port SAW filters have been demonstrated for identification and sensing, losses limit the useful range of the far-field UHF tags [78, 76]. To our knowledge, only one study of SAW tags for gas sensing (carbon dioxide) has been reported [94]. We specifically address the detection of ozone due to the existing need discussed in Chapter 1 and because the necessary equipment is available at Georgia Tech.

The broad goal of this chapter is to demonstrate and characterize detection of ozone and other relevant chemical parameters on a passive UHF band acoustic wave sensor. Arrays of discrete, wired SAW sensors have already been successfully applied in the oscillator configuration to discriminate multiple analytes in the vapor phase [30, 25]. We set out to determine whether a single passive dispersive device could support this arrayed sensing objective for ozone. Prior to this investigation we believe it was not known whether SAW devices operating in the UHF band could conclusively detect ozone using a polymer film. Furthermore,

[1]The "RFID" acronym has been used by other researchers, but we prefer to write "SAW tag" to avoid confusion with RFID standards.

the loss tradeoff and interference of confounding factors had not been investigated on the SAW platform.

On March 12, 2008 the EPA revised the national air quality standards (NAAQS), reducing the "8-hour primary ozone standard" from the 1997 level (80 ppb) to 75 ppb. Consequently we have characterized radio frequency sensors operating within this range. The RF sensor technology appears to be suitable for personal dosimetry in the workplace or production facilities, and especially for closed environments in which people work alongside electrical equipment for extended periods of time. In these situations the level and duration of exposure to ozone may create health hazards. For instance, prior studies have shown significant production and concentration of ozone (beyond OSHA threshold) in the vicinity of copy machines and electric motors, and furthermore, those researchers used acoustic wave sensors to determine the concentration [27, 12]. We identify several application areas such as industrial clean rooms, underground mines, or onboard sealed vessels such as submarines or spacecraft.

Moving toward these applications, we have simulated, fabricated, and characterized several prototype passive SAW sensors for the detection of ozone. The operating principle is essentially that of radar: an RF query signal is modulated by the presence of multiple reflectors having different apertures, phases, etc. The key difference is that the scattering of interest occurs in the acoustic domain within a one port SAW device. In this configuration, the passive sensors need no batteries and can be coupled to planar antennas making the sensors suitable for wear as exposure monitoring badges or for placement on assets. With this concept in mind, we now review the design challenges that we explore in this chapter:

- Surface functionalization with a chemically selective film, without introducing too much loss at UHF frequencies
- Determination of the ozone sensitivity and that of interferants such as temperature
- Estimation of parameters useful in personal dosimetry: saturation dose, shelf life, limit of detection, and degradation over time
- Use of the designed dispersive response (time multiplexed) to compensate for the

confounding effect of temperature

We begin by reporting our interdisciplinary work that demonstrated the feasibility of acoustic wave ozone dosimetry on SAW devices at hundreds of megahertz.

## *7.2 Proof of concept*

### 7.2.1 Reactive film

Other researchers have already demonstrated polybutadiene (PB) to be selective for ozone [27]. That study was conducted at the Danish Welding Institute, testing for ozone in the presence of complex gaseous byproducts of welding. The authors found less than 6% interference across many salient gas constituents including toluene, nitric oxide, and water vapor. Relative humidity and solvent absorption are important factors affecting acoustic properties of polymer films, so the relatively low interference makes this PB film a good choice. A typical ozonolysis reaction between an alkene and ozone is shown in Figure 7.1. A key feature is the increase of mass of alkene polymer units due to additional oxygen atoms remaining in the film after oxidation.

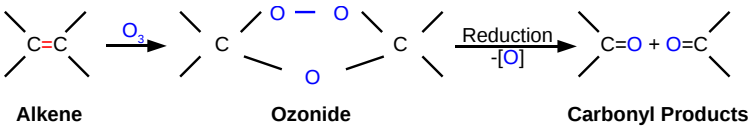


**Figure 7.1:** Ozonolysis reaction after which oxygen is incorporated at C=C bond locations.

Several secondary reactions are known to occur, depending upon environmental conditions. Neglecting these effects and possible evaporation of byproducts, we can reasonably expect the film mass to increase in response to ozone. This agrees with prior QCM results since 1985. Furthermore, the effect of an initial ozone exposure lasted for at least several days in ambient indoor conditions above 20°C. We give this result in Section 7.4.1.1. The sensor reaction, in a way similar to the polymerization process, also saturates the double bonds to form higher molecular weight molecules. Thus, there may be some change in the film viscosity. The literature indicates that cross linking and viscosity change do occur during ozone exposure [3].

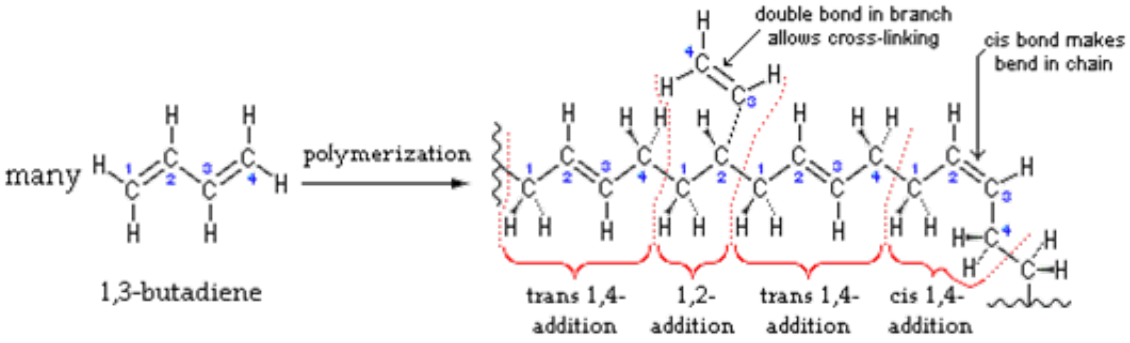


**Figure 7.2:** Constituents of polybutadiene yield one double bond per polymeric unit. (source: http://www.wikipedia.org)

### 7.2.2 Sensor preparation (functionalization)

We coated the acoustic devices with a solution of polybutadiene (PB) and toluene. PB, at approximately 4500 molecular weight (CAS No. 9003-17-2; Scientific Polymer Products #894 ), is a viscous liquid at room temperature and pressure. Dilution to less than 10 weight percent in toluene produced a suitable solution for spin coating. The PB solution was spin cast at 5600 RPM for 60 seconds. The film thickness was generally less than 500 nm on several surfaces including gold, $LiNbO_3$, and silicon. After deposition the sensors were baked at approximately 110 degrees Celsius for two hours, at which time the film was more plastic (scratch test). Though we believe baking in air promotes saturation of some sites in the film, subsequent tests still demonstrated excellent sensitivity to ozone attack. We found evidence of the expected reaction for these films in the spectroscopy data of Figure 7.3, which we reported in 2008 [98, 96].

For some experiments we masked the devices prior to coating in order to obtain reference paths for subtraction of nonspecific effects (temperature, etc.). In Figure 7.4, we show the tape mask and spinner mount for selective coating of packaged devices.

### 7.2.3 Experimental setup

We used calibrated equipment for ozone testing. The experimental setup is shown in Figure 7.5. Professor Mike Bergin of Georgia Tech provided the lab space and equipment for gas phase tests. Figure 7.5 shows the general configuration. The objective was to deliver to

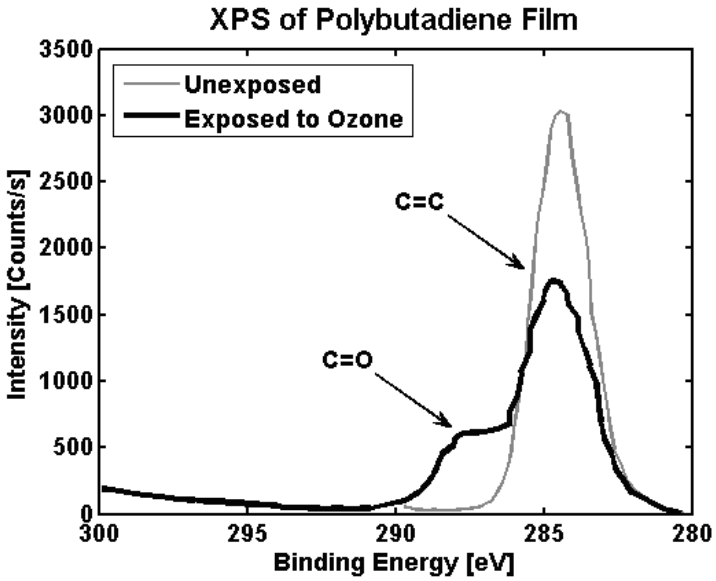


**Figure 7.3:** X-ray photoelectron spectra (XPS) of exposed and unexposed polybutadiene film. A "shoulder" is clearly visible after ozone exposure. The data were smoothed to enhance clarity.

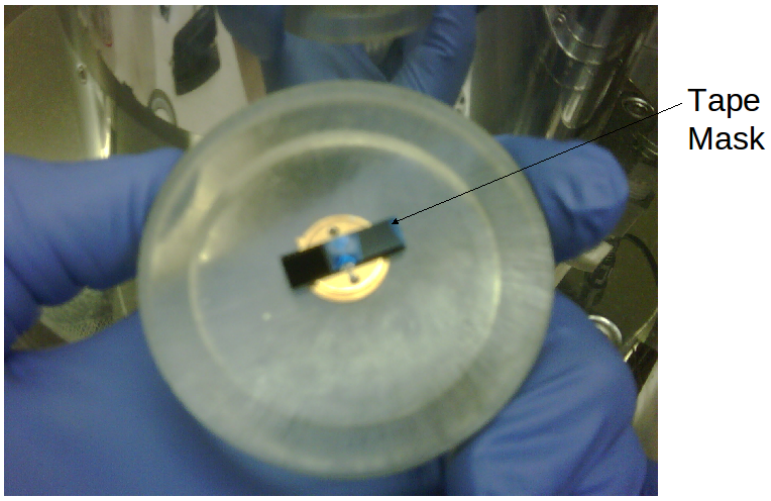


**Figure 7.4:** A tape mask covers reference delay paths during spin coating. The device is mounted on a gold plated TO-8 package with 4 leads (two of which are used).

the sensor a stream of dry room air containing no particulate matter and no significant interfering substances.

Ambient room air was drawn through a filter into a pump and delivered to the Thermo Electron Inc. ozone calibrator unit (Primary Standard) after passing through a DrieRite desiccant dryer and an activated carbon filter. The gas flow rate was 3.70 SLPM, as measured with a DryCal DC-2 flow calibrator (BIOS International). The calibrator's outlet was

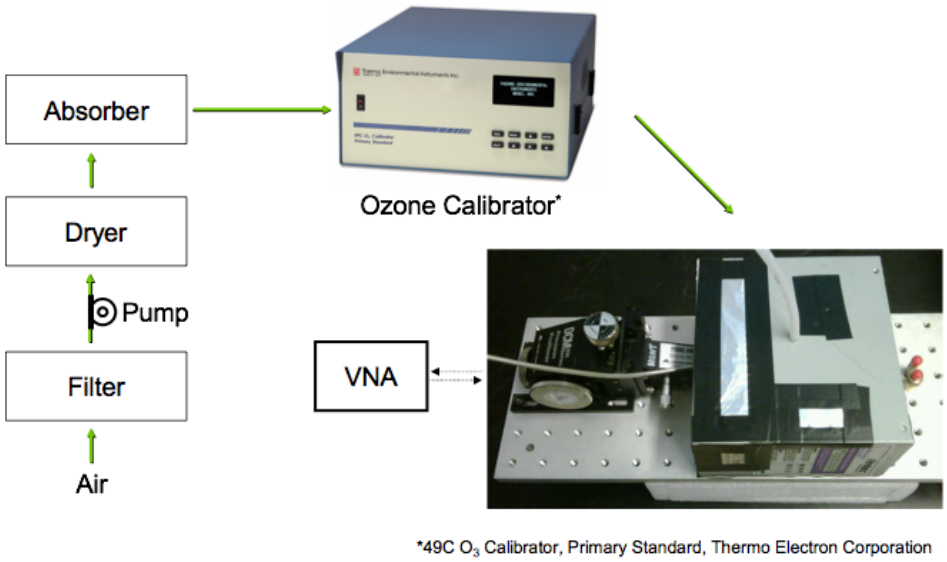


**Figure 7.5:** Diagram of the experimental setup for delivery of sample air

connected by 1/4 inch polyethylene tubing to custom-built aluminum and steel box which housed the sensor(s) and provided entry for a probe arm with calipers.

The ozone calibrator, a primary standard instrument, allowed digital entry of ozone concentration. It used ultraviolet photometry and closed loop control capability to maintain a concentration set point. A stepwise change in the concentration set point from 0 ppb to 200 ppb usually produced a rise time of less than one minute after the calibrator had warmed up (UV lamp at operating temperature). For most experiments we varied the ozone concentration in step increments between 0 and 400 ppb.

### 7.2.4 Quartz Crystal Microbalance (QCM)

In order to verify the response of the sensitive layer, we conducted trials with quartz crystal microbalance (QCM) devices. In the particular case of ozone detection, we show our results agree with those of Black, et al. [12]. We used the conventional Sauerbrey equation (1.1) to determine the effective mass of the deposited film (over the active region) on the QCM. With $f_0$=9970268 Hz, $A_c$=10 mm$^2$, $\rho_q$=2.648 g/cm$^3$, $\mu_q$=2.947·10$^{11}$ g/cm-s, and $\Delta f$=20.591 kHz, the PB mass is computed to be 82 $\mu$g. For an active area of 0.282 cm and $\rho_{\mathrm{PB}} \approx 1.3$ g/cm$^3$, the thickness is computed to be roughly 700 nm using polymer density of 1.3 g/cm$^3$. This total calculated thickness, approximately twice what was expected, is justified because

inspection revealed the QCM was coated on both sides. From Figure 7.6 we extracted

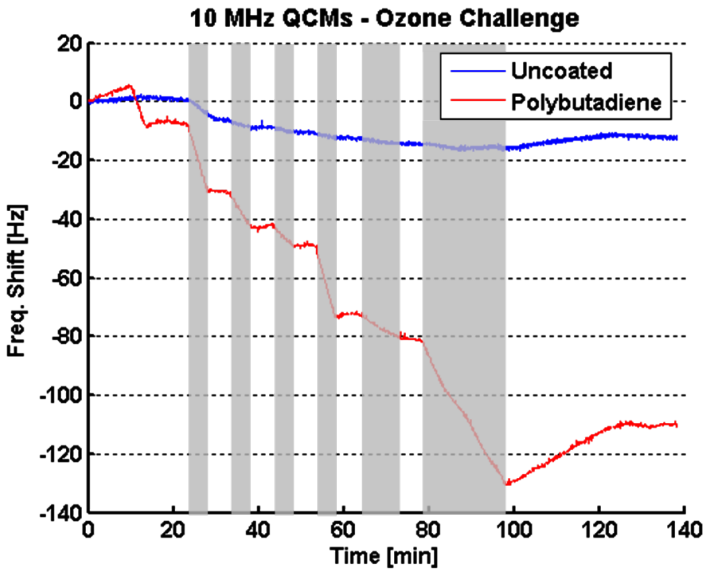


**Figure 7.6:** Comparison of QCM responses to varying durations and concentrations of ozone.

the response slopes and averaged them in cases for which the concentration was identical. This gave a response line indicating the response (Hz/min) versus ozone concentration (ppb), as in Figure 7.7. Though the linear sensitivity fit appears less suitable at the lowest

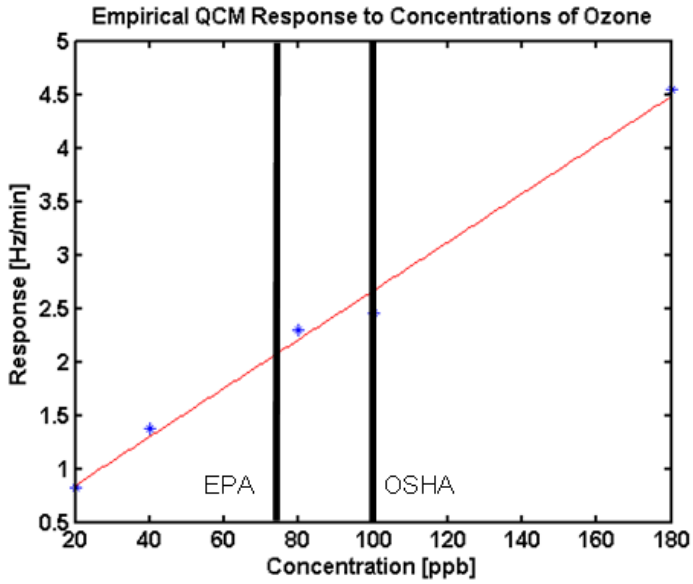


**Figure 7.7:** Dose and response curve for ozone. Vertical bars indicate the regulatory thresholds.

concentrations (non-zero intercept), it is useful well below and above the EPA and OSHA standard thresholds. We believe both the volatility of ozone and the extreme sensitivity of the acoustic wave devices enable the successful detection at such low concentrations.

We also checked the shelf life of the sensors when stored in ambient room air in a laboratory for two weeks. First we exposed both coated and uncoated 10 MHz QCM sensors to an estimated total dose of 64 ppb-hours. Then we carefully inserted the sensors into fitted metal sleeves (HC-49 package "cans;" provided with the crystals from ICM Co., Inc.). The packages were not otherwise sealed, except a rubber band was wrapped around the seated can and base to maintain contact. Sufficient gap remained for air to diffuse in and out of the cans, but the devices were effectively shielded from light. The devices were then placed in a secondary container, a clear plastic box typically used for the transport of 3-inch wafers, and this container was carried from the Ford ES&T building at Georgia Tech to lab 258 of the Petit building, where it was placed on a shelf.

After two weeks of storage, the sensors were carried back to the ES&T building, removed from the packaging, and reinstalled in the crystal monitors of the MaxTek frequency counter system. The response of the coated stored sensor is given in Figure 7.8. We plotted the extracted response slopes alongside those of the prior measurements, and we noted the sensitivity, while still approximately linear (prior to the onset of saturation), decreased by 67%. The saturation of the response became noticeable approximately one hour into the experiment, after an additional dose of approximately 64 ppb-hours (i.e. the dose does not include the exposure prior to storage). We note that the aging effect might be reduced by storage in sealed individual containers backfilled with dry nitrogen. This seems to be a reasonable packaging method for delivery of prepared sensors, such that they may be stored for a while before use. We did not investigate the effect of ambient lighting. Ultraviolet light from the fluorescent indoor lighting may have contributed to the aging of the films. We suggest opaque packaging to eliminate this possibility. When possible, we sealed and covered the sensors before use to improve the consistency of measurements.

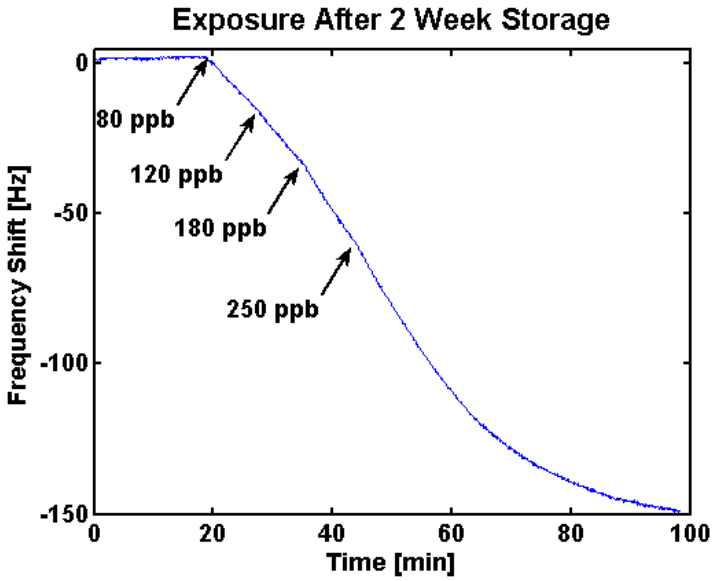


**Figure 7.8:** Response of sensor aged two weeks. Varying concentrations were applied and the sensor was allowed to approach saturation.

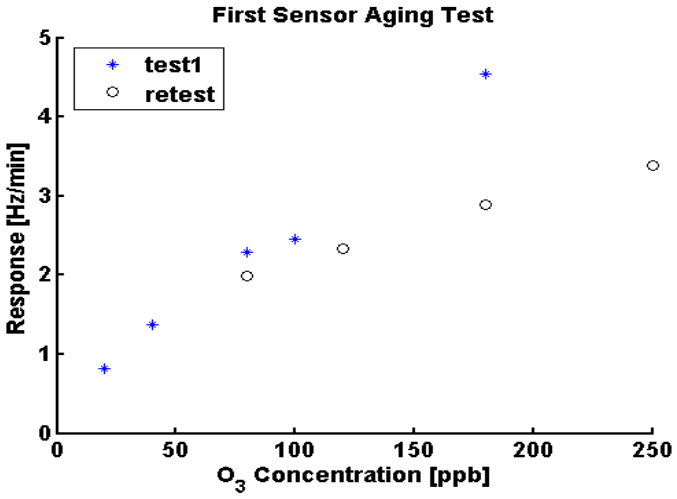


**Figure 7.9:** Sensitivity curve for sensor exposed to air for two weeks. The sensitivity (linear slope) decreased by 67%.

### 7.2.5 Surface Acoustic Wave Resonator (SAWR)

In a move toward the much higher frequency SAW tag sensors, we tested SAW resonator responses to ozone exposure. The resonators operated in a SAW PRO-250 (Microsensor Systems, Bowling Green, KY; acquired by MSA in 2005) oscillator circuit, in single sensor configuration, at 250 MHz. Though both Rayleigh and surface transverse wave (STW) sensor types were prepared, only the STW device successfully operated after coating with

the polybutadiene film. In this instance, the film was deposited by aerosol vapor coating, produced by flow of dry nitrogen through a Collison nebulizer containing the usual dilution of PB to 5% weight in toluene. Though this method worked with the STW device, the random deposition of aerosolized droplets on the device surface provided neither a more uniform nor a thinner coating than obtained in the spinning process. We abandoned the aerosol approach in favor of spin coating in the remainder of the experiments. As shown in

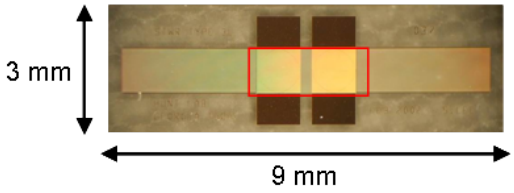


**Figure 7.10:** Photograph of the uncoated surface transverse wave (STW) resonator. The sensitive region is enclosed by a rectangle. (Device: Sang-Hun Lee [55])

Figure 7.10, the STW resonator features two electrical ports (each a set of opposing electrical pads, dark in the figure), and two long grating structures to the left and right. Between these is the cavity in which the standing surface wave is formed (illustrated rectangle). This is the active region of the device.

The STW SAW resonator experiments were conducted in the same way as the QCM experiments. A quartz device bonded to a TO-8 package was allowed to equilibrate in flowing air with 0 ppb ozone. Subsequently the ozone generator was set to various concentrations while the SAW resonance frequency and air temperature were monitored. The sensor showed distinct irreversible changes to ozone exposure. When the concentration returned to zero, the reaction appeared to cease because the resonance frequency remained nearly constant.

### 7.2.6 Comparison of QCM and SAWR

Though the QCM experiments demonstrated excellent sensitivity in the low parts per billion range, the SAW resonators gave orders of magnitude increase in sensitivity. In Figure 7.12, the responses are displayed separately due to the large difference in scales. Data for linear fits are provided. The SAW data reveal a larger spread according to the residues.

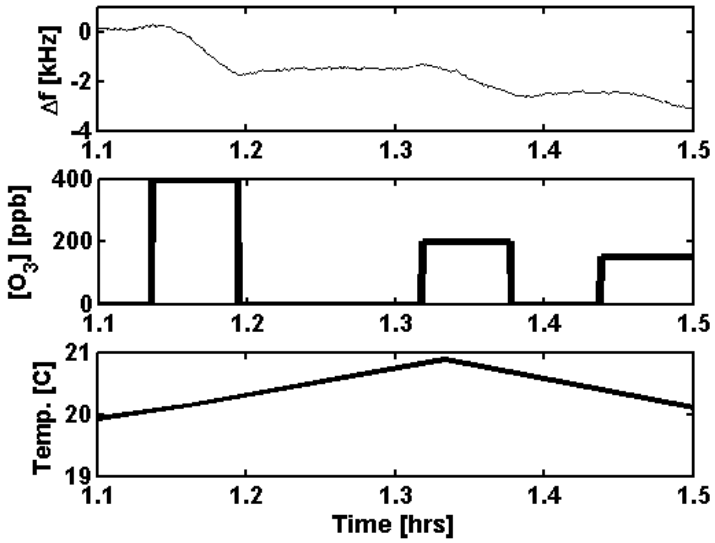


**Figure 7.11:** Response of SAW resonator to change of ozone concentration and air temperature. Top to bottom: resonance frequency shift, ozone challenges, and temperature fluctuation of at most one degree during the test.

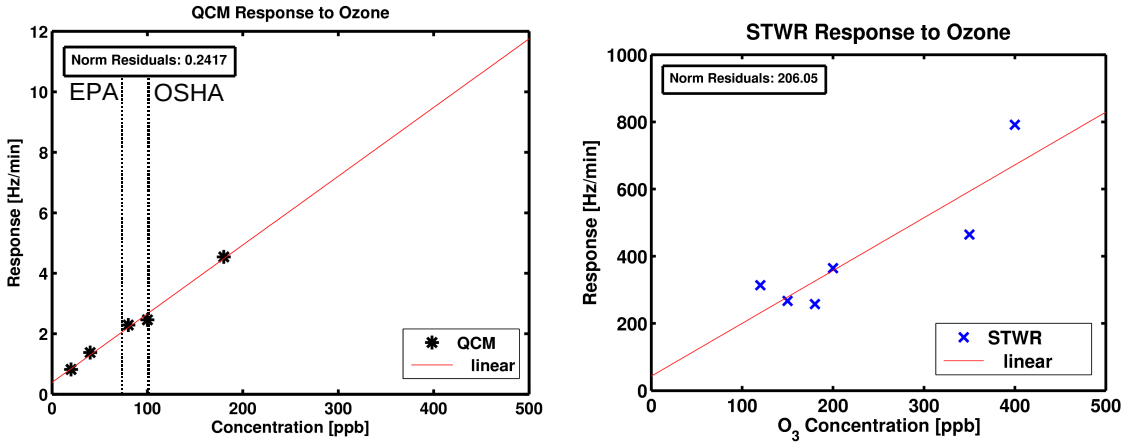


**(a)** QCM response curve (10 MHz)

**(b)** STWR response curve (250 MHz)

**Figure 7.12:** Comparison of QCM sensitvity with that of a SAW resonator.

As we have discussed, the absolute frequency change of a resonant acoustic device is proportional to the square of its center frequency, $f_0$: $\Delta f \propto \mathrm{MF} {f_0}^2$, where MF represents a mode factor depending upon the acoustic mode and film parameters such as stiffness ($\mu$). This relationship implies that the fluctuations due to temperature and other effects over the course of an experiment are greatly exaggerated at the higher operating frequency of the SAW devices. As the frequency is 25 times greater, the response deviations are expected to

be $25^2 = 625$ times greater. In fact, the norm of the residuals (square root of the sum of squares vertical deviation from the line of fit) increased by a factor of 858; Figure 7.12b vs. Figure 7.12a. Considering identical noise sources in both QCM and SAW measurements (which is not truly correct since different oscillators were used), this would imply that the constant of proportionality is also greater for the SAW device: $\mathrm{MF_{SAW}} = 1.37\mathrm{MF_{QCM}}$. The SAW device had a smaller sensitive exposed area which would further increase the relative sensitivity if we took this parameter into account.

### 7.2.7 SAW tag sensor prototypes

We have constructed several prototypes, using both conventional ultraviolet lithography and electron beam lithography. The latter was used to obtain higher operating frequencies. Both

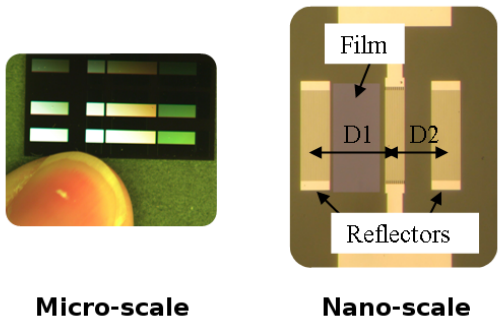


**Figure 7.13:** Two SAW devices which operate at center frequencies approximately one decade apart (220 MHz vs. 2.4 GHz).

of the devices depicted in Figure 7.13 have a center transducer structure flanked by delay paths "D1" and "D2" of varying distance. The acoustic reflectors at the lateral extremes return the acoustic signal to the transducer where it is reradiated electromagnetically a defined time after the initial stimulation. This is a simple overview of the passive SAW tag technique, which was described in Chapter 1.

In Table 7.1 we compare the dimensions and operating frequencies of devices we have fabricated in our lab. The higher frequency devices afford greater communication bandwidth and also greater sensitivity to surface perturbations. Figure 7.14 is a photograph showing a recent STW device that operates at 580 MHz (64° YX $LiNbO_3$) and features three separate signal tracks. When a signal is received, the device generates three principal reflections

**Table 7.1:** Comparison of dimension and bandwidth highlights the usual advantages of high frequency operation: small size and greater bandwidth for a given design.

| | Micro | Nano |
|---|---|---|
| Critical Dimension | 1.5 $\mu$m | 0.018 $\mu$m |
| Center Frequency | 0.25 GHz | 2.5 GHz |
| 2% Bandwidth | 5 MHz | 50 MHz |

encoded to signify the device identification, "ID," temperature, or ozone "$O_3$" concentration. The preparation and test of these devices represents an advancement beyond reports found in the literature which were not used for gas sensing [87, 54].

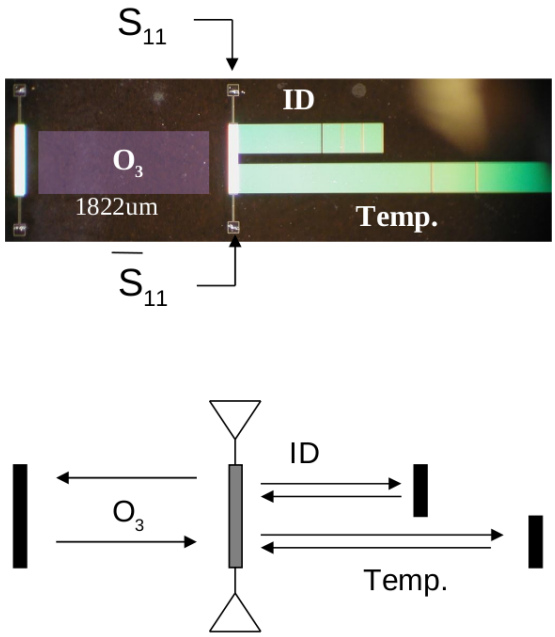


**Figure 7.14:** Optical micrograph and diagram of an STW multiplexed ozone sensor showing sensing "$O_3$," "ID," and "Temp." signal paths. Triangles signify terminals of the transducer and represent the points to which an antenna may be connected.

For most sensors, and especially the 435 MHz devices, we chose YZ-$LiNbO_3$ for the substrate due to its relatively high coupling coefficient, tolerance to misalignment, and production of conventional Rayleigh polarized modes. The coupling coefficient is approximately 4.5 %, the misalignment tolerance is approximately 6 degrees, and the Rayleigh mode suitably bears the film loading, as we show in subsequent results.

## *7.3 Characterization*

### 7.3.1 Measurement Technique

#### *7.3.1.1 Pulse Mode Measurement*

Our first measurements of the devices were conducted using a custom pulser/receiver unit. The measurement system consisted of off-the-shelf components, custom microcontroller firmware, and LabVIEW software for generation and measurement of pulses, respectively[2]. A photograph of the equipment is shown in Figure 7.15. Because of the significant acoustic delay, we took advantage of the isolation properties of an RF switch rather than a directional coupler. This is a larger version of the sort of system that would be used in the field.

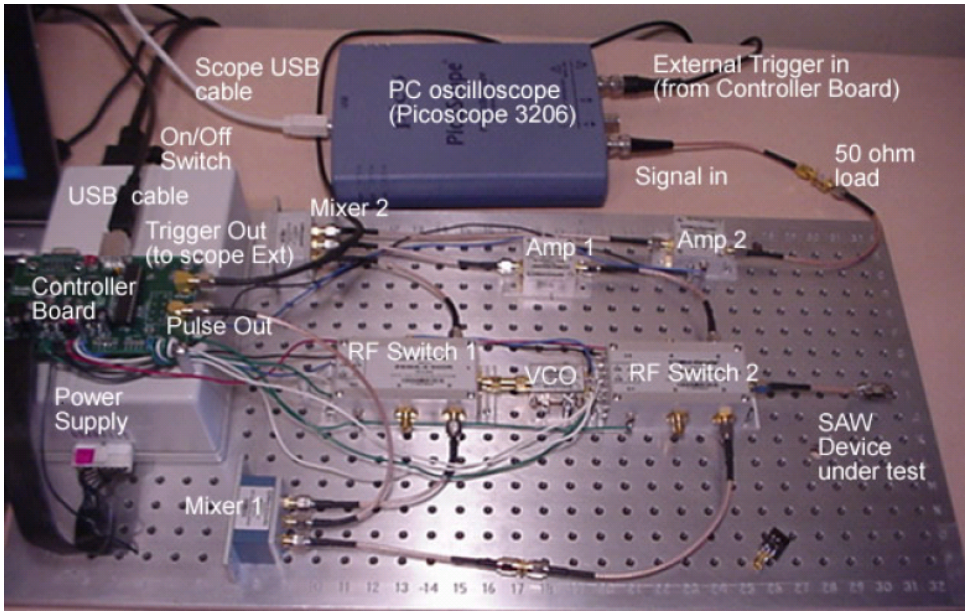


**Figure 7.15:** Pulse interrogation system utilizing commercial components and custom software.

However, for device design and characterization, we needed the full one port scattering parameters.

#### *7.3.1.2 Continuous Wave Measurement*

The majority of our experiments were conducted using a VNA to obtain calibrated S-parameter data over a programmable frequency band and with excellent sensitivity. Use

[2]Zen Sensing, LLC funded and built the system.

of the inverse Fourier transform allowed us to work with the time response as well. For laboratory testing, we preferred the flexibility and precision of this approach; the expensive equipment offered a sort of best-case assessment of device response.

We used an inverse fast Fourier transform (iFFT) to convert the complex frequency data to the time domain. We note the response obtained is a "pulse" (rather than "impulse") response because of the finite bandwidth used in the measurement and iFFT. We set the VNA frequency span wide enough to include the significant part of the transducer response; at least the main lobe and first side lobes in the frequency domain. For our 435 MHz devices, the span was 10 MHz. SOLT (short-open-load-through) calibration was performed using a GS/SG-1250 calibration kit from Cascade Microtech and using the front panel interface of the VNA. After this, the data collection ran unattended because we developed software to collect data over the IEEE-488 "GPIB" communications bus. The VNA settings and calibration were held constant throughout each experiment; the software was used only for measurement and subsequent processing.

#### *7.3.1.3 Software*

We used the LabVIEW (National Instruments) and MATLAB (MathWorks) applications to create custom software to automate data collection and processing. Because we collected full 1601 point complex S-parameter responses at 0.1 Hz, this amounted to more than 20 Megabytes of data per hour, in addition to temperature and relative humidity data. The environmental data were at first extracted from a Davis Vantage Pro 2 environmental monitoring unit inside the room (1 °C resolution as in Figure 7.11), but we opted for a small Humirel HTF3000 sensor placed inside the steel box that housed the sensor and probe assembly (the box and probe arm are shown in Figure 7.5). We implemented a lookup table in the LabVIEW software to interpolate the calibration curves for the sensors; this gave temperature resolution much better than the quoted accuracy of the sensor. The system then was able to resolve temperature fluctuations to better than 0.1 °C, and with the manufacturer's quoted absolute accuracy.

We used two HP33401A digital multimeters to measure the temperature and relative

humidity signals: resistance and frequency, respectively. These instruments were also connected by GPIB, such that all data passed through one GPIB to USB interface adapter attached to a laptop computer. The electrical instruments and laptop computer are shown in Figure 7.16.

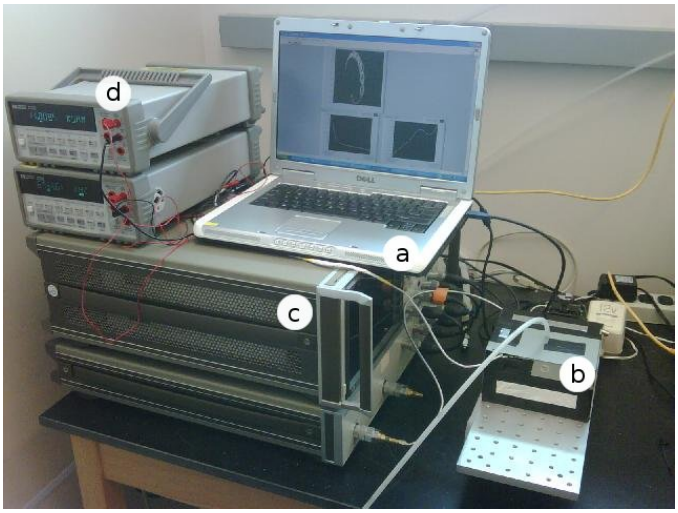


**Figure 7.16:** Photograph of the instruments used to collect the RF data and environmental fluctuations: (a) computer displaying and recording the data, (b) probe chamber, (c) VNA, (d) multimeters for temperature and relative humidity.

#### *7.3.1.4 Time domain acquisition*

The devices utilize the technique of multiply-delayed reflections of the interrogation signal to give multiplexed sensing information. This is important to separate the perturbations to each sensor. The sensor identification (ID) sequence, its temperature, and the cumulative effect of ozone attack of the sensitive film must all be returned to the interrogation unit in response to the query signal.

In a wireless application, time gating can reduce the problem of non-specific multipath, i.e. responses that never encounter the acoustic sensor. Consequently, and following common practice in passive SAW tags [78, 54], we have positioned the reflectors to achieve pulse delays greater than one microsecond after the query pulse. This corresponds to electromagnetic reflectors at free-space distances up to 150 meters away.

As a first check of the multiplexed bidirectional acoustic aperture (Figure 7.28), we conducted water loading tests using the pulse-and-receive setup of Figure 7.15. In Figure

7.17, we show how placement of deionized water on one sensor area significantly attenuates the corresponding reflection without disturbing the preceding tone bursts (to the left). The additional data eliminated to the right of the red circle is due to multiple reflections of the eliminated pulse. With computer processing, we expect the multiple images of the first reflection can also be used to improve the signal to noise ratio (SNR), as in a "rake receiver."

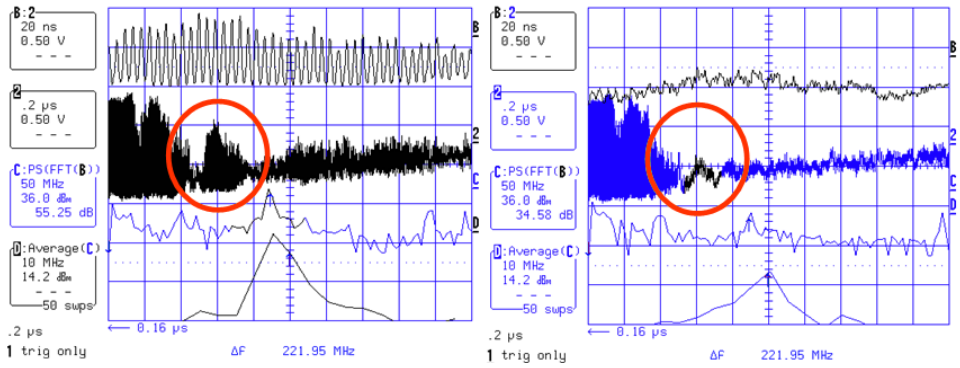


**Figure 7.17:** Space and time multiplexing demonstration allows selective attenuation of one acoustic reflection (within the red circle) without disturbing the preceding one (left of the red circle in each frame). The time span of the grid in each panel is 2 $\mu$s.

As a preliminary sensing measurement, we examined the temperature coefficient of the SAW tag devices using the pulse-and-receive setup shown in Figure 7.15. We used Cascade Microtech's air coplanar probe tips (ACP40, GS-1250) to probe SAW delay line devices on 128° YX lithium niobate, applying 220 MHz continuous wave signals modulated with an approximately square envelope of 100 ns duration. By measuring the center frequency of each return pulse (by FFT), we were able to observe the substrate temperature coefficient, in agreement with literature values: between 75 and 80 ppm/°C (Figure 7.18). This demonstrates capability to measure device changes in the ppm range, and we expect knowledge of the device temperature can also be useful for calibration of chemical sensors. We investigate the confounding effect of temperature later in this chapter. The frequency shift observed due to temperature change is attributed to the change of the acoustic velocity *within the transducer*. For these time domain tone burst measurements, the time of arrival of the pulse does indicate the temperature coefficient of delay in propagation across the substrate, but the received frequency depends upon the local wave velocity at the transducer.

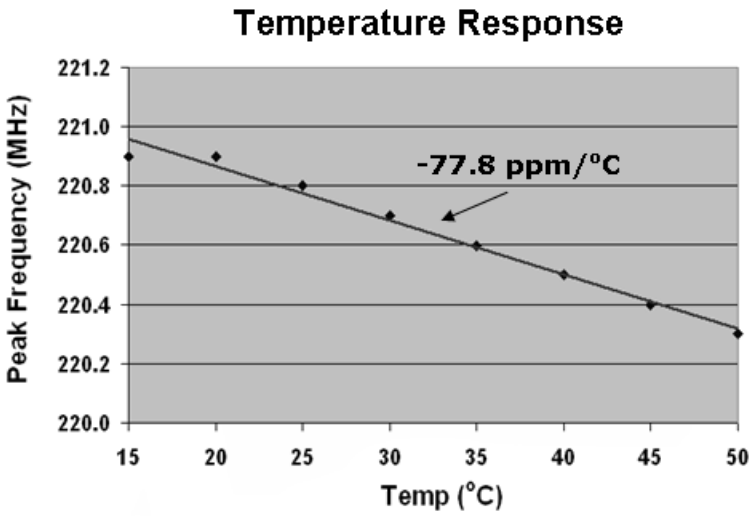


**Figure 7.18:** Measured frequency shift of received tone burst in response to temperature change. The slope (linear coefficient) is within 5% of literature values for 128° YX $LiNbO_3$.

This behavior indicates that for even a single transducer and reflector, one could distinguish temperature change of the substrate from other effects along the propagation path: measure the received center frequency ($S_T^f$, sensitivity of frequency to temperature), and measure the time of arrival ($S_T^\tau$, sensitivity of delay to temperature + loading). Such a measurement approach would require excellent frequency precision and time precision, but it allows comparison of local and accumulated effects. In the rest of this study, we have chosen to work primarily with the time of arrival, thereby measuring either the phase velocity or group velocity.

#### *7.3.1.5 Frequency domain acquisition*

We electrically characterized the SAW tag sensors to obtain the baseline scattering parameter responses prior to sensor experiments. This is a much-needed step in exploration of the needs and design constraints of passive gas sensors. The sensors we next describe use conventional one dimensional PnC reflectors, i.e. narrowband Bragg gratings, that are spatially distributed to temporally disperse the signal.

The bandwidth of the SAW tag is typically limited by the transducer design. In Figure 7.19a we compare the responses for identical devices having different transducers: ten finger pairs ($N_p = 10$) *versus* fifty finger pairs ($N_p = 50$). The transducer with $N_p = 10$ has 5

times greater bandwidth and yields sharper resolution of the reflections. This is because the fractional bandwidth for an unapodized quarter wavelength interdigital transducer (IDT) is given by $BW_{-4dB} = 100\%/N_p$ [15]. This result follows from the *sinc* frequency response that naturally results from the square windowed impulse response that is the delta function model of the transducer. The reflected power plotted in Figure 7.19a was converted to the time domain using the inverse Fourier transform. It is the band-limited "pulse" response. We use this extensively in the characterization work. The Smith chart of Figure 7.19b reveals the better overall match to 50 Ω obtained by the device having the $N_p = 50$ transducer.

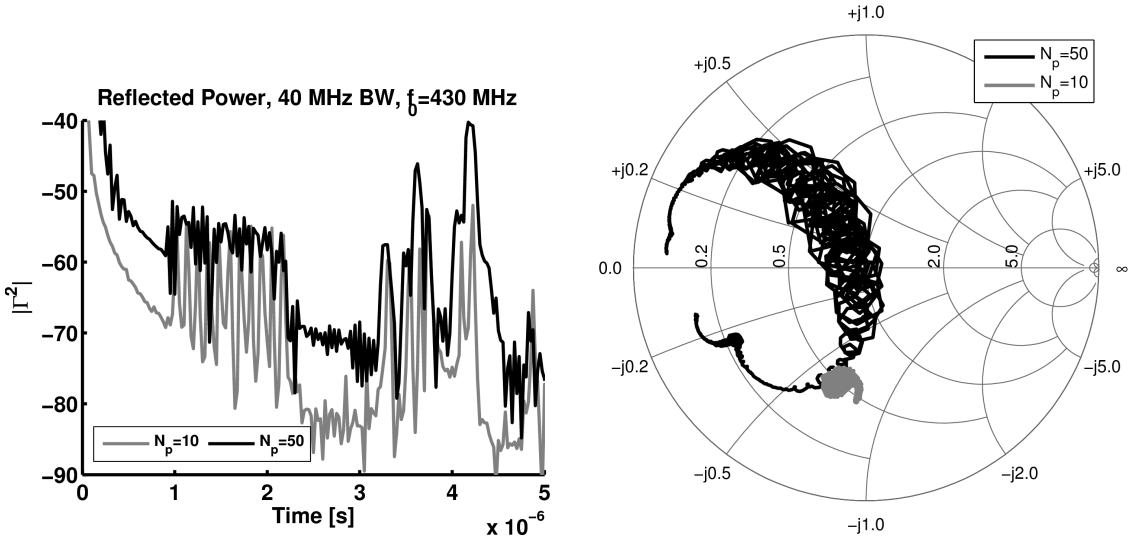


**(a)** Reflected power vs. time

**(b)** Reflection coefficient vs. frequency

**Figure 7.19:** Comparison of $S_{11}$ magnitude and Smith chart responses for two IDTs having different numbers of finger pairs ($N_p = 10$ vs. $N_p = 50$)

To compute the reflection response, each acoustic delay path may be treated as a long reflection grating with large sections of many strips removed. Therefore we applied (to good approximation) the delta function modeling technique we applied in Chapter 2. An iFFT of the frequency domain reflection response, $R(\omega)$, yields the pulse response. Figure 7.20 shows a comparison of the pulse response computed using the mask parameters (Figure 7.28) with measurements taken via VNA and inverted to the time domain. Eleven identification pulses and two groups of larger pulses for sensor measurements were included by way of 17 total reflectors.

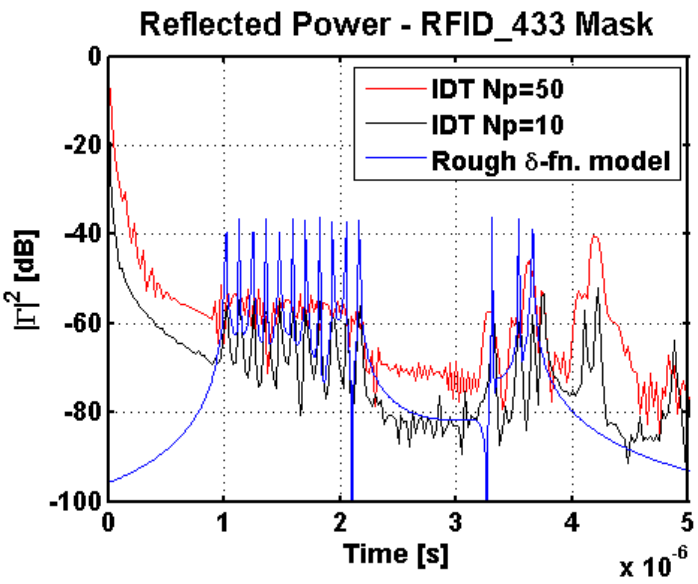


**Figure 7.20:** Comparison of measured pulse response for two physical delay line sensor devices with one simulation.

There is especially good agreement between the wider bandwidth signal ($N_p$=10) and the simulation. This is due to the improved resolution of impulse-like features with the greater transducer bandwidth, and we note both traces demonstrate device linearity and weak individual reflections, in agreement with the convolutional model. The discrepancy between the simulation and measurements at early times is because the computation does not consider electromagnetic feedthrough or acoustic regeneration effects at the transducer. Multiple reflections are not considered, and the coresponding component of the dispersion (pulse spreading) is not reproduced by the simulation.

We next show the impedance responses to better reveal the modulations with respect to frequency (Figure 7.21). Although better temporal resolution was obtained with the broadband transducer, Figure 7.21 shows the poorer 50 Ohm match and acoustic energy transfer (lower radiation resistance). The entire response in the given bandwidth gives an impedance near $Z = 27 - j32\ \Omega$. The acoustic radiation resistance, $R_a$, was about 27 Ohms, and the net capacitance, $C_0$, was about 11 pF at the center frequency, 435 MHz. These values must be considered in design of a matched antenna. For instance, 50 Ohm match may not be desired since a balanced folded dipole or similar looped planar antenna might be used. However, electrically small 50 Ohm patch antennas may be readily purchased for

this frequency band, ≈433 MHz.

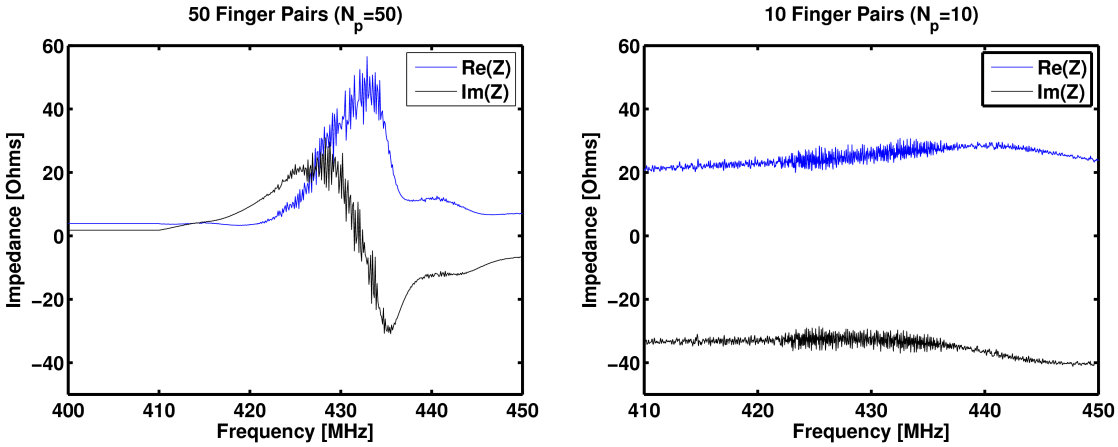


**(a)** Impedance using narrowband transducer

**(b)** Impedance using broadband transducer

**Figure 7.21:** Comparison of device impedance for two transducers: $N_p = 50$ (2% BW) *versus* $N_p = 10$ (10% BW). The narrowband transducer achieves a greater acoustic radiation resistance.

### 7.3.2 Loss Due to the Film

The preceding characterization was useful for unloaded devices, but the device response changes when the devices are loaded with a chemically sensitive film. We characterized SAW tag sensors both before and after the PB coating procedure, examining the return loss (a critical factor for passive devices). We compare the responses in Figure 7.22. The primary notch corresponds to minimum reflection, i.e. energy transfer to (and dissipation in) the structure. We note absolute reduction in energy return (more return loss) after coating, and the passband ripples are notably absent (at the lower frequency "shoulder"), implying the reflections are greatly damped.

Another way to examine this loss is in the time domain. As in Figure 7.19a, we transformed the S-parameters to the time domain such that the vertical axis corresponds to the reflected power, $|S_{11}(t)|^2$. We measured the loss due to surface functionalization consisting of a spin cast polybutadiene film on a YZ $LiNbO_3$ substrate (Figure 7.23). The thickness of the film was less than 500 nm, as determined from prior ellipsometric measurements for the same deposition protocol.

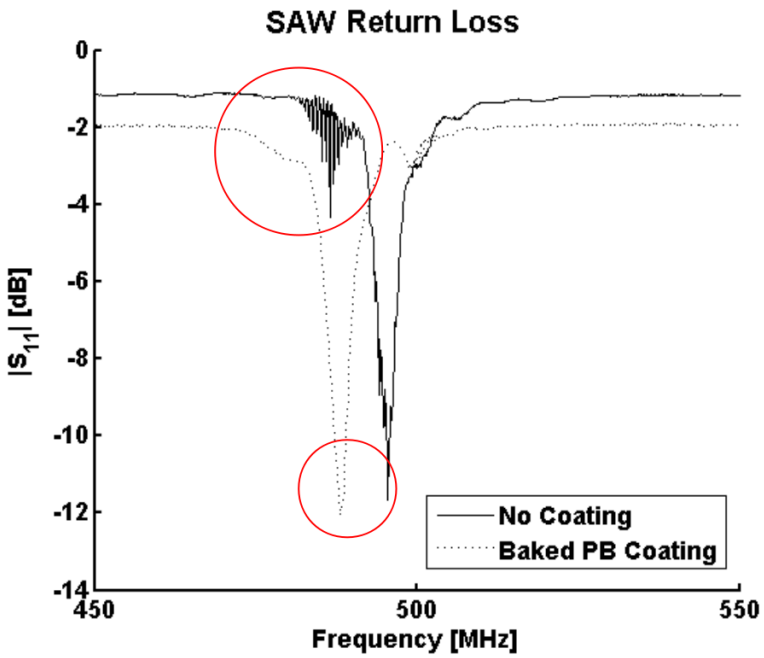


**Figure 7.22:** Frequency domain return loss for a Rayleigh mode device (128° YX $LiNbO_3$) both before and after coating with polybutadiene. The circles highlight the damped modulation (reflections) and the usual mass loading shift.

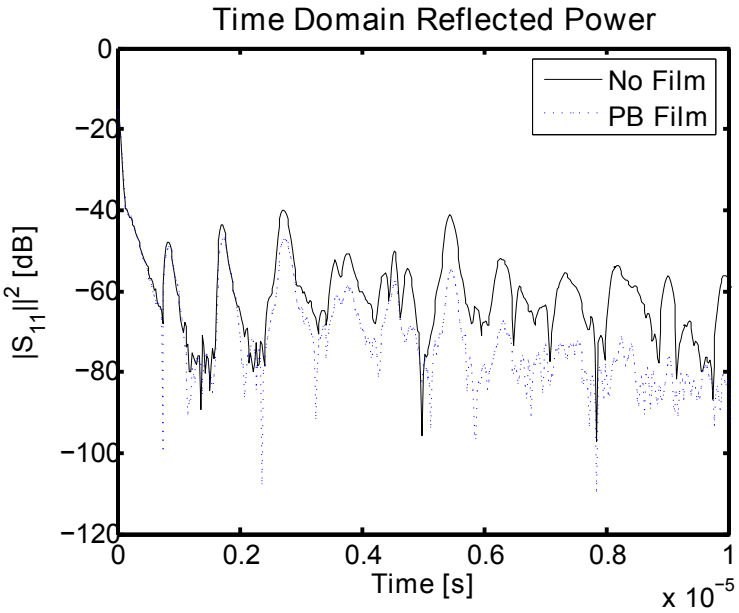


**Figure 7.23:** Time domain responses of a YZ $LiNbO_3$ SAW device both before and after coating with an ozone-sensitive film. The center frequency for this structure is approximately 435 MHz.

We next determined the linear loss coefficient introduced by the PB film, for a device operating at 435 MHz on lithium niobate. We differenced the reflected power point-wise at

each reflection peak. The linear fit is shown in Figure 7.24.

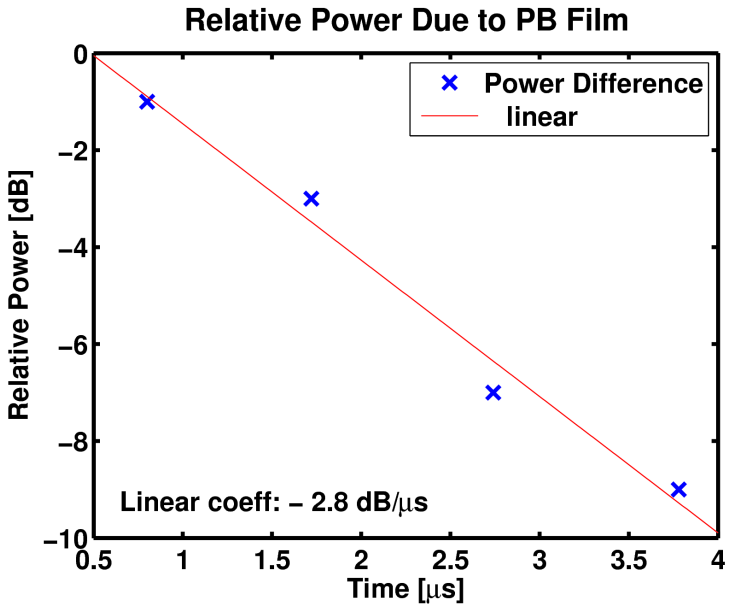


**Figure 7.24:** A linear fit to the difference between magnitudes of reflection peaks from Figure 7.23 gives the power loss with respect to time. The center frequency was approximately 435 MHz.

### 7.3.3 Temperature Sensitivity

We also conducted temperature measurements using the VNA. We again transformed to the time domain to determine the sensitivity (Figure 7.25). Lithium niobate substrates have temperature coefficients of delay (TCD) of approximately -50 to -80 ppm/°C near room temperature, as we and others have reported. We compared the phases of echoes returned from the SAW tags and quantified phase shift sensitivity of about 177 ppm/°C. The responses shown in the preceding temperature comparison were measured during the increase and decrease ramp of a temperature cycle. A Temptronic thermostat system was used to ensure the wafer chuck of the Cascade Microtech probe station reached each temperature set point. There appeared to be some degree of hysteresis in the response, possibly due to a lagging effect of moisture as the substrate temperature was changed relative to the air temperature. This effect can be observed in the mismatch of three of the five pairs of like-colored traces in Figure 7.25. Below a substrate temperature of 10 °C, condensation visibly occurred on the device surface, so we preferred temperature measurements at or

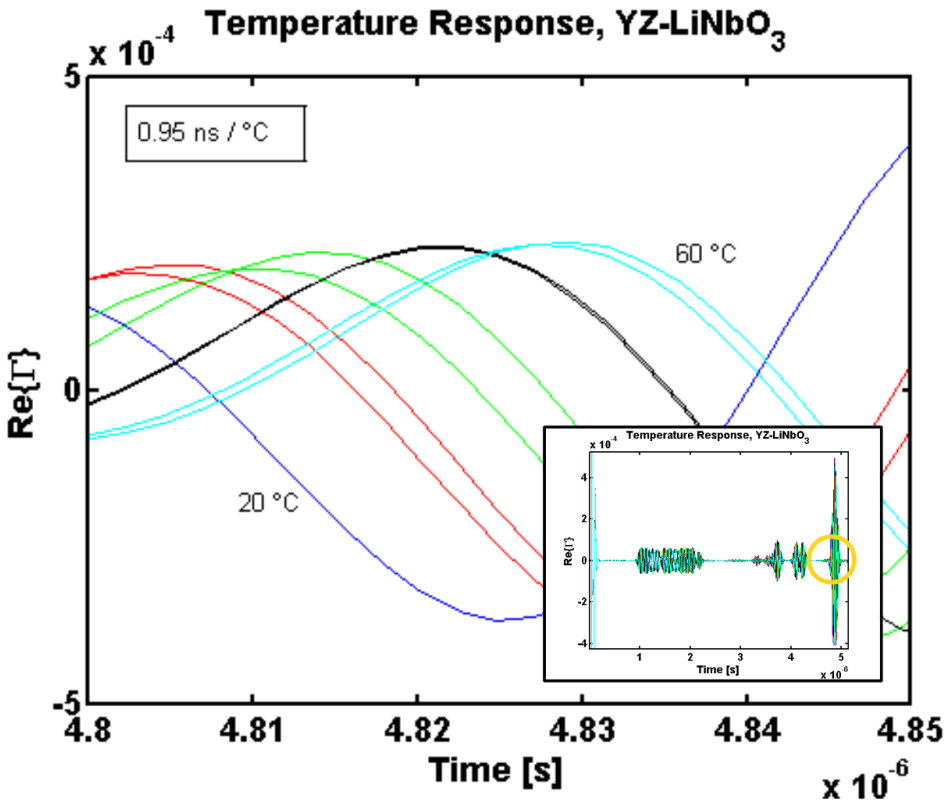


**Figure 7.25:** Real part of the reflection coefficient of a SAW tag sensor versus time (at 10 °C increments from 20 to 60°C). The inset shows the full response.

above the ambient air temperature.

The inset of Figure 7.25 shows the entire response and the reflection that was tracked. For this device, the temperature can change at least 80 °C before absolute phase ambiguity occurs. The device design does allow removal of the phase ambiguity by examination of the entire response (multiple reflector spacings) [49], and simple tracking techniques can be used when the rate of change is sufficiently low during the measurement interval. Using a first backward difference approach to phase tracking, the temperature may change 8 °C per second if the device is polled every 10 seconds. The measurement rate was limited by the data transfer rate from the VNA. Other systems can collect many more samples per second, e.g. the pulser/receiver we showed in Figure 7.15.

We also calculated the group delay for the same data as in Figure 7.25, and it is shown in Figure 7.26. The group delay sensitivity was 105 ppm/°C; approximately 41% less than the phase sensitivity.

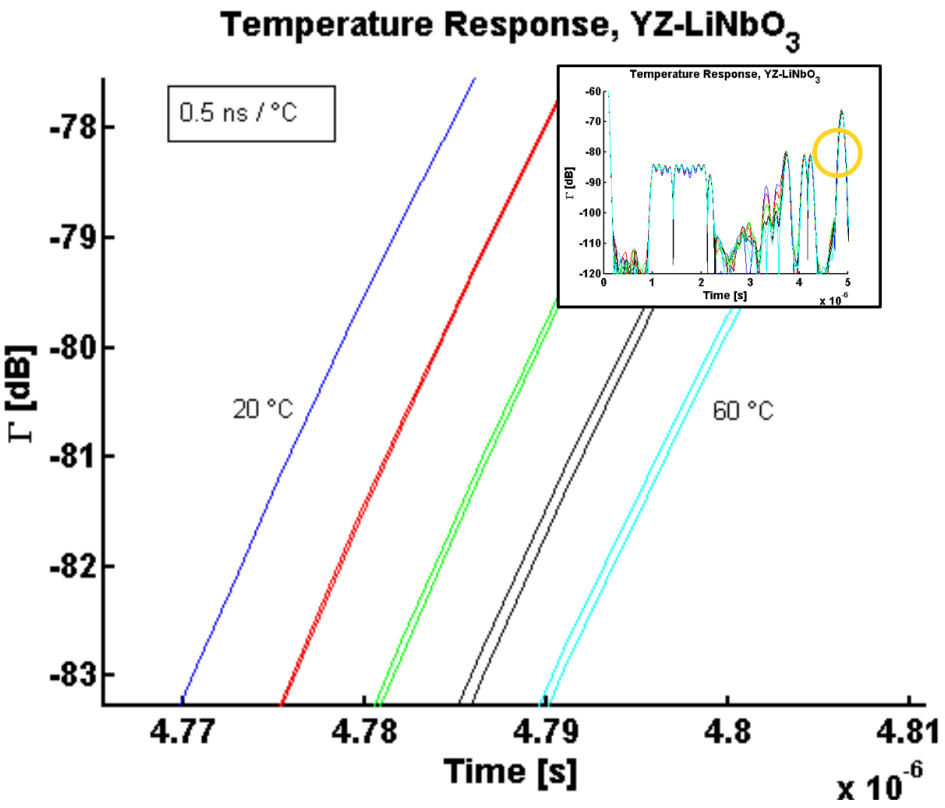


**Figure 7.26:** Reflected power from a SAW tag sensor versus time (at several temperatures: 20 to 60 °C). The inset shows the full response.

### 7.3.4 Phase Tracking

As one means to resolve phase ambiguity for large changes, we adjusted the processing script to retain memory of the last zero crossing point; each subsequent search was limited to one half wavelength from the prior zero crossing. This approach works as long as phase perturbations are less than one zero crossing interval (half cycle) during a sample period. For a 435 MHz device with phase delay of 4 $\mu$s and sampled every 10 seconds, the maximum phase delay rate of change is approximately 27 ppm/sec.

Group delay tracking can be performed in the same way, but we did not follow that approach because the group delay is approximately equal to the phase delay for sufficiently dispersionless changes such as that due to temperature. Methods to improve absolute group delay sensitivity may be derived from radar techniques as discussed in Chapter 6.

**Table 7.2:** Comparison of sensitivities of acoustic wave devices to ozone, using polybutadiene as the sensitive layer. Sensitivities are in units of ppm/min/ppb$O_3$ and represent either relative frequency or relative delay.

| Device | Substrate | Frequency, $f_0$ | $S_m^X$ |
|---|---|---|---|
| QCM | ST Quartz | 10 MHz | 0.002 |
| STW SAWR | ST-X+90° Quartz | 250 MHz | 0.006 |
| Rayleigh SAWDL | Y-Z $LiNbO_3$ | 435 MHz | 1.06 |
| STW SAWDL | 64°Y-X $LiNbO_3$ | 580 MHz | 1.25 |

## *7.4 Results*

In 2009 we reported the ozone sensitivity of a SAW tag delay line operating at 580 MHz [96]. The phase of a particular reflector was monitored versus time as the ozone concentration was controlled stepwise (Figure 7.27).

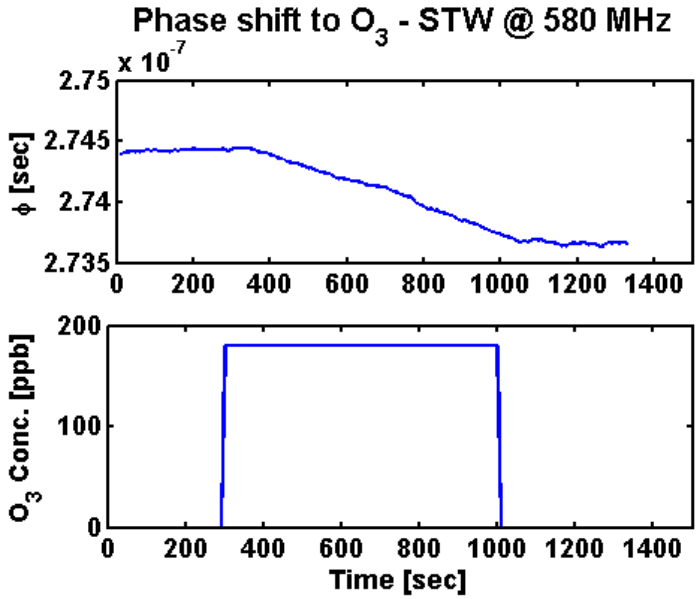


**Figure 7.27:** Plot of the phase delay versus time as a step-wise change of ozone concentration was applied. The device operated at 580 MHz on 64° Y-X $LiNbO_3$.

We compared the average linear coefficients of sensitivity for all device types in Table 7.2. Although the Rayleigh delay line was not the highest frequency device, only half the acoustic aperture, the "ID" path, was used for the ozone measurement. Furthermore the delay time was 1.39 $\mu$s. This gave a queried area (twice traversed) of just 0.0091 cm$^2$.

In addition to the excellent sensitivity, our measurement of the full scattering parameters

over the bandwidth allowed us to show the return loss (Figure 7.22) and other characteristics important to passive devices. High frequency functionalization was important, but we also needed to determine the degree to which the passive sensors are *robust*. Chemical selectivity had already been established for the polybutadiene films, but we still needed to investigate the influence of confounding factors for the passive ozone sensors.

### 7.4.1 Cross-sensitivity

Despite using conditioned air for delivery of the ozone, small fluctuations did occur in the experiments. For example, the relative humidity changed by 10% and the temperature varied several degrees. Furthermore, the particle filter at the intake of the air pump did not remove tiny particles (i.e. $< 10\ \mu$m) from the air stream. These relatively small confounding factors allowed us to gain insight into the challenges the devices will face operating outside the laboratory. We demonstrate that it is possible to measure and compensate for interfering effects to find the component of the response due to ozone attack of a thin film.

We use an acoustic multiplexing approach commonly found in the literature [54]: the aperture is divided into independent paths such that each produces a weaker reflection but with little interference from the response of the neighboring path. Figure 7.28 shows how this was done in our experiments.

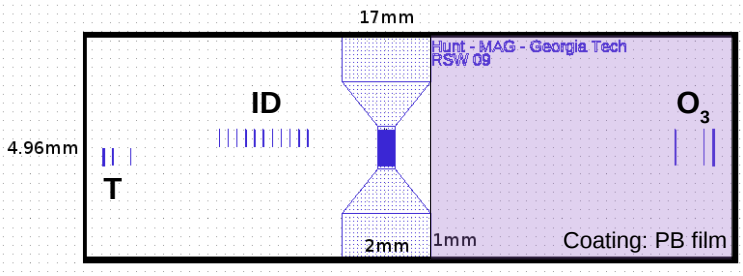


**Figure 7.28:** The ID and temperature (T) reflectors share the acoustic aperture on one side, whereas the ozone path ($O_3$) spans the full aperture.

Due to the aforementioned loss when the SAW propagates in the film-coated region, the "$O_3$" reflector spans the entire acoustic aperture in order to return twice as much energy as from the temperature reflectors. Although this only compensates for approximately 1 $\mu$s of propagation in the film (Figure 7.24), it serves to illustrate a benefit of the multiplexing

approach. Another benefit is that the film can be differentially applied to half of the device, using a convenient tape mask illustrated in Figure 7.4.

#### *7.4.1.1 Temperature*

The author wrote a phase tracking script to follow the zero crossings corresponding to certain reflectors on the device. In Figure 7.29 we tracked the fractional (ppm) phase delay change for two different reflectors, one corresponding to a PB-coated path, and the other to an uncoated path. The differential response due to ozone challenge intervals and also the corresponding slope change due to the concentration is clear. Furthermore, the common mode response due to temperature is also plainly evident in both traces. The total dose

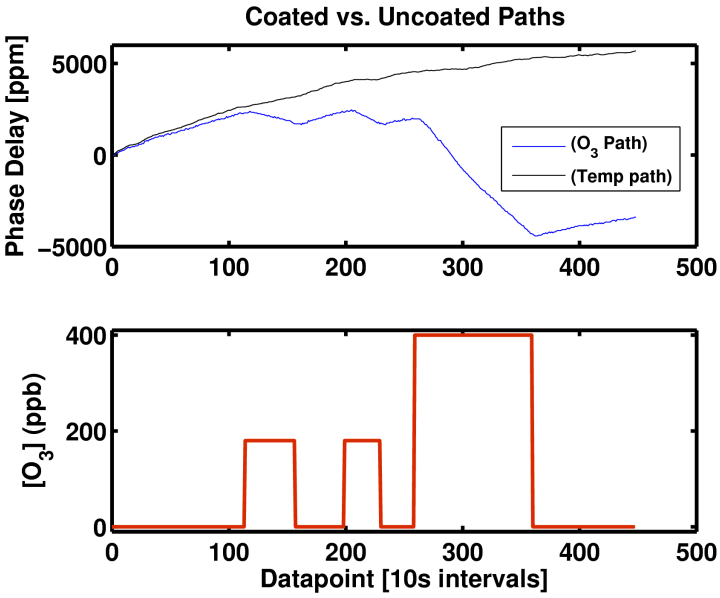


**Figure 7.29:** Phase tracking applied to coated and uncoated paths. The ozone calibrator's concentration setpoint is shown in the lower panel. The duration of the first ozone interval was approximately 500 seconds.

was approximately 150 ppb-hours. One may compare this to the EPA threshold: 75 ppb averaged over 8 hours, or 600 ppb-hours (NAAQS 2008).

We next tracked five different reflection delays alongside the temperature (Figure 7.30). The lesser delays show smaller fractional changes due to ozone and temperature. This is because the received phase is proportional to the distance, giving greater sensitivity at greater delays. The five traces correspond to delays: 1 $\mu$s, 1.16 $\mu$s, and 1.39 $\mu$s from the

"ID" reflectors; as well as 4.16 $\mu$s and 4.79 $\mu$s from the "T" reflectors. Note that in this particular experiment, the coating was reversed from the illustration in Figure 7.28; the PB coating was on the half of the device having the "ID" reflectors, thus the early arrivals were expected to be sensitive to ozone.

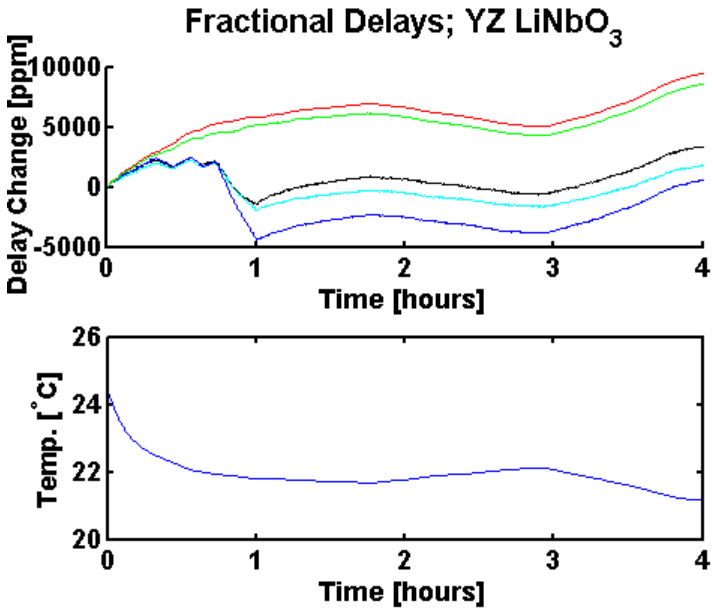


**Figure 7.30:** The effect of the negative temperature coefficient is clearly common to both coated and uncoated paths. Three tracked reflections are displayed for the coated path and two for the uncoated path.

The data collection was allowed to continue with the device resting in ambient air for more than 5 days. The ambient temperature varied no more than 3.4 °C during the entire experiment. During that time, two of the three ozone-altered delays remained clearly separated from the reference delays, although the ozone delays did "recover" toward the reference delays by approximately 50% (Figure 7.31). The first delay (1 $\mu$s) eventually recovered to nearly coincide with the two reference paths, however the average ozone response remained separable from the average response of the references by $75\sigma_{O_3}$. Another effect was the phase delay increase common to all of the delay paths. When comparing the left and right panels, for approximately the same temperature, the right panel shows greater delay. We have observed common delay increase in other devices exposed to the air stream for prolonged periods. We suspect it is due to deposition of particulate matter on the device surface, slowing all surface waves and increasing all delays. Indeed, we did observe a general

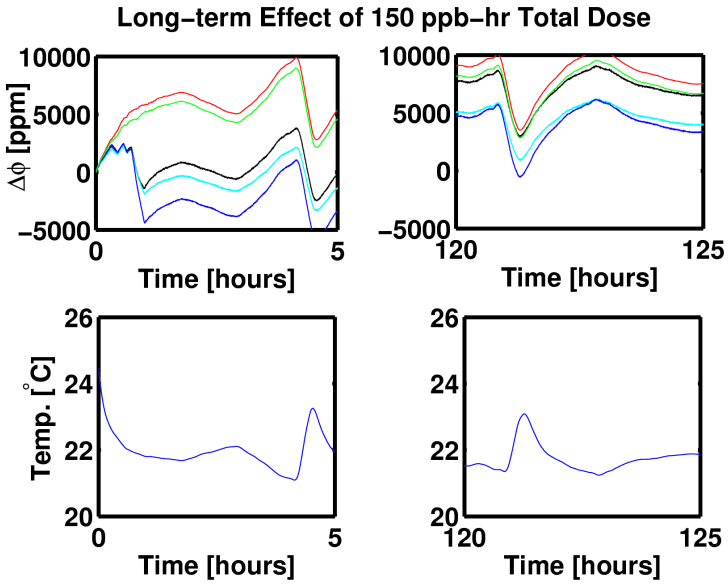


**Figure 7.31:** The first 5 hours after ozone exposure (left) and the last 5 hours (5 days later, right). Two of the three ozone-altered delays never acquiesced to the pre-exposure values.

background trend of delay increase in other data, but as in the data of Figure 7.31, the use of reference paths helped compensate for the effect.

From the collected data we may estimate the temperature coefficient of phase delay, $S_T^\phi$ = -3075 ppm/°C, and the ozone sensitivity, $S_{O_3}^\phi \approx 1$ ppm/min/ppb$O_3$. The indoor temperature change was of order 1 degree, and the relevant ozone concentration was of order 100 ppb$O_3$. Therefore, the signal-to-interfernce ratio (SIR), is about 0.033 in typical indoor conditions. Clearly we must compensate for the confounding effect of temperature.

As a first step, we assume that the temperature coefficient and the ozone coefficient are linear and independent. This allows us to treat the total response as the sum of the independent responses:

$$\Delta X = S_{[O_3]}^X \, \Delta[O_3] + S_T^X \, \Delta T \ , \tag{7.1}$$

where $S_{[O_3]}^X$ is the sensitivity of quantity $X$ to ozone concentration, $[O_3]$, and $T$ is the temperature.

Figure 7.32 shows that this referencing technique can successfully compensate for temperature, at least for the fluctuations encountered in an indoor laboratory.

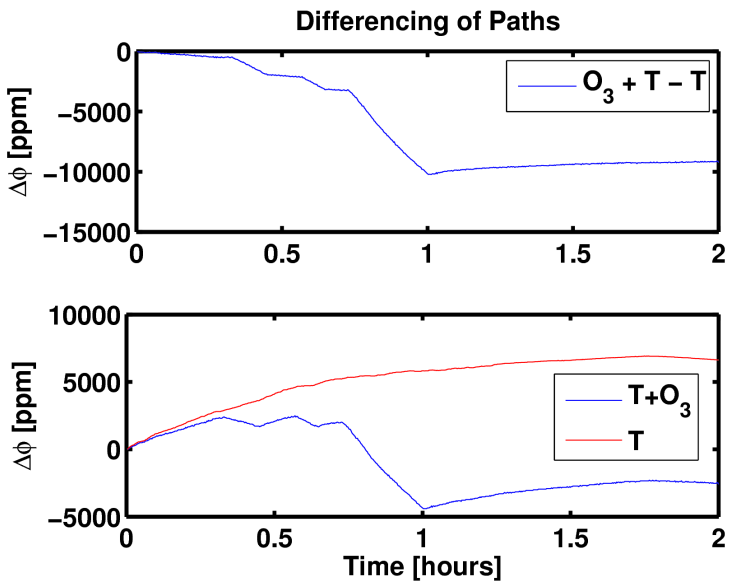


**Figure 7.32:** Subtraction of the normalized temperature response leaves the response primarily due to ozone. The lower panel displays the combined responses for comparison.

By subtracting the two normalized curves, we can see the differential response of the film to ozone exposure. There was a useful range of linear sensitivity for the specified surface functionalization of Rayleigh SAW devices near 435 MHz, and a linear fit to each of the response slopes gave an average linear coefficient of delay: 1.06 ppm/min/ppb$O_3$.

This coefficient allows us to calculate the expected response of the sensor to the effective dose of the EPA standard level, 36000 ppb$O_3$-min: 38160 ppm delay.

### 7.4.2 Limit of Detection

To evaluate the chemical limit of detection, we adopted the IUPAC convention [67] of $3\sigma_N$, corresponding to the reading at which one obtains 99.7% confidence the that a measurement is not due to the noise (assumed normally distributed with variance ${\sigma_N}^2$) present under the "blank" condition, i.e. without the analyte.

Again we used the very sensitive phase measurements at 435 MHz. We quantified the limit of detection using several intervals over which the temperature remained constant and the ozone concentration was set to 0 ppb$O_3$. We then found the standard deviation of the samples. This gave $\sigma_N$ = 22.87 ppm delay and LOD = $3\sigma_N$ = 68.6 ppm delay. For temperature measurements this corresponds to 0.05 °C, and for ozone measurements, it

corresponds to 64.7 ppb$O_3$/min. Specifically, this figure means that at least 64.7 ppb$O_3$ must be present for one minute under the specified conditions in order to obtain conclusive detection (99.7% confidence interval). For dosimetry applications intended to span several days, and considering standards specified by 8-hour averages, a more relevant figure may be in terms of hours: 1.08 ppb$O_3$/hr. Therefore the experimental data reveal a limit of detection better than that required by relevant standards.

We also thought it was interesting to consider the signal-to-interference ratio with respect to the ozone limit of detection and in a particular environment. For the tests conducted in an indoor laboratory, the perturbations due to ambient effects (primarily temperature) provided interference to the ozone signal of interest. We experimentally determined the SIR before and after compensation using the reference: 0.576 vs. 2.88, respectively. This revealed an improvement of 5x or 14 dB after subtracting the reference signal.

### 7.4.3 Dispersion

We also examined the effect of ozone attack in the pulse response data. For the time dispersive (time multiplexed) device of Figure 7.28, the individual components of the response are nominally *dispersionless*. In other words, the dispersed total response comprises several temporally orthogonal reflections. Indeed a general impulse response may be assembled using a basis of translated Dirac delta functions.

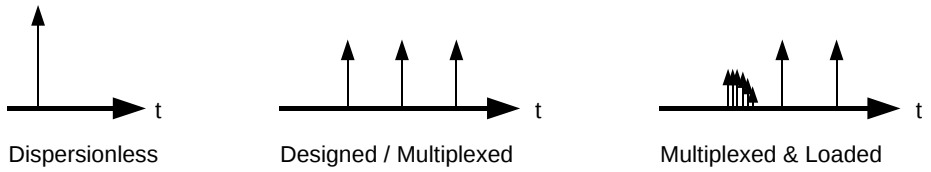


**Figure 7.33:** Examples of dispersionless, multiplexed, and loaded multiplexed impulse responses.

We take as an example the ozone sensor used in the previous section. We have provided 100 responses overlaid in Figure 7.34. The 100 responses correspond to the datapoints between "200" and "300" (16.7 total minutes) in the ozone exposure plot of Figure 7.29. Both the ozone concentration and the temperature changed during that time interval. For the large peaks (reference pulses, "R," 4 $\mu$s to 5 $\mu$s) there was a small translation of the

envelope and phase due to small perturbations of the reference path.

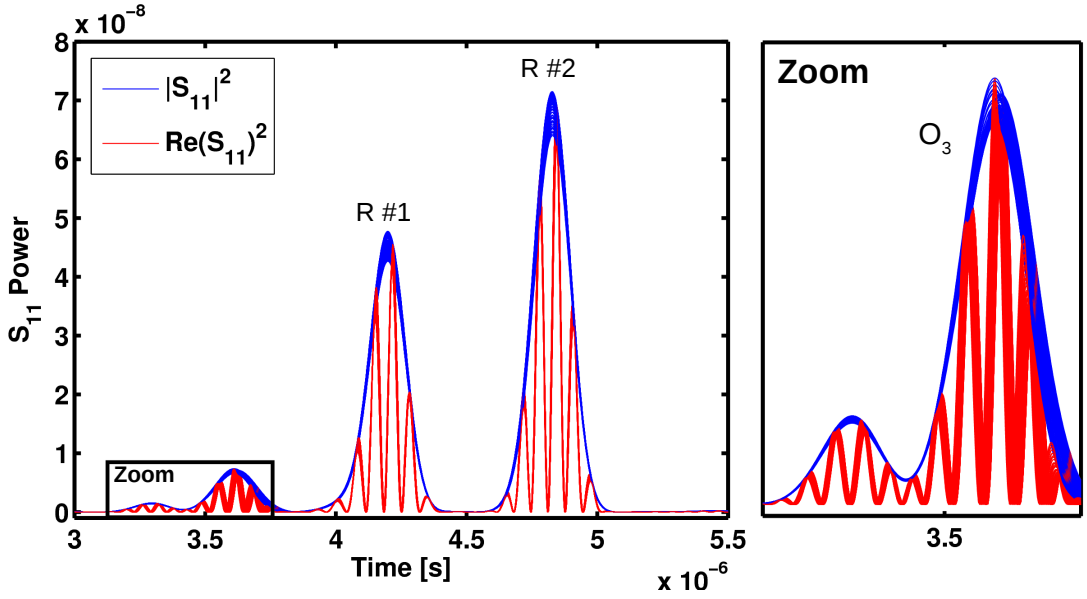


**Figure 7.34:** Comparing the real reflected power and the envelope; the dispersive loading effect is evident only in the early reflection corresponding to the film-laden path (100 measurements during 16.7 minutes).

The dispersion introduced by the reaction of the film is clear in the "$O_3$" reflection of Figure 7.34. The same trend occurs in the earlier reflections (i.e. from the coated "ID" reflectors), but the absolute shift is proportionally less, making it difficult to see on a useful scale. Both the envelope and phase show larger changes than either of the reference reflections.

To quantify the changes to phase delay and group delay, we measured the spreads for three of the reflections over the 16.7 minute time interval. For those *not* associated with the film and ozone attack, the phase and group velocity spreads are identical within the precision of the data (without explicit interpolation[3]). The path designed for ozone attack, i.e. coated with polybutadiene, showed different behavior of the envelope and the phase. The values are compared in Table 7.3.

Because the ozone-specific reflection exhibits dispersion while the other peaks do not,

[3]Interpolation was already implicitly applied by computing the iFFT over a wider bandwidth than the measured data.

**Table 7.3:** Comparison of phase and group delay spreads for reflections corresponding to ozone attack and temperature, etc.

| Reflection | Max. Phase Spread | Max. Group Spread | Result |
|---|---|---|---|
| Ozone | 21 ns (5833 ppm) | 14 ns (3888 ppm) | $v_p \neq v_g$ |
| Reference #1 | 7 ns (1944 ppm) | 7 ns | $v_p = v_g$ |
| Reference #2 | 3 ns (833 ppm) | 3 ns | $v_p = v_g$ |

there are opportunities to distinguish this effect within the multiplexed response of the sensor. If the amplitude of the pulse is to be tracked, for instance, the neighboring peaks can be used as references, and likewise for the delay. We determined the phase delay to be the most sensitive measure of the ozone exposure for this device design and measurement technique. Still other considerations must me made; if the devices are to be used in a wireless environment, one may choose amplitude or phase based upon the channel characteristics, the encoding scheme or compression used in the receiver, etc. It is possible, for instance, to perform interferometry either in software or acoustically (on-chip) to subtract one or more reference signals from the composite return signal. The author has designed additional devices that provide multiple distinct reflection peaks but also feature phase-shifted reflectors to nominally cancel certain peaks prior to loading. There are many ways to "package" the variably dispersed sensor signal into the designed device response, i.e. accommodating sensor dispersion within the designed dispersive response.

We note that, for the ozone sensitive path, the energy (group) spread decreases upon ozone exposure, but the leading edge does not advance. That is, the wave front velocity has not increased, but rather the first moment of the energy has advanced. This observation is causally consistent and corresponds to a reduction in the normal dispersion along that path; the group velocity approaches the phase velocity.

This is indicative of an *unloading* effect: i.e. reduced dispersion. This led to a narrowing of the wave packet without increasing the velocity of the wave front beyond that of the dispersionless case (the substrate SAW velocity). We cannot yet conclude why the unloading effect appears; it contrasts with all of the proof-of-concept experiments using BAW and SAW resonator devices. After considering many possibilities including conductivity of the

film, viscosity, etc., we suspect a subtle difference in film preparation is responsible. In experiments with the packaged SAW delay line devices, we began to reduce the film bake times and determined that this did not adversely affect the performance of the Rayleigh SAW sensors. In fact, it was somewhat advantageous because of a dewetting effect that often occurred during the rapid solvent evaporation associated with baking.

It is possible that residual toluene solvent remained and was attacked by the ozone and the byproducts evaporated. Toluene is a liquid at room temperature and pressure, with a vapor pressure of 20 mmHg at 20°C. Although toluene is a volatile solvent, its vapor pressure is approximately one quarter that of benzene and one half that of isopropyl alcohol at room temperature. Having a correspondingly slower evaporation rate than these other familiar volatile chemicals, and being dispersed with polymer in a thin surface film, the residual toluene may have a very low effective vapor pressure. Therefore baking is justified to help remove it. Although it would be interesting, study of the simultaneous ozone attack of polybutadiene and toluene is beyond the scope of this work. We have demonstrated the utility of the sensors, regardless the direction of the phase shift.

## *7.5 Summary*

In this chapter we reported the functionalization, characterization, and test of surface acoustic wave ozone sensors operating at hundreds of megahertz. We began with reference measurements using quartz crystal microbalances (10 MHz) and SAW resonators (250 MHz). After establishing the mass loading response and linear sensitivity to ozone in the low ppb range relevant to the NIH, EPA, and OSHA, we reported linear sensitivity in that same range even after two weeks of storage in laboratory air.

We then investigated the viability of extension to passive SAW tags. We established the Rayleigh SAW loss coefficient of 2.8 dB/$\mu$s for the ozone sensitive paths, imposing an important constraint for loss-critical applications. Although a thinner film and shorter path might be preferred from a loss perspective, each has a tradeoff: lower saturation dose (useful life), and less absolute phase sensitivity, respectively.

We determined that the group delay and its spread nearly equaled the phase delay

(dispersionless condition), except for the ozone-sensitive wave path, which exhibited lossy dispersion. In the impulse responses we observed an unloading effect that corresponded to reduced dispersion in the ozone sensitive path. This was a repeatable phenomenon useful for the detection of ozone.

By examining the change of phase delay during ozone exposures, we determined the limit of detection to be approximately 65 ppb$O_3$ per minute, which does not appear to be sufficient for real-time applications at relevant concentrations. However, this is at least one order of magnitude better than required for dosimetry over one or more days and at relevant concentrations.

The interference of several confounding effects was expected, but temperature was the largest interferant. The known temperature coefficients of high coupling piezoelectric substrates give coefficients near 100 ppm/°C, two orders of magnitude greater than the ozone sensitivity per ppb$O_3$. We experimentally determined a signal-to-interference ratio improvement of 5x or 14 dB after linear compensation by subtraction of the reference signal. Thus the time dispersed sensor response was of great benefit in this application.

A continued monitoring test spanning several days gave an important indication of device and film stability for indoor dosimetry. This was continued monitoring, indicating the sensors are capable of monitoring a 5-day work week. Although we believe degradation of ozonides and other secondary effects may be responsible for partial recovery of the reflection responses for the ozone coated path, the average ozone response remained separable from the average reference response by $75\sigma_{O_3}$, despite resting in a covered enclosure at ambient conditions. The performance and stability of the sensors supports our objective to enable ozone dosimetry for passive SAW devices operating in the UHF range.

# CHAPTER VIII

# CONCLUSIONS

The overall objective of the work has been to investigate *surface* phononic crystals for use in passive sensing applications, particularly passive SAW tag sensors. Because loss is a critical factor for both range and sensitivity of such sensor devices, the analysis of dispersion and loss in SAW phononic crystals was of primary importance.

We began with review and calculations of SAW dispersion and its relation to material anisotropy, BAW generation, and material inhomogeneity. Because even these relatively simple cases required solution of systems of equations, we employed a finite element solver to compute the acoustic and electric fields in the inhomogeneous and piezoelectric structures. We focused on lithium niobate for relevance to the passive sensor objective, and we also simulated silicon structures found in the literature and which are known to be inexpensive and integrable with conventional electronics.

We then compared the computations to measurements using both a laser acoustic spectrometer and a microwave wafer probe station. To find potentially useful PnC structures, we extended our characterization work beyond the ineffective weak scattering structures; we tried "hole," "filled hole," and "pillar" PnCs exhibiting greater acoustic impedance contrast. We measured each such PnC in two orientations and at multiple wavelengths from 12 to 32 microns. A polymer pillar surface phononic crystal yielded the strongest frequency-selective dispersion we experimentally observed; the height of the scatterers was approximately 3 microns, and $h/\lambda \approx 0.14$.

The experimental PnC characterizations revealed small general attenuation for PnC structures relative to unimpeded paths. This is because the majority of the acoustic energy "tunnels" through the finite extent superlattice, even at frequencies expected to lie within a gap. Furthermore, some energy is reflected, some dissipated, and some scattered to the bulk. To determine the ideal responses (infinite periodic superlattices), we turned to computer

simulations.

Because the fabricated structures yielded only modest dispersion, our finite element simulations were particularly useful. We computed SAW dispersion for periodic structures with various parameters in attempt to find SAW band gaps. We solved the piezoelectric acoustic eigenproblem for single unit cells and devised a total energy criterion analogous to measurement in quantum mechanics. This allowed the software to automatically extract measurable surface modes without *a priori* knowledge of the mode type.

For the 1-D crystals, we did find surface wave band gaps for relatively large aspect ratio structures, i.e. for strong scattering, but bulk modes were not eliminated and complete acoustic gaps were not obtained. For the 2-D lattices, we explored both "dot" and "hatch" lattices of varying thickness and at multiple filling fractions. These simulations were performed for both silicon and lithium niobate substrates. In final analysis of the computed results, we demonstrated the utility of Brillouin diagrams in transducer design for operation within a guided wave band gap, i.e. partial gap, and we used a histogram approach to compute the surface density of states, showing its connection to the surface sensitivity of an acoustic wave device. We expect this approach to evaluation of the sensitivity will be particularly useful for very general PnCs having analytically intractible band structures.

Considering applications, the computations for both strongly scattering PnCs and more conventional weakly scattering reflector arrays did not reveal a clear need for the canonical surface phononic crystals. We found that it was advantageous to encode information into low $Q$ responses rather than using typical resonator approaches. Therefore we leveraged the more conventional dispersive SAW approach (using weak reflection) that was historically found in radar pulse compressors and passive SAW tags. Through application of the transmission line approach to compute device responses, we found that the dispersion of chirp gratings and discrete phase encoded gratings allowed spatial multiplexing of sensor information and also increased duration bandwidth products – an important measure in compressive tag readers. Furthermore, we highlighted the distinction between intentional dispersion and attenuation useful for compression and processing gain (as achieved by prescribed placement of "defects") in contrast to parasitic dispersion and loss (such as that

encountered in low quality materials).

Finally, we returned to the ozone sensing application to first make use of a relatively simple dispersive design. We decided to adopt a well-known dispersive multiplexing scheme using pulse position coding and separate delay paths in order to subtract linear confounding effects. After our first tests with ppb ozone concentrations demonstrated the increased sensitivity achieved with SAW resonators relative to QCMs, we worked with multiplexed Rayleigh mode SAW devices (e.g. Y-Z cut LiNbO3), which showed less loss compared to other modes when operating between 400 MHz and 600 MHz using a polybutadiene sensing layer less than 500 nanometers thick. In the course of this experimental work, we established a limit of detection for the devices (65 ppb$O_3$ $\text{min}^{-1}$), and we showed that subtraction of a reference signal within the dispersive response reduced the cross-sensitivity to temperature fluctuations by a factor of five. Data collected over 120 hours of exposure indicated the physical and chemical stability of the sensors allow continuous operation indoors.

# REFERENCES


[1] "Ambient monitoring program." `http://www.georgiaair.org/amp/`.

[2] Adibi, A., Lin, S.-Y., and Scherer, A., eds., *Two-dimensional phononic crystal slab defect mode micromechanical resonators*, vol. 7223, SPIE, 2009.

[3] Anachkov, M. P., Rakovsky, S. K., and Zaikov, G. E., "Ozonolysis of polybutadienes with different microstructure in solution," *Journal of Applied Polymer Science*, vol. 104, no. 1, pp. 427–433, 2007.

[4] Anhorn, M., Engan, H., and Ronnekleiv, A., "New SAW velocity measurements on y-cut $LiNbO_3$," in *IEEE 1987 Ultrasonics Symposium*, pp. 279–284, 1987.

[5] Ash, E. A., "Surface wave grating reflectors and resonators," IEEE Symposium on Microwave Theory and Techniques, (Newport Beach, CA), May 1970.

[6] Auld, B., *Acoustic Fields and Waves in Solids*, vol. I. John Wiley & Sons, Inc., 1973.

[7] Auld, B., *Acoustic Fields and Waves in Solids*, vol. II, pp. 92, 275–285, 102–103, 114–131. Malabar, FL: Krieger Publishing Company, 1973, 2nd ed. 1990.

[8] Auld, B., Kunkel, H., Shui, Y., and Wang, Y., "Dynamic behavior of periodic piezoelectric composites," in *1983 Ultrasonics Symposium*, pp. 554 – 558, 1983.

[9] Benchabane, S., Khelif, A., Rauch, J.-Y., Robert, L., and Laude, V., "Evidence for complete surface wave band gap in a piezoelectric phononic crystal," *Physical Review E (Statistical, Nonlinear, and Soft Matter Physics)*, vol. 73, no. 6, p. 065601, 2006.

[10] Bendickson, J. M., Dowling, J. P., and Scalora, M., "Analytic expressions for the electromagnetic mode density in finite, one-dimensional, photonic band-gap structures," *Phys. Rev. E*, vol. 53, pp. 4107–4121, Apr 1996.

[11] Bernal, M. P., Roussey, M., Baida, F., Benchabane, S., Khelif, A., and Laude, V., *Ferroelectric Crystals for Photonic Applications*, ch. Photonic and Phononic Band Gap Properties of Lithium Niobate, pp. 307–336. Springer, 2009.

[12] Black, D., Harley, R., Hering, S., and Stolzenburg, M., "A new, portable, real-time ozone monitor," *Environmental Science & Technology*, vol. 34, pp. 3031–3040, JUL 15 2000.

[13] Brauer, M. and Brook, J., "Ozone personal exposures and health effects for selected groups residing in the Frazer Valley," *Atmos Env*, vol. 31, pp. 2113–2121, 1997.

[14] Brekhovskikh, L. M., "On the Attenuation of Rayleigh Waves during Propagation Along an Uneven Surface," *Soviet Physics Doklady*, vol. 4, pp. 150–+, Jan. 1959.

[15] Campbell, C., *Surface Acoustic Wave Devices for Mobile and Wireless Communications*, p. 601. Academic Press, 1998.

[16] Corso, C. D., Dickherber, A., and Hunt, W. D., "An investigation of antibody immobilization methods employing organosilanes on planar zno surfaces for biosensor applications," *Biosensors and Bioelectronics*, vol. 24, no. 4, pp. 805 – 811, 2008.

[17] Cross, P. S. and Schmidt, R. V., "Coupled surface-acoustic-wave resonators," *Bell System Technical Journal*, 1977.

[18] Deflorian, F., Rossi, S., and Fedrizzi, L., "Silane pre-treatments on copper and aluminium," *Electrochimica Acta*, vol. 51, no. 27, pp. 6097 – 6103, 2006. Charge Transfer at Electrochemical Interfaces "Two Hundred Years of Electrolysis".

[19] Dowling, J. P. and Bowden, C. M., "Atomic emission rates in inhomogeneous media with applications to photonic band structures," *Phys. Rev. A*, vol. 46, pp. 612–622, Jul 1992.

[20] Durgin, G., *Space-time wireless channels*. Prentice Hall communications engineering and emerging technologies series, Prentice Hall PTR, 2003.

[21] Edmonson, P. J. and Campbell, C. K., "Encoded saw rfid tags and sensors for multi-user detection using idt finger phase modulation." U.S. Patent No. 6827281, December 2004.

[22] Edmonson, P. J. and Campbell, C. K., "Dual track surface acoustic wave rfid/sensor." U.S. Patent No. 7005964, February 2006.

[23] Edmonson, P. J. and Hunt, W. D., "Sensing systems utilizing acoustic wave devices." U.S. Patent No. 7608978, October 2009.

[24] Edmonson, P. J., Hunt, W. D., Corso, C. D., Dickherber, A., and Csete, M. E., "Acoustic wave sensor assembly utilizing a multi-element structure." U.S. Patent No. 7771987, August 2010.

[25] Edmonson, P., Hunt, W., Stubbs, D., and Lee, S., "Analogies between digital radio and chemical orthogonality as a method for enhanced analysis of molecular recognition events," *International Journal of Molecular Science*, vol. 9, no. 2, pp. 154–168, 2008.

[26] Enguang, D., "Theory and implementation of wireless transponders," *Microwave Theory and Techniques, IEEE Transactions on*, vol. 49, pp. 823–826, Apr 2001.

[27] Fog, H. and Rietz, B., "Piezoelectric Crystal Detector for the Monitoring of Ozone in Working Environments," *Analytical Chemistry*, vol. 57, no. 13, pp. 2634–2638, 1985.

[28] Friedt, J.-M., Droit, C., Martin, G., and Ballandras, S., "A wireless interrogation system exploiting narrowband acoustic resonator for remote physical quantity measurement," *Review of Scientific Instruments*, vol. 81, no. 1, p. 014701, 2010.

[29] Furstenberg, R., Kendziora, C. A., Stepnowski, J., Stepnowski, S. V., Rake, M., Papantonakis, M. R., Nguyen, V., Hubler, G. K., and McGill, R. A., "Stand-off detection of trace explosives via resonant infrared photothermal imaging," *Applied Physics Letters*, vol. 93, no. 22, p. 224103, 2008.

[30] Grate, J. W., Rose-Pehrsson, S. L., Venezky, D. L., Klusty, M., and Wohltjen, H., "Smart sensor system for trace organophosphorus and organosulfur vapor detection employing a temperature-controlled array of surface acoustic wave sensors, automated sample preconcentration, and pattern recognition," *Analytical Chemistry*, vol. 65, no. 14, pp. 1868–1881, 1993.

[31] Hartley, R., "Transmission of information," 1928.

[32] Hartmann, C., "A global SAW ID tag with large data capacity," in *Ultrasonics Symposium, 2002. Proceedings. 2002 IEEE*, vol. 1, pp. 65–69 vol.1, Oct. 2002.

[33] Hartmann, C., Brown, P., and Bellamy, J., "Design of global SAW RFID tag devices," in *Proc. 2nd Int. Symp. Acoustic Wave Devices for Future Mobile Communications Systems*, (Chiba, Japan), pp. 15–19, March 2004.

[34] Hartmann, C. and Claiborne, L., "Fundamental limitations on reading range of passive IC-based RFID and SAW-based RFID," in *RFID, 2007. IEEE International Conference on*, pp. 41–48, March 2007.

[35] Hashimoto, K., *Surface Acoustic Wave Devices in Telecommunications: Modelling and Simulation*, pp. 266–268. Springer-Verlag, 2000.

[36] Hearn, A. G., "The absorption of ozone in the ultra-violet and visible regions of the spectrum," *Proceedings of the Physical Society*, vol. 78, no. 5, 1961.

[37] Huang, Y.-S., Chen, Y.-Y., and Wu, T.-T., "A passive wireless hydrogen surface acoustic wave sensor based on Pt-coated ZnO nanorods," *Nanotechnology*, vol. 21, no. 9, p. 095503, 2010.

[38] Hunsinger, B., "Research to provide a theoretical determination of surface acoustic wave velocity and impedance differences between metal strips and free surface regions of metallic gratings," Tech. Rep. RADC-TR-81-173, Rome Air Development Center, University of Illinois at Urbana Champaign, July 1981.

[39] Hunt, W., Stubbs, D., and Lee, S.-H., "Time-dependent signatures of acoustic wave biosensors," *Proceedings of the IEEE*, vol. 91, pp. 890 – 901, june 2003.

[40] Joannopoulos, J. D., Johnson, S. G., Win, J. N., and Meade, R. D., *Photonic Crystals: Molding the Flow of Light*. Princeton University Press, 2008.

[41] Josse, F., Andle, J., Vetelino, J., Dahint, R., and Grunze, M., "Theoretical and experimental study of mass sensitivity of PSAW-APMs on ZX-LiNbO3," *Ultrasonics, Ferroelectrics and Frequency Control, IEEE Transactions on*, vol. 42, pp. 517 –524, jul 1995.

[42] Keller, H., Simak, P., Schrepp, W., and Dembowski, J., "Surface chemistry of thiols on copper: an efficient way of producing multilayers," *Thin Solid Films*, vol. 244, no. 1-2, pp. 799 – 805, 1994.

[43] Khelif, A., Choujaa, A., Rauch, J.-y., Petreni, V., Moubchir, H., Benchabane, S., and Laude, V., "The omnisaw device concept (omnisaw: Omnidirectional band gap for surface acoustic wave)," in *Ultrasonics Symposium, 2008. IUS 2008. IEEE*, pp. 304 –307, Nov. 2008.

[44] Khelif, A., Achaoui, Y., Benchabane, S., Laude, V., and Aoubiza, B., "Locally resonant surface acoustic wave band gaps in a two-dimensional phononic crystal of pillars on a surface," *Phys. Rev. B*, vol. 81, p. 214303, Jun 2010.

[45] Kim, Y. and Hunt, W. D., "Acoustic fields and velocities for surface-acoustic-wave propagation in multilayered structures: An extension of the Laguerre polynomial approach.," *Journal of Applied Physics*, vol. 68, no. 10, p. 4993, 1990.

[46] Klauder, J. R., "Theory & design of chirp radars," *Bell System Tech. Journal*, vol. 39, no. 745, 1960.

[47] Kone, I., Domingue, F., Reinhardt, A., Jacquinot, H., Borel, M., Gorisse, M., Parat, G., Casset, F., Pellissier-Tanon, D., Carpentier, J. F., Buchaillot, L., and Dubus, B., "Guided acoustic wave resonators using an acoustic bragg mirror," *Applied Physics Letters*, vol. 96, no. 22, p. 223504, 2010.

[48] Kushwaha, M. S., Halevi, P., Dobrzynski, L., and Djafari-Rouhani, B., "Acoustic band structure of periodic elastic composites," *Phys. Rev. Lett.*, vol. 71, pp. 2022–2025, Sep 1993.

[49] Kuypers, J., Reindl, L., Tanaka, S., and Esashi, M., "Maximum accuracy evaluation scheme for wireless SAW delay-line sensors," *Ultrasonics, Ferroelectrics and Frequency Control, IEEE Transactions on*, vol. 55, pp. 1640–1652, July 2008.

[50] Länge, K., Rapp, B. E., and Rapp, M., "Surface acoustic wave biosensors: a review," *Analytical and Bioanalytical Chemistry*, vol. 391, pp. 1509–1519, July 2008.

[51] Laude, V., Robert, L., Daniau, W., Khelif, A., and Ballandras, S., "Surface acoustic wave trapping in a periodic array of mechanical resonators," *Applied Physics Letters*, vol. 89, Aug 21 2006.

[52] Laude, V., Wilm, M., Benchabane, S., and Khelif, A., "Full band gap for surface acoustic waves in a piezoelectric phononic crystal," *Phys. Rev. E*, vol. 71, p. 036607, Mar 2005.

[53] Lee, K., Parkhurst, W. J., Xue, J. P., Ozkaynak, A. H., Neuberg, D., and Spengler, J. D., "Outdoor/indoor/personal ozone exposures of children in Nashville, Tennessee," *Journal of the Air & Waste Management Association*, vol. 54, pp. 352–359, 2004.

[54] Lee, K., Wang, W., Kim, T., and Yang, S., "A novel 440 MHz wireless SAW microsensor integrated with pressure-temperature sensors and ID tag," *Journal of Micromechanics and Microengineering*, vol. 17, no. 3, pp. 515–523, 2007.

[55] Lee, S.-H., *Theoretical and Experimental Characterization of Time-Dependent Signatures of Acoustic Wave Based Biosensors*. PhD thesis, School of Electrical and Computer Engineering, Georgia Institute of Technology, 2006.

[56] Lee, S. H., Massey, E., Westafer, R., and Hunt, W., "A novel method to investigate dependence of SAW resonator sensor signatures on localized surface perturbations," in *Sensors, 2006. 5th IEEE Conference on*, pp. 1203–1206, Oct. 2006.

[57] Lefebvre, J. E., Zhang, V., Gazalet, J., and Gryba, T., "Conceptual advantages and limitations of the laguerre polynomial approach to analyze surface acoustic waves in semi-infinite substrates and multilayered structures," *Journal of Applied Physics*, vol. 83, no. 1, pp. 28–34, 1998.

[58] Liu, J., Dierauer, P. P., and Repko, M. A., "Passive wireless acoustic wave chemical sensor." U.S. Patent No. 7205701, April 2007.

[59] Liu, L. J. S., Olson, M. P., Allen, G. A., Koutrakis, P., McDonnell, W. F., and Gerrity, T. R., "Evaluation of the Harvard ozone passive sampler on human-subjects indoors," *Environmental Science & Technology*, vol. 28, pp. 915–923, 1994.

[60] Maslov, V. I., "Use of radar methods in increasing sensitivity in emission spectral analysis. Part I. Use of correlation," *Journal of Applied Spectroscopy*, vol. 2, pp. 131–134, 1965. 10.1007/BF00655114.

[61] Massey, E. W., "Measurement of material Q in Rayleigh waves with a laser based acoustic spectrometer," Master's thesis, School of Electrical and Computer Engineering, Georgia Institute of Technology, 2006.

[62] Matthews, H., *Surface wave filters: design, construction, and use*, p. 434. John Wiley & Sons, 1977.

[63] Maznev, A. A., "Band gaps and Brekhovskikh attenuation of laser-generated surface acoustic waves in a patterned thin film structure on silicon," *Phys. Rev. B*, vol. 78, p. 155323, Oct 2008.

[64] Maznev, A. A. and Every, A. G., "Surface acoustic waves in a periodically patterned layered structure," *Journal of Applied Physics*, vol. 106, no. 11, p. 113531, 2009.

[65] Maznev, A. A. and Every, A. G., "Surface acoustic waves with negative group velocity in a thin film structure on silicon," *Applied Physics Letters*, vol. 95, no. 1, p. 011903, 2009.

[66] McHale, G., Martin, F., and Newton, M. I., "Mass sensitivity of acoustic wave devices from group and phase velocity measurements," *Journal of Applied Physics*, vol. 92, no. 6, pp. 3368–3373, 2002.

[67] McNaught, A. D. and Wilkinson, A., eds., *Compendium of Chemical Terminology*. Oxford: Blackwell Scientific Publications, 2nd ed., 1997.

[68] Milsom, R. F., Reilly, N. H. C., and Redwood, M., "Analysis of generation and detection of surface and bulk acoustic waves by interdigital transducers," *IEEE Transactions on Sonics Ultrasonics*, vol. 24, pp. 147–166, May 1977.

[69] Milton, G. W., Eyre, D. J., and Mantese, J. V., "Finite frequency range Kramers-Kronig relations: Bounds on the dispersion," *Phys. Rev. Lett.*, vol. 79, pp. 3062–3065, Oct 1997.

[70] Mobley, J., "Finite-bandwidth Kramers-Kronig relations for acoustic group velocity and attenuation derivative applied to encapsulated microbubble suspensions," *The Journal of the Acoustical Society of America*, vol. 121, no. 4, pp. 1916–1923, 2007.

[71] Mobley, J., Waters, K. R., Hughes, M. S., Hall, C. S., Marsh, J. N., Brandenburger, G. H., and Miller, J. G., "Kramers–Kronig relations applied to finite bandwidth data from suspensions of encapsulated microbubbles," *The Journal of the Acoustical Society of America*, vol. 108, no. 5, pp. 2091–2106, 2000.

[72] Mohammadi, S., Eftekhar, A. A., Khelif, A., Moubchir, H., Westafer, R., Hunt, W. D., and Adibi, A., "Complete phononic bandgaps and bandgap maps in two-dimensional silicon phononic crystal plates," *Electronics Letters*, vol. 43, pp. 898–899, Aug 2 2007.

[73] Mohammadi, S., Eftekhar, A. A., Khelif, A., Hunt, W. D., and Adibi, A., "High-Q micromechanical resonators in a two-dimensional phononic crystal slab," *Applied Physics Letters*, vol. 94, no. 1, 2009.

[74] Ostermayer, G., "Correlative signal processing in wireless SAW sensor applications to provide multiple-access capability," *Microwave Theory and Techniques, IEEE Transactions on*, vol. 49, pp. 809 –816, Apr. 2001.

[75] Pasternak, M. and Pietrasinski, J., "Quasi-loop antenna for SAW RFID device," in *Microwaves, Radar and Remote Sensing Symposium, 2008. MRRS 2008*, pp. 201–203, Sept. 2008.

[76] Plessky, V. and Reindl, L., "Review on SAW RFID tags," *Ultrasonics, Ferroelectrics and Frequency Control, IEEE Transactions on*, vol. 57, pp. 654 –668, Mar. 2010.

[77] Plessky, V., Biryukov, S., and Koskela, J., "Harmonic admittance and dispersion equations - the theorem," vol. 1, pp. 159 –162 vol.1, Oct. 2000.

[78] Pohl, A., "A review of wireless SAW sensors," *Ultrasonics, Ferroelectrics and Frequency Control, IEEE Transactions on*, vol. 47, pp. 317–332, Mar 2000.

[79] Rayleigh, L., "On the reflection of light from a regularly stratied medium," *Proc. Royal Society of London*, vol. 93, pp. 565–577, 1917.

[80] Reindl, L., Scholl, G., Ostertag, T., Scherr, H., Wolff, U., and Schmidt, F., "Theory and application of passive saw radio transponders as sensors," *Ultrasonics, Ferroelectrics and Frequency Control, IEEE Transactions on*, vol. 45, pp. 1281 –1292, Sept. 1998.

[81] Reindl, L. and Shrena, I., "Wireless measurement of temperature using surface acoustic waves sensors," *Ultrasonics, Ferroelectrics and Frequency Control, IEEE Transactions on*, vol. 51, pp. 1457 – 1463, Nov. 2004.

[82] Rogers, J. A., Maznev, A. A., Banet, M. J., and Nelson, K. A., "Optical generation and characterization of acoustic waves in thin films: Fundamentals and applications," *Annual Review of Materials Science*, vol. 30, no. 1, pp. 117–157, 2000.

[83] Rosenbaum, J., *Bulk acoustic wave theory and devices*. The Artech House acoustics library, Artech House, 1988.

[84] Sato, A., Menges, B., and Knoll, W., "The importance of the photonic mode density in bioassays based on evanescent optical waves," *Journal of Applied Physics*, vol. 105, no. 1, p. 014701, 2009.

[85] Sauerbrey, G., "Use of vibrating quartz for thin film weighing and microweighing (in German)," *Z. Phys.*, vol. 155, pp. 206–222, 1959.

[86] Schulz, M. B., "Temp. effects in surface wave devices," in *IEEE 1972 Ultrasonics Symposium*, Oct. 1972.

[87] Seifert, F., Bulst, W.-E., and Ruppel, C., "Mechanical sensors based on surface acoustic waves," *Sensors and Actuators A: Physical*, vol. 44, no. 3, pp. 231 – 239, 1994.

[88] Sievenpiper, D. F., "Steerable leaky wave antenna capable of both forward and backward radiation." U.S. Patent No. 7071888, July 2006.

[89] Slobodnik, A., "Microwave acoustics handbook, volume 2, surface wave velocities - numerical data," Tech. Rep. AFCRL-TR-74-0536, Air Force Cambridge Research Laboratories, Hanscom AFB, MA 01731, October 1974.

[90] Smith, P., "Dyadic Green's functions for multi-layer SAW substrates," *Ultrasonics, Ferroelectrics and Frequency Control, IEEE Transactions on*, vol. 48, pp. 171 –179, jan. 2001.

[91] Soljačić, M., Johnson, S. G., Fan, S., Ibanescu, M., Ippen, E., and Joannopoulos, J. D., "Photonic-crystal slow-light enhancement of nonlinear phase sensitivity," *J. Opt. Soc. Am. B*, vol. 19, no. 9, pp. 2052–2059, 2002.

[92] Stubbs, D. D., Lee, S.-H., and Hunt, W. D., "Investigation of cocaine plumes using surface acoustic wave immunoassay sensors," *Analytical Chemistry*, vol. 75, no. 22, pp. 6231–6235, 2003.

[93] Stutzman, W. L. and Thiele, G., *Antenna theory and design*. J. Wiley, 1998.

[94] Wang, W., Lee, K., Kim, T., Park, I., and Yang, S., "A novel wireless, passive $CO_2$ sensor incorporating a surface acoustic wave reflective delay line," *Smart Materials and Structures*, vol. 16, no. 4, pp. 1382–1389, 2007.

[95] Wang, Y. and Auld, B., "Acoustic wave propagation in one-dimensional periodic composites," in *IEEE 1985 Ultrasonics Symposium*, pp. 637 – 641, 1985.

[96] Westafer, R., Levitin, G., Hess, D., Bergin, M., Edmonson, P., and Hunt, W., "Functionalization of high frequency saw rfid devices for ozone dosimetry," in *Sensors, 2009 IEEE*, pp. 1747 –1752, 25-28 2009.

[97] Westafer, R., Mohammadi, S., Adibi, A., and Hunt, W., "Computation of surface acoustic wave dispersion and band gaps," in *COMSOL Conference 2009*, Oct. 2009.

[98] Westafer, R. S., Levitin, G., Hess, D. W., Bergin, M. H., Edmonson, P. J., and Hunt, W. D., "Ozone sensors for real-time passive wireless application," in *EPA International Environmental Nanotechnology Conference*, Oct. 2008.

[99] Wohltjen, H. and Dessy, R., "Surface acoustic wave probes for chemical analysis. I. Introduction and instrument description," *Analytical Chemistry*, vol. 51, pp. 1458–1464, August 1979.

[100] Wong, K. and of Electrical Engineers, I., *Properties of lithium niobate*. EMIS datareviews series, INSPEC/Institution of Electrical Engineers, 2002.

[101] Yamamoto, Y., Nishihara, H., and Aramaki, K., "Self-assembled layers of alkanethiols on copper for protection against corrosion," *Journal of The Electrochemical Society*, vol. 140, no. 2, pp. 436–443, 1993.

# VITA

Ryan Sloan Westafer was born in Pensacola, Florida and graduated from Gulf Breeze High School in 2001. He then enrolled at Georgia Tech as a President's Scholar. During the academic semesters Ryan led a robotics team, served in leadership roles in the Eta Kappa Nu and Tau Beta Pi honor societies, engaged in freelance IT consulting, and attempted to court his future wife, Kristin, while she attended Mississippi State University in pursuit of her Doctorate of Veterinary Medicine. During the summers, Ryan served as a research assistant under the direction of Dr. Anil Raj at the Institute for Human and Machine Cognition in Pensacola, FL. In 2005, he graduated from Georgia Tech with a Bachelor of Science degree in Computer Engineering and the designation, "With Highest Honor."

After graduation Ryan took an internship position with Broadcom Corporation in Duluth, GA before returning to Tech in pursuit of the Ph.D. degree. In 2006 he received the MSECE degree while conducting research under the advisement of Professor Bill Hunt. During his doctoral study, Ryan investigated properties of surface phononic crystals for application to surface acoustic wave (SAW) sensors. One outcome was the use of a passive and dispersive SAW sensor to detect ozone in the parts-per-billion range. At conferences he received awards for oral presentations and for a poster.

Ryan's diverse professional interests also include embedded systems, open-source software, and entrepreneurship. His recent personal interests included volleyball, several student/professional organizations, InVenture Prize, Enterprise 2 Empower, self-study, and independent consulting. Past hobbies included: cooking, snowboarding, flatland BMX, windsurfing, arc welding, flying, and making music. Spiritually, Ryan is a follower of Christ.